Modelling Of Protostellar Jets Using Intense Lasers

Jonathan Nicholas Waugh

PhD

The University of York

Physics

September 2010

Abstract

Using telescopes such as the Hubble Space Telescope, astronomers observe parsec-scale plasma jets emerging from Young Stellar Objects and colliding with the interstellar medium, generating shock structures. A set of mathematically rigorous scaling transformations exists allowing dynamic scaled models of radiative, yet otherwise ideal, hydrodynamic flows to be created in the laboratory. In this thesis two experiments are presented in which plasma jets were produced using high-intensity lasers. In the first of these, the effects on jet collimation of radiative emission and the presence of a gaseous ambient medium were studied, with a view to learning about the effects of these factors on YSO jets by studying their scaled laboratory counterparts. The second experiment was designed to be similar to the first in order to investigate applying the scaling relations to scaling between laboratory experiments.

Previous work in this area has shown that jets made in vacuo from materials with a higher mean atomic number form narrower, better-collimated jets (e.g. [1]). Also, for jets propagating into a gas, shock structures similar to those seen in simulations of the interaction of a YSO jet with the interstellar medium have been observed (e.g. [2]). In this thesis, both of these results are replicated, and the collimation work extended with a study of the collimation of jets in 50 mb He gas.

The energies of the laser pulses used in the first experiment were over an order of magnitude lower than those used in previous studies of cylindrically-symmetric jets. This gives the replication and development of previous work added significance, showing that the same physics can be used to describe the behaviour of a plasma on a smaller energy scale and demonstrating that jet modelling experiments can potentially be done using university-scale laser facilities.

Contents

List of Tables

List of Figures

Acknowledgements

Over the four years and a half years that it has taken to carry out this PhD, many have been involved whom I would like to acknowledge and thank here. Some names, owing to involvement with the work of this thesis at different levels, appear more than once.

I would like to thank God first of all for giving me this project to work on and sustaining me through it to the end. Next, I would like to express my thanks to my PhD supervisor Nigel who has helped in many ways including arranging funding for the thesis and a travel grant, organising and planning experiments, advising on papers to read, giving instruction and insight on analysis of experimental results, and proof-reading an annual report, a conference proceedings paper and most of this thesis. Third, I would like to thank my parents. They have not only been a sympathetic ear on the phone, but their scientific knowledge, experience of scientific research, advice on writing the thesis and care for me during the last three months of the writing have been very valuable.

In the course of the PhD, I have been involved in eight experiments: four at the Central Laser Facility (CLF) at Rutherford Appleton Laboratory (RAL) in England, three at the Institute of Laser Engineering (ILE) at Osaka University in Japan and one at LULI (Laboratoire pour l'Utilisation des Lasers Intenses) in Paris, France. Of the eight experiments, only two are discussed in this thesis, specifically an experiment using the Astra laser system at the CLF in July and August 2007, and an experiment using the GEKKO XII laser system at ILE in November 2008. Both of these experiments are part of an on-going collaborative effort between the University of York, Osaka University and LULI in which high-intensity lasers are used to study astrophysically-relevant plasma phenomena in the laboratory. I would like to acknowledge and thank those involved as experimentalists in the two presented experiments here, specifically H. Aoki, H. Tanji, T. Morita, S. Dono, Y. Kuramitsu, Y. Sakawa, L. A. Wilson, C. D. Gregory, N. C. Woolsey, B. Loupias, E. Brambrink and M. Koenig.

In addition, I would like to thank the various support staff both in York and at the various laser facilities listed above. In particular, I would like to acknowledge the work of M. Streeter in running the Astra experiment, D. Symes for building the probe laser system for this experiment, D. Coulthard for polishing and coating targets for the November 2008 experiment and C. Spindloe for taking images of some of these targets, some of which are reproduced in section 6.1.2 by permission. I would also like to thank C. D. Gregory for his Abel inversion software and advice in analysing experimental

results.

As well as experimental work, a large part of this thesis is in the form of computer simulations using the codes HYADES and h2d [3]. I would like to thank J. Larsen, the author of the codes, for his advice, and likewise from the University of York N. C. Woolsey, J. Pasley and my fellow PhD student L. Gartside. I would also like to thank R. Trines for his maintenance of the system and work in regularly updating the software.

I would also like to acknowledge the contribution of those in the laser-plasma group with whom I have shared a large amount of office time, among whom are I. Hall, D. Applegate, B. Dudson, D. Whittaker, M. Edwards, N. Booth, A. Rossall, E. Wagenaars, L. Gartside, H. Huang, I. Al'miev, H. Qu, S. Safraz and L. Wilson.

I am grateful to EPSRC for funding my PhD studentship, to APS for providing funding towards a trip to the High Energy Density Laboratory Astrophysics (HEDLA) conference in St. Louis, Missouri, U.S.A. in 2008, and also to the Royal Society for funding four overseas data-collection trips, specifically a trip to the LULI laboratory in Paris in 2008, and trips to the Institute of Laser Engineering at Osaka University, Japan in February 2007, November 2007 and November 2008. Last, I would like to acknowledge EPSRC, STFC, the Royal Society and JSPS for contributing funding to either one or both of the experiments presented in this thesis.

Author's Declaration

This thesis contains seven chapters, all of which were written by the author. Chapter 1 is purely introductory. Chapter 2 is a survey of literature published by the astrophysics community relating to jets from Young Stellar Object systems, while chapter 3 is a review of work done by the laboratory plasma physics community relating to the creation of scale models of Young Stellar Object jets. None of the papers referred to in these two surveys were written by the author. However, the author was involved as an experimentalist in two of the laboratory experiments mentioned in chapter 3, and as such appears in two of the cited papers [4, 5] as a co-author.

Chapter 4 and 6 contain experimental details and results for two laboratory astrophysics experiments, one using the Astra laser system [6] and one using the GEKKO XII laser system [7]. Both of these experiments were carried out by a large group of people, among whom the author was included as an experimentalist. The author did not play a significant role in the planning of the Astra experiment. The author was, however, involved in the process of designing targets for the GEKKO XII experiment. All of the analysis of results which is presented in chapters 4 and 6 was carried out by the author. The techniques used for this are not novel and, except where explicitly stated, the computer software used for the analysis was not written by the author; its sources are acknowledged in the text. Two publications have come from the Astra experiment [8, 9], on both of which the author of this thesis was the lead author. The analysis of the results in these articles is at an early stage compared to the analysis presented in this thesis.

In chapter 5, numerical simulations of aspects of the Astra experiment are presented, and a combination of experimental and simulation results are used to assess whether some of the laboratory jets can be scaled to Young Stellar Object jets. All of the simulations were carried out by the author using the numerical codes HYADES and h2d [3] written by J. Larsen. The author is indebted to J. Larsen, N. C. Woolsey, J. Pasley and L. Gartside for their advice while doing this. All of the post-processing of the simulation results was done by the author, and the sources of the software used for this are acknowledged.

Any data used in chapters 4 to 6 that has been contributed by others has its source acknowledged in the text. This thesis was prepared using LyX [10]; images were prepared using Microsoft® Paint [11] and ImageJ [12].

1 Introduction

The focus of this thesis is on a particular topic in laboratory astrophysics, namely the creation of scale models of the collimated plasma jets seen to emerge from Young Stellar Objects (YSOs). Two laboratory experiments are discussed, one carried out using the Astra laser system at the Central Laser Facility of the Rutherford Appleton Laboratory in Oxfordshire, UK, and the other using the GEKKO XII laser system at the Institute for Laser Engineering, Osaka University, Osaka, Japan. In addition, the results of numerical simulations of the first of these experiments are presented.

The thesis is divided into seven chapters, of which this short introduction is the first. The other six chapters are as follows:

Chapter 2 is a survey of the astrophysical literature relating to Young Stellar Objects, and in particular the plasma jets associated with them. The purpose of this chapter is to introduce the phenomenon being modelled to the reader, providing the context for the laboratory experiments discussed in subsequent chapters.

Chapter 3 also takes the form of a literature survey. In the first part of the chapter, the mathematical basis for creating dynamic scale models of astrophysical plasmas is discussed in some detail. Then, the previous work that has been done in creating models of astrophysical jets in the laboratory is outlined.

Chapter 4 is the first of two chapters on experimental work. This chapter contains experimental details and results from the experiment using the Astra laser.

Chapter 5 is a computer simulation chapter. Aspects of the experiment described in chapter 4 were simulated using the one-dimensional and two-dimensional radiation-hydrodynamics codes HYADES and h2d, and in this chapter the use of these codes and the results obtained with them are discussed, and simulated and experimental results are compared. In addition, using a combination of experimental results from chapter 4 and simulation results the possibility of scaling between some of the jets created in the experiment and jets from Young Stellar Objects is analysed.

Chapter 6 is the second of the chapters on experimental work. In this chapter, the second of the experiments, that using the GEKKO XII laser system, is described and results from the experiment are presented.

Chapter 7 is a conclusory chapter in which the work presented in the preceding chapters of the thesis is summarised.

2 The Young Stellar Object (YSO) System

2.1 Chapter structure

In this literature survey chapter is presented a description of observations of YSO systems, as well as insights into their behaviour that have been gained from numerical modelling of their jets by the astrophysics community. Explicit discussion of laboratory astrophysics will be left to the second literature survey chapter, chapter 3, which contains both a discussion of the scaling theory that makes scaled experiments possible and a survey of previous YSO jet modelling experiments.

The structure of this chapter is as follows. First, a short introduction to astrophysical jets as a whole will be given. Then, there follow a set of subsections in which certain aspects of jets are discussed in more detail, focusing specifically on YSO jets. The method by which plasma jets are launched from YSO systems is still somewhat under debate but a short discussion of jet launching is included. Finally, a summary is given.

The aims of this chapter are two-fold. The first aim is to introduce to a reader unfamiliar with the subject the astrophysical jets that are being modelled. The second is to present a sufficiently detailed description of astrophysical jets that a fair assessment can be made as to the worth, as scale models, of the model jets created in the laboratory.

2.2 Introduction to astrophysical plasma jets

The astrophysical jets with which this thesis is concerned are outflows of high-velocity plasma material that are seen to remain highly collimated over large distances. By "highly collimated" it is meant that the jet aspect ratio - the ratio of jet length to jet width - is much greater than 1. Such outflows are found in many astrophysical systems. The largest jets are those associated with supermassive black holes at the centres of galactic discs[1]. These black holes accrete matter from the discs and emit jets of matter at relativistic speeds perpendicular to them; such "Active Galactic Nuclei" (AGN) jets are seen to extend for over a megaparsec [13][2].

The jets associated with Young Stellar Objects (YSOs) are much smaller than those associated with AGN, typically being seen to extend less than 1 parsec, though some

[1] Within the literature, there seems to be a mixture of spellings. Throughout this thesis "disc" will be used rather than "disk".

[2] 1 megaparsec = 10^6parsecs = 3.26 x 10^6 light years = 1.19 x 10^9 light days = 3.09 x 10^{19} km.

giant flows extending over 5 parsecs have been seen. At the centre of a YSO system is a protostar, a star that is still gaining mass from a surrounding accretion disc and has not yet joined the Main Sequence. As with AGN, jets of high-speed material are emitted perpendicular to the disc, though the speed of the emitted material is much lower in the YSO case, being a few hundred km s^{-1} [14, 15].

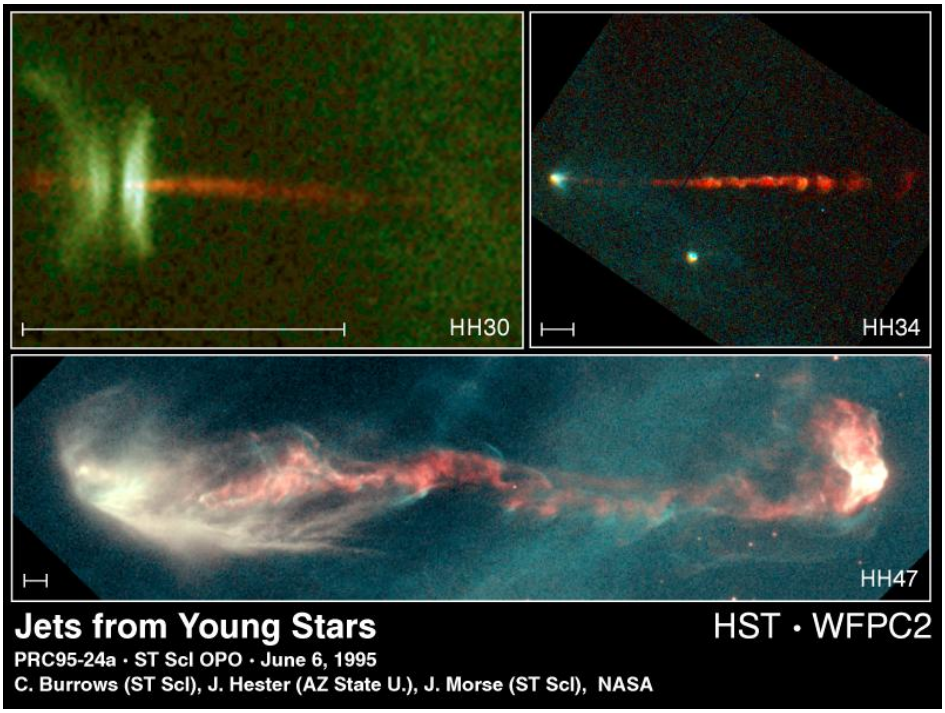

Figure 1: Three images of plasma jets associated with YSOs. The small scalebars in the images indicate distances of 6 lightdays. Image credit: C. Burrows (ST ScI & ESA), J. Hester (Arizona State University), J.Morse/ST ScI and NASA.

Figure 1 shows 3 examples of YSO jets imaged using the Hubble Space Telescope at visible wavelengths. The top left image shows the HH30 system[3]. On the left side of the image there is an accretion disc, which is visible as a dark vertical stripe dividing the bright, light green region in two. Two jets are emitted from the centre of the disc, one to the left and one to the right, and these are shown in red. The right hand jet can be seen to be very well collimated. The same is true for the jet shown in the top right image, the image of HH34, though in this image it can be seen that the jet beam (again shown in red), rather than being homogeneous, is visible as a series of blobs. These are referred to as knots. The third image, the image of HH47, looks somewhat different. In this case, the jet is emerging from a protostar on the far left of the image which is obscured from view. A jet propagates to the right and appears to terminate in a wide, bright feature. Unlike the top two images, the jet is not straight but has a wiggle in it.

[3]HH stands for "Herbig-Haro", George Herbig and Guillermo Haro being two astronomers.

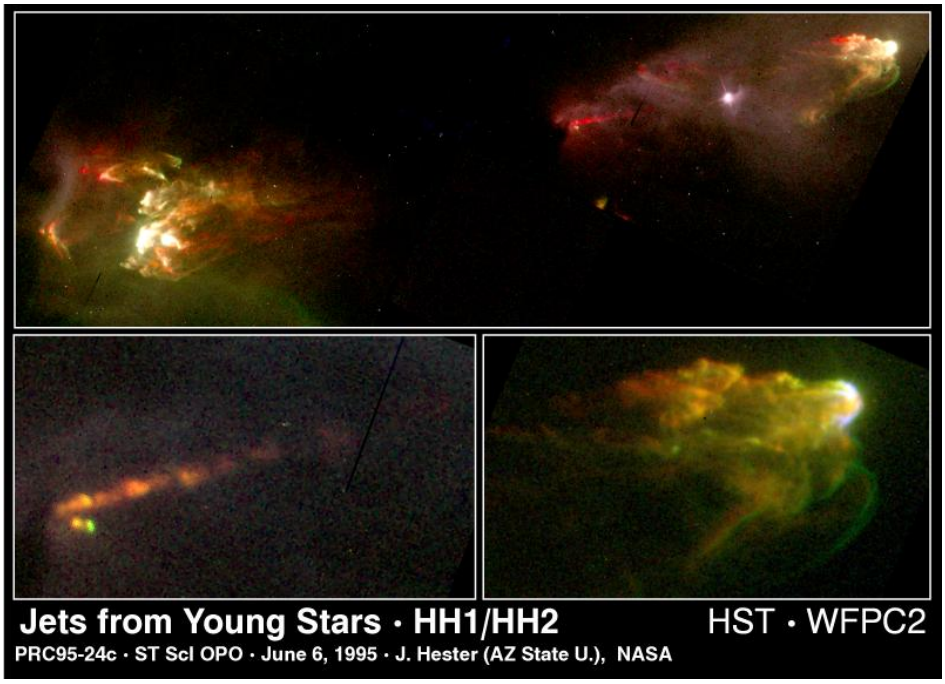

Figure 2: Images of the HH1 and HH2 nebulae. These are sites where jets from a YSO are interacting with the ambient interstellar medium at supersonic speeds, producing shock structures. Image credit: J. Hester (Arizona State University), the WFPC 2 Investigation Definition Team, NASA/ESA.

The top image of figure 2 shows the HH1 and HH2 nebulae. In the centre of this image, invisible due to dust obscuration, is a star. A pair of jets proceed from the star in opposite directions. One of the jets is visible in red just to the right of centre, and a blow-up of this region is shown in the bottom left image of the figure. It can be seen that this jet consists of a series of emitting knots, just like the jet in the HH34 image of figure 1. Returning to the top image of figure 2, the two very large, bright regions, one on the left and one on the right, are the HH1 and HH2 nebulae themselves. They are produced where the high-velocity jets run into the interstellar medium. The bottom right image of figure 2 shows a close-up of the right hand nebula.

Having presented several images of jets in order to give a pictorial idea of what is being discussed, over the next few subsections individual aspects of astrophysical jets are treated in more detail.

2.3 YSO temporal development

It is thought that YSO systems form from the collapse of dense regions of molecular clouds. In [16], Ray gives a description of how this happens, and a very brief outline of the process is as follows. It can be split into two main stages. In stage one, the dense region of a molecular cloud collapses, becoming hotter and denser in the centre

as it does so. At the end of this stage, there is a protostar in the centre of an accretion disc, and around the protostar-disc structure is an envelope of infalling material. The pressure in the protostar prevents it undergoing further gravitational collapse. In stage two, the protostar continues to gain mass by accretion from the disc and the envelope, and eventually it becomes a main sequence star. The second stage is split into three phases known as class 0, I and II. The class 0 phase ends when the protostar reaches 50% of its final mass, which would take about 10^5 years[4] for a star that would end up with about the same mass as the sun. The subsequent class I phase lasts until the protostar is only a few percent from its final mass. Last is the class II phase, during which the protostar completes its journey to become a Main Sequence star; T Tauri and Herbig Ae/Be stars are protostars in this phase.

Collimated jets are seen in all three of the class 0, I and II phases [17]. In the class 0 phase, the amount of matter in the envelope is large and the base of the jet is obscured at optical wavelengths. At micron wavelengths (near-infrared) emission knots are visible a few hundred AU[5] from the star, while at centimetre wavelengths the innermost jet regions can be observed. For class I and II jets, the innermost regions are seen in the near-infrared while the extended jets can be seen at visible wavelengths. For class II jets the mass accretion rate has been found to be correlated with the rate at which mass is ejected in jets (see the discussion of this in [17]).

2.4 Jet basic structure and terminology

Figure 3 on the following page shows a cartoon representation of the basic structure of an astrophysical jet, a description of which is given in, for example, [18]. In the centre of the jet is a collimated "beam" of plasma moving away from the centre of an accretion system. This beam, as seen in section 2.2, may contain a series of knots. The bulk flow speed of the beam plasma is faster than the sound speed in the surrounding medium, so where the beam plasma meets the ambient medium a shock structure is set up. This structure contains three boundary surfaces. First there is the "Mach disc", a shock front at which the plasma in the beam is rapidly decelerated. This is often referred to as the "jet shock". Second there is a bow shock where the ambient medium is rapidly compressed, heated and accelerated. Between the two shocks lies the

[4]The summary presented here reflects current scientific opinion rather than that of the author of this thesis, who grants that these systems have a large apparent age but currently thinks it unlikely that they have genuine antiquity on theological grounds.

[5]1 AU = 1.496 x 10^{11}m; AU stands for Astronomical Unit, 1 AU being the mean distance between the Earth and the Sun over one orbit.

contact discontinuity, which is the boundary between the shocked beam plasma and the shocked ambient medium material. The region between the two shocks is known as the "working surface". The pressure between the two shock surfaces forces the shocked beam and ambient medium material out sideways, where it forms a two-layer cover separating the beam from the ambient medium. Using the standard terminology found in the literature, it is said that the shocked ambient medium material forms a "shroud" around the "cocoon" of shocked beam material.

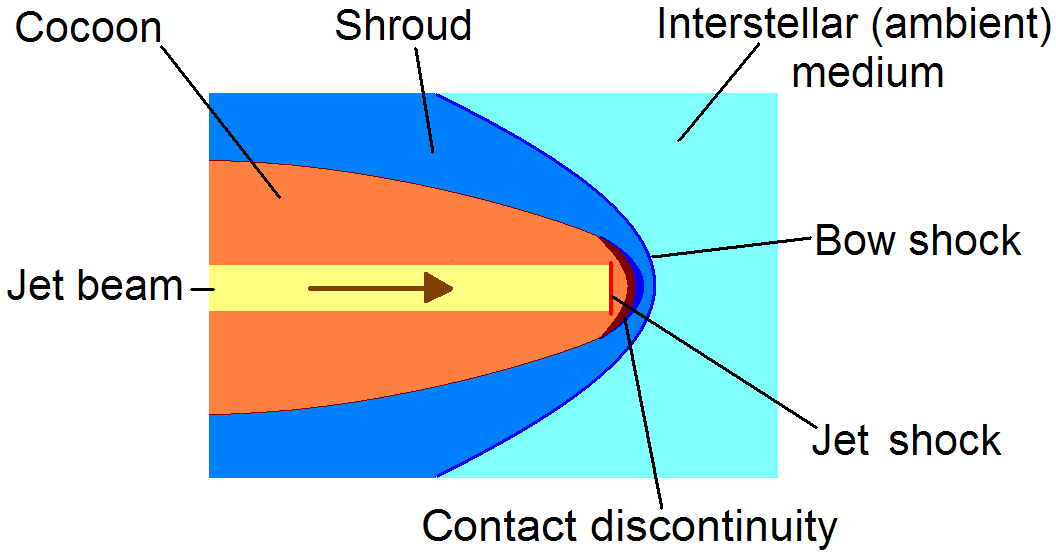

Figure 3: A cartoon showing the basic structure of an astrophysical jet.

2.5 Emission of radiation

The emission of radiation can have direct effects on the hydrodynamics of a jet and hence on its structure. Wherever the local timescale for radiative emission of a plasma's internal energy is comparable to, or less than, the local timescale over which the plasma evolves hydrodynamically, the effect of radiative energy loss on the hydrodynamic evolution of the plasma has to be considered. The reason for this is that radiative energy loss leads to local loss of pressure, and pressure differences act to drive hydrodynamic motion. The significance of radiative energy loss can be very different in different regions of a jet, reflecting the local temperatures and densities.

Blondin *et al.* [18] have presented a detailed study of the effects of radiation on jet structure. In their paper, they present results of simulations of axisymmetric jets propagating into homogeneous ambient media, in which they assume the same composition for the beam and the ambient medium. A YSO jet is "overdense", typically by a factor of about 10, meaning that the density of the plasma in the jet beam is about ten times the density of the ambient medium into which it propagates. In their analysis, Blondin *et al.* explain how different radiative behaviour of the plasma in the beam and the

plasma in the ambient medium can be expected for such a jet. An overdense jet is difficult for an ambient medium to slow down due to its inertia. This means that the speed at which the bowshock propagates through the ambient medium is of the same order as the bulk flow speed of the plasma in the beam. The high shock velocity in the bowshock leads to heating of the ambient medium to a high temperature, and it takes a long time for the ambient medium to cool down to the threshold temperature below which radiative emission is no longer significant. The jet shock, where the beam plasma is decelerated, has a shock velocity which is of the order of the difference in the beam and bowshock speeds. As these speeds are similar, the jet shock's shock velocity is small, meaning that the beam material is heated far less than the ambient material and consequently takes less time to cool to the threshold temperature.

When material shocked at either a jet shock or a bow shock cools over a distance which is comparable to, or less than the radius of a jet, which may be regarded as a hydrodynamic length scale, the cooling of the plasma is sufficiently rapid to strongly affect the structure of the working surface in several ways. First, the radiating plasma (be it originally from the jet or from the ambient medium) becomes compressed into a thin, high-density "shell" on the jet axis at the position of the contact discontinuity; for an overdense YSO jet, most of the mass of the shell comes from beam material. This shell can be subject to instabilities such as Vishniac thin shell [19] and Rayleigh-Taylor (see, for example, [20], chapter 11) instabilities. In general it does not remain in a steady state but breaks up into clumps, and for any particular situation the details of the evolution can be quite complicated. Second, the pressure reduction caused by the gas radiating reduces the sideways driving of shocked gas into the shroud/cocoon, resulting in a weakening and narrowing of these features. Third, if the shocked ambient medium material cools quickly the shape of the bow shock is dominated by the ram pressure of the shell behind it rather than the pressure of the shocked ambient medium material. Rather than being a smooth arc, it follows the shape of the shell as it distorts.

Blondin *et al.* [18] state that for adiabatic jets, i.e. jets for which radiative emission is not dynamically significant (such as those associated with AGN), the structure of the jet is found to depend on the ratio of the density in the jet beam to the density of the surrounding ambient medium. The dependence on the internal Mach number of the material in the jet beam, $\mathcal{M}$, which is equal to the ratio of the flow speed and the sound speed, is "relatively weak once $\mathcal{M}$ is above a few" ([18], p. 373). For radiative jets, there are additional parameters determining the structure. There are cooling lengths associated with the cooling of the shocked beam and ambient medium plasmas (only

one of these is needed if the jet and the ambient medium have the same composition). Additionally, where the radiative cooling function for a jet does not obey a simple power law the structure depends on the absolute temperature in the cooling jet.

2.6 The jet beam

When looking at a YSO jet, the parts that emit sufficient amounts of radiation to be directly visible are knots within jet beams, bowshocks (either within knots, or where beam material is impacting the interstellar medium) and sometimes the beam itself. S. Cabrit [17] describes measurements of beam widths and divergence angles of jets in class II YSOs using optical wavelength images taken by the Hubble Space Telescope. Beyond about 50 AU from the centre of an accretion disc, measuring along a jet's axis, the divergences of the beams of jets such as CW Tau and RW Aur are found to be only a few degrees. The jet widths at 50 AU are about 20-40 AU. Within the 50 AU nearest to the disc centre, however, the divergence angles are seen to be much higher, around 20-30°, indicating that collimation happens after about 50 AU. While the class II jets from which these measurements were made are visible over distances of less than 1000 AU from their source, Cabrit reports that class I jets are visible over greater distances, up to about 10^4 AU (0.05 parsecs). Their widths, at the time of writing her paper measured only beyond 1000 AU, are consistent with the observed widths of the shorter class II jets extrapolated out to larger distances. In addition, Cabrit reports that widths of class 0 jets near their source are consistent with measurements of class II jets, and measurements of CO and SiO molecular jets from class 0 sources are consistent with measurements of class I jets.

Conveniently, the timescale over which knots move and evolve in YSOs is of the order of years, meaning that it has proven possible to observe their propagation and development by taking sets of observations a few years apart (see [21] for an example). Examination of the spectra of knots indicates the presence of low-velocity shocks, of order ~ 30 - 80 km s^{-1} [15, 16]. These shock speeds are much smaller than the bulk flow speeds of beam plasma, which are of the order several hundred km s^{-1}. Two theories put forward to account for the presence of knots and their low velocity shocks are as follows [22]. First, it has been suggested that knots are produced by oblique shocks in the jet beam, occurring when, for example, Kelvin-Helmholtz instabilities (see, for example, [23], chapter 5, p. 202) at the interface between cocoon and shroud material lead to the cocoon material pinching the beam and driving internal shocks into it [18].

In [22], Bacciotti *et al.* proposed a variant on this model, in which emission from knots is produced as a result of the beam flowing along a channel of uneven width: the beam becomes heated and emits where the channel is narrower, the narrowing being caused by phenomena such as damped Kelvin-Helmholtz instabilities. Second, it has been suggested that knots are a result of variability in the rate and speed with which matter is emitted by the jet source. If the speed of the plasma emitted by the source varies, plasma emitted at higher speeds can catch up with plasma emitted at lower speeds creating a forward shock in the slower plasma and creating a reverse shock in the faster plasma. If the variation in the speed of the plasma emitted by the source is small with respect to the average speed of plasma in the beam, the shocks seen in the knots will have the relatively low speeds observed.

While the first of these theories sounds reasonable for AGN jets, the second of these theories is currently in favour for YSO jets ([14]; Bacciotti *et al.* state in [24] that at the time of writing computer models required pulsed ejection of matter in order to reproduce observations). This is down to the differing significance of radiation for the hydrodynamics in the two cases. For AGN jets, the rate of radiative emission is too slow to directly affect the hydrodynamics - AGN jets evolve approximately adiabatically. However, in the YSO case, the strong radiative emission of the shocked plasma in the working surface at the head of the jet results in significant reduction of the energy, and hence pressure, of this plasma. This lowering of pressure reduces the squeezing of shocked material sideways into the cocoon and shroud, and the consequently weaker cocoon and shroud are less capable of pinching the beam and producing internal shocks [18].

The material within a jet beam is predominantly hydrogen. It is not fully ionised, and the ionisation fraction is difficult to calculate accurately. This leads to uncertainties in the determination of the mass density within the flow, which is estimated using inferred values of the electron density and the ionisation fraction. Using the ratio of the [SII][6] lines at 6716 and 6731 Å [25], beam electron densities for different jets are found to range from 10 to $> 10^5$ cm^{-3} [14] . In [25], Bacciotti describes a method first suggested by Bacciotti, Chiuderi and Oliva [22] and uses it to gain spatially-resolved information on the ionisation fraction. The basis of the method is as follows. For situations where electron temperatures are not too high and for which there are no external sources

[6]The notation [SII] requires some explanation. The "[..]" symbols indicate an electric-dipole forbidden transition. The "S" is the symbol of the emitting element, in this case sulphur. The "II" indicates that the element is singly ionised ("I" is used to indicate a neutral species).

of high-energy photons then, as long as the ionisation fraction is below about 0.5, it is found that the ionisation of oxygen and nitrogen is dominated by charge exchange interactions with hydrogen. By assuming a particular value for the relative abundance of the elements N and O, it is possible to express line ratios for neutral O and singly-ionised N as functions of the hydrogen ionisation fraction and the temperature, and hence by comparing line ratios to estimate these quantities.

Bacciotti reports results for several astrophysical jets. In some cases, the hydrogen ionisation fraction is seen to decrease with distance from the source. This is consistent with the explanation that hydrogen is strongly ionised near the source of an outflow and slowly recombines as it moves away from the source. If internal shocks in the beam are not very strong, corresponding to shock speeds below 30-35 km s^{-1}, shock-induced re-ionisation within the beam is negligible. However, for some of the jets the behaviour of the hydrogen ionisation fraction is more complicated, either remaining roughly constant down the length of the observed part of the beam, or showing a pattern of sections of re-ionisation interspersed with sections in which the ionisation fraction stays roughly constant or falls off gradually. It is suggested that the re-ionisation episodes are due to strong internal shocks in the beam. In terms of absolute values, the hydrogen ionisation fraction for the observed jets is reported to be in the range 0.05-0.4, with temperatures between 4500 and 7000 K, and a total (i.e. including both atoms and ions) hydrogen number density of 10^3 - 10^4 cm^{-3}.

The internal Mach number for a flow is defined as the ratio of the flow speed to the sound speed of the plasma within the flow, while the external Mach number is the ratio of the flow speed in the jet beam to the sound speed in the ambient medium into which the jet moves. Using the temperature of the plasma in a beam, which is found by spectroscopy to be of order 10^4 K, one can estimate the sound speed. Then, using the observed beam flow speeds of a few hundred km s^{-1}, the internal Mach number for the plasma in the beam of a YSO jet is found to be in the region 10-40 [14, 16].

2.7 Jet launching

So far, only the jets produced in YSO and AGN systems have been mentioned. There are other intermediate-scale systems in which jets are observed, such as massive X-ray binaries. Although these systems may have very different spatial scales, they are observed to be structurally similar [14]. At the centre of each system is a compact object which accretes matter from a disc around it and produces (a) collimated jet(s) perpen-

dicular to the disc. In addition, the beams of the jets are found to contain chains of roughly evenly spaced knots, the jets often terminate in emission lobes believed to be working surfaces, and the systems are found to have associated with them large-scale magnetic fields. The bulk flow speed of the plasma in a jet is always seen to be of the order of the escape velocity of the compact object at the centre of the disc. Livio states that this links the origin of the jets to the compact object ([26], p. 231). The common morphology of jet systems has lead to the suggestion that there is a single mechanism by which jets are produced.

In [17], Cabrit gives a detailed overview of jet launching methods in YSOs, looking at the advantages and shortcomings of various models that have been proposed. As discussed above, the environment within which a jet finds itself depends on the apparent age of the YSO. In the review, Cabrit focuses on class II sources, YSOs that are highly developed with thin accretion discs. The topic is treated in two parts, first looking at how a collimated axial flow could be created, and second looking at how the matter in the flow could be accelerated to the observed high speeds.

The first collimation model Cabrit considers is where an isotropic wind emitted from the central object/the centre of the accretion disc is redirected into an axial flow by the thermal pressure of the disc. It is concluded that, on their own, the discs in class II sources are far too thin to redirect the wind to produce the observed collimation, and that the pressure of the ambient medium into which the class II jets emerge is too low to make up the shortfall. A second model in which magnetic pressure, either from an organised large-scale field with its axis aligned with that of the disc, or from a turbulent magnetic field, acts to collimate a central wind is then discussed. In the case of the organised field, a calculation of the amount of (poloidal) flux that needs to be within a distance of 100 AU from the axis shows it to be quite high; in the case of the turbulent field, it is not known how a sufficiently large turbulent region could be created and maintained.

Another model, the magneto-centrifugal launch model, works as follows [27]. The plasma in the accretion disc of a YSO is magnetohydrodynamic (see section 3.1.3). This means that the plasma and any magnetic field passing through it are effectively tied together: if one moves, the other has to move with it. As a consequence, the magnetic field lines entering the accretion disc are constrained to move with it. If, above the disc, these lines are not vertical but rather curve out to large radii, then plasma which starts moving along these field lines moves out to large radii. As the

magnetic field rotates rigidly with the disc, this results in the outward moving plasma accelerating until eventually its kinetic energy exceeds the energy locally stored in the magnetic field. After this point, instead of the plasma moving with the rigidly-rotating magnetic field, the magnetic field moves with the plasma, which moves at a radial velocity below that for rigid rotation. The combination of the co-rotating magnetic field at smaller radii and the sub-co-rotating field at larger radii results in a very wound-up magnetic field, i.e. a field with a large toroidal component at large radii. This strong toroidal component acts via the Lorentz force to re-direct outgoing plasma onto the axis of the system and form a collimated jet ([17], p. 32). The poloidal flux needed to provide a collimated flow in this model is several orders of magnitude smaller than the field needed in the model above where a wind is collimated simply by the pressure of a surrounding organised field.

In the review, having considered collimation mechanisms Cabrit considers five different acceleration mechanisms. First, there is a model in which radiation pressure from the protostar at the centre of the YSO accelerates the flow. However, only very luminous protostars emit enough for this mechanism to be viable. Second, there is a model in which a wind is accelerated by thermal pressure gradients. If this model was the main acceleration mechanism, it is predicted that the densities and temperatures at the wind base would result in orders of magnitude greater X-ray Bremsstrahlung emission than is observed. In a variation on the model, it has been proposed that the wind "is "cold" at its base (thus producing negligible X-rays), and enthalpy is provided to the flow further up" ([17], p. 43), but it seems that consideration of the overall efficiency of this process makes it unlikely. In the third model, acceleration is produced by deposition of energy into a wind by magneto-hydrodynamic waves which could come from, for example, the protostar's surface. However, the required overall luminosity of the waves seems unreasonably large.

Acceleration mechanisms four and five are complex magneto-hydrodynamic processes. Model four has several variants. First, there is the magneto-centrifugal launch model discussed above in the context of jet collimation. There, the magnetic field lines along which plasma is accelerated are anchored in the rotating accretion disc. This mechanism can easily account for the observed value of the jet luminosity but only, however, if there is some kind of heat source near the disc surface to act to load mass onto field lines. This could be, for example, X-ray emission from the protostar. In one variant, known as the reconnection X-wind model, magnetic reconnection between the fields of the star and the disc leads to mass being sporadically loaded onto field lines. Another

variant of the model has magneto-centrifugal launching along field lines anchored not in the disc but in a rapidly-rotating protostar, but this model struggles to correlate with observations of jets coming from protostars rotating well below their break-up rotation speeds.

The fifth acceleration mechanism is the "Magnetic Tower" scenario. In this scenario, there are closed magnetic field lines linking the protostar to the disc, the ends of which are constrained to rotating with the body to which they are attached. As the star and the disc rotate at different rates, magnetic field lines become stretched out around the axis, resulting in storage of energy in the toroidal component of the field, magnetic field lines being forced upwards and the appearance of an axial flow. Eventually magnetic reconnection re-orders the field lines and a new outflow episode begins. Though the outflows produced in this model are naturally episodic, explaining knot formation, Cabrit states several major problems with it. These include difficulties in explaining the observed collimation of jets from class II sources and in explaining the observed correlation between mass accretion by the central object and mass emission in jets.

Currently, magneto-centrifugal launching is considered by Cabrit to be the best model for jet formation. One of the predictions of the magneto-centrifugal jet launching model is that a jet, at least close to its source, should be rotating about its axis. Observation of the radiation emitted by YSO jets has given some evidence consistent with this expectation. For example, Coffey *et al.* [28] used the STIS instrument on the Hubble Space Telescope to look at the variation with transverse position of the Doppler shifting of radiation emitted by a selection of YSO jets. In general, they found the shifting of the emitted radiation was not the same on the two sides of a jet's axis. An asymmetry in Doppler shifting across a jet indicates that one side of the jet is moving towards the observer faster than the other. Whilst this is consistent with the expectation of a rotating jet, there are other causes of these signatures to consider. For example, it is possible that the jet axes are precessing rather than remaining fixed in direction. It has been suggested that precession can occur if an accretion disc is twisted/tilted, or if an emitting YSO has a binary companion.

2.8 Effect of magnetic field on jet propagation

In the discussion of jet launching, the preferred magneto-centrifugal models rely on the presence of a large-scale magnetic field during the jet launching and collimation. The importance of the magnetic field for the dynamics far from the launch region is

uncertain. Two examples of areas in which the field may play a significant role are in knots in jet beams [15], and in determining the shapes of the bow shocks at the heads of jets (see, for example, [29]).

Hartigan *et al.* [15] state that magnetic fields within jets cannot usually be measured directly as the line-radiation observed from jets is unpolarised and does not show Zeeman splitting. However, in shocks far from the source of a jet the component of the magnetic field parallel to the plane of the shock front can be measured. The plasma within a YSO jet behaves as an ideal magnetohydrodynamic plasma (see section 3.1.3), meaning that the magnetic field is effectively "frozen in" to the plasma material. Across a strong shock front, and in the cooling region after the shock, plasma density increases many times and magnetic field strength increases with the density. This results in an increase in the magnetic pressure, which scales as the square of the magnetic field strength, and when this becomes large enough it acts to inhibit further compression. Hartigan *et al.* state that "The difference between the electron densities inferred from emission-line ratios such as [S II] 6716/6731 for a nonmagnetic and weakly magnetized shock can be as large as 2 orders of magnitude. Hence, one can easily measure the component of the magnetic field in the plane of the shock by simply observing the [S II] line ratio, provided the preshock density and the shock velocity are known from other data." ([15], p.911). In the interstellar medium, the magnetic field strength is typically 1 μG or greater [18]. Although this is weak, it can become sufficiently amplified in shocks by the mechanism described above to limit compression.

2.9 Summary: why create models of YSO jets?

In this chapter a brief introduction to the plasma jets produced by Young Stellar Objects has been presented. As a result of a complex magneto-hydrodynamical process, jets of plasma with speeds of order 100 km s^{-1} are launched into the lower-density interstellar medium. Where the head of a jet meets this medium, a working surface consisting of two shocks, one which slows the plasma in the jet beam and one in which the interstellar medium is accelerated, is set up. The morphology of this structure is found to depend on the ratio of the density in the beam to that in the surrounding medium, on the internal Mach number of the plasma in the beam, on the rate of radiative cooling behind the jet and and bow shocks and also, in general, on the absolute values of the temperature in the flow.

More information on YSO jets can be found in, for example, the review article by

Reipurth and Bally on Herbig-Haro flows [30] and the "Jets from Young Stars" books produced from lectures in the series of JETSET schools [31]. There remain a variety of open questions about these objects. While a magneto-centrifugal model is favoured, there is still some debate as to the exact mechanism by which jets are launched. Other questions relate to topics such as the cause of the variability in the emission from the jet source [32, 33] and the effect of binaries on jets and accretion discs [30, 32].

Currently, most of what is understood about jets comes from analytical calculations and computer simulations. While there are difficulties in creating scale models of jets in the laboratory, this approach potentially provides an alternative method of studying jets. The physical processes in laboratory plasmas are not necessarily the same as in their astrophysical counterparts: for example, the dominant radiative emission processes in the laboratory might be Bremsstrahlung and line emission, while recombination might dominate in a YSO jet. However, plasmas created in laboratory experiments evolve fully three-dimensionally, their processes are fully non-linear and they can become fully turbulent, all of which are aspects that are difficult to capture in computer simulations.

3 Laboratory Astrophysics: Justification, Application, Previous Work

In chapter 2, the plasma jets associated with YSOs have been described in detail. Typically, these jets have spatial scales of $\sim$ 0.01-1 pc, have plasma bulk flow speeds of $\sim$ 300-900 km s^{-1} and are observed to evolve on timescales of years. Plasmas created in the laboratory can have similar speeds, but they extend over much smaller distances, typically 1 mm to 30 cm, and evolve on nanosecond or microsecond timescales. Thus, the spatial scales and evolutionary timescales of YSO and laboratory jets differ by many orders of magnitude.

Sometimes, the evolution of an astrophysical plasma and a laboratory plasma can be described with the same differential equations. When this is the case, in certain circumstances one can establish mathematically a quantitative scaling relationship between the evolution of the two plasmas. Then, the laboratory plasma evolves as a very small scale model of the astrophysical plasma, though on a much shorter timescale.

There are two aims to this chapter. The first is to introduce the mathematical theory which makes scaled hydrodynamic experiments a possibility. This is covered in detail in section 3.1 and applied to YSO jets in section 3.2. The second aim of the chapter is to summarise previous laboratory jet-creation work. This is done in section 3.3. Finally, the chapter is summarised in section 3.4.

3.1 Scaling theory

In order to describe mathematically the evolution of a plasma, one needs to specify both the initial conditions of the system and the differential equations governing its evolution from these conditions. In this section, scalings between plasmas that can be described by the differential equations of ideal, compressible magnetohydrodynamics (MHD) are discussed. Where magnetic fields are absent or too weak to directly affect the motion of a plasma, these MHD equations simplify to what will be referred to as the (ideal) hydrodynamic equations (HD).

In this section, scaling will be treated theoretically. The approach is as follows. In the first two sub-sections, sub-sections 3.1.1 and 3.1.2, scalings between plasmas governed by first the HD equations and then the MHD equations will be explored. In these sub-sections, the discussion of scaling proceeds *from* the HD and MHD equations; in

the third sub-section, 3.1.3, assumptions behind the use of these equations will be examined. The HD and MHD equations used in the first three sub-sections do not include terms to account for the emission of radiation by a plasma; in sub-section 3.1.4 the impact on scaling of having to include radiation is discussed.

3.1.1 Scaling between two hydrodynamic (HD) plasmas

The argument in this sub-section is based on a paper by Ryutov [34]. This paper looks at the possibility of scaling between two systems that are governed by the equations of ideal, compressible hydrodynamics and which have materials that can be described using polytropic equations of state. The equations governing the evolution of such systems are

$$\begin{aligned} &\frac{\partial \rho}{\partial t} + \nabla.(\rho \mathbf{v}) = 0 \qquad\qquad && \rho(\frac{\partial \mathbf{v}}{\partial t} + \mathbf{v}.\nabla \mathbf{v}) = -\nabla p \\ &\frac{\partial p}{\partial t} - \gamma \frac{p}{\rho}\frac{\partial \rho}{\partial t} + \mathbf{v}.\nabla p - \gamma \frac{p}{\rho}\mathbf{v}.\nabla \rho = 0 \end{aligned} \tag{1}$$

where $\mathbf{v}$, p and ρ are the velocity, pressure and density within the fluid, and t represents time. γ is the polytropic index, which is assumed to be homogeneous in space and constant in time (though this condition can be relaxed somewhat - see sub-section 3.1.3). These equations are the continuity equation (related to mass conservation) and the momentum and energy[7] conservation equations. In the form presented, use has already been made both of the polytropic equation of state, in which the energy density per unit volume is proportional to the pressure, and also the fact that an ideal HD fluid behaves adiabatically (see sub-section 3.1.3), for which $p \propto \rho^{\gamma}$.

Suppose that two systems, hereafter denoted using the subscript $i = 1, 2$, are at one time ($t_1 = 0 = t_2$ for convenience) geometrically similar, i.e. that the *shapes* of the velocity, pressure and density distributions in the two systems are the same, but the spatial scales of these distributions are different. Mathematically, this situation can be written

$$\begin{aligned} \mathbf{v}_1|_{t_1=0} &= \tilde{v}_1 \cdot \mathbf{F}(\mathbf{r}_1/h_1) \qquad & \mathbf{v}_2|_{t_2=0} &= \tilde{v}_2 \cdot \mathbf{F}(\mathbf{r}_2/h_2) \\ p_1|_{t_1=0} &= \tilde{p}_1 \cdot G(\mathbf{r}_1/h_1) \qquad & p_2|_{t_2=0} &= \tilde{p}_2 \cdot G(\mathbf{r}_2/h_2) \\ \rho_1|_{t_1=0} &= \tilde{\rho}_1 \cdot H(\mathbf{r}_1/h_1) \qquad & \rho_2|_{t_2=0} &= \tilde{\rho}_1 \cdot H(\mathbf{r}_2/h_2) \end{aligned} \tag{2}$$

where the values $\tilde{\mathbf{v}}_i$, $\tilde{p}_i$ and $\tilde{\rho}_i$ are constants throughout system i, and h_1 and h_2 are

[7] The equation for energy conservation here is equivalent to a condition for entropy conservation.

a pair of corresponding lengths in the two systems. To give an analogy: the Earth is geometrically similar to a football, both being spherical, though the spatial scale of the Earth and a football are very different. A pair of corresponding lengths would be the radius of the Earth and the radius of the football.

The functions $\mathbf{F}$, G and H, describing the shapes of the $\mathbf{v}$, p and ρ distributions, are the same in the two systems. The actual values of $\mathbf{v_2}$, p_2 and ρ_2 at position $\mathbf{r}_2$ are related to the values of $\mathbf{v_1}$, p_1 and ρ_1 at the corresponding position $\mathbf{r}_1 = (h_1/h_2) \cdot \mathbf{r}_2$ by the ratios $(\tilde{v}_2/\tilde{v}_1)$, $(\tilde{p}_2/\tilde{p}_1)$ and $(\tilde{\rho}_2/\tilde{\rho}_1)$, all three of which are numerical constants. Let it be assumed that γ is the same in both systems. Then, analysis of the HD equations shows that, if two systems are initially geometrically similar in the fashion described, scaling between the two systems using the ratios $(\tilde{v}_2/\tilde{v}_1)$, $(\tilde{p}_2/\tilde{p}_1)$ and $(\tilde{\rho}_2/\tilde{\rho}_1)$ is possible at later times as long as the condition

$$\frac{\tilde{v}_2}{\tilde{v}_1} = \sqrt{\frac{\tilde{p}_2}{\tilde{p}_1} \cdot \frac{\tilde{\rho}_1}{\tilde{\rho}_2}} \tag{3}$$

is met. The two systems do not evolve at the same rate. Rather, the timescales differ by the ratio

$$\frac{t_2}{t_1} = \frac{h_2}{h_1} \cdot \sqrt{\frac{\tilde{p}_1}{\tilde{p}_2} \cdot \frac{\tilde{\rho}_2}{\tilde{\rho}_1}} \tag{4}$$

Equation 3, the condition for scaling, can be re-written in another form. The internal Mach number at a point within a flow is defined as the ratio of the flow speed to the sound speed at that point. The sound speed within a plasma is given by ([20], chapter 10, pp. 217-218)

$$c_s = \sqrt{\frac{\gamma p}{\rho}} \tag{5}$$

If M is then used to denote internal Mach number, the scaling condition becomes

$$\frac{\tilde{v}_2}{\tilde{v}_1} = \frac{M_2}{M_1}$$

as $M_i = \tilde{v}_i/c_{s,i}$. The above argument shows that HD systems of very different spatial scale can evolve as scaled versions of one another, albeit on different timescales.[8] Importantly, one can even scale between fluids containing shock waves. A shock front has a finite width, within which dissipative processes like viscosity and thermal conduction, which are negligible within the rest of the fluid, are very important. However,

[8] In the literature, this scaling of the HD equations is known as the "Euler" similarity ([34]).

the values of $\mathbf{v}$, p and ρ on either side of the shock front can be related using conservation laws without knowing about the structure within the front, resulting in a set of equations known as the Rankine-Hugoniot relations ([20], chapter 10, pp. 219-224). Hence, shocks in ideal HD systems can be modelled as surfaces of discontinuity in $\mathbf{v}$, p and ρ as long as the shock widths are much smaller than the size of the fluid volume. For a system which scales as described, if the Rankine-Hugoniot relations are satisfied in one fluid, they are also satisfied in its scaled partner with the same jump ratios for the quantities varying discontinuously across the shock front.

There is another method to find scaling transformations using Lie group analysis, details of which are given by Coggeshall and Axford in [35]. However, rather than applying it to the three-dimensional, pure hydrodynamics equations given above (equations 1), in their paper Coggeshall and Axford apply the method to a set of equations for one-dimensional hydrodynamics with the inclusion of a term for radiative transport. This approach is further discussed in sub-section 3.1.4, where consideration is given to the implications of radiative transfer for scaling.

3.1.2 Scaling between two magnetohydrodynamic (MHD) plasmas

In the previous sub-section, the scaling between two HD plasmas was discussed. The HD equations can only be used in cases where the magnetic field strength is sufficiently weak that it cannot directly affect the hydrodynamic evolution of a plasma. In another paper by Ryutov [36], the scaling between two systems governed by the equations of ideal, compressible MHD is considered; the equations of MHD reduce to the equations of HD in the limit that the magnetic field is sufficiently weak. The derivation of the scaling in [36] proceeds in exactly the same fashion as for the HD scaling. The relevant evolution equations, again assuming a polytropic equation of state, are

$$\begin{aligned} &\frac{\partial \rho}{\partial t} + \nabla.(\rho \mathbf{v}) = 0 \qquad && \rho(\frac{\partial \mathbf{v}}{\partial t} + \mathbf{v}.\nabla \mathbf{v}) = -\nabla p - \frac{1}{4\pi}\mathbf{B} \times \nabla \times \mathbf{B} \\ &\frac{\partial \mathbf{B}}{\partial t} = \nabla \times \mathbf{v} \times \mathbf{B} \qquad && \frac{\partial p}{\partial t} - \gamma \frac{p}{\rho}\frac{\partial \rho}{\partial t} + \mathbf{v}.\nabla p - \gamma \frac{p}{\rho}\mathbf{v}.\nabla \rho = 0. \end{aligned} \tag{6}$$

Again, it is required that two systems start off geometrically similar if a scaling is to

be possible. This leads to the initial conditions

$$\mathbf{B}_1|_{t_1=0} = \tilde{B}_1 \cdot \mathbf{K}(\mathbf{r}_1/h_1), \quad \mathbf{B}_2|_{t_2=0} = \tilde{B}_2 \cdot \mathbf{K}(\mathbf{r}_2/h_2) \tag{7}$$

for the magnetic field in addition to the velocity, pressure and density initial conditions for geometrical similarity in the ideal HD case (equations 2). Even when systems start off being geometrically similar, for ideal MHD scaling to be possible it is required that condition 3 (equation 3) is satisfied, just as in the HD case, and also the additional condition,

$$\frac{\tilde{B}_2}{\tilde{B}_1} = \sqrt{\frac{\tilde{p}_2}{\tilde{p}_1}}. \tag{8}$$

When both conditions are satisfied, scaling between two systems is possible, with the timescale on which evolution occurs scaling as for ideal HD (equation 4)[9]. Just as it is possible to scale between ideal HD systems containing shocks, the same is true for ideal MHD systems.

3.1.3 Assumptions behind the use of ideal HD and MHD equations and a polytropic equation of state

The use of the ideal, compressible HD and MHD equations presented in the previous two sub-sections relies upon a set of assumptions being satisfied. Examination of these assumptions is important in order to understand the limits of application of these equations to physical systems, and by extension the limits of applicability of scaling between systems.

First, the HD and MHD equations are *hydrodynamic* equations. This means that they describe systems for which the fluid approximation is valid. At a simple level, a neutral gas can be modelled as a region of space in which neutrally charged particles move freely, interacting via collisions when particles get sufficiently close to one another. If a gas has a sufficiently high density, particles collide frequently and have a mean free path between collisions much smaller than the size of the gas volume. On a scale of about ten times the mean free path the behaviour of the gas particles can be approximately described using a Maxwell-Boltzmann distribution, and on scales greater than this the behaviour of the gas can be treated mathematically by considering quantities such as pressure that are statistical averages over many particles, rather than

[9] In the literature, this scaling of the MHD equations is known as the "Euler-Alfvén" similarity.

having to take account of the position and momentum of every particle within the gas individually. A gas for which this is possible, i.e. for which collisions between particles happen on timescales much shorter than the evolutionary timescale for the gas, and over distances small compared to the lengthscales on which the properties of the gas change significantly, is in the fluid approximation and can be described as "collisional".

The astrophysical and laboratory systems with which this thesis is concerned are plasmas rather than gases of neutrally-charged particles, and this can be significant when considering the validity of using the fluid approximation, and hence of using the HD and MHD equations. The reason for this is that many plasmas, particularly astrophysical plasmas, are not collisional: whereas the fluid approximation requires that the mean free paths for collisions between particles are much smaller than the lengthscales of the plasmas, for low density plasmas this is not the case. However, if a magnetic field is present it can provide an effective collisionality even if it is very weak [34]. This happens as follows. A charged particle with a component of motion perpendicular to a magnetic field experiences a $q\mathbf{v}\times\mathbf{B}$ force and consequently spirals around the magnetic field with a radius of orbit given by the Larmor radius. As it is a moving charge, its motion feeds back on the magnetic field, changing it. When there are many particles in even a weak magnetic field, the deflections of the particles in the field, due to the field, and the tangling of the magnetic field due to particle motion, conspire to give an "effective collisionality" over lengthscales of order the Larmor radius. For even a weak magnetic field this can be less than lengthscales within the plasma, and hence the fluid approximation can be satisfied; such a plasma is referred to as collision-less.

Second, the HD and MHD equations used in sub-sections 3.1.1 and 3.1.2 are *ideal* (dissipationless). For the HD equations, this means simply that the transport of momentum and energy within the fluid is totally dominated by advection. In particular, it means that viscosity, thermal conductivity and energy losses by radiation can be neglected. The quality of the approximation of neglecting viscosity and thermal conductivity is measured using two dimensionless numbers, the Reynolds number, denoted Re, and the Peclet number, denoted Pe (see, for example, [34]). The Reynolds number is defined as the ratio of inertial force to viscous force within the fluid, and the Peclet number is defined as the ratio between advective and conductive heat transport. They

are given by [34]

$$Re = \frac{hV}{\nu} \quad Pe = \frac{hV}{\chi} \tag{9}$$

where h is a typical length over which the fluid changes appreciably, V is a characteristic flow speed, ν is the kinematic viscosity coefficient and χ is the thermal diffusivity coefficient. As already mentioned in sub-section 3.1.1, in ideal hydrodynamic flows shock fronts are often modelled as discontinuities. This works well as long as the thickness of the shock fronts is much smaller than other lengthscales over which the hydrodynamic flows vary. Within a shock front, a gas or plasma is by necessity non-ideal, with viscosity and heat conduction both being important (see chapter VII of [37]). Radiative losses will be considered in the next sub-section.

In using the ideal MHD equations of sub-section 3.1.2, additional assumptions are involved. In calling the MHD "ideal", it is additionally assumed that dissipation of magnetic field within the plasma due to electrical resistance is negligible. This is determined using a magnetic Reynolds number, Re_M, defined by

$$Re_M = \frac{hV\mu_0}{\eta} \tag{10}$$

where η is the resistivity. When Re_M is large, magnetic field lines are tied into the flow and move with it [38]. Physically, this means that in a region where the flow compresses, the component of the magnetic flux density perpendicular to the direction of compression increases in proportion to the compression.

The effect of magnetic fields also has to be taken into account when calculating the Reynolds and Peclet numbers for an MHD plasma [34]. Ryutov states that the transport of heat parallel to a magnetic field can be inhibited by microfluctuations and stochastisation of the magnetic field, and that consequently the value for the thermal diffusivity used in calculating the Peclet number should be the minimum of the unmagnetised and magnetised values. For the kinematic viscosity used in calculating the Reynolds number, different expressions pertain depending upon whether the fluid approximation is satisfied by particle collisions or by a magnetic field providing an effective collisionality.

In addition to a plasma having to satisfy the fluid approximation and be dissipationless to be described by the HD and MHD equations as presented, there is a further necessary property of the plasma to consider. Within a plasma, it is quite possible that the electron and ion distributions are both in local thermodynamic equilibrium,

but that the temperatures of the two distributions are different. This is a result of two factors. First, some processes predominantly impart energy either to electrons or to ions. Examples include the heating caused by a caused by a shock wave, which imparts energy primarily to ions, and the absorption of energy from a laser pulse, where energy is imparted primarily to electrons. Second, in the relaxation of the distributions towards equilibrium the timescale for the establishment of equilibrium between electrons and ions is much longer than the timescales for equilibrium to be established among the electrons and the ions separately (see, for example, [20], chapter 9, p.188). This is a result of energy transfer being more efficient between particles of equal mass than between particles of very different mass. There is a variety of different approaches used to describe plasmas for which the electron and ion temperatures are different. For example, some such plasmas can be described using two-temperature, two-fluid equations, in which the electrons and the ions are treated separately as a pair of totally inter-mixed fluids that can exchange energy with one another (see, for example, [20] chapter 3, p. 51). The HD and MHD equations as presented in sub-sections 3.1.1 and 3.1.2 are single-temperature, single-fluid equations, in which the electrons and ions are assumed to be in local thermodynamic equilibrium with one another and are treated together as a single fluid. This is the simplest fluid description.

In order to investigate the scaling of the HD and MHD equations in sub-sections 3.1.1 and 3.1.2, a relation expressing the dependence of the energy density on pressure and mass density was assumed. As the description of the scaling followed the work of Ryutov [34, 36], his assumption that the energy density was proportional to the pressure was used, specifically

$$\varepsilon = \frac{p}{\gamma - 1}. \tag{11}$$

In the absence of external sources of energy, and the absence of dissipative processes, a flow is adiabatic and the energy conservation equation takes the form given in the HD and MHD equations (equations 14 and 6), leading to the result

$$\frac{p}{\rho^{\gamma}} = constant\ . \tag{12}$$

Here the constant γ is the index of the mass density, justifying a name of "adiabatic index" in this case; more generally it is known as the "polytropic index" (see, for example, p. 20 of [23]). The form adopted for the energy density in equation 11 includes the case of a fluid that behaves as an ideal gas with constant specific heats.

The value of a specific heat increases with the number of ways that energy is stored within a medium. For example, consider a low-density, diatomic gas. At very low temperatures energy is stored in the translational motion of the molecules. At higher temperatures, rotational states become available for the molecules; energy becomes stored within the gas in rotation of molecules and heat capacities rise. At yet higher temperatures vibrational states become active and the heat capacity rises yet further.

Within a plasma that is sufficiently hot that all atoms are fully stripped of all their electrons, the assumption of constant heat capacities holds as additional energy can only be stored in translational motion of ions and free electrons. However, the plasmas with which this thesis are concerned are not of this sort, but rather contain ions in a mixture of ionisation states. If the mean ionisation of a volume of plasma changes, then not only the energy stored within the plasma associated with the ionisation energies of the atoms/ions changes, but also, as ionisation results in the release of free electrons, a change in the number of particles contributing to the storage of energy in translational motion occurs. Overall, the result is that γ changes with the degree of ionisation of a plasma.

In the discussion of the scaling of the HD and MHD equations in sub-sections 3.1.1 and 3.1.2 it was assumed that γ, and hence the ionisation of the fluid, was homogeneous in space and constant in time. However, in [39] Ryutov discusses how this condition can be somewhat relaxed. Provided mean free paths in a plasma are sufficiently short, the composition of volumes of fluid remains unchanged as they move with the flow as the diffusion of species within the plasma is negligible. Therefore, fluid volumes with initially different compositions, and hence γ values, do not change their value of γ as they move. For scaling, it is then only important that the distributions of γ in the laboratory and scaled systems be identical (to within spatial scaling factors).

3.1.4 Inclusion of the effects of radiation in scaling

The HD and MHD equations as so far presented do not contain terms to take account of the emission of radiation. Rather, they assume that this emission is sufficiently weak that it does not directly affect the hydrodynamic motion of a plasma, i.e. that advective energy transport totally dominates radiative transport [34]. There are different conditions for this to be the case depending upon whether the plasma is optically thick or thin. In the optically thick case, the mean free path for photons is much smaller than lengthscales over which significant changes in plasma properties occur. In this

case, radiation transport is diffusive. Just as the Peclet number is estimated to assess the significance of thermal conductivity, a radiative Peclet number can be estimated using either a calculated radiative diffusivity or, as this can be hard to evaluate, by treating the plasma as a blackbody to set an upper bound on its radiative losses. The optically thin case is much simpler: it is simply required that the timescale over which radiative losses occur is much longer than the timescale over which the plasma evolves hydrodynamically.

It is important now to consider the case where a plasma satisfies the fluid approximation and has large enough Reynolds and Peclet numbers that viscosity and thermal conductivity can be neglected, but for which the effects of radiative emission on the dynamics are important. The key question to answer is whether scaling is possible in such a situation. The reason this is important is that, as discussed in section 2.5 of chapter 2, radiative emission can be dynamically significant within parts of the structures associated with YSO jets.

The effects of radiation within a hydrodynamic problem can be very complicated. The reasons for this include the following. First, it is necessary to consider many processes by which radiation can be emitted and absorbed within a plasma, for example Bremsstrahlung, line emission and absorption, and synchrotron radiation. Second, emission and absorption depend upon local values of bulk properties such as plasma density and temperature. Third, both emission and absorption are wavelength dependent, and may have angular dependencies. Fourth, radiation transfer within a plasma can be non-local: whereas hydrodynamic momentum and energy transfers occur between adjacent masses of fluid, radiation emitted in one part of a fluid can potentially travel through a large optically thin region and be re-absorbed by an optically thick region some distance away. For such reasons as these, radiation-hydrodynamics is in general very hard to model numerically.

In [39], Ryutov considers the scaling between MHD systems for which radiation is dynamically important, though only relatively weakly, so that the radiative energy flux is significant while the energy density and pressure of the radiation is negligible. In this case, the energy/entropy equation gains a term to account for radiative losses. In the case when the whole plasma is optically thin, radiation emitted in part of the plasma travels out of the plasma without further interacting with it, and hence the term in the energy equation is simply a function of the pressure and density which accounts for the radiative loss of energy. Whether a scaling relationship exists between

two plasmas in the optically thin case depends upon the functional form of the loss term. In general, even if this is the same in two systems there is not a mathematical relationship allowing for scaling between them. In the case that the functional forms in the two plasmas can be approximated with an identical power-law form, specifically that the energy loss can be written as $A_1 p_1^{\alpha_1} \rho_1^{\alpha_2}$, where α_1 and α_2 are constants, Ryutov states that a scaling transformation is possible, though with the introduction of a new constraint, specifically

$$\frac{A_1}{A_2} = (\frac{\tilde{p}_1}{\tilde{p}_2})^{\alpha_1 - 3/2} (\frac{\tilde{\rho}_2}{\tilde{\rho}_1})^{\alpha_2 + 1/2} \frac{h_2}{h_1}. \tag{13}$$

Ryutov also briefly discusses the case when a whole plasma is optically thick, in which the radiation mean free path is much shorter than the lengthscales over which the plasma changes and the radiative energy transport is diffusive.

As mentioned at the end of sub-section 3.1.1, there is an approach to scaling based upon the use of Lie group analysis of differential equations rather than the method of "dimensional analysis" so far described. Application of Lie group analysis to a set of differential equations is a mathematically involved process, but it is a more general method of finding transformations that leave the form of the differential equations unchanged, which is what is needed for the creation of scaled experiments. In [40], Coggeshall gives details of the method and applies it to a set of one-dimensional hydrodynamics equations for a perfect gas with constant specific heats. The particular equations he chooses describe a situation where viscosity and electron/ion thermal conductivity are negligible, but the transport of energy by radiation is not negligible. It is modelled by the inclusion of a diffusion term and thus corresponds to the optically thick case.

In [41, 42] Falize et al. apply a restricted form of the Lie group analysis technique to the following set of equations:

$$\begin{aligned} &\frac{\partial \rho}{\partial t} + \nabla.(\rho \mathbf{v}) = 0 \qquad\qquad \rho(\frac{\partial \mathbf{v}}{\partial t} + \mathbf{v}.\nabla \mathbf{v}) = -\nabla p \\ &\frac{\partial p}{\partial t} - \gamma \frac{p}{\rho} \frac{\partial \rho}{\partial t} + \mathbf{v}.\nabla p - \gamma \frac{p}{\rho} \mathbf{v}.\nabla \rho = -(\gamma - 1) L(\rho, T). \end{aligned} \tag{14}$$

These equations are identical to the HD equations (equations 14) but with the extra term $-(\gamma - 1)L(\rho, T)$ in the energy equation to account for energy sources or losses of the fluid. The polytropic relation relating the energy density to the pressure and the mass density (equation 11) is assumed, just as in the HD and MHD equations, though

it is not initially assumed that γ is a constant. Before beginning the analysis, Falize *et al.* make two further assumptions. First, it is assumed that the energy source/loss function is a sum of at most two terms of the power law form $Q_{0,i}\rho^{\epsilon_i}P^{\varsigma_i}x^{\theta_i}$, where x is a spatial coordinate and $Q_{o,i}$, ϵ_i, ς_i and θ_i are constants. Second, as equations 14 contain four dependent variables ρ, p, $\mathbf{v}$, and T a fourth equation is needed to close the set of equations. The equation of state $P = \varepsilon_0(Z)\rho^{\mu}T^{\nu}$ is chosen for this, where ε_0 is a function of the ionisation, Z.

The restricted form of Lie group analysis used in the paper is based on the "one-parameter homothetic group". It is assumed that all of the constants and both the dependent and independent variables in the differential equations scale by a factor a^{δ_i}, where the constants δ_i are in general different for each of the constants and variables. a is known as the group parameter, and the δ_i are known as the homothetic exponents. Consideration of the invariance of equations 14 under rescaling leads to a set of six quantities which need to be invariant. The ratio of the product of velocity and time to length, vt/x, is found to be an invariant, as are γ, the Mach number and a parameter related to mass conservation. Then, there is one invariant cooling parameter for each of the energy source terms. In the case that there are two energy loss terms, one ends up with four free parameters - the homothetic exponents for rescaling distance, density, pressure and ε_0. Overall, this approach allows a wider variety of scalings than those found by Ryutov *et al.*.

The discussion so far in this section has been concerned with scaling the hydrodynamic behaviour of radiative plasmas. In [43], Castor discusses the possibility of creating replicas of the spectra from astrophysical objects in the laboratory. In general, the difference in density between astrophysical and laboratory plasmas is found to prohibit this.

3.2 Application to a YSO system.

In this section the possibility of scaling between a YSO jet and a laboratory plasma jet is discussed. This section thus provides a link between the previous section, in which scaling between hydrodynamic plasmas of different spatial scales has been discussed generally and purely theoretically, and the next section, which is a survey of previous experimental work in creating scale models of astrophysical jets.

In order to scale between two plasmas, it must be shown that the differential equations governing their evolution have the same form. In order to be mathematically rigorous,

the functional forms of the terms in the individual equations must match in the two cases, and also, to within constant scaling factors, the values of the constants in the individual terms within the equations. Consider now an energy conservation equation. In general, this contains several terms, for example terms describing advective energy transport, viscous energy transport, thermal conduction, and radiative emission. If, at a specific point within a hydrodynamic plasma, the ratio of two of the terms, for example the advective and thermal conduction terms, were to be calculated, the result would be a dimensionless quantity, the value of which would express the relative importance of the two terms within the equation at that specific point. In the case of the advective and thermal conduction terms, the dimensionless quantity is the Peclet number; if the Peclet number is calculated to be much greater than 1, it shows that locally energy transport dominates thermal conductivity. One can define a whole series of dimensionless quantities for a set of differential equations. If one evaluates these quantities at any pair of corresponding positions within two plasmas that scale to one another, the values of the full set of scaling parameters should be the same for both plasmas.

In [43] Castor considers a set of different astrophysical phenomena (not, as it happens, including YSO jets), discussing whether there is any theoretical possibility of creating scale models of these phenomena in the laboratory. The approach used to make the decision in each case is as follows. First, a set of dimensionless quantities is evaluated for the phenomenon using typical values of parameters such as viscosity and temperature found within it. Then, the values of the set of dimensionless quantities are calculated using typical values of the plasma viscosity, temperature etc. within laboratory plasmas created using a variety of different methods. If the values of the full set of parameters calculated for one of the laboratory methods match those of the astrophysical phenomenon, then it is decided that it might be possible to model the phenomenon using that method.

The approach used by Castor does not, by itself, establish that two systems are scale models of one another, but only that it *might be* possible to create scale models using a particular technique, for example by the use of a Z-pinch or a specific laser system such as NIF. The calculated dimensionless quantities reflect the relative importance of different processes within the phenomenon, and as such may determine which physical processes it is important to include within the differential equations describing it. However, this is not sufficient to determine that the differential equations describing an astrophysical case and a laboratory case are identical, or that an appropriate scaling

transformation between the two cases exists.

To see that this is the case requires a little further elaboration. When the dimensionless parameters for the astrophysical case are calculated then, for example, the energy transferred by radiation is compared to the energy transferred by advection. The amount of energy transferred by radiation is estimated either by consideration of the dominant radiative process in the astrophysical system or by using an approximation, such as that of black-body emission. Similarly, the value of the same dimensionless parameter for a laboratory system is either estimated by consideration of the dominant radiative process in the laboratory system or by an approximation. Therefore, if the dominant radiative processes are different in the astrophysical and laboratory cases, even when the same values of the dimensionless parameter are obtained the radiation terms in the differential equations describing the two cases may be different.

In practice, the analysis of most laboratory experiments in which radiative jets have been created has involved calculating the values of a set of parameters using typical values of quantities inferred from the experimental data, such as the jet speed, and making a comparison with the values of the set of parameters calculated for the plasma within a YSO or AGN jet; many examples of this will be given in the next section. Whereas Castor's work stops at deciding that it might be possible to create a model of an astrophysical system in the laboratory, this analysis of the scaling of experimental work goes further by showing first of all that radiative jets (of some kind) can be made in the laboratory, and second that some or all of the parameters of these jets are similar to their astrophysical equivalents. To establish that a scale model of an astrophysical jet has been created requires going further, however, by showing that the differential equations are the same in the laboratory and astrophysical cases, that a suitable scaling transformation exists for these specific equations, and finally that at some point the laboratory and astrophysical situations are geometrically similar.

The parameters that have often been calculated from the results of jet experiments fall into two groups. First, there are parameters relating to whether a plasma jet behaves as an ideal (except for radiation effects) fluid. The parameters calculated here are a collisionality parameter, the Reynolds number and the Peclet number. They are denoted by δ, Re and Pe respectively. The collisionality parameter is the ratio of the collisional mean free path for ions to a typical lengthscale over which the plasma flow changes significantly. It is used to determine whether the fluid approximation is satisfied, i.e. whether the plasma can be described using hydrodynamic equations

at all; the fluid approximation is satisfied if $\delta \ll 1$. The values of the Reynolds number and the Peclet number determine whether viscosity and thermal conductivity are significant; as discussed previously, they are negligible when $Re \gg 1$ and $Pe \gg 1$.

The second group of parameters that are calculated relate to the jet structure. The parameters calculated here are the internal Mach number of the jet, the ratio of the mass density of the jet beam to the mass density of the ambient medium, and a cooling parameter, defined as the ratio of the lengthscale over which cooling occurs to a typical lengthscale over which the plasma flow changes significantly. They are denoted by M, η and χ respectively. The reason for this choice of parameters comes from astrophysical simulation work such as that of Blondin *et al.* [18] discussed in section 2.5. The structure of the working surface at the head of a jet is shown to depend upon the ratio of the mass density of the plasma in the jet beam to that in the surrounding medium and the values of the cooling parameters for shocked ambient gas cooling after the bow shock and shocked jet material cooling after the jet shock. The structure of the working surface is not found to be so crucially dependent on the Mach number, as long as it is greater than a few.

Parameter	Value in YSO jet
δ	10^{-7}
Re	10^{7}
Pe	10^{6}
v_{jet}	100 km s^{-1}
M_{int}	10-40

Parameter	Value in YSO jet
η	1-10
χ	0.1-10
t_{hydro}	300 years
t_{hydro}/t_c	1

Table 1: YSO parameter values. δ is the ratio of the ion-ion mean free path to the jet radius. Re and Pe are the Reynold's and Peclet numbers. v_{jet} is the speed of the plasma in the jet beam. M_{int} is the internal Mach number. η is the ratio of the mass density in the beam to that of the interstellar medium. χ is the ratio of the cooling length to the jet radius. t_{hydro} is the hydrodynamic timescale, the ratio of jet radius to beam speed. t_{hydro}/t_c is the ratio of the hydrodynamic and cooling timescales. The table was compiled using values from [1, 14, 16, 44].

Table 1, compiled using values from [1, 14, 16, 44], summarises the typical values of the chosen scaling parameters for a YSO jet. It can be seen that the values of the Reynolds and Peclet numbers are large, very much greater than 1, and so viscosity and thermal conduction are negligible. In a typical laboratory experiment, high values for the Reynolds number can be achieved, while the value of the Peclet number is typically much lower, meaning thermal conduction is not truly negligible.

3.3 Previous jet experiments

Over the last decade, many experiments have been carried out in which fast-moving, collimated plasma flows were created with a view to simulating at least some aspects of astrophysical jets and the systems producing them. Inspecting the literature, it is found that the experiments can be divided into three groups according to the major piece of apparatus used in the jet creation, specifically experiments using intense laser systems, a Z-pinch or a coaxial gas gun. In this section of the thesis, a survey of jet-creation experiments and their major results is presented treating each of the three classes one at a time. High-intensity laser experiments are presented first, as they are most directly relevant to the experimental work presented in chapter 4.

3.3.1 Jets created using intense lasers

Jet creation experiments using intense lasers can be divided into two sub-groups according to whether the axial flows created by the laser-target interaction propagated on the far side of the target from that which the laser struck or whether they propagated on the near side. These sub-groups will be referred to as "rear-side" and "front-side".

3.3.1.1 Rear-side targets

Figure 4 on the next page shows a set of sketches of targets that have been used in rear-side jet experiments. The basic idea behind the use of rear-side targets is as follows. First, an intense laser pulse strikes the front side of a solid material. This drives a shock wave through it. Provided certain conditions are met (for example, that the target is sufficiently thin) a plasma is created on the rear side of the solid target; the geometry of the target is arranged such that this plasma is collimated into a jet.

Figure 4a shows a sketch of a target used by a group in experiments [45, 46] on the Omega laser system [47] at the University of Rochester; a very similar target has been used on an experiment [48] at the National Ignition Facility [49] at Lawrence Livermore National Laboratory. In the experiment reported in [45] by Foster *et al.*, the laser-target interaction at the front of the target drove a shock through a flat plane. Behind this plane was a washer with a hole in the centre, followed by an enclosed tube filled with a low-density foam. First, plasma that travelled from the flat plane at the front of the target straight down the hole in the washer entered the foam as a jet, generating a shock wave. This was followed by a collimated, denser jet created by the collapse of

the sides of the hole in the disc onto the hole's axis under the influence of the shock travelling through the washer.

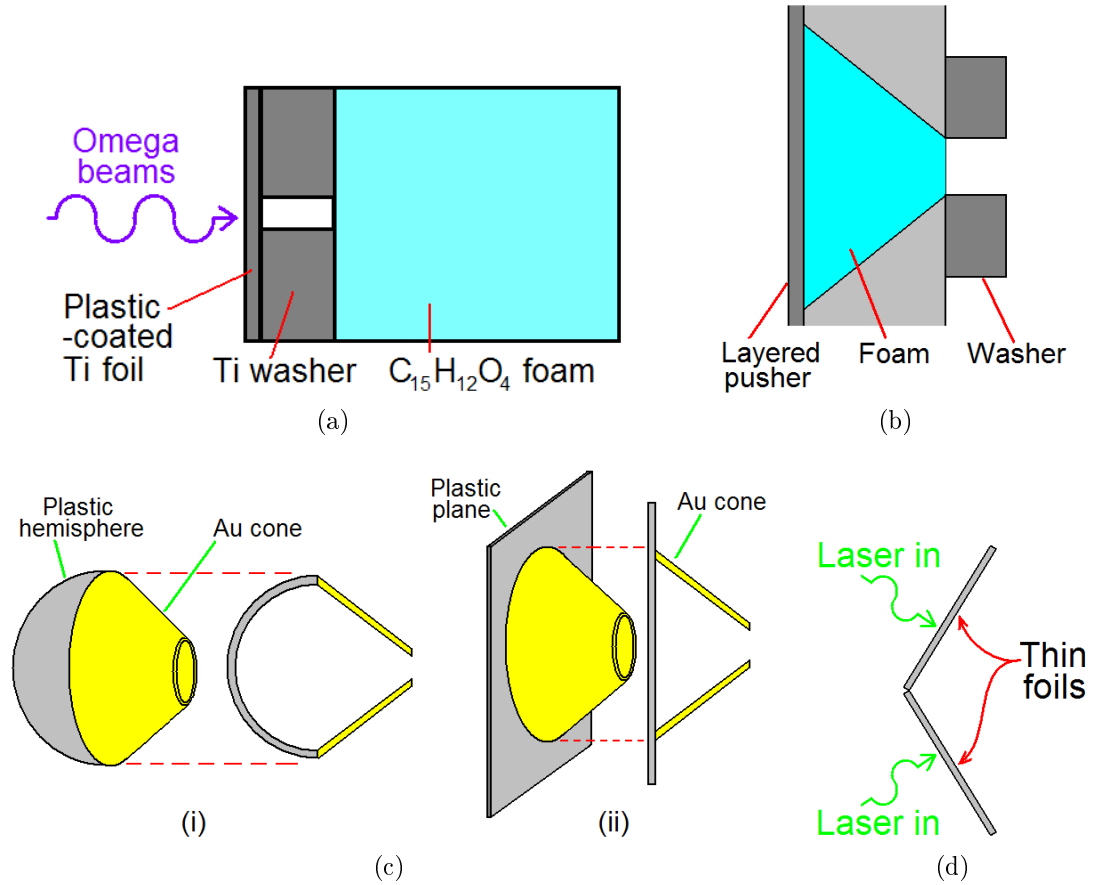

Figure 4: Rear-side targets: (a) Target for creation of jets propagating into foams (b) LULI cone target (c) (i) ILE hemisphere-cone and (c) (ii) ILE plane-cone targets (d) Reduced dimensionality target

The first of these jets was reported to have an internal Mach number of 3 and a jet-ambient medium mass density ratio of 1; the second jet was reported to be nearly liquid-state, rather than fully gas/plasma-state. The Reynolds number was found to be high, $\sim 10^6$, indicating that viscosity was negligible. The Peclet number was also high, $\sim 10^3$, indicating that thermal conductivity could be neglected. Unlike YSO jets, the jets created in this experiment were non-radiative.

The experiment reported by Rosen *et al.* in [46] differed from the experiment reported by Foster only in the driving of the target. Rather than illuminating the flat foil at the front of the target directly, beams of the Omega laser were focused into an Au hohlraum, heating it. Then, X-ray emission from the hot gold ablated the foil from the front of the target. Related experiments, using slightly different targets, are reported by Logory *et al.* [50], Foster *et al.* [51] and Blue *et al.* [48]. Logory *et al.* report the creation of purely hydrodynamic, 60 km s^{-1}, internal Mach number 17 jets propagating into foams.

Foster *et al.* report the production of jets which propagated into polystyrene blocks. The purely hydrodynamic, 50 km s^{-1}, internal Mach number 3, jets were created using a converging shock wave propagating through an Al block, and the group studied the interaction of jets with planar, counter-propagating shocks. Lastly, Blue *et al.* report the creation of $\sim$ 30 km s^{-1} jets which propagated into an aerogel foam; some of their jets were cylindrically symmetric, while others were deliberately made asymmetric.

Figure 4b shows a sketch of a target type developed by a group at LULI [52] in Paris. When this target was shot, the laser ablated the surface of a layered, planar pusher, driving a shock through it and through a low density foam contained in a cone behind it. This resulted in an axial jet of plasma being produced at the far end of the cone [5]. A washer was placed at the end of the cone on some targets in order to enhance the collimation of the flow. This type of target has been used in a series of experiments [5, 53]. In [5], Loupias *et al.* report that, when the target was used in a vacuum with a total laser drive energy of 400 J provided by the two beams of the LULI2000 laser system [54], the axial speed and rate of radial expansion of the resulting jets were dependent on the density of the foam in the target, changing from $\sim$ 90 km s^{-1} and $\sim$ 20 km s^{-1} for a foam density of 200 mg cm^{-3} to $\sim$ 190 km s^{-1} and $\sim$ 50 km s^{-1} for a foam density of 20 mg cm^{-3} . When jets were created in a background of Ar gas, interferometry measurements showed a large ovoid shock envelope in the gas. Comparing the size of the envelope with X-ray radiography measurements of a jet in a vacuum, the overall structure was found to be that of a dense axial jet surrounded by an envelope of lower density material. Both interferometry and proton radiography show that the shock envelope was not smooth but had a perturbed surface. The Mach number of the jet was estimated at about 10 and the ratio of the density in the jet to that in the ambient medium was about 1-10, both consistent with values of these parameters for YSO jets. However, while YSO jets are radiative, radiative emission was not dynamically significant for the jets created in this experiment.

Figure 4c shows two targets used by a group from ILE [55]. When using these targets, the main laser struck either the outside of a plastic hemisphere or the surface of a plastic plane. This drove a shock wave through the solid plastic, generating a plasma on the rear side. A cone was used to funnel this plasma onto the axis, and a jet emerged at the open end of the cone. Sakawa *et al.* report in [4] the creation of jets of speed 380 km s^{-1} and 480 km s^{-1} from the hemisphere-cone and plane-cone targets respectively.

Figure 4d shows a "V-foil" target used in an experiment in Target Area West of the Vulcan laser facility [56] as reported by Gregory *et al.* in [44] and [57]. Two thin (0.8 μm), planar Al foils, at an angle of 140° to one another and joined along one edge, were simultaneously illuminated by 80 J laser pulses with 260 μm diameter focal spots, generating plasmas on the rear sides of the foils. In the plane sketched in figure 4d the plasmas converged on the axis, and the interferometry data from the experiment suggests that this resulted in stagnation of some of the motion of the plasmas perpendicular to the axis and the formation of a confined axial flow with a speed of 300 km s^{-1}. However, in the plane perpendicular to this there was no plasma convergence, and interferometry data for this plane shows no evidence of the formation of an axial flow. The flows created in this experiment are therefore fundamentally different from those of YSO jets, which are approximately cylindrically symmetric. As well as creating flows that propagated into vacuum, a gas jet was used to create a 5 mb N_2 gas environment on the rear side of the target for the flows to propagate into. The experimental results show evidence of structure at the head of the axial flows when gas was present, as might be expected by analogy with the observations of structures at the heads of YSO flows. The presented analysis of the scaling parameters for the experiment suggests values of 20-40 for the Mach number, 0.1-1 for the cooling parameter, and a density ratio between the axial flow and the ambient medium of 10-50.

3.3.1.2 Front-side targets

A front-side target works as follows. A solid target is illuminated using one or more intense laser beams. These heat the surface of the target and turn material into a plasma, which ablates away from the solid surface. This ablating plasma is then collimated into a jet, the mechanism responsible for the collimation depending upon the laser illumination of the target and the target geometry.

On the following page figure 5a shows a target used by Shigemori *et al.* [1] in an experiment using the GEKKO XII laser with the HIPER beam arrangement [7]. Five beams were used to illuminate the interior surface of a cone of diameter 1.6 mm and full opening angle 120° with a total laser energy of about 500 J. The ablation plasma produced from the region illuminated moved away from the target along the local normal to the surface, with the result that plasma converged onto the axis of the cone. In the convergence, the radial component of the plasma's motion was arrested, leaving a mass moving in the axial direction, the "jet". Three diagnostics were used

to observe the plasma. An X-ray framing camera was used to record images of the X-ray emission. The images were taken from the side of the jet with an exposure time of 80 ps. A second X-ray framing camera, also placed side-on to the jet, was used to record as a two-dimensional image the X-rays that were transmitted through the jet from a source located on the far side of the jet from the detector, a technique known as X-ray backlighting. The $\sim$ 1 keV X-rays were produced by laser-illumination of a uranium foil. Third, an X-ray streak camera was used to record time-resolved images of the X-ray emission from a narrow region about the axis of the cone targets.

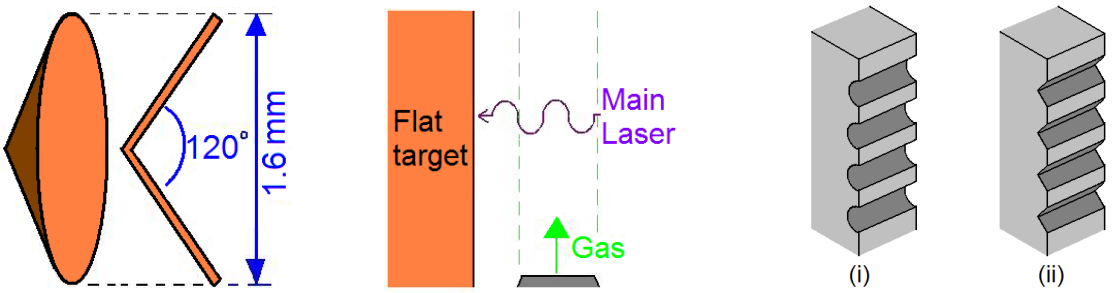

Figure 5: Front-side targets: (a) Cone target as used by Shigemori *et al.* (b) Sketch of the set-up for experiments using PALS (c) Grava and Purvis reduced dimensionality targets: (i) hemispherical grooves (ii) triangular grooves.

The X-ray framing camera images from the experiment (see figure 2 of [1]) show narrower regions of self-emission from jets made of higher atomic number cones. The reason for this is as follows. Higher atomic number ions in a plasma radiate energy more efficiently than lower atomic number ions. For plasma from high atomic number cones, the plasma in the axial stagnation region loses energy by radiation on a timescale shorter than the hydrodynamic timescale. As energy loss leads to a loss of pressure, the plasma in the axial region consequently becomes compressed into a tighter jet as a result of the ram pressure of the plasma ablating from the target which arrives at the axis later in time. An earlier paper by Farley *et al.* [58] showing experimental results and simulations for a very similar experiment illuminating Au cone targets with the Nova laser ([59]) includes a two-dimensional image from a simulation in cylindrical symmetry. The region of strongest radiative emission is predicted to be slightly off-axis at the time shown, +1.1 ns, as by this time the plasma in the axial region has already cooled very strongly by radiative emission due to its high density and as a consequence no longer emits as brightly as the less dense region around it.

The X-ray radiography from the experiment of Shigemori *et al.* showed that the region of highest mass density was along the jet axis in their experiment, as expected. Using

the X-ray streak camera to infer a velocity for the jets, they report that the internal Mach number of Au jets created in their experiment was in the region $10-50$, and that the value of the cooling parameter was about 0.7, consistent with values for YSO jets (see section 3.2). However, the jets produced propagated into a vacuum rather than into an ambient medium, and hence the shock structures/working surfaces of YSO jets were not simulated in this experiment.

Figure 5b shows the experimental geometry used in a series of experiments by a group using the Prague Asterix Laser System (PALS) [60]. The results of these experiments merit a detailed discussion here as they are very similar to the results obtained in the Astra experiment discussed in detail in chapter 4, which forms a major part of this thesis. The PALS laser was used to illuminate a flat, massive slab of material, producing a jet that propagated either into a vacuum or into a column of gas produced by a gas jet placed near the target. The mechanism by which jets were produced in these experiments, being experiments involving a single laser beam and a flat target, has been debated within the group that carried out the work, two particularly relevant papers being [61] and [62].

In [62], Nicolaï *et al.* present experimental results and simulations for the production of jets that propagated into a vacuum. The experimental results show that, when using 100 J pulses frequency-tripled to a wavelength 0.438 μm with a focal spot of radius 300 μm, axially collimated flows were produced when using Al, Cu and Ag targets (which have atomic numbers 13, 29 and 47 respectively). In the paper, their simulation results, carried out using the code FCI2 [63], were used to evaluate the effect of four factors on the plasma flows created, notably magnetic fields generated by the laser-target interaction, radiative cooling, target material atomic number and focal spot size. Simulations for a Cu target under the laser conditions used in the experiment showed negligible change when magnetic fields generated in the laser-target interaction were included, ruling out magnetic collimation as a mechanism. Comparison of simulations performed with and without the inclusion of radiation loss showed that this is very significant for the flow; without radiation loss the flow after 5 ns is far more isotropic. When the target material was varied, it was found that narrower, slower jets are produced from higher atomic number materials, consistent with the more efficient radiative losses from these materials. The experimental results in [62] are in at least partial agreement with this, as Cu jets were observed to be much narrower than Al jets. However, a difference between Ag and Cu jets is not obvious.

The effect of varying the focal spot size shows that more isotropic (less jet-like) flows are produced for smaller spot size. The explanation given for this is as follows. For the same beam energy, the laser intensity is higher when using smaller spot sizes, resulting in a higher plasma temperature. This leads to a reduction in the hydrodynamic timescale for the radial expansion of the plasma, as this is proportional to the inverse of the sound speed and the sound speed depends on the square root of the temperature. On the other hand, the radiative timescale increases as the energy density of the plasma rises faster with temperature than the rate of radiative energy loss. (This was demonstrated in the paper using a simple model considering only Bremsstrahlung losses; however, line radiation can dominate in high atomic number plasmas.) Therefore, the ratio of the hydrodynamic timescale to the radiative timescale reduces as the laser focal spot size is reduced, implying a reduction in the significance of radiative energy loss, and hence a more isotropic flow.

While the simulation results in [62] are useful in determining the relative importance of various parameters for the production of collimated flows, comparison of simulated and experimental flows suggests that collimation is underestimated by the simulations as the experimental jets are observed to be slower and narrower. Although the authors of the paper report that simulations they had performed show "that the effect of jet formation is robust and does not depend too much on the laser intensity distribution", only laser pulses which had their peak intensity on the axis were used in the simulations [64]. However, when using all five amplification stages in the generation of the PALS beam, the intensity produced is higher at the edge of the beam than in the centre, the degree of this hollowing being greater for higher laser energies and even more pronounced after frequency-tripling (see, for example, [65]). In [64] Kasperczuk *et al.* present time-resolved X-ray self-emission data which was obtained using a streak camera that viewed the surface of the target from the side. During the laser pulse the emission is strongest away from the axis, where the laser intensity is greatest, for both plastic and Cu targets. After the end of the pulse, the region of strongest emission moves onto the axis for plastic, while for Cu it remains away from the axis. Kasperczuk *et al.* conclude that it is the "annular" distribution of the laser pulse that is the dominant factor in determining whether a jet forms, rather than the strength of radiative emission; for a low-atomic number jet, near to the target the initial annular nature of the plasma is lost soon after the end of the laser pulse, and hence a well-collimated jet is not formed. Radiative losses may, however, affect the collimation of jets at later times.

Using temperature values from simulations to calculate sound speeds, the jets prop-

agating in vacuo reported by Nicolaï *et al.* in [62] were estimated to have had an internal Mach number of about 15. The values of the Reynolds and Peclet numbers are estimated to have been $\sim 10^6$ and ~ 20, showing that while viscosity was negligible this was only approximately true for thermal conduction. However, as these jets were created in a vacuum the interaction between YSO jets and the interstellar medium was not simulated in these experiments. In later papers the group using PALS report subsequent work in which jets were created that propagated into a column of gas from a gas jet. In [2], Nicolaï *et al.* report that two gases were used, He and Ar, at various particle number densities between 2 x 10^{17} and 8 x 10^{18} cm^{-3}. Ionisation and heating of the gas in the column before the arrival of the jet was produced both by the main laser on its way to the target and, to a greater degree, by X-rays emitted from the heated target. Nicolaï *et al.* report that at +2 ns a He column would have been fully ionised with a temperature of about 2 eV, while Ar would been $8-9$ times ionised and at a temperature of $70-80$ eV. However, [66] reports that the He would have been less than a quarter ionised while the Ar ionisation would have been about 4.

Using a flat Cu target and 100 J pulses of frequency 3ω, Nicolaï *et al.* report the creation of highly collimated, 390 $\pm$ 50 km s^{-1} jets which slowed down upon entering a gas. Shadowgrams taken using the same equipment otherwise used for interferometry show the formation of an axial flow with a complicated working surface structure at the head of the jet, and an approximately hemispherical shock out to the sides of the jet. The given explanation of the working surface structure is the same as that of the YSO jets described in section 2.4 of chapter 2. At the head was a bowshock where the ionised gas of the gas column was accelerated, compressed and heated. At the rear of the working surface was a reverse shock where the Cu plasma in the beam of the jet was decelerated. In between the two shocks were regions of shocked ionised gas and shocked Cu plasma, the surface separating these regions again being referred to as a contact discontinuity. The hemispherical shock to the sides of the jet was explained as being the result of the expansion of the volume of gas which was near the laser focal spot on the target at the time of the laser pulse, this volume being ionised and heated primarily by X-rays from the target.

The shape of the bow shock in the ionised gas was seen to change with time and also to depend on the type and initial pressure of the gas. When using Ar, for low gas densities, or at intermediate times for intermediate gas densities, the bow shock has an approximately conical shape in the axial region and lies in advance of the hemispherical shock that is seen out to the sides of the jet. For high gas densities, or at late times for

intermediate gas densities, the structure appears different. No independent bow shock is visible: instead, the only departure from the hemispherical bow shock seen at the sides of the jet is a funnel-like nose along the axis. On the other hand, when using He the bow shock in the axial region was approximately hemispherical, and the shape was not seen to vary over the range of pressures used.

The difference in bow shock behaviour is a result of the differing radiative cooling of the gases in the post-bow shock region. The shocked He does not rapidly cool, and hence the bowshock maintains its shape over time. However, the radiative cooling of the shocked Ar gas is sufficiently rapid that the gas in the post-bow shock region becomes compressed into a thin shell, leading to a change in the observed bow shock shape. In the paper, this conclusion is confirmed using both X-ray self-emission images, which show emission of X-ray radiation from the shocked Ar gas but not from the shocked He gas, and also by an extensive set of simulations.

The scaling parameters for the experiment when using an Ar background gas are quite similar to those found for astrophysical jets. In [2] Nicolaï *et al.* state that the Mach number was around 6, the ratio of the timescale for radiative cooling to the timescale for radial hydrodynamic expansion was about 3, and the ratio of the mass density in the jet beam to the mass density of the ambient gas could be varied between 0.1 and 10. The Mach number and the cooling parameter in the corresponding astrophysical case are stated to be about 9 and 1.5 respectively, and the density ratio corresponds to that of YSO jets. However, the Peclet number in the experimental case is estimated to have been only about 5, showing that thermal conduction cannot be ignored.

The group working at PALS has obtained several important results. The creation of a jet from a flat target rather than the more complicated target geometries used in other jet experiments is very advantageous, as targets with complicated geometries are expensive, and can also be time consuming, to make. Additionally, the minimum laser pulse energy of 13 J [67] used in the PALS experiments is far lower than the pulse energies used in the other rear-side and front-side experiments discussed so far, and this shows that the use of very high energy facilities is not a necessity for this kind of experiment. Even though the pulse energies used were low, the size of the jets produced was still sufficiently large that they were easy to observe with interferometry, the lengths of the plasmas produced using 13 J pulses being 2.5 mm, with the diameter of the collimated region of the plasma being about 0.4 mm. Both the interferometry system used in all the experiments done by the PALS group, and the X-ray framing

camera used to take images of the self-emission in the case when jets propagated into a background gas, yielded multiple time-resolved images per shot, each image taken at a different time during a jet's evolution. The advantage of taking multiple images per shot is that this shows how a particular jet evolved. In experiments where only one image is taken per shot, a time series for the evolution of a plasma has to be built up over a series of shots using nominally identical target, laser and gas conditions. In this case, one has to establish the effect of shot-to-shot variability on the time series.

Figure 5c shows a sketch of targets used in experiments reported in [68] and [69] by Purvis *et al.* and Grava *et al.*, respectively. In their experiments, instead of producing a circular laser focal spot in the centre of a cylindrically-symmetric target, a line focus was created within an extended groove machined into a solid metal block. The grooves used were either hemispherical or triangular (with a 90° angle at the apex) in cross-section. By taking this approach, fully two-dimensional jets were created using laser pulse energies of only 0.8 J, and these were investigated by using X-ray interferometry to probe the electron density distribution, by taking time-integrated, two-dimensional images of the radiation emitted from the plasma and by X-ray spectroscopy. For the triangular grooves, the results reported by Grava *et al.* show a collimated axial flow at early times which widens and becomes divergent later on. The Mach number of the jets was about 5, with the cooling parameter being about 1 early on, while the jet was seen to be collimated, but being much larger later on. The Peclet number was about 10. As the experiments were performed in a vacuum, the ratio of the density in the jets to that in the ambient medium was very large.

3.3.1.3 Discussion The greatest advantage of using rear-side targets for jet experiments is that the laser and the propagation of the jet, either into a vacuum or into an ambient medium of some kind, are isolated from one another. For front-side targets for which the laser pulse is near-normally incident on the target, jets moving into an ambient medium move into a channel that has been pre-ionised by the laser as it focused down onto the target. The significance of this has been shown by Edens *et al.* [71] in an experiment where a pinhead was illuminated with an intense laser within a static gas. This created a shock wave that expanded outwards in all directions from the head of the pin. For shocks in N_2, the shock front was smooth except where it encountered the channel left by the laser.

3.3.2 Jets created using Z-pinches

A considerable body of work (see, for example, [72, 73, 74, 75, 76, 77, 78, 79, 80, 81, 82, 83, 84]) has been produced by a group using the MAGPIE Z-pinch facility [85] at Imperial College, London. An explanation of a basic jet-creation approach is given in [72] (p. 114) and is summarised as follows. Initially, a conical array of fine wires links the edge of a circular hole in a metal plate to a central column. A very large current, of order 1 Mega-Ampere, is then sent through the plate, down the wires and into the central column. This current flow heats the wires, the outer layers of which are ionised into plasma. Associated with the high current is a high magnetic field which interacts with the plasma, accelerating it towards the axis of the conical array. The convergence of plasma onto the axis leads to the formation of a conical shock front at which the converging plasma has its radial motion arrested and is thus redirected into a collimated axial flow, the "jet".

As in the laser experiment of Shigemori *et al.* discussed in sub-section 3.3.1, the collimation of the jets produced in this manner is found to depend upon the atomic number of the ions within the plasma. Higher atomic number jets were found to have a smaller diameter at their base and to diverge less down their length. The reasons for these results were as follows. First, the additional radiative emission of the higher atomic number plasmas in the region after the conical shock meant that they experienced a greater compression on axis as the reduction in pressure due to radiative energy loss had to be compensated for by an increase in density. As the jet plasmas were more tightly compressed their diameters were smaller. Second, the additional radiative losses within higher atomic number jets reduced the internal pressures acting to cause the jets to expand once they had formed; hence the higher atomic number jets diverged less.

The development of Z-pinch experiments has been carried out with scaling to astrophysical situations using the scaling relations discussed in section 3.1 in mind. For the basic jet-creation experiment described above, the fluid approximation was found to be easily satisfied for the plasma within the axial jet itself, but not very well satisfied in the axial region where plasma converges to first form the jet. There, plasma volumes arriving from opposite sides of the axis interact with one another with a high relative radial velocity and consequently collisional mean free paths are high ([72] p.115). The Reynolds number for the jet plasma was estimated to be 10^4, indicating that viscosity was negligible, but the Peclet number was estimated to only be about 10. This indi-

cates that energy transport by convection was dominant over thermal conduction, but not overwhelmingly so, and Lebedev *et al.* suggest [72] that thermal conduction could act to smooth out features in the plasma on scales smaller than three-tenths of the jet radius.

In their paper, Lebedev *et al.* conclude that the magnetic field, while vital in forming the jet, was not dynamically significant within the jet. This conclusion, when combined with the satisfaction of the fluid approximation and the values of the Reynolds and Peclet numbers, implies that the dynamics of the plasma within the jet can be approximated using HD rather than MHD equations. However, as radiative losses are dynamically significant, determining the divergence of the jet, care has to be taken to consider radiative effects as discussed in sub-section 3.1.4.

In other MAGPIE Z-pinch experiments, additional processes of astrophysical interest have been explored. Some YSO jets are observed to be curved. This could be the result of a nearby massive star causing ionisation or producing a cross-wind, or from relative motion between the system producing jets and the interstellar medium surrounding the jets' source ([74], p.988). Lebedev et al. [74] simulated this by creating a jet using the basic jet-creation method previously outlined but with a plastic foil placed near the axis. During the experiment, X-rays emitted from the wires and the conical shock ablated the surface of the foil, producing a plasma that moved away from the foil towards the jet; in effect, the jet emerged into a cross-wind. The experimental results showed deflection of the jet by the wind, and the creation of oblique shocks within the jet, consistent with simulations of the problem.

One of the most important advances made by the group using MAGPIE was the inclusion of angular momentum in a model jet experiment (see [78] and the longer, later paper [81]). In the basic jet-creation experiment described at the start of the subsection, it was explained how a jet can be produced by passing a very high current through a conical array of very fine wires linking the edge of a circular hole in a metal plate to a conducting central column. Each wire lies in a poloidal plane; viewed from above, the wires appear to be purely radial. However, as the central column has a finite radius, it is possible to connect the metal plate and the central column using wires lying out of the local poloidal plane. In the experiment with angular momentum included, this is exactly what is done: each wire is set at an identical angle to the local poloidal plane, making it appear, when viewed from above, just as if the central column in the basic jet-creation experiment had been given a twist.

When a current passed through the wires in the twisted array, as the wires were no longer in poloidal planes, the current had a toroidal component, and hence the global magnetic field had an axial component. The $\mathbf{J} \times \mathbf{B}$ interaction of the global magnetic field with the plasma created near the wires exerted a toroidal force on the plasma, and hence it moved with angular momentum. Images of the plasma obtained in this case indicate that the conical shock and jet formed were hollow, and that the jet was wider and more divergent for a larger twist of the wire array.

The last advance made by the group using MAGPIE to be mentioned here is the creation of a simulated magnetic tower outflow [75, 77, 78, 79, 83]. A description of this method of jet launching and collimation in an astrophysical context has already been given in section 2.7. In the basic jet-creation experiment discussed above, jets were created by $\mathbf{J} \times \mathbf{B}$ induced convergence on-axis of plasma created about the wires of a conical wire array. In the magnetic tower outflow case, a radial wire array is used rather than a conical array (i.e. the wires are all directed radially and lie in the same plane, like spokes on a wheel).

Two kinds of axial flow were generated in this case. When a current was passed through the wire array, the wires were heated and turned into plasma, the outside of the wires heating and ablating first. Geometrical concerns resulted in a predominantly axial flow with a density peaked on-axis. After this first kind of axial flow, full wire burn-through first occurred at the ends of the wires which were connected to the central column. When burn-through had occurred, current could no longer flow in wires but had to flow in the plasma. The interaction of the magnetic field with the radial current caused loops of current to rise out of the plane of the wire array. The arches of current-carrying plasma joined together to form a magnetic cavity; current flowed from the metal plate over the outside of the cavity and down an axial plasma into the central column. The magnetic pressure of the toroidal field within the cavity drove its expansion; as the cavity expanded, the axial plasma elongated. In this model, the axial plasma was the jet, and the growth of the axial plasma by cavity elongation was the jet "propagation". Plasma created before burn-through acted as an ambient medium into which the cavity moved and it radially confined the cavity.

This experimental method could be set up to naturally produce an episodic axial plasma flow [83]. The magnetic field-plasma interaction removed the current-carrying plasma from the wire array plane when the cavity was first launched. Eventually, plasma refilled the gap between the metal plate and the central column and, due to a

combination of energetic favourability and the disruption of the axial column and/or the cavity, current started flowing through this re-fill plasma. This resulted in the launching of a second cavity, the out edge of which was composed of the re-fill plasma. The second cavity moved into the channel left by the first cavity. The process of re-filling and cavity launching repeated, creating a series of axial plasma columns. It has been suggested that there is an analogy here with the knots in a YSO jet; this would be the case if such knots were created by episodic emission from the jet source, rather than by oblique shocks in the jet beam or by variations in the velocity of the jet (see section 2.6).

3.3.3 Collimated axial plasmas created using coaxial plasma guns

Another way in which axial plasma columns have been created is by using a coaxial plasma gun [86, 87, 88, 89]. Figure 6 below shows a sketch of the apparatus used (figure 6a) and how the technique works (figure 6b). Two coaxial metal discs with a small gap between them are located inside a vacuum chamber at one end. The two discs each contain 8 small holes through which gas can enter the chamber from gas feed lines. Behind the discs is a coil of wire through which a current can be sent to create a magnetic field inside the chamber.

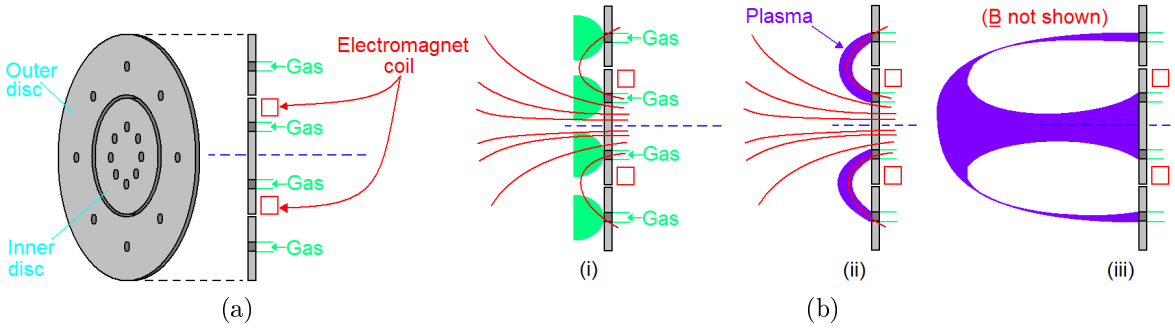

Figure 6: Coaxial plasma gun. (a) is a cartoon of its design. (b) is a cartoon illustrating how it works: (i) A gas is puffed in, and the magnetic field turned on. (ii) A voltage is applied between the discs. (iii) The "spider legs" of plasma merge to form an axial plasma column.

The experiment proceeds as follows. First, the air is pumped out of the vacuum chamber. Then, a current is sent into the coil to create a magnetic field, and a gas is pumped through the small holes in the two discs. A voltage is set up between the discs and breakdown of the gas between the discs occurs along magnetic field lines which happen to pass through both discs. This results in arches of plasma linking the gas

sources (the holes) on the two discs. As the experiment evolves, the arches of plasma extend further and further from the discs. Eventually, the ends of the arches located on the inner disc merge to form a central plasma column. This collimated central column of plasma, which over time extends further and further from the discs, is the plasma "jet".

As mentioned in chapter 2, astrophysical jets are seen to emerge from systems in which a central object is accreting matter from a disc around it, and which have associated with them large-scale magnetic fields. The geometry of the coaxial plasma gun experiment is supposed to simulate the topology of the magnetic field linking a star and an accretion disc: magnetic flux lines passing through the centre of the central disc in the plasma gun correspond to open magnetic field lines of the central object in the astrophysical case, while magnetic field lines linking the two discs of the plasma gun correspond to magnetic field lines linking the central object to the accretion disc. The voltage applied between the two static discs of the plasma gun corresponds to the electric field induced between a central object and an accretion disc due to "sheared toroidal rotation of the disc in the presence of a magnetic field" ([86] p. 257).

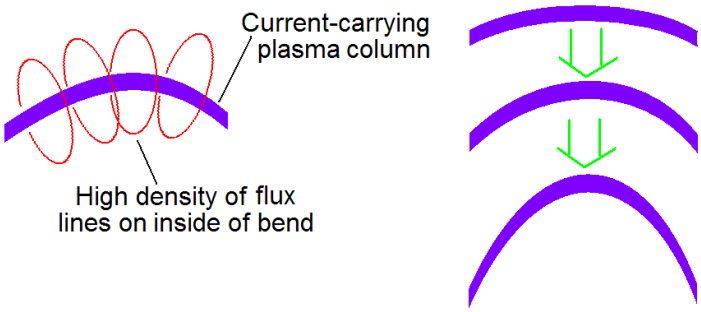

Figure 7: Illustration of the kink instability.

One feature of the experiment worth noting is that, depending on the magnetic field and the current linking the discs, the central plasma column becomes unstable to disruption via the kink instability. The mechanism by which this operates is sketched in figure 7. Associated with the current along the plasma column is a toroidal magnetic field. If the column is not perfectly straight, but contains a small bend, the result is that the magnetic flux density on the inside of the bend is greater than the flux density on the outside of the bend. As magnetic pressure depends on the square of magnetic flux density, the magnetic pressure is greater on the inside of the bend than on the outside and so the plasma in the bend is forced further outwards by the pressure imbalance. Eventually the column can be totally disrupted.

The co-axial gun work has illustrated experimentally that, for an ideal MHD plasma, a collimated, axial plasma column can be produced from a realistic star-disc magnetic field topology. The mechanism is somewhat similar to the magnetic tower scenario of jet launching. The analogy between the experiment and an astrophysical case is limited, however. First, the modelling of the effects of disc rotation using an applied electric field is only an approximation. Second, the model only includes that part of the accretion disc linked magnetically to the star: in the magneto-centrifugal models of jet launching discussed in 2.7, the jet material can start further out in the accretion disc, travelling along open magnetic field lines that have their fixed end in the accretion disc. Third, the experiment is not designed to be geometrically similar to, and cannot be scaled to, an astrophysical case.

Also, there are some important features of YSO jet systems that have not so far been included in the coaxial plasma gun model. One of the most significant of these is that the experiment was performed in an initially evacuated vacuum chamber, resulting in the ratio of the central column density to the initial density in the vacuum chamber being very high. Astrophysical plasma columns propagate into a surrounding ambient medium: for YSO jets the ratio of the density in the jet beam and the density in the interstellar medium is typically $\sim$ 1-10, while for an AGN jet the relevant ratio is about 0.1.

3.4 Summary: how far has the development of scaled experiments progressed?

In this chapter, an overview has been given of the mathematical basis allowing for the creation of scale models of hydrodynamic systems and of previous attempts to create models of astrophysical jets in the laboratory. Mathematically, the scaling of ideal, purely hydrodynamic systems is straightforward. However, when magnetic fields and the emission of radiation are dynamically important, such as is the case for YSO jets, the creation of scale models is more restricted. In order to demonstrate quantitatively that a laboratory system is a true scale model of an astrophysical object, one has to demonstrate that the equations governing the behaviour of the experiment and its astrophysical analogue are of the same form, that a set of scaling parameters are the same in the two systems, and that at some point the laboratory and astrophysical systems are geometrically similar.

Of the experiments performed to date, there has been achievement in several areas.

Laboratory experiments have been used to reproduce qualitatively, and often quantitatively, a lot of the features seen in observations and numerical models of YSO jets. Experiments involving high-intensity lasers and Z-pinches have demonstrated the importance of radiation for jet formation by showing that jets made from higher atomic number, and hence more radiative, plasmas form narrower jets. Z-pinch experiments have also shown that radiation can affect how collimated a jet remains after leaving the region where it forms. Other laser experiments have been particularly successful in modelling the interaction of a YSO jet with the interstellar medium, reproducing the working surface structure seen in numerical simulations. In addition, Z-pinch experiments have been able to create jets with angular momentum and to model the effects of a plasma crosswind on a jet and the interaction of a jet with a "cloud" of material lying in its path.

As discussed in section 2.7 of chapter 2, the launching of YSO jets is believed to be a complex magnetohydrodynamic process. Z-pinch and gas gun experiments are suited to modelling this as they create jets using magnetohydrodynamic processes; so far, the processes by which jets have been created in laser experiments have been purely hydrodynamic. Two experiments, one involving a coaxial plasma gun and one using a Z-pinch, have been able to show that a collimated axial flow can be generated from a initially flat MHD plasma in which radial currents are flowing, thus simulating the magnetic tower outflow launch model. These experiments are also the only ones to include a magnetic field that is dynamically important for the propagation as well as the launching of a jet. In addition, the Z-pinch experiment is the only experiment in which an episodic axial plasma flow has been created, simulating periodic mass ejection by a YSO source.

4 The Astra Experiment

In the previous chapter, a mathematical framework allowing for the creation of scale models of certain astrophysical plasma flows in the laboratory was examined. This was followed by an overview of previous work, focusing specifically on the attempt to create models of jets from Young Stellar Objects. In this chapter, details of two experiments are presented. The first was carried out using the Astra laser system at the Central Laser Facility (CLF) of the Rutherford Appleton Laboratory (RAL) near Oxford, U.K., in July and August 2007. The motivation behind this experiment, hereafter referred to as the Astra experiment, was a desire to examine the importance of three factors that can potentially affect the collimation of YSO jets by examining the effect of these factors on their laboratory counterparts. These three factors are the strength of the radiative emission from the plasma in the jet, the nature of the ambient medium into which the jets propagated, and the presence of a large-scale magnetic field.

The second experiment, hereafter referred to as the ILE experiment, was performed using the GEKKO XII laser system at the Institute of Laser Engineering (ILE), Osaka University, Japan in November 2008. In the Astra experiment, the intent was to use the mathematical basis that allows for scaling to gain insight into an astrophysical situation via a laboratory experiment. In the ILE experiment, the intent was to use the same scaling relations to scale between plasma flows created using two different laser systems, a technique known as lab-to-lab scaling. Whereas the Astra experiment was solely a study of laboratory plasma jets, this was not the case with the ILE experiment, where the plasma jets with which this thesis is concerned comprised only one part.

In section 4.1 of this chapter, an overview is given of the experimental method used in the two experiments to create plasma jets and vary their properties. The rest of this chapter is then devoted to a discussion of the Astra experiment. Sub-sections 4.2 and 4.3 contain the experimental details and a detailed discussion of the techniques used in analysing the interferometry data. After this, results from the experiment are presented in sections 4.4 and 4.5. Finally, the chapter is summarised in sub-section 4.6. The ILE experiment is covered in chapter 6, following the presentation of simulations of various aspects of the Astra experiment in chapter 5.

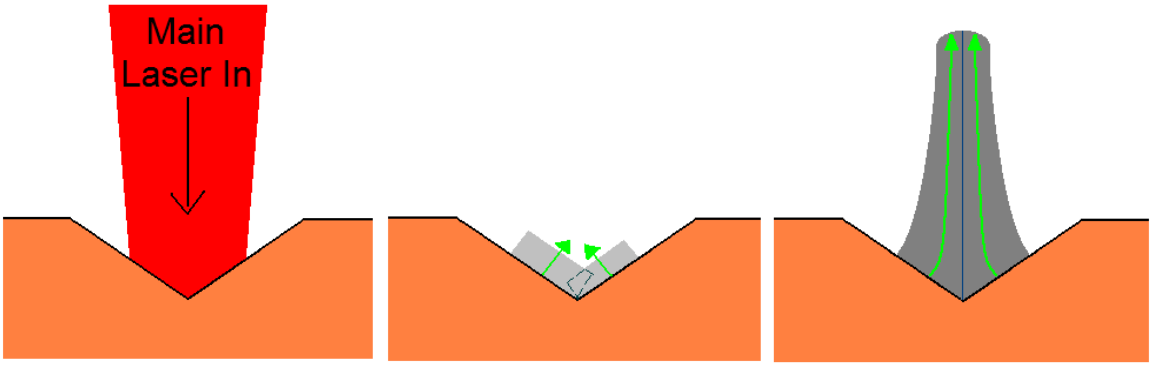

(a) (b) (c)

Figure 8: Cartoon of jet formation from a conical target. In (a) the main laser pulse illuminates the centre of a cone. The first plasma coming from the target surface is fast and low density and interpenetrates as shown in (b). This is followed by slower, denser plasma which stagnates on the axis, producing an axial flow as shown in (c).

4.1 Outline of the experimental method

The basic method for creation of jets in the Astra and ILE experiments was the same as that previously used by Farley *et al.* [58] and Shigemori *et al.* [1], the experiments of which are described in sub-section 3.3.1. The jet creation method is outlined in the cartoon in figure 8. A short-pulselength, high-power laser was used to illuminate a conical recess machined into a block of metal alloy, as shown in figure 8a. This resulted in heating and ionization of the surface material, which subsequently moved away from the target along the local surface normal and converged on the axis of the recess. The first plasma to leave the surface would have been fast-moving and low density. Hence, the plasma volumes arriving at the axis from opposite sides of the cone would initially have had long collisional mean free paths and so they would have interpenetrated; this is shown in figure 8b. Later on, as slower, denser plasma arrived at the axis the interaction would have become collisional. When this occurred, plasma volumes arriving from opposite sides, having arrived at the axis with radial velocities equal in magnitude but opposite in direction, would have had their radial motion arrested, leading to plasma stagnation on the axis. As the plasma volumes would have had identical axial velocity components, this radially-stagnated plasma would have continued to move axially, giving the scenario shown in figure 8c.

In view of this method of creating an axial flow, it is important to define the meaning of the word "jet" as used hereafter. The reason for this is that it is a valid question to ask whether "jet" describes the whole of a flow of plasma as it leaves a target and subsequently propagates, or whether "jet" only describes the plasma after the point of

radial stagnation. In the rest of this thesis, "jet" will be used to refer to the whole of the plasma flow leaving a target; within this definition, the plasma flow from a flat target also qualifies as a "jet".

In the introduction it was mentioned how the Astra experiment was motivated by a desire to study the importance of three factors that can potentially affect the collimation of a YSO jet. These parameters are radiative emission, inertial confinement (i.e. the radial confinement of a jet by the pressure of the surrounding ambient medium) and the presence of large-scale magnetic fields. It was originally conceived that in the Astra experiment a large-scale magnetic field could be created using an electromagnet. However, due to a problem with the power supply this did not prove possible, and as a result only radiative emission and inertial confinement were investigated.

Simulations of laboratory jets from Au cone targets by Mizuta *et al.* [101] show that the combined effect on jet collimation of radiative emission and an ambient medium may be expected to be greater than the effect of either of these factors in isolation when jets radiate strongly. In the paper, four sets of results are shown, two for jets created in a very low density ambient medium and two for jets in a higher-density ambient medium. In each of these pairs, one set was carried out with the radiative emission routines in the code turned on, and one with them turned off. Both the inclusion of radiative emission and the presence of an ambient medium on their own result in a narrower jet than in the vacuum, no-radiation case. The effect of including both radiation and an ambient medium together is much greater still: as the ambient medium inhibits the expansion of a jet once it has formed, the electron density in the axial region is kept higher, and hence the effect of the radiative cooling, which depends non-linearly on the electron density, is enhanced.

In the Astra and ILE experiments, the radiative property of the jets was varied by changing the target coating material. As discussed in section 3.3.1 of chapter 3, plasmas made from materials with a higher atomic number radiate energy more efficiently, and consequently radiative losses have a larger effect on the plasma dynamics. In the Astra experiment, an ambient medium was provided for the jets by evacuating the air from the vacuum chamber in which the target was situated and refilling the chamber with a pure gas, the pressure of which could be set as desired.

There are three terms it is helpful to define before discussing the details of the experiments and their results. The firing of a laser pulse onto a material to generate a plasma and the subsequent observation of the plasma over its lifetime is referred to as a "shot".

The object struck by the laser is referred to as the "target". Finally, "target normal" is used to refer to the direction normal to the target as a whole. In the case of a flat target, the target normal direction is the same as the local surface normal direction at every point on the surface. However, for a conical target the target normal direction is that of the axis of the cone, and is nowhere the same as the local surface normal direction.

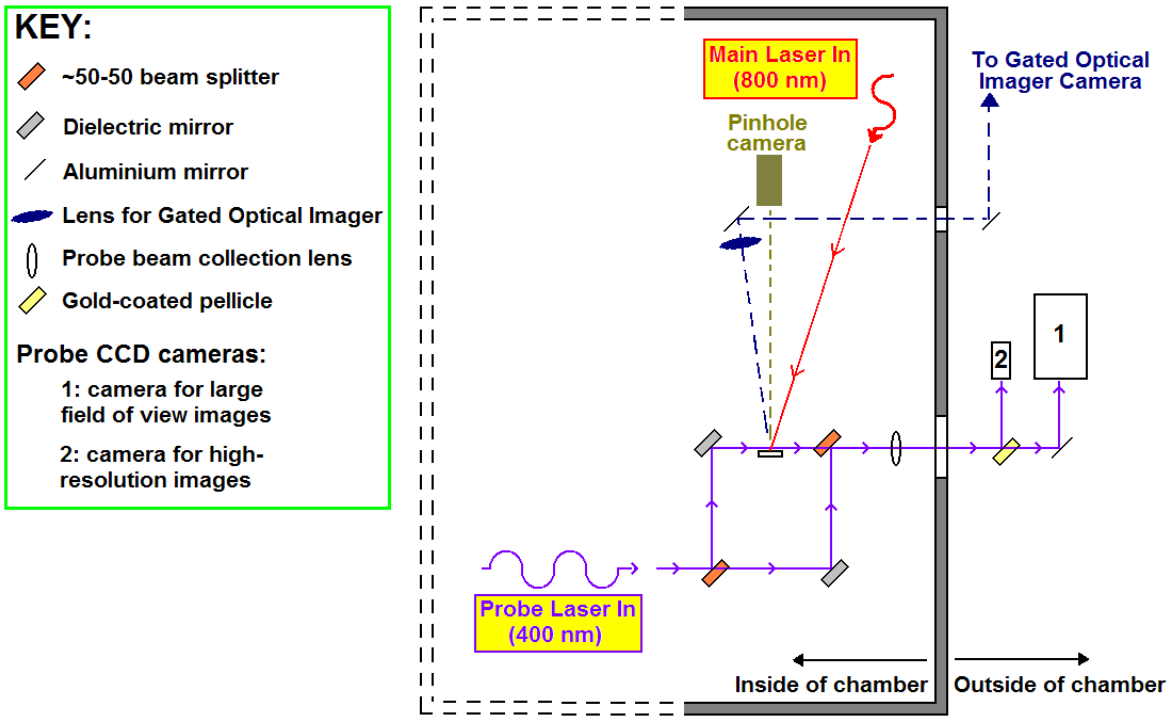

Figure 9: A diagram of the set-up for the Astra experiment, viewed from above.

4.2 Experimental details

4.2.1 The main laser beam

Figure 9 above shows the set-up for the Astra experiment. The target was situated in a vacuum chamber where it was illuminated by the main beam, producing a plasma. The Astra laser system [6] uses a titanium-sapphire crystal as a gain medium and provides a single main beam of ~ 0.5 J pulses, on demand, at a wavelength of 800 nm and at a rate of up to 2 Hz. It is capable of producing pulses as short as 40 fs, but in the experiment pulses stretched to ~ 2 ps were used for most shots. In each shot, a single pulse of the main Astra Target Area 2 beam was used to illuminate a target and thereby create a plasma. The beam was focused onto the targets using an f/6.5 off-axis parabola, the central axis of the parabola lying at 8° with respect to target normal. An off-axis parabola was used so that laser light reflected from the target would not travel back through the laser system as this can result in damage to optical

components. The focal spot diameter at the target position was ~ 100 μm FWHM[10], the focal position of the laser lying 650 μm behind the target. Assuming that the pulse energy was evenly distributed in time and was fully contained within the FWHM gives an average intensity within the focal spot of 3×10^{15} W cm^{-2}.

4.2.2 The targets

During the experiment the rate at which main laser pulses could be delivered did not play a part in limiting the rate at which data could be gathered. The laser pulses could be provided at up to 2 Hz, giving a minimum time of half a second between pulses. However, the time taken for the cameras observing the plasmas produced by the pulses to readout was much longer than this, as long as several minutes for the CCD camera with the largest chip. This meant that the laser system could not be operated at anywhere near its maximum rate. In order to gather data as fast as possible, it was important that the time taken to align targets between subsequent shots was as short as possible. For this reason, strips of metal alloy containing multiple targets were used. Between shots, all that was required was to move the strip to bring the next target into position.

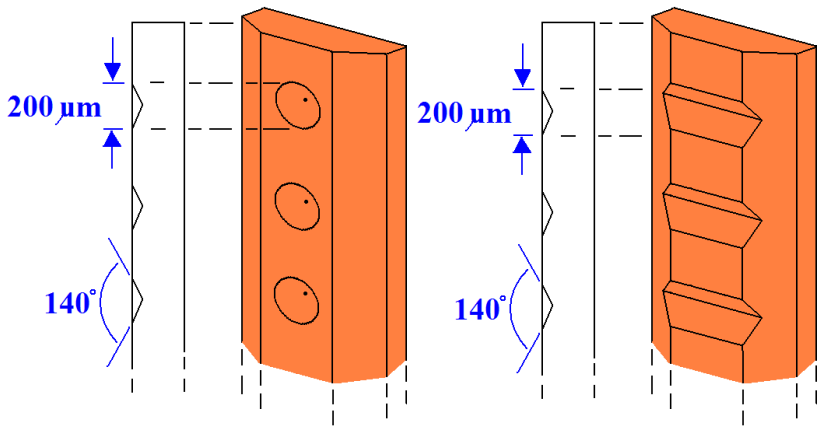

Figure 10: Cartoons of targets used in the Astra experiment. (a) shows a strip of cone targets and (b) shows a strip of groove targets.

Figure 10a shows a cartoon of the basic target used in the Astra experiment. A series of cones was machined into a strip of alloy which was then given a thin surface coating. Each target strip was 50 mm long and 5 mm wide. The centres of adjacent cones were 1 mm apart, and 48 cones were put onto each strip. Each cone had a diameter

[10]FWHM stands for " full width at half maximum intensity".

of 200 μm and a full opening angle of 140°. Initially, cuboid target strips were used. However, during the experiment the corners of the strips were cut off to leave the strip shape shown in figure 10a. This reason for this is that the most important diagnostic instrument was located transverse to the axis of the cones and it was a concern that the region just above the target surface would be obscured by the edges of the strip in the case that the rotation of the target strip was not set perfectly.

Figure 10b shows a second target type used during the experiment, the so-called "groove" target. This is very similar to the cone target, with the only difference being that grooves of diameter 200 μm and a full opening angle of 140° were machined into the strip of alloy rather than cones. The reason for shooting groove targets was to provide a link between the conical target shots and the work of Gregory *et al.* [44, 57]. As discussed in section 3.3.1, the "V-foil" targets used by Gregory *et al.* consisted of a pair of thin planar foils which touched along one edge, making a V with an opening angle of 140° on the rear side. The front sides of these targets were illuminated, resulting in the propagation of shocks through the foils and the production of plasmas at the rear. These then converged onto the plane of symmetry. The experimental results suggest there was stagnation of some of the plasma motion transverse to this plane, resulting in the production of an axial flow. Perpendicular to this, parallel to the plane of symmetry, the plasmas did not converge and a confined flow was not seen. The groove targets shot in the Astra experiment can be expected to work in a similar way to these "V-foil" targets, although in the Astra experiment the plasmas were generated on the front rather than the rear side.

Other previous work to which the use of the groove targets is relevant is that reported by Grava *et al.* [69], also previously discussed in section 3.3.1. In their experiment, Grava *et al.* illuminated the insides of grooves using a laser beam with a long line focus, thereby generating fully 2-D plasma flows. This is somewhat different from the situation in the Astra experiment in which the insides of the grooves were illuminated with a beam with a small, circular focal spot rather than a line focus. This meant that plasmas could freely spread out in the along-groove direction, and were thus not fully two-dimensional.

In addition to those from conical targets, results from flat targets will be presented in this chapter. At the start of the experiment the flat targets used were polished, coated target strips into which no cones or grooves had been machined. However, later in the experiment the flat regions between cones were used for the sake of expedience. Flat

targets were shot in order to allow an assessment to be made as to how useful the conical geometry was for jet production.

After machining, the front surfaces of the target strips were given a thin coating, the depth being of order 1 μm. Five coating materials were used: plastic (specifically n-type polypropylene), aluminium, copper, smoked copper and gold. All of the coatings except that of the smoked copper were deposited as uniform layers. The smoked copper target was somewhat different. A target is given a "smoked" coating by placing the target and the coating material into a vessel containing only a few millibars of an inert gas and evaporating the coating material [90]. Following this procedure produces a low-density, microstructured coating rather than a solid-density, even coating on the surface of the target. Hereafter, the names of the coatings will be abbreviated to CH, Al, Cu, Cu-smoke and Au.

By varying the coating material, plasmas containing ions of different mean atomic number could be created. The mean atomic numbers of CH, Al, Cu and Au are 3.5, 13, 29 and 79, respectively. Ions of higher atomic number emit radiation more efficiently than ions of lower atomic number. As a result, varying the target coating material led to a variation in the importance of radiation for the plasma dynamics. In this way, it was hoped to explore the importance of radiative emission for jet collimation. The use of Cu targets with a microstructured coating layer in addition to those with an even coating was an attempt to create plasmas with a higher energy content using laser pulses of the same energy, effectively allowing energy to be varied as a parameter over a larger range: the microstructure on the surface of a smoked target means that it absorbs light at optical frequencies more efficiently than a uniform coating [90].

It is important to consider whether the thickness of the coating layers was such that the plasmas observed by the diagnostics were composed only of coating material, or whether the alloy substrate material was also present, having been ablated by the laser pulse after the coating had been burnt through. This question will be discussed in more detail in section 5.2 of chapter 5. Here it will only be noted that experimentally the plasmas created from targets with different coatings under nominally identical laser conditions were observed, using interferometry, to have significantly different behaviours; from this it can be concluded that the plasmas were composed mainly of coating material.

4.2.3 Ambient gas

In chapter 2 it has been discussed how the jets emerging from a YSO system propagate into the low density plasma of the interstellar medium rather than into a vacuum. In the Astra experiment, the target was contained in a vacuum chamber which was pumped down to a pressure of 10^{-4} mb before every series of shots. Shots taken with the chamber at this pressure created jets that propagated into a vacuum. Once the chamber was pumped down, it was possible to re-fill it with a pure gas to a desired pressure. This was done by using a pressure gauge to monitor the pressure within the chamber and manually starting and stopping the flow of gas, which was supplied either from a gas bottle or, in the case of nitrogen, from the vacuum chamber let-up line[11]. In this way a static ambient medium was created into which jets could propagate.

	He	N_2	Xe
Atomic number, Z	2	7	54
Mass number, A	4.0026	14.007	131.29
Pressure ranges used /mb	10-200	10-200	4-32
Number densities used / $\times 10^{16}$ cm^{-3}	25-500	25-500	9.9-79
Mass densities used / $\times 10^{-6}$ g cm^{-3}	1.6-33	23-460	22-170
1st ionisation energy / eV	24.6	14.5	12.1

Table 2: Properties of gases used in the Astra experiment. The 1st ionisation energy given for nitrogen is that of an isolated nitrogen atom.

The gas types and pressure ranges used in the experiment are summarised in table 2 above. The use of three gases of different atomic number was an attempt to vary the radiative emission of the ambient media into which jets moved, while changing the gas pressure was an attempt to vary the inertially confining effect of the ambient medium. As the atomic masses of the atoms in the three gases are different, use of a different gas at the same pressure would have simultaneously changed the radiative and inertially confining properties of the ambient medium; assuming that it is the bulk properties of the ambient medium that determine jet collimation, rather than the properties of individual particles, an attempt can be made to isolate the radiative effect when analysing results by comparing data for gases of equivalent mass density rather than equivalent pressure.

[11] The Astra chamber vacuum system is designed such that the chamber is returned to atmospheric pressure - "let up" - by filling it with nitrogen.

4.2.4 Diagnostics

The main diagnostic used in the experiment was optical probe interferometry. The probe beam was created by splitting off a part of the main Astra beam and frequency-doubling it to 400 nm before it entered the vacuum chamber in which the target, the parabola used to focus the main beam and the optics making up the interferometer were contained. The collimated, ~ 0.8 cm diameter probe beam was sent into a Mach-Zehnder interferometer, the design of which is illustrated in figure 9. The probe beam was split at the first beam splitter, one half of the beam being sent down a reference path and the other half being sent past the target surface perpendicular to target normal.

As the probe beam originated as a part of the main Astra beam, its bandwidth would have been of the same order as that of the main Astra pulse. Hence, the coherence time of the probe would have been of the order of the shortest possible main beam pulselength, which was around 50 fs, corresponding to a coherence length of (50 fs x 3 x 10^8 m s^{-1} =) 15 μm. This meant that the two paths of the interferometer had to be aligned accurately: if the two paths had differed in length by 15 μm or more then pulses travelling down the two paths would have been spatially separated by more than the coherence length when they arrived at the second beam splitter, and consequently they would not have interfered with one another. In order to achieve the best contrast between light and dark fringes, a path length of zero is necessary. The interferometer was aligned by B. Loupias and L. Wilson using a white light source. This was used as it also has a short coherence length.

After leaving the Mach-Zehnder, the probe beam light was collected and focused using an $\sim f/3$ collecting lens. It left the vacuum chamber through a window anti-reflection coated for 400 nm, and was then split using a gold-coated pellicle, both the reflected and transmitted beams being imaged onto charge-coupled device (CCD) cameras filtered with 400 nm interference filters. The first camera had a 16-bit detector chip. This was a square array of 2048 x 2048 square pixels each of side length 13.5 μm. The second camera had a smaller-area, 10-bit detector chip with 1392 x 1040 square pixels each of side length 6.45 μm. The large physical area of the chip of the first camera meant that it could be used to take large field of view images of plasmas. The field of view was calculated using two methods, both based on the imaging of an object of known size, and was found to be 3.0 x 3.0 mm, giving an image magnification at the detector of about 10. Owing to its smaller pixel dimensions, the second camera could be used

to provide higher-resolution images of the central regions of the plasmas seen with the first camera without having to introduce extra optics after the pellicle beam-splitter to alter the magnification from that used for the first camera. These two cameras will hereafter be referred to as the large-area CCD and the high-resolution CCD.

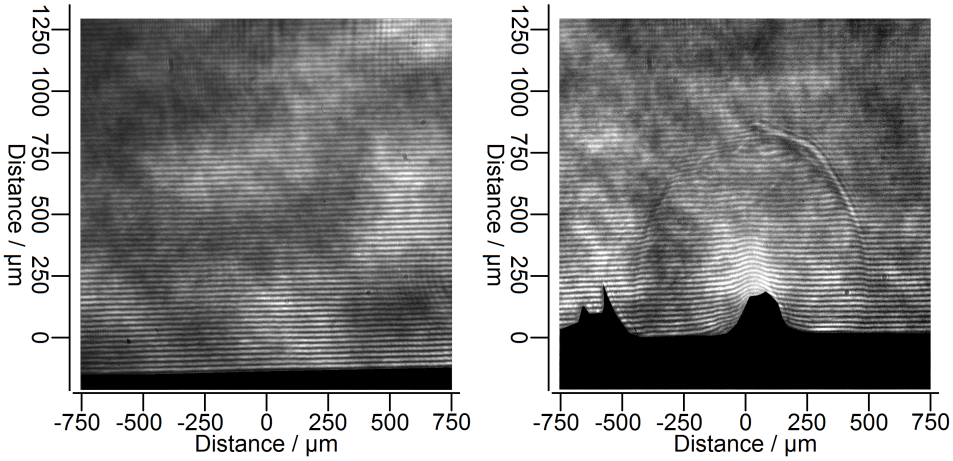

Figure 11: Close-ups of the region of interest from a pair of reference and data interferograms recorded during the experiment by the large-area CCD. (a) is the reference image and (b) is the data image.

The interferometer was set up such that, in the absence of a plasma in front of the target, the detector cameras recorded a pattern of parallel, straight fringes, with the direction of the fringes roughly perpendicular to target normal. The presence of a plasma resulted in a departure from this pattern. During the experiment, the interferometry cameras were used to take two types of image, first reference images showing the fringe pattern in the absence of a plasma and second data images showing the distorted fringe pattern in the presence of a plasma. Figure 11 shows an example of the two types of image, showing close-ups of the regions of interest from a pair of reference and data interferograms recorded by the large-area CCD. Reference images were not taken before every shot, but rather only one or two reference images were taken during a shot series. This saved a lot of time as the readout time of the large-area CCD was at least two minutes, and it generally produced an acceptable result as the spacing of the fringes, the spatial intensity variations across the width of the probe beam and the position of the target usually varied little between subsequent shots.

The pulselength of the probe beam was 2 ps. Such a short pulselength was necessary in order to minimise the effect of motion blurring in the data. In the experiment, shock waves were formed which moved at maximum speeds in the range 100-1000 km s^{-1} (see section 4.5), travelling up to 2 µm in the 2 ps for which the probe beam was on.

Taking into account the magnification of 10 on both of the interferometry cameras, this means that the motion of each element of a plasma influenced a region of up to about 20 μm at the detector, corresponding to the width of 1.5 pixels in the large-area CCD images and 3 pixels in the high-resolution CCD images. Looking ahead to section 4.5, it is seen that the plasmas had a diameter of up to 2 mm, a distance which it would have taken the probe beam approximately 7 ps to cross. Considering that the 1.5 and 3 pixel values are upper bounds, and that the time taken for the probe beam to cross the plasmas is already much longer than the pulselength, a shorter pulselength would not have been of great benefit in further reducing motion effects.

Between the location where the probe beam was split off from the main Astra beam and the position of the target, the probe beam and the main beam followed different paths. By attaching some of the optical components in the probe path to platforms that could be slid along a rail, it was possible to adjust the physical length of the probe path. This meant that it was possible to equalise the optical path lengths the probe and main beams travelled in order to reach the target, and hence to synchronise their arrival. Synchronisation[12] was done over a series of shots by firing the main Astra beam onto an Al target and reducing the length of the probe path until the disturbance to the fringe pattern in the interferometry data images vanished. This indicated that no plasma had been created at the target surface and hence that the probe beam was taking a snapshot just as the main beam was hitting the target. Having synchronised the main and probe beams, the positions of the platforms on the rail were marked. Then, by moving one of the platforms along the rail, and using the fact that in 1 ns light travels 30 cm in air, it was possible to delay the arrival of the probe beam with respect to the main beam by a known amount and hence to use the probe beam to sample plasmas at different times in their evolution. Results for delays of up to +20 ns are reported in this chapter.

Two other diagnostics were fielded, a pinhole camera and a gated optical imager. The pinhole camera was used to record images of the X-ray self-emission from the plasmas which were time-integrated over the entire plasma lifetime. A front-illuminated CCD camera was used as the detector, and the camera was filtered with Be. The combination of the Be filter and the electrode structure on the front of the CCD chip meant that the chip was only sensitive to X-rays with energies above 1.0-1.5 keV. The gated optical imager was used to take snapshots of the optical self-emission from the plasma. The collecting and focusing lens was $f/3$, and it was placed 16 cm from the target along a

[12] This procedure of synchronising the arrival of two beams at a target is known as "timing".

line at 9° to target normal. The camera used as a detector was an Andor i-Star DH734 Intensified CCD (ICCD) camera; it was filtered with a 632 nm interference filter and a neutral density filter of optical density 2.0. The minimum exposure time of the camera was around 2 ns. This information is included only in order to make a complete record of the experiment; no data from either the pinhole camera or the gated optical imager is presented in this thesis.

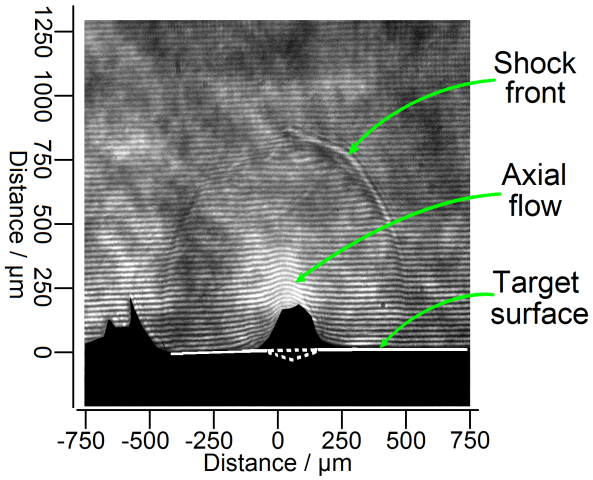

Figure 12: Raw interferometry data for a shot onto a Cu-coated conical target in 50 mb He at +5 ns. The image was taken using the large-area CCD camera. The approximate position of the conical target is indicated in white.

4.3 Analysis of interferometry data

In the Astra experiment, interferometry was the most important of the diagnostics. In this sub-section a detailed discussion of the techniques used to analyse the gathered data is given. Figure 12 above, which shows the region of interest taken from an interferogram obtained using the large-area CCD camera, will be used throughout the sub-section for purposes of illustration. This particular image was taken for a shot onto a Cu-coated conical target in a 50 mb He gas environment at +5 ns. The original target position, lying at the bottom of the image, is indicated in white. In the shot, the main Astra beam has illuminated the centre of the conical target, travelling along a near-vertical path down from the top of the image. Just above the position of the conical target there is a masked region where no fringes are present. Above this, moving along the axis of the target, there is a region of curved fringes, indicating the presence of an axial flow of plasma. Some of the radiation emitted by the plasma at this location was at the same frequency as the probe beam, explaining why this region seems brighter than the rest of the image.

Further out from the centre of the image there is a hemispherical feature of diameter 0.9 mm corresponding to a shock front travelling through the gas. Outside the shock

front the fringes are parallel and equally spaced, just as in a reference image taken without a plasma present. In the bottom left of the image is a spike of material extending out from the target surface. This is either a defect in the target strip or a piece of debris resulting from shooting a conical impression further along the strip.

4.3.1 Phasemap extraction from raw interferometry data

It was discussed in sub-section 4.2.4 how two types of interferometry image were taken in the experiment. Reference images show the pattern of equally-spaced, parallel fringes obtained from the interferometer when no plasma was present. In data images, the presence of plasma leads to a departure from this simple fringe pattern. Using computer software, it is possible to compare a data image and a reference image in such a way as to calculate, for each pixel in the image, a value for the shift in phase due to the presence of the plasma. For example, if, for a specific pixel, the fringe pattern in the data image is found to be shifted by 3 whole fringes from the fringe pattern in the reference image, one "whole" fringe constituting a dark fringe-light fringe pair, the shift in phase for the pixel is (3 x 2π =) 6π radians. In order to get absolute fringe shift values, at least part of the data image must contain unshifted fringes.

In analysing the Astra data, the computer program IDEA [91] was used. The output from using this program to analyse a reference image-data image pair is a 2-D image known as a phasemap. The values of the pixels in a phasemap are the values of the phaseshifts induced by the presence of the plasma. The procedure followed when using this software is discussed in detail in Appendix 1.

Figure 13 on the following page shows some of the steps in the procedure when applied to the data shown in figure 12. Figure 13a shows the data image. Both the target and the region near the target surface where there are no interference fringes have been masked in black. A fast Fourier transform was applied to the masked data image to generate figure 13b. It can be seen that there are three bright spots, one of which is in the centre of the image and the other two of which are arranged symmetrically on either side. The bright spots to the sides are at plus or minus the spatial frequency of the evenly spaced, horizontal fringes in the interferogram, while the spot in the centre is related to the background intensity of the probe beam onto which the pattern of fringes is superposed.

The Fourier transform image was masked to cover everything except the region within the yellow box, and an inverse fast Fourier transform applied to generate the modulus-

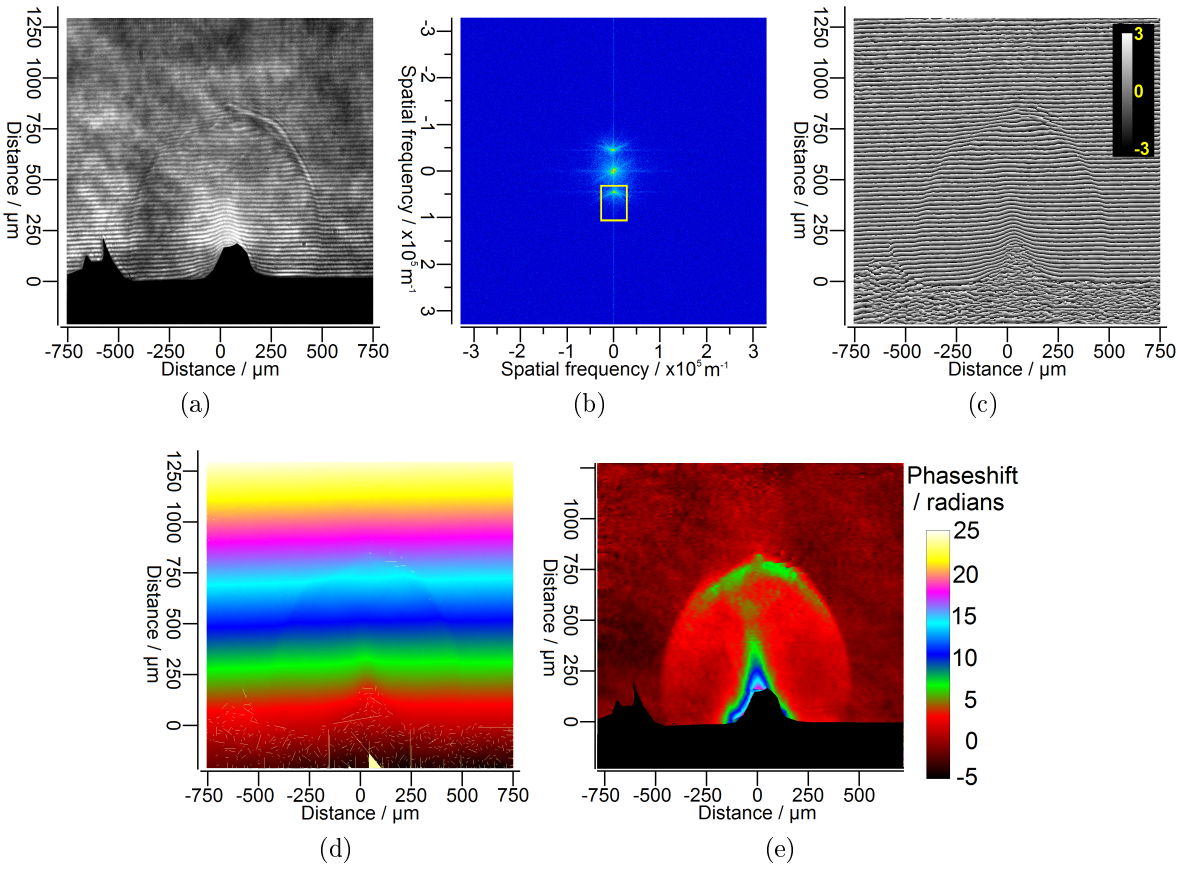

Figure 13: IDEA interferometry analysis for a shot onto a Cu cone target in 50 mb He at +5 ns. (a) The raw interferometry data with the fringe-free region masked. (b) The Fast Fourier Transform (FFT) of the raw data. (c) A modulus 2π image generated by performing an inverse FFT using only the region of (b) within the yellow box. (d) A phasemap for the data image generated from the modulus 2π image. (e) The final phasemap produced by subtracting the phasemap derived from the data image from that derived from the reference image.

2π image in figure 13c. Here, the values of the pixels are assigned values between -π and π, with dark pixels having a value near -π and bright pixels a value near π. A reference point in the region of unshifted fringes outside of the shock was then chosen and the "Local Minimum Cost Matching Branchcuts" algorithm used to scan across the modulus 2π image, starting from the reference point, and calculate the phase of the pixels relative to that of the reference point, resulting in the phasemap shown in figure 13d.

After applying the same procedure to the reference interferogram, the phasemap generated from the data image was subtracted from that generated from the reference image (not shown) to produce the final phasemap shown in figure 13e. In each use of the analysis procedure three phasemaps are produced in total: one from the data image, one from the reference image, and a final one generated by subtracting the data phasemap from the reference phasemap. As the first two of these are internal to the

analysis procedure, the term "phasemap" will hereafter be used only to describe the final, post-subtraction phasemap.

The time taken to produce a decent final phasemap from a pair of data and reference images varies depending on the size of the images being processed and the quality of the data. If the quality of the data is not good, for example if the fringe pattern is hard to make out due to the contrast between light and dark fringe regions being low, then phasemap extraction can be quite time consuming. In this case, it may be required to carry out the procedure previously described using several different FFT masks to see which produces the best results, or even to vary the procedure slightly.

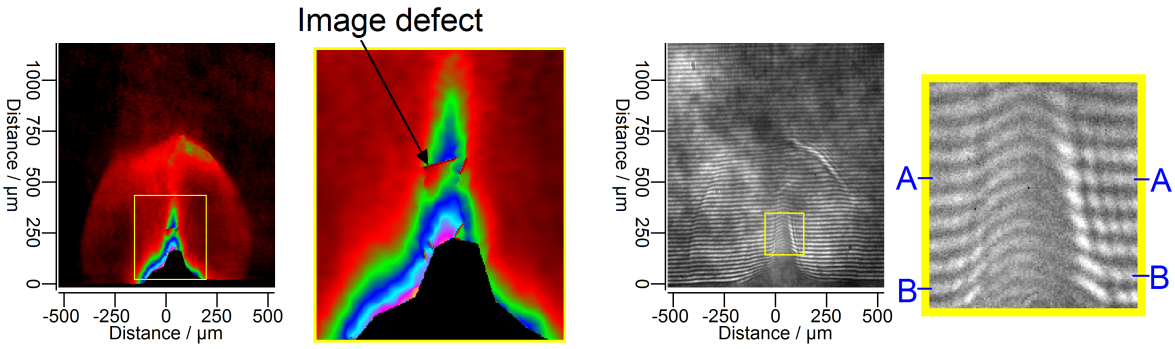

Figure 14: Illustration of the cause of fringe-splitting defects in phasemaps. (a) shows a phasemap for a Cu target in He gas at +4 ns. There is a sizable image defect visible half way up the axial flow as indicated in close-up (b). (d) shows a close-up of the axial region of (c), the interferogram from which the phasemap was extracted.

Figure 14a shows a phasemap containing a sizable image defect commonly seen in the Astra data. Starting from the tip of the axial flow and moving down towards the target surface, the value of the phaseshift increases with the colourscheme changing from red to green to dark blue. However, at the point labelled "Image defect" in figure 14b, a close-up of the axial region, the value of the phaseshift suddenly skips back by 2π, with the colour changing discontinuously from green/blue back to red.

Figures 14c and 14d show the interferogram from which the phasemap in figure 14a was extracted and a close-up of the axial region. It can be seen that there is a continuous pattern of curved fringes from the tip of the jet down to the edge of the black region, implying that one should expect a continuous increase of phase along the axis of the jet. The reason for the appearance of the discontinuity in the phasemap is that some of the fringes in the interferogram are split. This can be seen by examining the close-up of the central part of the jet. If one moves between the fringes labelled A and B by travelling on the left hand side of the jet, one travels across five whole fringes,

corresponding to a change in phase of $5 \times 2\pi = 10\pi$. However, if one moves from A to B by travelling on the right hand side of the jet one travels across four whole fringes, corresponding to a change in phase of 8π: the four white fringes between A and B on the left hand side of the jet become only three white fringes on the left hand side of the jet. As a result, if the phase of fringe A is known to take a specific value, the phase value of fringe B cannot be single-valued; it has two values which differ by 2π. When a numerical algorithm such as those used by IDEA works through an image and calculates a value of phaseshift for each pixel, the result of fringes having multiple phase values is the appearance of 2π discontinuities in the phasemap such as the image defect in figure 14a.

While the effect of fringe splitting events is clear to see, their cause is harder to explain. Refraction may well play a part; other possible contributors are the motion of the plasma, local inhomogeneities and asymmetries in the overall flow.

4.3.2 Phasemap interpretation and extraction of electron density maps by Abel inversion

In the Astra experiment, plasmas were created in both vacuum and static gas fill environments. Before a shot, the gas within the chamber, and hence the refractive index, which will be denoted $n_{ambient}$, would have been homogeneous in both cases. For a vacuum the value of $n_{ambient}$ is exactly equal to 1, while for a gas fill it would have been close to but not quite equal to 1. For an optical frequency probe, and in the absence of a magnetic field, to first approximation the refractive index of a plasma is simply a function of the free electron density. The relation between the two is given by the formula

$$n(\mathbf{x}, t) = \sqrt{1 - \frac{n_e(\mathbf{x}, t)}{n_c}} \tag{15}$$

where the critical electron density for a probe laser frequency of $\nu_{probe} = (\omega_{probe}/2\pi)$ is given by the expression

$$n_c = \omega_{probe}^2 \cdot \frac{\varepsilon_0 m_e}{e^2} = \nu_{probe}^2 \cdot \frac{4\pi^2 \varepsilon_0 m_e}{e^2} \,. \tag{16}$$

A derivation of this result can be found in pages 87-95 of chapter 4 of [92], leading to equation 4.2.1. In addition to the real part, the refractive index of a plasma also has an imaginary part, which results in absorption of energy from the probe beam as it propagates.

It should be noted that the refractive index in a sub-critical density plasma is less than 1. The phase speed of light v_{phase} is related to the refractive index by the relation $v_{phase} = c/n(\mathbf{x}, t)$, where c is the speed of light. Hence, the phase speed in a sub-critical density plasma is superluminal. The group velocity remains below the speed of light, however.

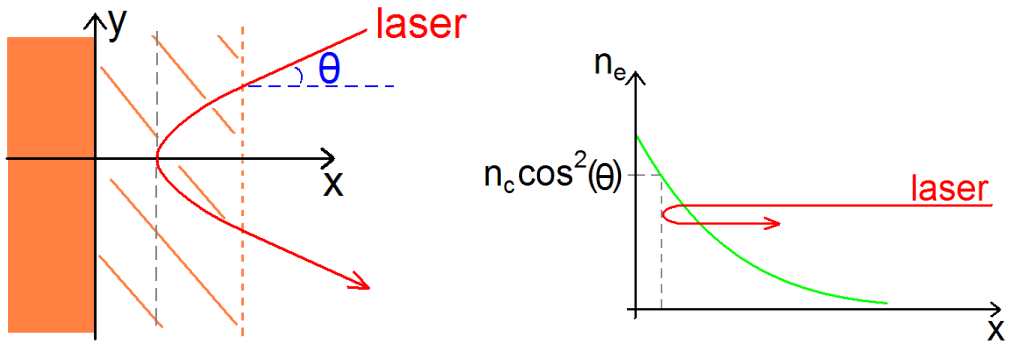

Figure 15: Cartoons to illustrate refraction of a probe beam in a planar electron density gradient. Laser rays propagate through the sub-critical electron density plasma in front of the target until they reach a surface of electron density $n_c \cos^2(\theta)$, where n_c is the critical electron density and θ the angle of incidence.

A probe beam cannot freely propagate through a plasma with an electron density above the critical value. If a beam is normally incident on an electron density gradient, the beam propagates until the critical density is reached, at which point the beam is reflected, with only an evanescent wave penetrating beyond the critical density. A beam obliquely incident on the electron density gradient becomes deflected via refraction before reaching the critical density surface. In the case that the electron density profile varies only in one dimension, the maximum electron density to which the beam penetrates is given by $n_c \cos^2(\theta)$, where θ is the angle of incidence. This is illustrated in the cartoons in figure 15. It will be assumed for now that the electron density gradients encountered by the probe in the Astra experiment were sufficiently small that refraction can be neglected; the validity of this assumption will be returned to in sub-section 4.3.3.

When refraction is negligible, the values recorded in a phasemap have a simple interpretation. In this case, probe photons follow straight line paths through the plasma, and the value of each pixel in a phasemap is equal to the plasma-induced change in the phase accumulated by probe photons in travelling along a straight path to the detector. In the Astra experiment, the time taken for the 2 ps probe beam to pass through the $\sim$ 2 mm plasma was under 10 ps, a timescale much shorter than the 0.1-1 ns timescale over which the plasma evolved hydrodynamically. Hence, the properties of

the plasma, including its electron density, were effectively frozen during the probe's passage through it. When the assumption that refraction is negligible is valid, the phaseshift of the probe in passing through the plasma along a straight line path with co-ordinate y (using cartesian co-ordinates) is given by ([92], chapter 4, pp. 98-99)

$$\Delta\phi = 2\pi \cdot \frac{\nu_{probe}}{c} \cdot \int \left(n(\mathbf{x}, t') - n_{ambient}\right) dy$$
$$\Rightarrow \Delta\phi = 2\pi \cdot \frac{\nu_{probe}}{c} \cdot \int \left(\sqrt{1 - \frac{n_e(\mathbf{x},t')}{n_c}} - n_{ambient}\right) dy \ . \tag{17}$$

The information stored within a phasemap is an array of values $\Delta\phi(x, z, t')$, where t' is the time at which the probe beam passes through the plasma. If a phasemap contains a high degree of axial symmetry, and the features of interest either lie at a large distance from the axis or are sufficiently broad, then the technique of Abel inversion (see, for example, chapter 4, pp. 124-125 of [92]) can be used to extract an electron density profile from a phasemap; $n_e(\mathbf{x}, t')$ is recovered from $\Delta\phi(x, z, t')$.

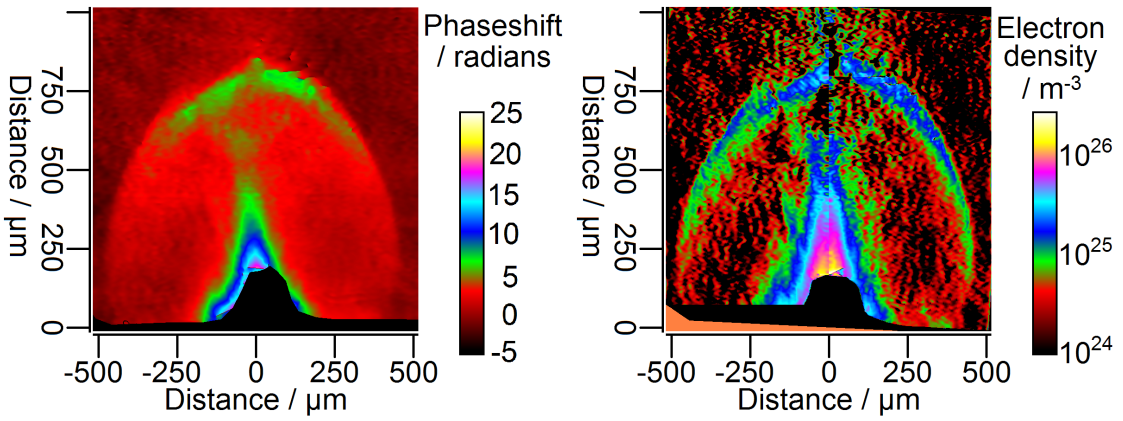

Figure 16: Figure showing a phasemap for a Cu cone target in 50 mb He at +5 ns and the electron density plot calculated from it. (a) Phasemap (b) Electron density map.

Figure 16b shows a result of using the Backus-Gilbert technique [93] to Abel-invert the phasemap of the +5 ns Cu-cone shot in 50 mb He previously shown in figure 13e. The program used to implement this algorithm was written for Matlab® [100] by C. D. Gregory. Although the use of Abel inversion assumes cylindrical symmetry, it can be seen that the two halves of figure 16b on either side of the axis are not identical. This is because the program treats the two halves separately, recombining them to make the final image. It is possible to enforce cylindrical symmetry, in effect averaging the two halves, but this results in a loss of detail in the final image.

The Backus-Gilbert method has one free parameter, which in effect determines the amount of smoothing applied to the image during the inversion process. In the imple-

mentation used here this takes values between 0 and 1, following the same approach as employed in IDEA [94], where the Backus-Gilbert technique can be used to Abel invert 1-D data. When the value of the parameter is 0 no smoothing is applied, while for a value of 1 the smoothing is so severe that the data is completely washed out. A value of 1.0×10^{-5} was used for all the images in this thesis.

For small images, the Backus-Gilbert algorithm is quick to run. However, for images of size 750 x 1000 pixels and above it is significantly slower. In these cases a 1-D median filter of order j was first applied to the data in the radial direction using the Matlab function medfilt1. For odd j, which were the only values of j used, this replaces every pixel in the data by the median of its value and the $(j-1)/2$ values on either side. This kind of filtering removes pixels with values that are particularly large or small compared to their neighbours, and in so doing reduces noise. The Abel transform was then taken using only every j'th pixel in the radial direction moving out from the centre. In this way the computational overhead was reduced, with use still being made of all of the data. Even with the largest images shown in this thesis it was unnecessary to use a value of j greater than three.

With regard to the implementation of the Abel-inversion, there are two further points worth remarking upon. First, it is necessary to rotate images to make the axis vertical prior to Abel-inverting. While the axis of symmetry of the parts of the shock to the side of the jet in figure 16a is approximately vertical, the axis of the jet is tilted slightly to the left, and hence a choice has to be made with regard to the axis to use for the Abel inversion when analysing shots into gas. Except where otherwise stated, the axes used in the Abel inversions in this thesis are the lines which were judged by eye to be the best lines of symmetry when considering simultaneously the jet near the target and the part of the shock ahead of the jet which was hydrodynamically driven by it; hydrodynamic driving is discussed in sub-section 4.5.3. There are Abel inversion methods available which allow the assumption of cylindrical symmetry to be somewhat relaxed, and these could perhaps be used in future work.

Second, and more importantly, in addition to assuming that refraction of the probe beam is negligible, C. D. Gregory's program uses the assumption that the electron density in the plasma being Abel-inverted is much less than the critical density, in which case the equation for the phaseshift, equation 19, can be approximated as

$$\Delta\phi \approx 2\pi \cdot \frac{\nu_{probe}}{c} \cdot \int \left(1 - \frac{n_e(\mathbf{x}, t')}{2 \cdot n_c} - n_{ambient}\right) dy \ . \tag{18}$$

The program was written for a plasma in a vacuum, for which $n_{ambient} = 1$, giving

$$\Delta\phi \approx -2\pi \cdot \frac{\nu_{probe}}{c} \cdot \int \left(\frac{n_e(\mathbf{x}, t')}{2 \cdot n_c} \right) dy \ . \tag{19}$$

However, the program can be equally well applied to a plasma in a background gas as long $n_{ambient}$ is sufficiently close to 1 that the contribution from the $(1 - n_{ambient})$ term is much less than that from the $(n_e(\mathbf{x}, t')/2 \cdot n_c)$ term. Using equation 16, the critical electron density for the 400 nm Astra probe beam is calculated to have been 6.97 x 10^{27} m^{-3}. In figure 16b, the calculated electron density values in the centre of the jet at the edge of the masked region go up to about 1.5-4.0 x 10^{26} m^{-3}, slightly under one tenth of the critical density, and the $(n_e(\mathbf{x}, t')/2 \cdot n_c)$ term in equation 19 therefore has a value of up to nearly 0.05. For He gas at a pressure of 1000 mb and room temperature, $n_{ambient} = 1.0000356$ for light at a wavelength of 589.3 nm ([98], ch. 1, p. 87). Consequently the assumption that the contribution of the (1-$n_{ambient}$)) term can be neglected is justified.

Finally, as the critical electron density is a constant dependent only on the wavelength of the probe beam, it can be brought outside the integral to leave the expression

$$\Delta\phi \approx -2\pi \cdot \frac{\nu_{probe}}{c} \cdot \frac{\int n_e dy}{2n_c} \tag{20}$$

from which it can be seen that $\Delta\phi$, the phaseshift, is directly proportional to $\int n_e dy$, the line-integrated electron density along the probe path. For the 400 nm probe beam used in the Astra experiment, putting numbers into equation 20 gives $\int n_e dy = 8.87 \text{ x } 10^{20} \ \Delta\phi$, where $\int n_e dy$ is in $m^{-3} \cdot m$ and $\Delta\phi$ is in radians. It can be seen from equation 19 that the value of the phaseshift caused by the presence of a plasma should be negative. This is a consequence of the phase speed of optical light being faster in a plasma than in a vacuum, with the result that the phase is advanced rather than retarded. In the phasemaps presented in this thesis the phaseshift due to a plasma is given as a positive quantity; the minus sign in equation 19 is neglected.

One situation relevant to analysing the data from the Astra experiment in which the approximations used in deriving equation 20 hold particularly well is in finding the electron density within the channel of gas ionised by the laser on its way to the target. The He gas pressures used in the experiment were varied between 10 and 200 mb. Using the relation $P = n_{He} k_B T$, the number density of He atoms, denoted n_{He}, within 200 mb of neutral He gas at a room temperature of 20°C is found to be 4.9 x 10^{24} m^{-3}. Hence, if such a gas were to be fully ionised by the laser, and assuming the gas did not have time

to evolve hydrodynamically, the free electron density would be 9.9 x 10^{24} m^{-3} as each He atom has only two electrons to lose. This is far below the critical electron density for the probe beam, which is 6.97 x 10^{27} m^{-3}. The other two gases used in the experiment were N_2 and Xe, which have atomic numbers of 7 and 54. The pressure of the N_2 was varied between 8 and 211 mb, giving a maximum free electron density of 7.3 x 10^{25} m^{-3}, and the pressure of the Xe was varied between 4 and 32 mb, corresponding to a maximum free electron density of 4.3 x 10^{25} m^{-3}. While both of these values are higher than that for He, they are still two orders of magnitude below the critical electron density.

Finally for this sub-section, the separation of the fringes in the interferometry data imposes a limit on the minimum phaseshift that can be resolved in the experiment. Inspecting the interferograms taken during the experiment, the average separation between adjacent light fringes was found to be 14.6 pixels, corresponding to a distance of 20.6 μm. If the fringes in the data had been perfect, phase changes greater than $(2\pi/14) = 0.45$ radians could therefore have been detected as adjacent light fringes differ in phase by 2π. Using equation 20 such a phaseshift is seen to correspond to a line-integrated electron density of $\int n_e dy = 4.0 \times 10^{20}$ $m^{-3} \cdot m$ in regions where the electron density is far below the critical value. However, the quality of the data was not perfect. Taking account of noise in the background of images, the minimum resolvable line-integrated electron density is somewhat greater than this, roughly $\int n_e dy$ = 1-2 x 10^{21} $m^{-3} \cdot m$, corresponding to a minimum detectable phaseshift of between one quarter and one third of a fringe. This calculation was performed assuming that refraction of a probe beam is negligible, in which case it is only the electron density that contributes to the phaseshift. However, where strong electron density gradients are present, refraction of the probe also makes a contribution.

4.3.3 Assessment of the effect of refraction

Observing the results of the Abel inversion in figure 16b, it can be seen that the value of the electron density on the axis of the plasma at the edge of the masked region, about 1-2 x 10^{26} m^{-3}, is less than one tenth of the critical density of 6.97 x 10^{27} m^{-3}. As there is no reason to expect there to be a discontinuity in the values of the electron density within this part of the flow, it can be concluded that the lack of interferometry data in the masked region, or at least at the edge of it, was not the result of the probe beam encountering plasma above the critical density and being reflected. This conclusion is supported by simulation results presented in section 5.3.4 of chapter 5.

There, simulations of a conical Cu target in a vacuum suggest that at +5 ns the critical electron density surface does not protrude out of the entrance of the cone.

A plausible explanation for the lack of data in the masked region is that it is a result of refraction. When a probe beam travels through a plasma with an electron density gradient transverse to its direction of propagation it gets deflected. Where gradients are sufficiently strong, the probe beam is deflected through a large enough angle that it does not travel through the collecting lens placed after the target. Consequently, it is not focused onto the detector, and hence no interference fringes are recorded.

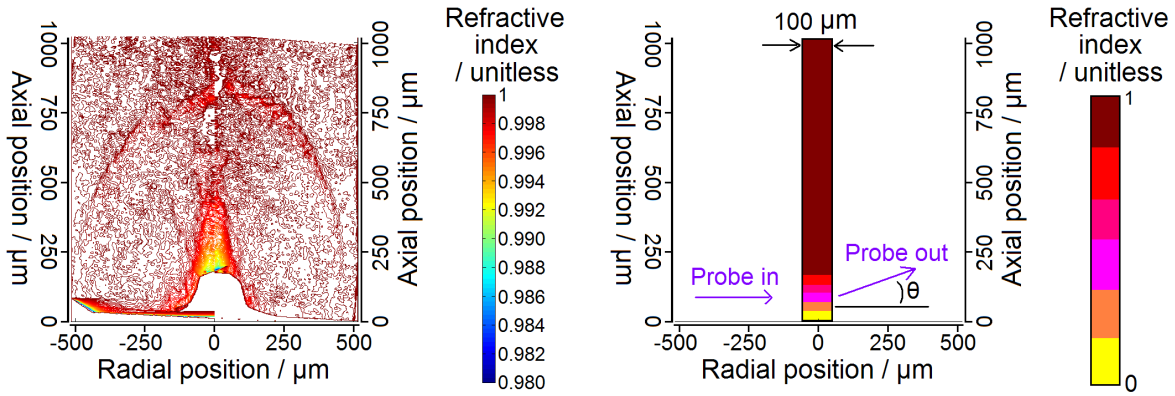

Figure 17: Refractive index for a shot onto a Cu cone target in 50 mb He at +5 ns. The plot in (a) is calculated from the experimentally-obtained electron density data shown in figure 16b. (b) shows a cartoon of a simplified model used in estimating the size of the angle through which the probe beam was refracted in passing through the data-free region at the base of the jet in (a).

Figure 17a shows a plot of the refractive index calculated using formula 15 for the shot onto a Cu cone target in 50 mb He discussed previously. Throughout the image the value of the refractive index is close to 1, dropping to a value of about roughly 0.986 on the axis at the edge of the fringe-free region where the electron density is highest. The refractive index inside the fringe-free region, where the electron density is higher, is lower still. As the simulation results suggest that the electron density at the entrance to the cone is roughly equal to the critical value, the refractive index at the position (0,0) in figure 17a is roughly 0.

A simple estimate based on the discussion of probe beam refraction in chapter 4 of [92] can be used to show that, sufficiently close to the target, refraction of the probe beam is significant. Figure 17b shows an illustration of the model used in making the estimate. The jet is modelled as a column 100 µm wide, within which the electron density, and hence refractive index, varies only in the axial direction. The refractive index values at the base of the column and at the top of the data-free region, axial positions of $z = 0$ µm

and $z = 150$ μm, are matched to the corresponding values in the experimental data in 17a, taking values of 0 and 1 respectively.

The wavefronts of the probe beam as it approaches the jet are parallel to the z-axis. In passing through the plasma column, the phaseshift acquired by the beam is dependent on the axial position and is equal to $(2\pi.n(z)\Delta x/\lambda)$, where $n(z)$ is the refractive index at position z and Δx is the width of the plasma column. The use of this expression assumes that the change of direction of the probe beam inside the column is sufficiently small that it has a negligible effect on the phase shift. As refractive index increases with z, the phaseshift of the probe beam on leaving the plasma is larger at larger z. Hence, beyond the plasma the wavefronts, which are lines of constant phase, slope upwards. The angle through which the beam is refracted is approximately [92]

$$\theta \approx \frac{d}{dz}\int n(z)dx = \frac{dn(z)}{dz}\Delta x \ . \tag{21}$$

In the Astra experiment, the lens used to collect the probe beam after the target was approximately f/3, i.e. its distance from the target was about three times its diameter. Hence, rays refracted by an angle greater than $\tan^{-1}(\frac{1}{2}/3) = 9.5°$, or 0.17 radians, would not have been collected, and would therefore not have been focused onto the detector. Using the formula above, the maximum refractive index gradient that the probe beam could have encountered and still made it to the detector is estimated at (0.17 radians / 100 μm =) 1700 m^{-1}. Using the experimental values of the refractive index, the average value of the refractive index gradient within the data free region is estimated at (1 / 150 μm)$\sim$ 7000 m^{-1}, much higher than the allowed maximum. In practice, in the ablation plume from a solid target the electron density falls off faster than linearly with distance, so the estimated refractive index gradient is an underestimate near to the target and an overestimate further out. Nevertheless, the explanation that the fringe-free regions in the interferograms result from refraction is reasonable.

4.4 Results for shots taken in a vacuum

In total, over 250 shots were taken during the experiment, enabling data to be gathered from a wide variety of target and gas configurations. In this section, results are shown for jets created from targets in a vacuum, while in the next, 4.5, results are shown for targets in a variety of types and pressures of ambient gas.

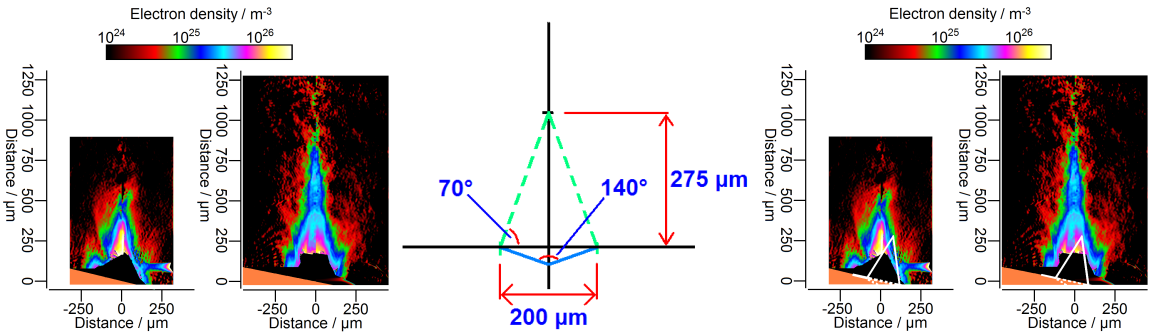

Figure 18: Electron density maps at +5 and +10 ns for axial flows created from Au cone targets in a vacuum. The electron density maps in (c) are the same as those in (a) with the addition of white lines to indicate the size of the convergence cone sketched in (b). The target position is indicated in orange.

Figure 18a contains a pair of electron density maps showing the plasmas from a pair of Au cone targets shot in vacuum at times of 5 and 10 ns after their creation, respectively. As with the other electron density images presented in this rest of this chapter, the position of the target strip is indicated in orange and the images are oriented such that the axes of the jets are vertical.

In both images in figure 18a, a roughly conical flow of plasma can be seen emerging from the target. The +10 ns image has a clear two-component nature. Near the target there is a wide conical flow reaching to about +400 µm. Out of the end of this there is a narrow flow extending to at least +800 µm. The formation of a narrow jet as a result of the convergence of plasma is what was aimed for in choosing the method of jet creation for the experiment. The projected direction of the main laser approach to the target in these images is near to target normal, i.e. nearly perpendicular to the surface of the target strip, which is indicated in orange. In the images the conical flows near the targets are not aligned with target normal but point off to one side; in both cases they lie to the left of the normal. This suggests that in both cases the laser focal spot was not perfectly aligned with the centre of the target but was offset to the right, resulting in a stronger ablation of plasma from the right hand sides of the cones than from the left.

In section 4.1 it was described how, when a laser ablates a target, the plasma leaving the surface initially moves away along the local surface normal. Later in time, this plasma can become deflected by pressure gradients in the flow. For a conical target a convergence cone in front of the target can be defined, the outer edge of which is the surface normal at the edge of the conical target. Figure 18b shows the geometry of the convergence cone for the conical targets used in the experiment. The conical target is

marked in blue, and the convergence cone using dashed green lines. The significance of the convergence cone is that, in the absence of pressure gradients, the convergence cone marks the outer edge of the flow from the cone as it converges onto the axis.

Figure 18c shows a duplicate of figure 18a with the approximate position of the convergence cone indicated in white. Neglecting asymmetry caused by the centre of the laser beam being offset from the centre of the target, the shapes of the plasma flows near to the target are seen to be similar to those of the convergence cone, though they exceed it in size.

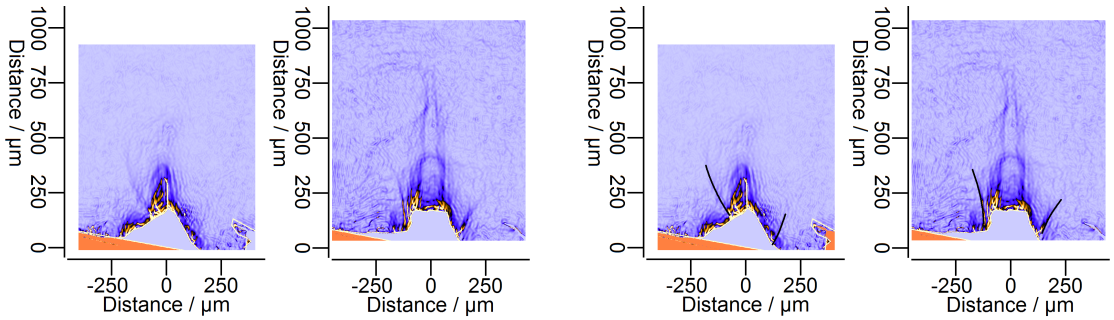

Figure 19: Results of applying an edge-finding algorithm to the jets from Au targets shown in figure 18. The edges within the flows that are referred to in the text are indicated in (b) using black lines.

4.4.1 Edges in the flow

The discussion in this sub-section leads to a way of inferring rough estimates of internal Mach number from experimental data. The flows in both the +5 and +10 ns images for Au cone targets in figure 18c contain sharp edges to the sides of the main jet. In order to remove any ambiguity in identifying the edges being referred to here, figure 19 has been included, which shows the results of applying an edge-finding algorithm to the electron density plots in figure 18a using ImageJ. In the +5 ns image there is a strong edge to the left of the jet, and possibly a smaller one on the right, and in the +10 ns image there are strong edges on both sides, indicated in 19b using curved black lines. As the situation is approximately cylindrically symmetric, these lines show the left and right boundaries of a conical structure around the central jet.

A similar feature has been seen in other jet experiments, for example those reported in Purvis *et al.* [68], Grava *et al.* [69] and Filevich *et al.* [70] in which, as previously discussed in section 3.3.1, two-dimensional jets were created by illuminating grooved targets with a line-focused laser beam. In Grava *et al.* a single peak in density is seen on the axis of the groove at early times. Later, secondary peaks termed "sidelobes"

form off-axis as the flow of plasma on the axis widens out and interacts with slow plasma that is heading in towards the axis from high-up on the sides of the groove. These features are also seen in the earlier paper of Purvis *et al.*, for example in the 10.7 ns image in their figure 3, though they are never explicitly mentioned.

In the most recent of these three papers, Filevich *et al.*, the ratio of the laser pulse FWHM to the width of the grooves was larger, with the result that a larger fraction of the laser energy fell onto the flat surfaces to either side of the grooves than in the experiments reported in the earlier papers. Off-axis shocks were seen on both sides of the plane of symmetry resulting from an interaction between laterally-expanding plasma from inside the groove and plasma formed from laser-ablation of the flat surfaces to either side. One possible explanation for the edges seen in the Astra data is that they are formed in the same way: while most of the energy strikes the surface of the conical target, some of the laser energy falls onto the flat surface around it, generating a plasma that moves parallel to the axis of the cone. The sharp edges then indicate where laterally-moving material from the inside of the cone meets the material coming from the flat surface.

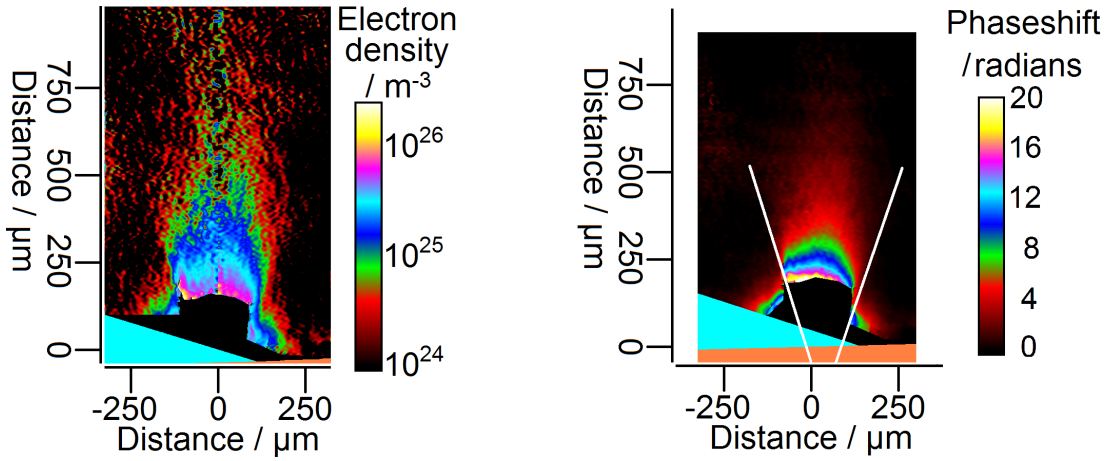

Figure 20: Electron density and phase maps for a plasma from a flat Cu surface at +5 ns. The target surface is marked in orange, and light blue is used to mark the position of a piece of metal attached to the target strip and lying in the line of sight of the interferometer.

However, observation of the plasma produced by a flat target, for example that shown in figure 20a, poses a challenge to this explanation. In flat target plasmas, edges are also seen even though there is no difference in target surface geometry across the region covered by the laser radiation. In this case, target geometry cannot be responsible for the creation of two separate plasma regions which subsequently interact to produce the edges. Nonetheless, examination of the plasma in figure 20 shows that it does appear

to have two components. In the centre there is an extended plume, bounded by a pair of edges. Outside of these edges, plasma is seen near to the target surface on both the left and right hand sides.

This behaviour has previously seen in the work by the group using the PALS laser system discussed in section 3.3.1. In their experiments, jets were created by the illumination of flat targets using laser pulses with a variety of energies and focal spot diameters. When using a 10 J pulse of 438 nm radiation with a focal spot radius of 300 μm to ablate a Cu target, only a single plasma flow with well-defined sides is seen at early times. At +5 ns, the flow appears to have a second component near to the target surface, similar to that seen in the flow from the Astra experiment shown in figure 20. These results can be seen in, for example, the +2 and +5 ns images for the Cu target in figure 6 of [61].

In their papers, little mention is made of these details. The lack of a second plasma component outside of the edges of the primary flow at early times would suggest that the sharp edges to this flow might not be the result of a plasma-plasma collision. Instead, they could simply be the result of pressure-driven radial expansion. The plasma ablating from the centre of the focal spot on the target moves supersonically and normal to the target surface. The plasma ablating from the edges of the focal spot also moves supersonically in the axial direction. However, its motion has a radial component due to the pressure difference caused by having hot plasma on one side and a vacuum on the other. The plasma expands radially at roughly the sound speed.

In this case, the plasma seen outside the edges near to the target surface at later times could be unrelated to the presence of the edges, and result from, for example, ablation of the target surface by X-rays emitted by the primary flow. By itself, this explanation doesn't seem fully satisfactory for explaining the edges in the Astra cone target flows, however, as if the edges simply mark the radial expansion of the jets from the cones they could be expected to be symmetrically arranged about the axes of the jets. This is not the case for the +10 ns image for the Au target shown in figure 19, where the edge to the right of the jet is at a steeper angle to the axis of the jet than the edge on the left.

If, for a flat target, the edges in the flow mark the thermal radial expansion of the plasma, the tangent of the angle that the edges make with the axis of the flow is roughly equal to the ratio of the sound speed and the axial speed, and thus approximately equal to the inverse of the Mach number. Figure 20b shows the phasemap from which the

electron density map in figure 20a +5 ns was derived. The edges in the flow are slightly curved, curving away from target normal. This does not, however, imply that the Mach number of the flow decreases with distance from the target: in an ablation plume the speed and Mach number of the flow is larger further from the target. It is more likely that near to the target plasma ablated from the flat parts exerts a confining effect on the flow from the cone, while further out the jet expands radially at an angle nearer to that appropriate to its Mach number. Two white lines have been added to figure 20b. They enclose an angle of 36°, giving an estimate of the Mach number of $(1/\tan(36/2)) = 3$ for the flow from a flat Cu target at +5 ns.

4.4.2 Comparison of time series for CH, Cu, Cu-smoke and Au targets

The +5 and +10 ns images for an Au cone target shown previously in figure 18a were taken on different shots, in which the arrival of the probe beam at the target was delayed by 54 and 10 ns, respectively, with respect to the arrival of the main beam. By creating a series of plasmas under nominally identical target, laser and gas conditions, and delaying the probe beam by a different amount on different shots, it is possible to build up a time series showing how a "typical" jet evolves. A concern with this method of reconstructing the time-evolution of a plasma is that if there is a significant shot-to-shot variation in plasmas created under nominally identical conditions, the evolution of the "typical" plasma in the time series will not represent well the time evolution of any one individual plasma.

In order to illustrate this, figure 21a on the following page shows the results of a pair of nominally identical shots onto Au cone targets. Both of the images were taken at a time of +10 ns. There is an obvious difference in the plasmas produced from the targets: the plasma in the left hand image is far more symmetrical, and the jet can be seen extending to a much greater distance from the target surface.

Figure 21b shows the phasemaps from which the electron density plots in 21a were calculated. The use of Abel inversion assumes that the image being inverted has a high degree of cylindrical symmetry. For the right hand image in the figure, the symmetry is poor, and so the values of the electron density in the corresponding plot in figure 21a, to which the poor symmetry of the phasemap is transmitted, may be regarded only as guideline values.

The symmetry of the left hand image in figure 21b is good, but not perfect: the best line of symmetry for the narrow jet protruding from the convergence cone lies at a

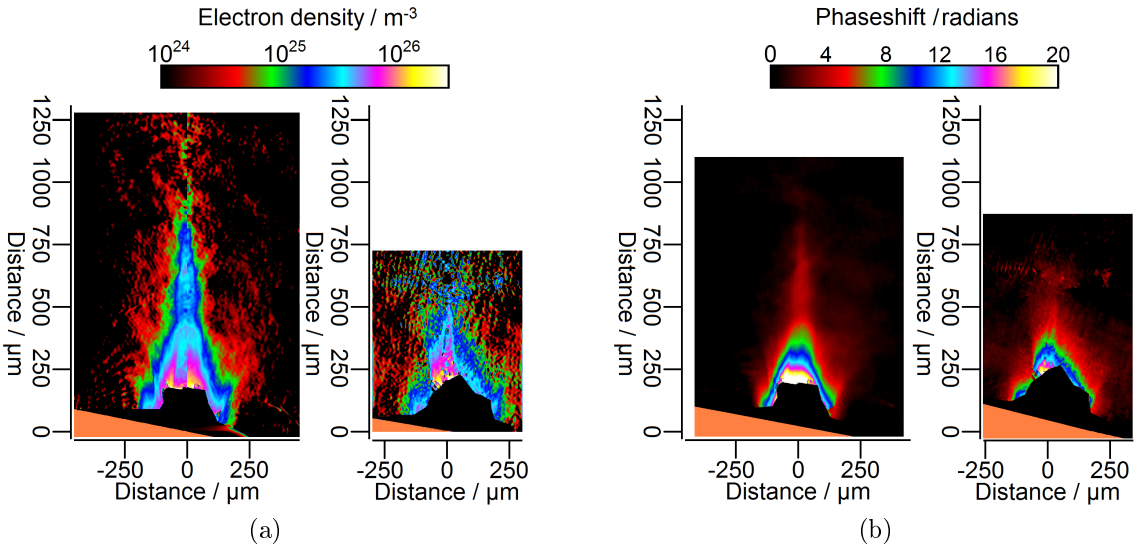

Figure 21: Images taken at +10 ns for two plasmas created from Au cone targets under nominally identical conditions. The electron density maps shown in (a) were created from the phasemaps shown in (b).

slight angle to the best symmetry line for the convergence cone itself. In generating the electron density plot in figure 21a, the symmetry line for the narrow jet was chosen. Comparison of the electron density and phase maps shows something interesting. Near the axis, at about 250 µm from the target, the pink region in the electron density plot appears to be split into two by a vertical light blue region. Examination of the phasemap suggests that this feature is not an artefact introduced in the Abel inversion, as it can be seen from figure 21b that the dark blue region has a perturbation near to the axis. This is suggestive of a partial hollowing of the electron density within the plasma around 250 µm from the target.

On the next page figure 22 shows a comparison of four time series for jets propagating into a vacuum. The targets used were CH, Cu, Cu-smoke and Au cones. The Au time series, figure 22d, contains two of the images previously seen in figure 18. In the Au time series it can be seen how the conical flow emerges from the target surface and, by +5 ns, how the narrow conical jet protruding from the top of the wider conical flow near the target starts to appear. After +5 ns, data was only taken at two subsequent times, +10 and +20 ns. At +10 ns, the flow near the target is still conical, and the narrow jet extends to over 800 µm from the surface of the target strip. In the +20 ns image, a narrow jet cannot be made out. However, it is hard to draw a firm conclusion from this as the flow appears very asymmetric, and in the asymmetric +10 ns image shown in figure 21 there is no narrow jet similar to that seen in the symmetric +10 ns image. Ideally, data would have taken at times between +5 and +10 ns, and between

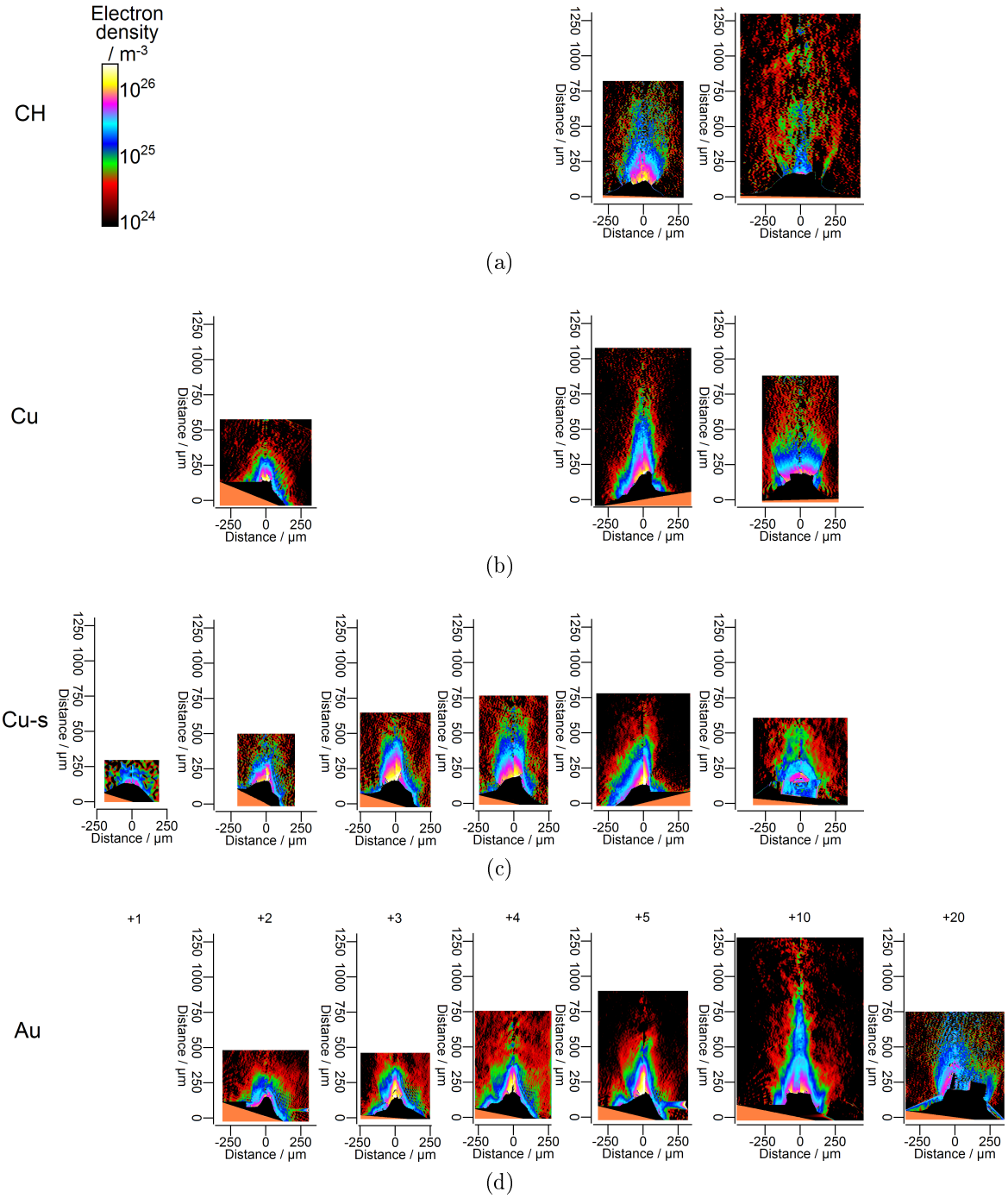

Figure 22: Electron density maps for jets from CH, Cu, Cu-smoke and Au targets propagating into a vacuum. Images at corresponding places in different rows are shown at the same time. Moving from left to right, the times are +1, +2, +3, +4, +5, +10 and +20 ns. The approximate positions of the target surfaces are indicated in orange.

+10 and +20 ns. Without such data it is impossible to know whether the narrow jet was still growing at +10 ns, when it reached its peak size, and how it changed after this.

Comparison of the +5 and +10 ns images in the CH, Cu and Au series shows that the choice of target coating material had a significant effect on the shape of the flow. At +5 ns, the plasmas seen in the Cu and Au series have a conical shape. In contrast, the flow from the CH was not conical, but is seen to have been more rounded. Later in time at +10 ns, the Au plasma still appears conical, and the narrow jet is very extensive. The Cu flow, however, has ceased to be conical and become divergent. The CH plasma at this time appears faint, though there appears to be a small jet on the axis, with edges on either side at radii of about 150 μm.

A quantitative comparison of the widths of different jets is difficult to do in a non-arbitrary way, with different approaches having different advantages and disadvantages. The first decision that has to be made is how to define the jet width. From consideration of other laboratory jet experiments [58, 1], one might expect the mass density of the jets to peak on axis, and from this an appropriate measure of jet width at a certain distance from the target would be the full-width-at-half-maximum of the mass density. Graphically, one could compare jets from different materials, which have different ion masses, by plotting the mass density normalised by its peak (on-axis) value as a function of radial position.

However, in the experiment it was electron number density, rather than mass density, that was measured. To relate electron density and mass density requires knowledge of the ionisation within the plasma. If the ionisation at a certain distance from the target were to be roughly constant across a jet, a plot of electron density normalised by its peak (on-axis) value would be equivalent to a plot of normalised mass density. However, there is good reason to suspect that in the experiment the radial variation of the ionisation was significant, at least for some of the experimental shots: the suspected hollowing of the electron density profile for the Au at +10 ns, in the region about 250 μm from the target, suggests that in that case the electron density might be lower on-axis, where the mass density is highest, than it is away from the axis. Other considerations are that the errors in electron density values calculated using Abel inversion are often worst on-axis, and asymmetries in the jets means that in some of the inferred electron density maps the peak electron density values are displaced to the sides of the axes.

Once a measure of jet width has been decided upon, there is a second decision to make

relating to how to make comparisons between different jets. The simplest approach is to plot on the same graph lineouts taken at the same distance from the target, at the same time, for each jet. However, due to their different ion mass, one might expect that the speeds of jets from different materials could vary significantly. Then, faster-moving jets from lower atomic number materials would converge on the axis and start to radially expand sooner, and would have a greater length. In this case it could be argued that, rather than comparing the widths of jets at the same distance from a target, it would be more appropriate to normalise both the radial and axial scales by the overall jet length, and then compare jet widths at equal distances from the target in this normalised coordinate system. However, there are several disadvantages to this. Like jet width, jet length is an ill-defined quantity, particularly for low atomic number materials and/or at late times, as experimentally the line-integrated electron density far from the target is below the lower limit detectable by the interferometer. Second, the width of the region of the target from which plasma was created was the same for all of the materials in the experiment, and hence different jets would start with different diameters in the normalised co-ordinate system. Finally, rescaling does not accommodate well the two-part nature of the flows in the experiment, in which there is a convergent flow near to the target and an expanding flow further out.

With these matters in mind, the approach to the quantitative comparison that is chosen is to plot radial lineouts of the electron density, normalising each lineout by its maximum value, whether this lies on the axis or off to one side. Lineouts from jets made from different materials are compared at the same distance from the target, and at the same shot time, without any spatial scale normalisation.

The results for a comparison between CH, Cu and Au jets are shown on the following page in figure 23. Figures 23a and 23c show lineouts at distances of 225 and 350 μm from the target at +5 ns, while figures 23b and 23d show lineouts at these positions at +10 ns. The distances of 225 and 350 μm were chosen as the lineouts at these positions are outside the fringe-free regions near to the target and are unaffected by off-axis fringe-splitting events. Each lineout is averaged over 5 pixels (7.5 μm) in the axial direction in an attempt to reduce noise. In the +10 ns plots, for the sake of clarity lines are only shown for Cu and Au.

From the results of previous research (see sub-sections 3.3.1 and 3.3.2) it can be anticipated that jets created from materials with a higher atomic number will be narrower and better collimated. In regions where plasma is converging to form an axial jet,

strong radiative emission from the dense plasma on the axis promotes energy loss in this region. The plasma then moves to increase the density on the axis further in an attempt to equalise the pressure. As a result, one would expect narrower jets to form from more radiative plasmas, where radiative losses, and hence loss of axial pressure, are more significant. Outside a convergence region, radiative losses reduce the pressure driving lateral expansion and so one would expect jets of more radiative material to have a lower angle of divergence. Comparing the plots at +5 ns in figure 23, at both distances from the target the width of the jet at a normalised electron density of 0.5 (i.e. the FWHM) is smaller for Au than for Cu, and smaller for Cu than for CH, consistent with the behaviour anticipated. The line for CH at 350 μm is noisy as the phaseshift at this distance from the target was relatively small. For Cu and Au the phaseshift was greater and the signal-to-noise ratio higher. However, the lineouts for these jets are still not smooth curves with a single peak on the axis. Their shape is influenced by asymmetry and noise in the pre-Abel inversion phasemap, and the choice of centre line when performing the inversion.

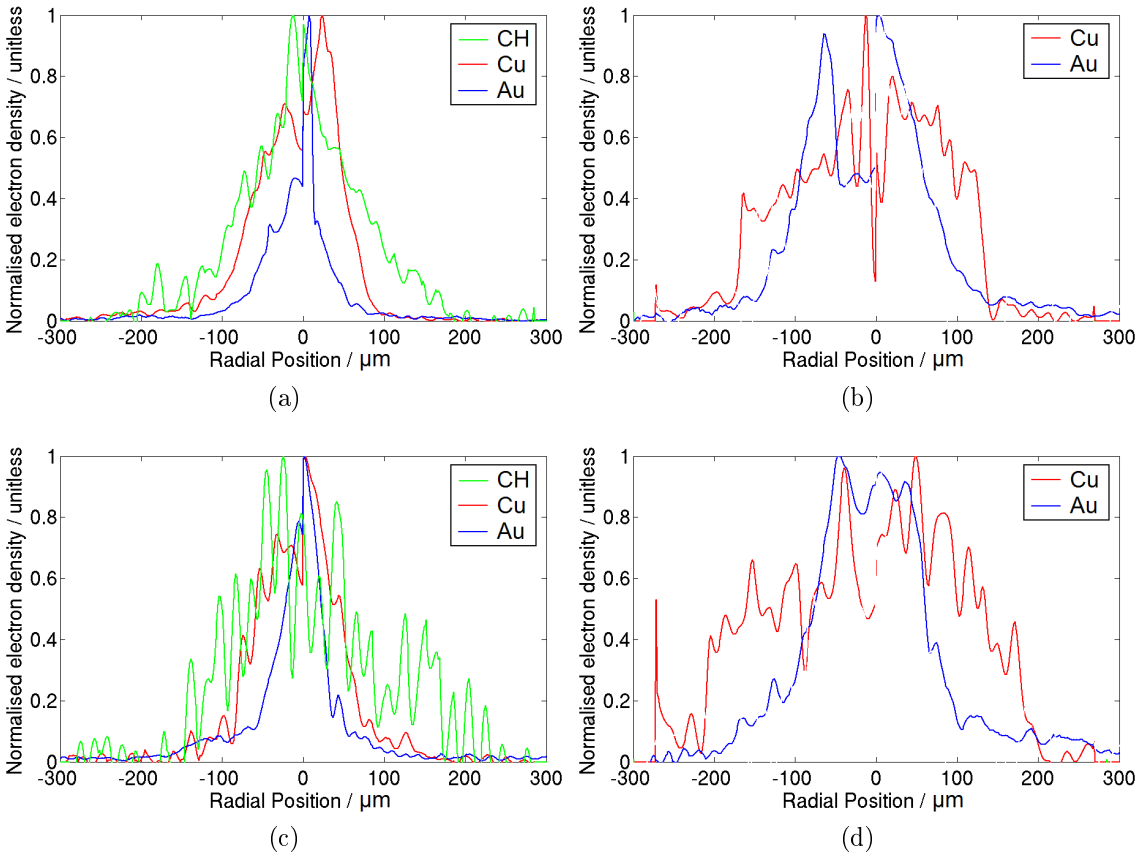

Figure 23: Normalised electron density plots comparing the widths of jets from CH, Cu and Au targets in a vacuum at distances of 225 and 350 μm from the targets. (a) +225 μm, +5 ns (b) +225 μm, +10 ns (c) +350 μm, +5 ns (d) +350 μm, +10 ns.

Inspection of the electron density maps in figure 22a shows that edges, of the type discussed in the previous sub-section, are visible for all three materials at +5 ns. However, the electron densities near the axes are sufficiently large that these edges don't play a significant part in determining the jet FWHM. At +10 ns, the same remains true for Au. However, the electron density plot for Cu lacks a central jet at this time, and the flow in figures 23b and 23d is delimited by a pair of edges.

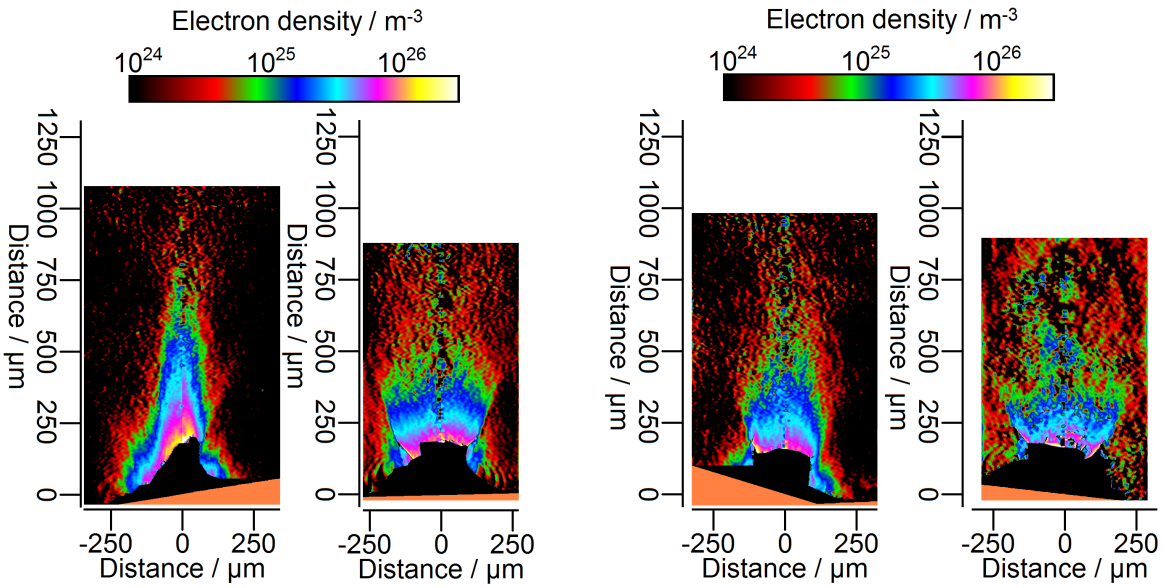

Figure 24: Comparison of Cu jets created from (a) conical and (b) flat targets in a vacuum. Images are shown for times of +5 and +10 ns in both cases.

Figure 24 shows a comparison between the jets produced from conical and flat Cu targets. At +5 ns there is a clear difference in the results: the flow from the conical target appears conical and has a narrow jet protruding from its tip, while the flow from the flat target is divergent and much wider. At +10 ns, the flows from the two target geometries are more similar: both are divergent, though the divergence of the flow from the flat target is noticeably greater.

Examination of the Au time series in figure 22 shows that all the jets are asymmetric in the same fashion, pointing slightly to the left of target normal. During the experiment, it was common that if one shot in an experimental run using a particular combination of target type, gas type and gas pressure produced an asymmetric plasma, other shots in the same series possess a similar asymmetry. This type of systematic error is not unreasonable given that when shooting a series all of the targets were on the same target strip and were aligned using the same procedure. The +5 ns shot in figure 22c, the Cu-smoke series, shows an exception to this.

The highly asymmetric nature of the +5 ns shot from the Cu-smoke target is unfortu-

nate as it makes a comparison between the jets from the smooth and microstructured Cu targets more difficult. At +2 ns the electron density maps from these two materials are similar, both showing a small, almost conical plasma propagating to the left of target normal. By +10 ns, the axial flows are more divergent in both cases, though the poor quality of the data in the +10 ns image for the smoked target hinders the comparison. Observation of the +5 ns shots seems to show similar behaviour, with the plasmas in both cases appearing conical and pointing to the right of target normal. However, comparing the +3 and +4 ns images from the smoked target with that at +5 ns it can be seen that the +5 ns image does not fit into the sequence very well, with considerably higher asymmetry and it is concluded that it is atypical for this target type. Comparing the +4 ns shot from the smoked target with the +5 ns shot from the smooth Cu target, while both flows are roughly conical, the flow from the smoked target is somewhat more rounded even though the image is taken at an earlier time, suggesting that the collimation from the smooth targets is better than that from the smoked targets, at least at early times.

The reason for using both smooth and smoked Cu targets in the experiment was that, as a result of smoked target surfaces absorbing energy from an optical laser pulse far more efficiently than smooth surfaces, it was hoped that plasma flows containing a higher amount of energy could be produced using a smoked target. This does not imply that plasmas created from smoked targets are necessarily hotter. The microstructure on the surface of a smoked target gives it a much larger surface area than a smooth target, and the result of this is that the mass ablation is higher; the temperature of the plasma depends more on the laser wavelength.

4.5 Results for shots taken in a gas

Figure 25a on the next page shows the result of taking a shot onto a Cu cone target in a 50 mb He environment at a time of +5 ns. For comparison, figure 25b shows a result for a jet from a Cu cone created under vacuum conditions. In the vacuum, the flow near the target is conical and the jet extends more than 750 μm from the target surface. The situation in the He gas is more complicated. In addition to the flow along the axis, a curved shock front is seen both in front of and to the sides of the flow. In other images taken at early times and/or when using a gas of sufficiently high pressure, the channel of gas ionised by the laser on its way to the target can be made out.

This section is divided into five parts. In the first, sub-section 4.5.1, a time series for

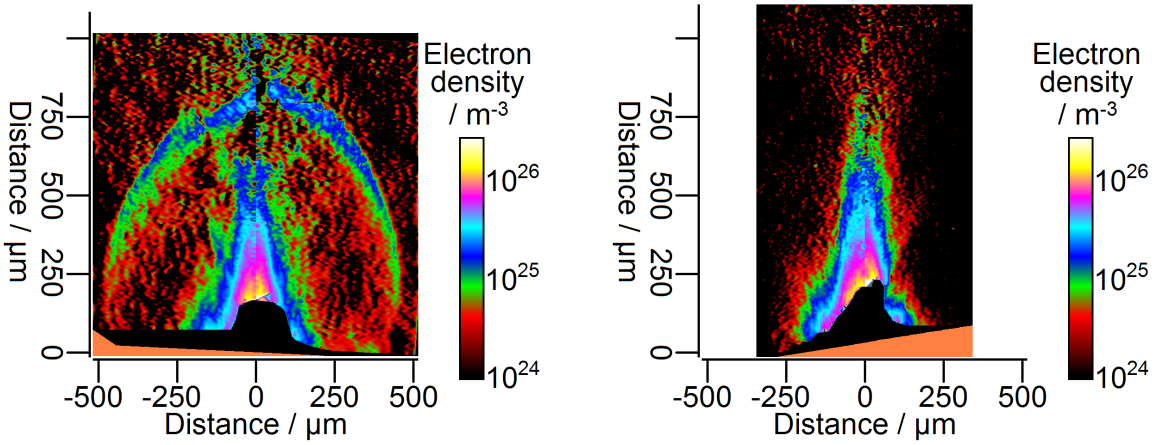

Figure 25: Jets from Cu cone targets at +5 ns (a) in 50 mb He (b) in a vacuum.

jets from Cu cone targets in 50 mb He is presented and laser ionisation of the gas is discussed. Following this, in sub-section 4.5.2 a comparison is made between jets from cone targets of different atomic number in 50 mb He, and also between jets produced in vacuum and in gas. In the third sub-section, 4.5.3, the relationship between the jets and the shapes of the bowshocks is analysed using results for cone targets in a higher pressure of He and for groove targets. Sub-section 4.5.4 shows results for shots onto Cu cones in a different gas, Xe. Finally, sub-section 4.5.5 contains a comparison of the radii of shocks in gases of different types and pressures.

4.5.1 Cu cone targets in 50 mb He, and laser channel ionisation

On the next page figure 26 shows a time series for Cu cone targets in 50 mb He. Electron density maps are shown for times of +2, +3, +4, +5, +10 and +20 ns. The persistence of the collimation of the jet is better than was observed for Cu jets in a vacuum. In a vacuum, at +5 ns the flow near the target was seen to be roughly conical. By +10 ns it had become fully divergent. In 50 mb He, the flow is again conical at +5 ns. At +10 ns the flow is more rounded, but has not yet become fully divergent, though this is the case by +20 ns.

The data points and solid line in figure 27a, also on the following page, show the maximum distance of the bowshock from the base of the jet as a function of time. For all of the data points the percentage error in measuring this distance is small. Using Matlab, a curve of the form $z = (At^B + C)$ has been fitted to the data, yielding $A = 310$ µm, $B = 0.69$ and $C = -77$ µm. As this fitting is non-linear, for simplicity only the data points have been included in the fitting, and the error bars have not been taken

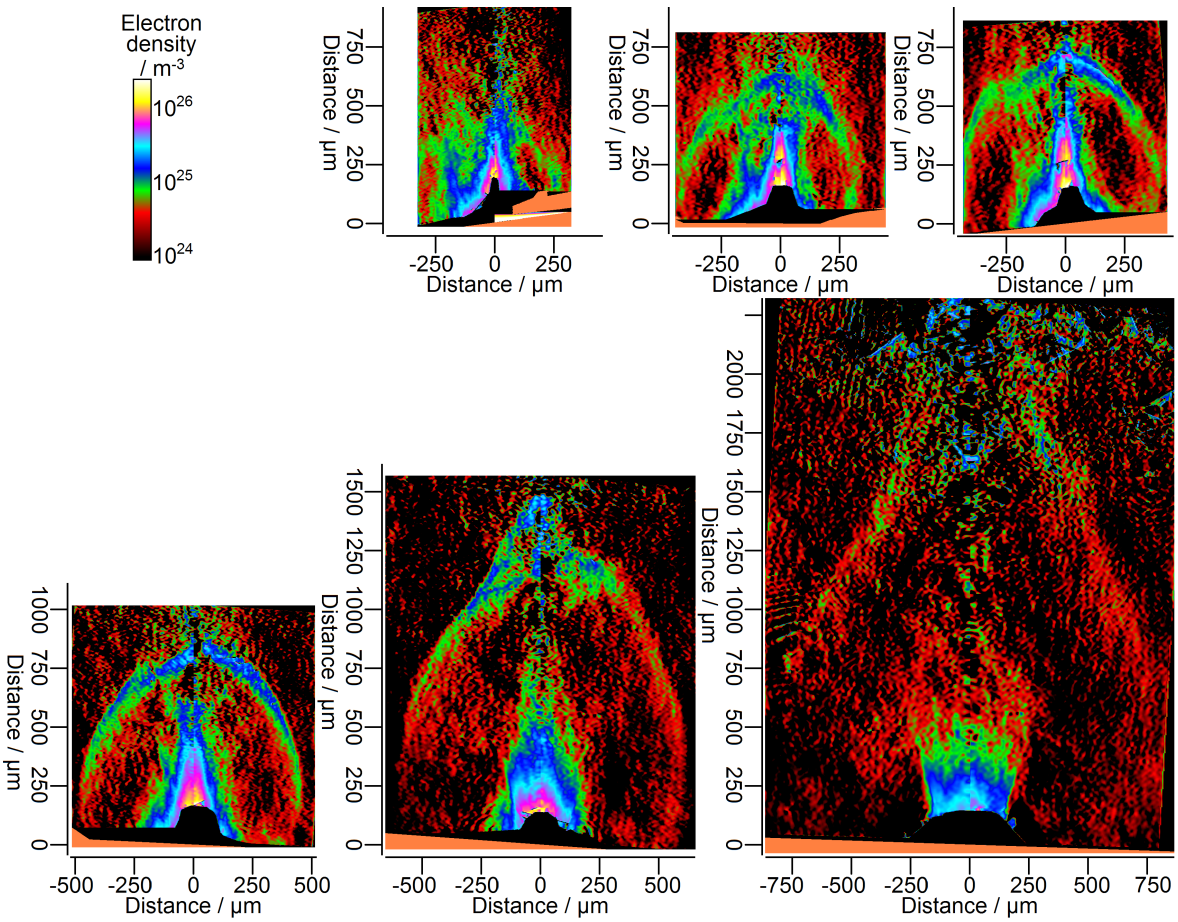

Figure 26: Time series for plasmas created from Cu cone targets in 50 mb He. Images are shown at times of +2, +3, +4, +5, +10 and +20 ns.

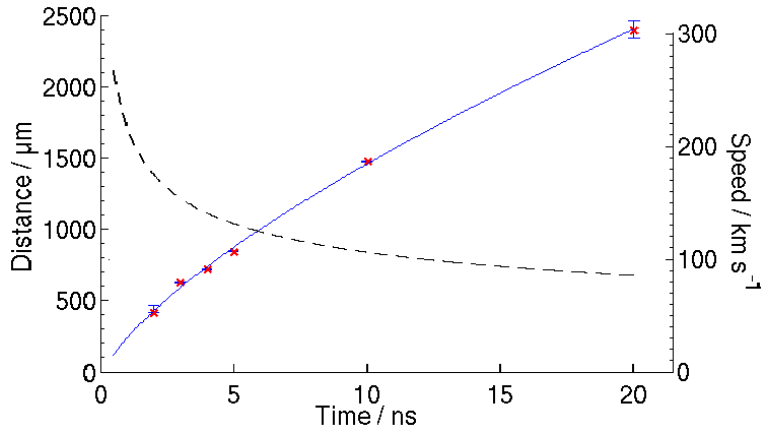

(a)

Figure 27: Plots of bow shock size (solid line) and speed (dashed line) as a function of time for jets from a Cu cone target in 50 mb He. The shock speed was calculated by differentiating the curve fitted to the shock position data.

into account. The dashed line in the figure shows the speed of the shock, estimated by taking the derivative of the fitted curve with respect to time. The estimated speed decreases from about 150 km s^{-1} at +3 ns to 120 km s^{-1} at +5 ns and 85 km s^{-1} at +20 ns.

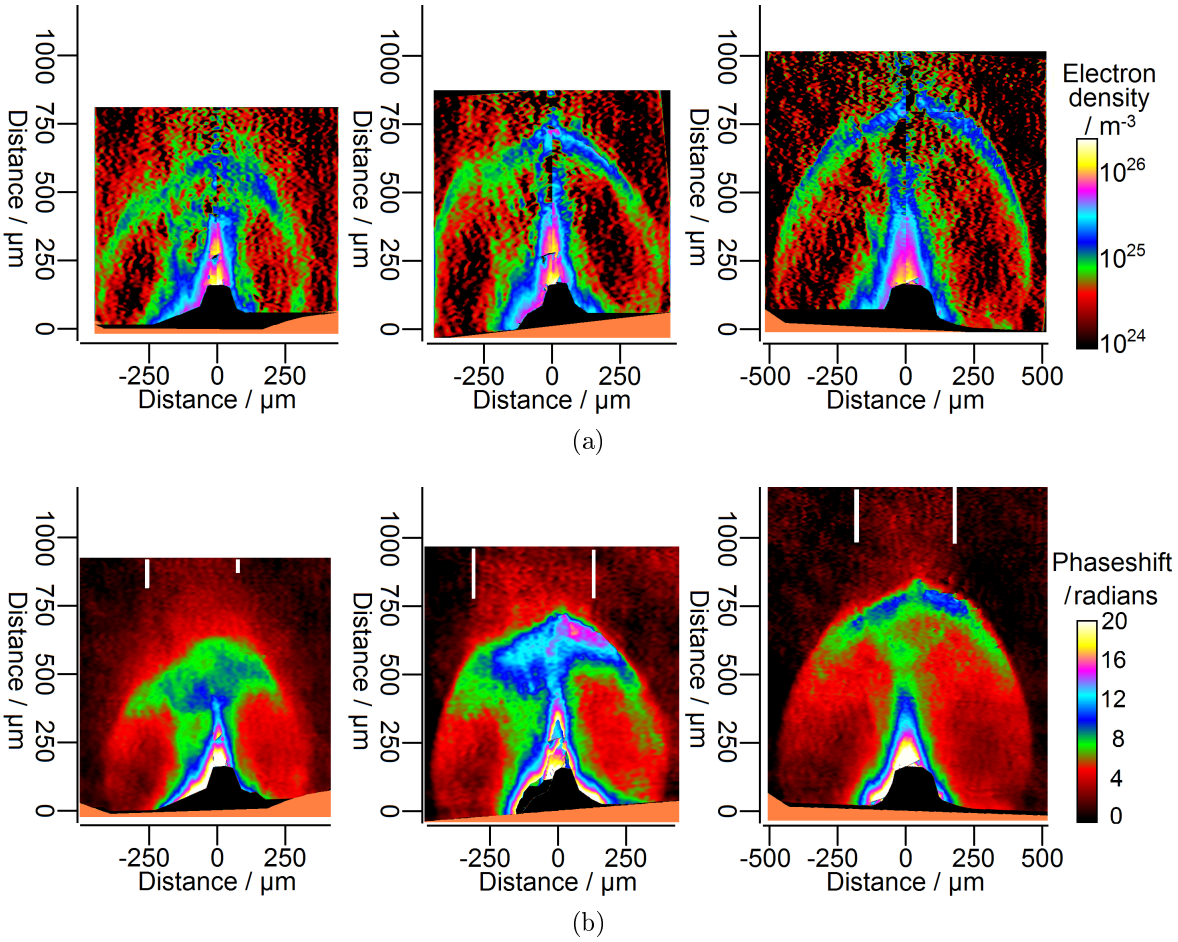

Figure 28: Images showing ionisation in the gas ahead of the shock for the +3, +4 and +5 ns shots onto Cu cone targets in 50 mb He in figure 26. (a) electron density maps (b) phasemaps. White lines have been added to the phasemaps to indicate the approximate position of the edge of the laser channel. In the +3 ns image there is, in addition to this channel, a region of phaseshift around the sides of the shock, indicating ionisation and pre-heating of the gas ahead of the shock front.

Figure 28 shows duplicates of the +3, +4 and +5 ns electron density maps in figure 26, along with the phasemaps from which they were derived. Ahead of the shock in the +4 and +5 ns images in figure 28b a channel of phaseshift can just be made out about target normal, the edges of which are indicated in the figures using white lines. This is the channel produced by the main laser beam directly ionising the gas it passed through on its way to the target. At +3 ns, a thin region of phaseshift is also seen around the edge of the shock, indicating that the material in this region is ionised and preheated before the shock's arrival. X-rays emitted by the heated target, the material ablating from the target and the shocked gas contribute to this; there could also be an electron

conduction contribution from high-energy electrons in the shocked gas running ahead of the shock front.

In [2], as has previously been mentioned in section 3.3.1 of chapter 3, Nicolaï *et al.* discuss the heating of a gas column by a laser pulse on its approach to a flat Cu target. The laser pulse in their experiment had a wavelength of 438 nm, an energy of 100 J, and an intensity on the target of 1.5 x 10^{14} W cm^{-2}. At this laser wavelength and intensity, the ionisation of the gas by the laser has to occur by multiphoton ionisation, as the 2.8 eV energy of each laser photon is far below the first ionisation energies of 15.76 eV and 24.59 eV for the atoms of the Ar and He gases used. They state that while Ar could be ionised, the laser intensity was too low for substantial ionisation of He to take place. In the Astra experiment the laser conditions were somewhat different, with a laser wavelength of 800 nm, corresponding to a laser photon energy of 1.5 eV, a pulse energy of 0.5 J and an intensity of 3 x 10^{15} W cm^{-2}. For such a laser wavelength and intensity, tunnel ionisation is operative as an ionisation mechanism (see, for example, [110]). Although the energy of an individual laser photon is less than the ionisation energy of a gas atom, the strong electric field of the laser suppresses the Coulomb potential that binds the electrons into the atoms and they can tunnel out. As a result, the Astra pulse can significantly ionise even He gas, for which the ionisation energies are very high.

On the next page figure 29 shows a particularly striking example of a laser channel. The image was taken on a shot in 52 mb N_2 at a time of +4.6 ns. On the left, figure 29a, is the phasemap and on the right, figure 29b, the electron density map. In the colour scheme used for the electron density map, the laser channel appears to have several components. In the centre in green is a high electron density core, with the electron density values in this region being from 6×10^{24} m^{-3} to over 10^{25} m^{-3} . Surrounding the core is a region of lower electron density, appearing red and having a value of ~3-5 x 10^{24} m^{-3}. At the axial positions labelled "A" and "B" in the figure, corresponding to a distance of roughly 600 μm from the target surface, the inner and outer widths of the laser channel are measured to be roughly 250 μm and 350 μm. The fractional ionisation of the nitrogen atoms in the laser channel can be estimated. The number density of nitrogen molecules in 52 mb of N_2 at 293 K is 1.3 x 10^{24} m^{-3}, corresponding to a nitrogen atom number density of 2.6 x 10^{24} m^{-3} when taking into account nitrogen molecules being diatomic. The maximum value of the free electron density that can be produced by ionising 50 mb of nitrogen gas is therefore 1.8 x 10^{25} m^{-3}, as each nitrogen atom has 7 electrons. Comparing this with the value of the electron density in the

centre of the laser channel in figure 29b shows that at +4.6 ns the ionisation in the channel is at over 30% of the maximum value.

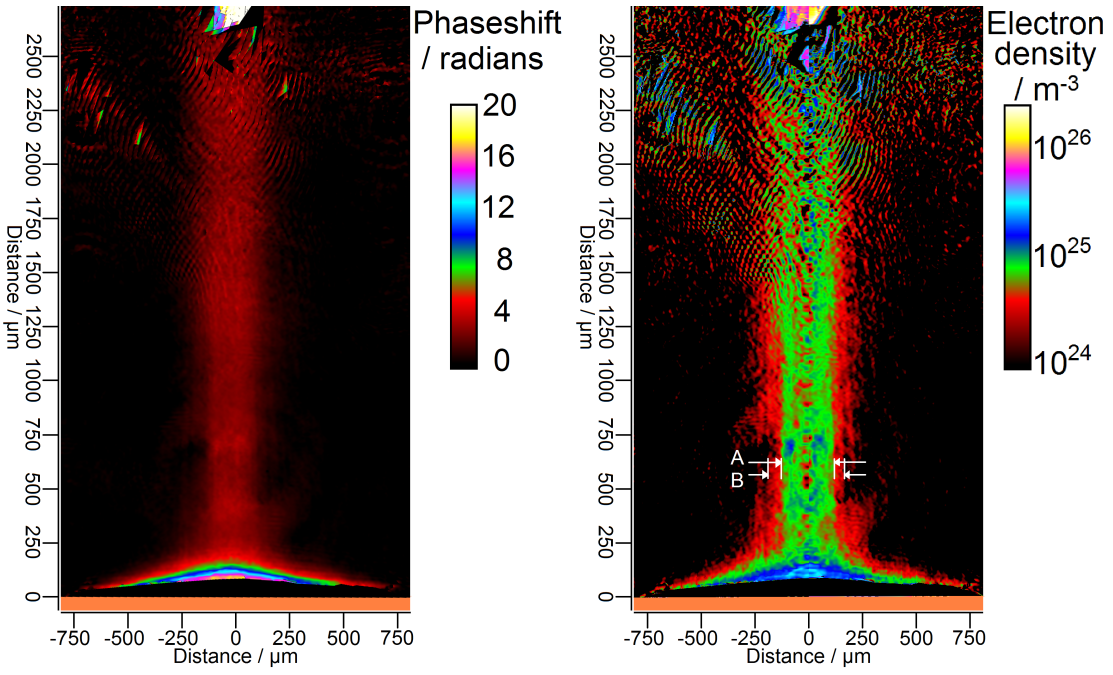

(a) (b)

Figure 29: Results for a shot through 52 mb of N_2 onto a flat Al target, seen at +4.6 ns. (a) phasemap (b) electron density map.

4.5.2 Comparison of jet widths for shots in gas and in a vacuum

Figure 30 on the following page shows results for conical targets in 50 mb He with four different coatings. Each of the four pairs of images shows the results for a different material, and within each pair there is one image for +5 ns and one for +10 ns. Comparing figures 30a, 30b and 30d, which are for CH ($\bar{Z} = 3.5$), Cu ($Z = 29$) and Au ($Z = 79$) respectively, it can be seen that the collimation of the axial flow is better for a higher atomic number material. For Au, the flow at +5 ns is conical near the target, becoming a narrow column further out. At +10 ns, the conical region extends much further from the target, and the jet emerging from the tip is again narrow. For Cu, at +5 ns the flow is conical out to 500 µm. By +10 ns, the Cu jet has changed considerably. While the electron density still peaks on the axis, the flow near the target no longer appears conical; the flow on the axis further out is much wider than that of the Au jet at the same time. For the CH, the +5 ns image resembles the +10 ns image for Cu. By +10 ns, the ionised part of the axial flow is weak.

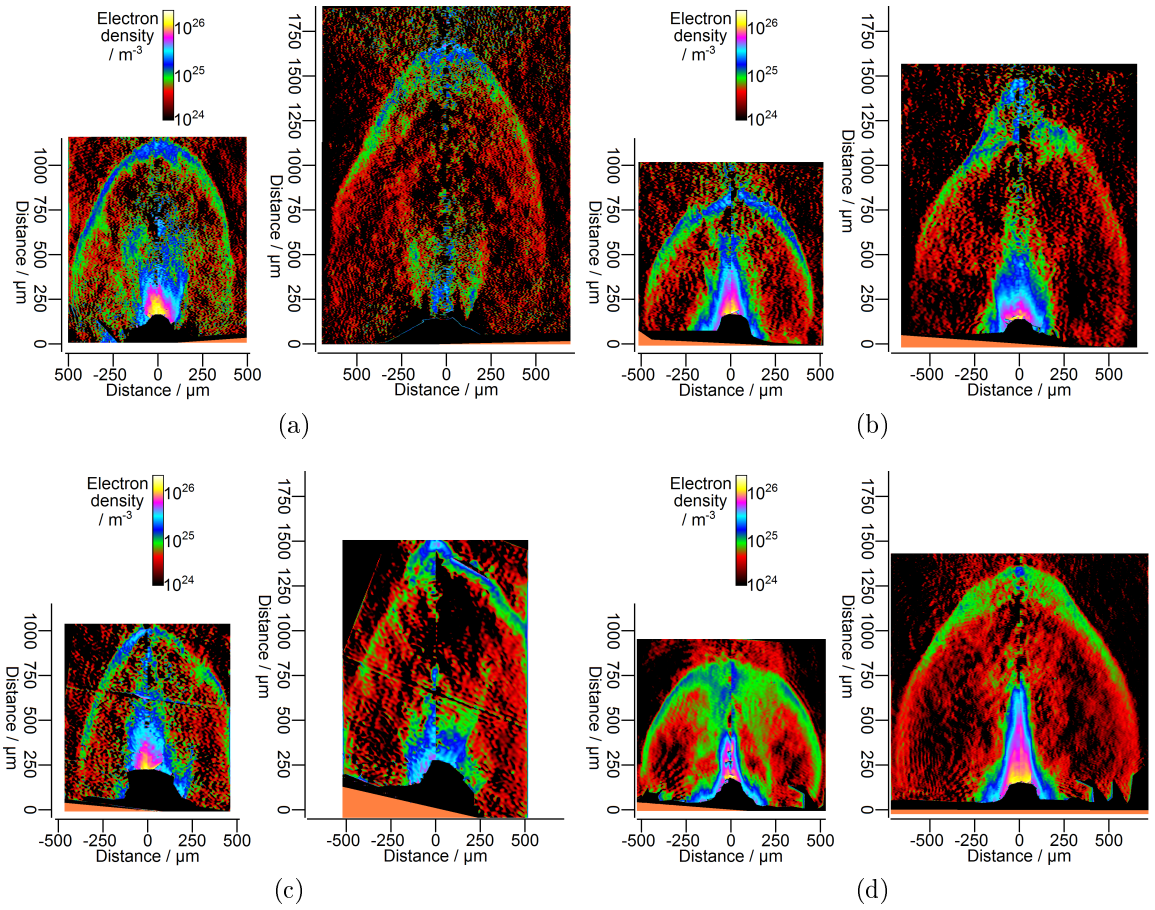

Figure 30: Effect of varying conical target material. The materials used were (a) CH (b) Cu (c) Cu-smoke (d) Au. The shots were all into 50 mb He gas, and each pair of images shows results at times of +5 and +10 ns.

Figure 30c shows a pair of images for a target which had a Cu-smoke coating. Comparing the results for this target at +5 ns with those in figure 30b for a standard Cu coating suggests that the collimation was better for the standard coating. However, there is noticeable asymmetry in the Cu-smoke images, indicating that the laser pulse did not illuminate the centres of the cones symmetrically. Experimentally it was found that the Cu-smoke targets were very hard to align as the cones were hard to see using the alignment cameras. In retrospect this is not surprising. As described in sub-section 4.1, the surface of a target with a "smoked" coating is not flat, but rather is covered with a low density microstructure. This results in a greatly enhanced absorption of optical wavelength (a few eV) light [99], and so smoked targets can appear much darker than flat targets under the same lighting conditions [90].

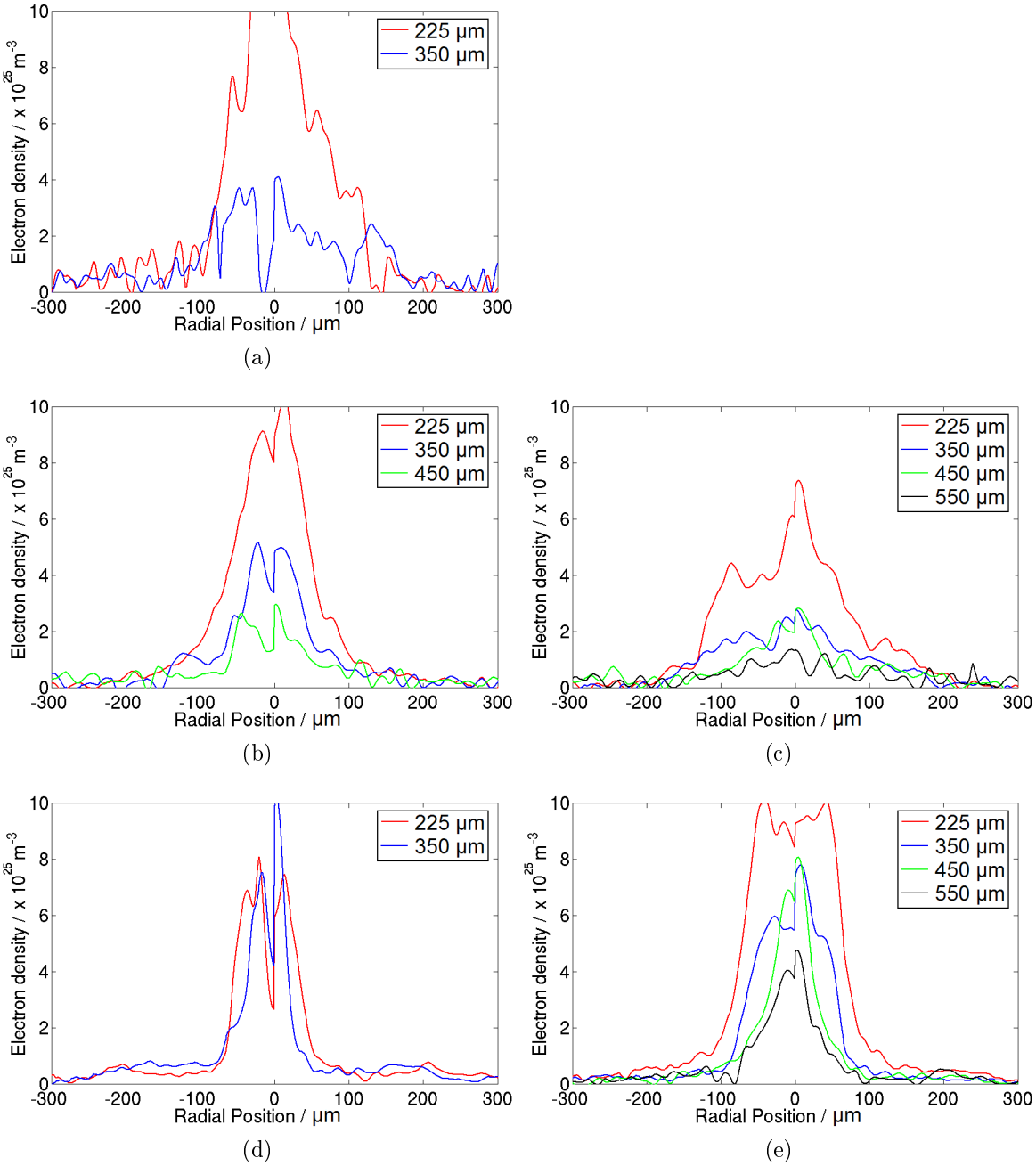

Figure 31: Electron density plots for CH, Cu and Au jets taken at lengths of 225, 350, 450 and 550 µm from the target. (a) CH, +5 ns (b) Cu, +5 ns (c) Cu, +10 ns (d) Au, +5 ns (e) Au, +10 ns.

Figure 31 shows sets of radial cross-sections through five of the images from figure 30, showing how the electron densities of individual jets varies down their length. Absolute values of electron density are plotted here, rather than normalised values, as such plots convey better the shapes of individual jets. The values are averaged over five pixels in the axial direction to reduce noise. Cross-sections are shown for distances from the target above 225 µm; below this, much of the area corresponds to the fringe-free region of the interferograms. As the jets are of different length, more cross-sections are shown for some jets than for others.

The cross-sections demonstrate the behaviour of the jet width previously described qualitatively. The plot for Au at +10 ns, figure 31e, shows that the width of the jet is less at greater distances from the target: for example, the peak at 450 μm from the target (green line) lies within the peak closer to the target at 350 μm (blue line). A similar result is seen for Cu at +5 ns in figure 31b. At +10 ns, the pattern for the Cu jet close to the target is different: the width of the peak for the 225 and 350 μm contours is roughly the same, though the height of the peak differs. This is consistent with the qualitative observation that close to the target the jet does not appear conical, in contrast to the jet at +5 ns. A similar pattern is seen for CH at +5 ns.

Figure 32 shows a comparison between the electron density maps of CH, Cu and Au jets in vacuum and in 50 mb of He. In the case of CH, the shapes of the axial flows in vacuum and in the gas are fairly similar at both +5 and +10 ns; the collimation might be slightly better at + 10 ns, though it is hard to tell due to the low signal strength, the possibility of shot-to-shot variation, and there being better symmetry in the vacuum image. For Cu, at +5 ns the flows are conical in both cases. At +10 ns, the collimation is better in the gas than in the vacuum, though direct comparison is again made difficult as the gas image is more asymmetric.

For Au, at +5 ns a narrow jet protrudes from the end of the conical convergence region in both the vacuum and the gas. It is hard to say for certain whether the collimation is improved, as in the gas the interpretation is complicated by the conical convergence region appearing to terminate closer to the target surface, and by the presence of serious image defects in the jet from fringe-splitting events in the interferogram. The jets in the vacuum and the gas at +10 ns are both narrow, particularly beyond 500 μm from the target. However, the tip of the jet in the gas appears far sharper than that in the vacuum. This is seen most clearly in the phasemaps, a comparison of which is shown in figure 33.

Figure 34 shows a quantitative comparison of Cu and Au jets in vacuo and in 50 mb He at both +5 and +10 ns. For each combination of material and time normalised electron density lineouts are plotted at two distances from the target. For Cu, at +5 ns the widths of the flows at the lineout positions can be seen to be essentially the same in the vacuum and in the gas. At +10 ns, the flow in the gas is definitely narrower at both positions. For Au, at +5 ns the widths at 350 μm are comparable; at the position closer to the target, there is a greater variation in width, but a significance cannot be attached to this because for the shot in gas fringe-splitting strongly affects the electron

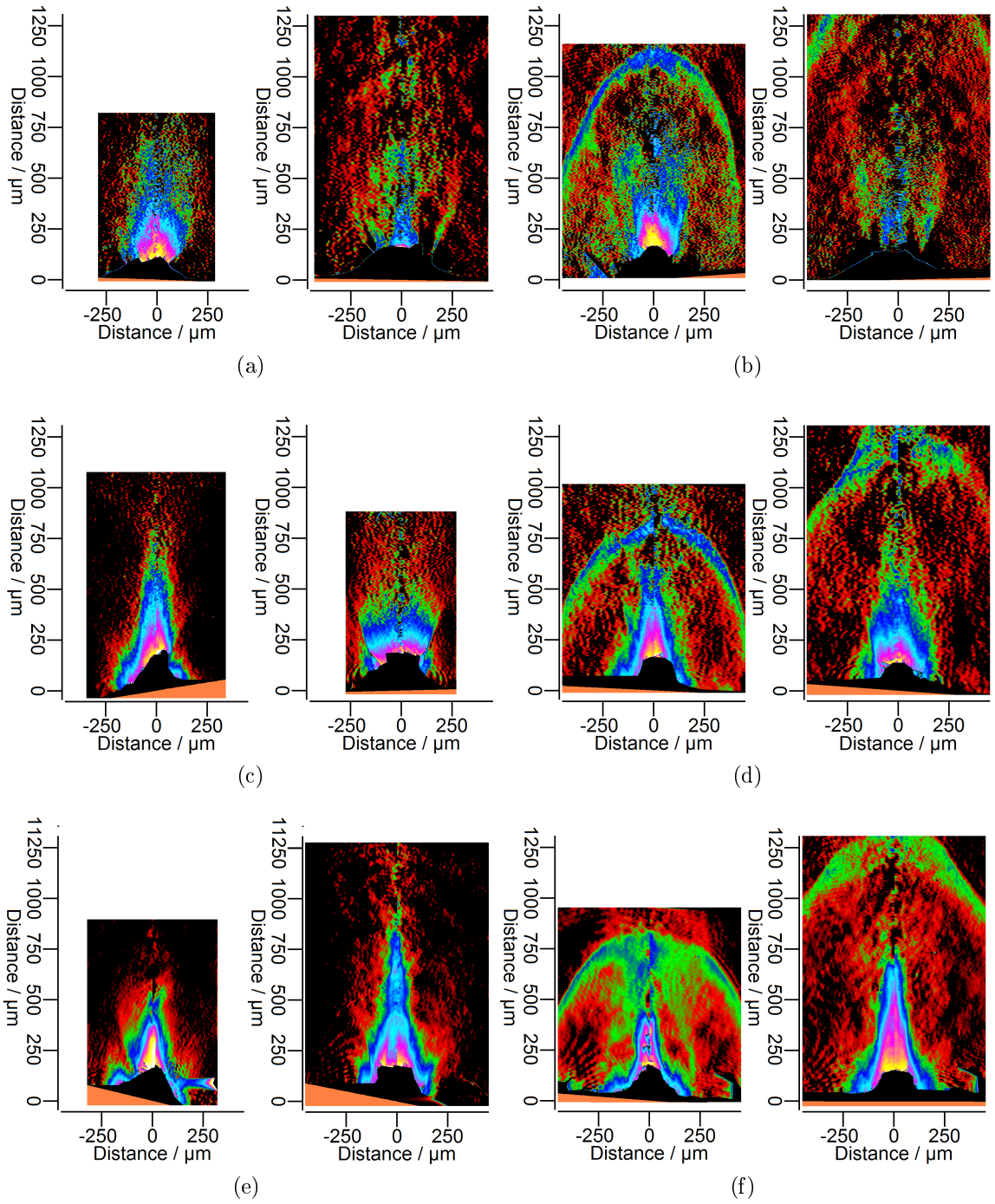

Figure 32: Comparison of jets from cone targets propagating into a vacuum and into 50 mb He. Each pair of images corresponds to a different combination of target material and gas pressure: (a) CH, vacuum (b) CH, 50 mb He (c) Cu, vacuum (d) Cu, 50 mb He (e) Au, vacuum (f) Au, 50 mb He. Within each pair, the left hand image was taken at +5 ns, the right hand image at +10 ns.

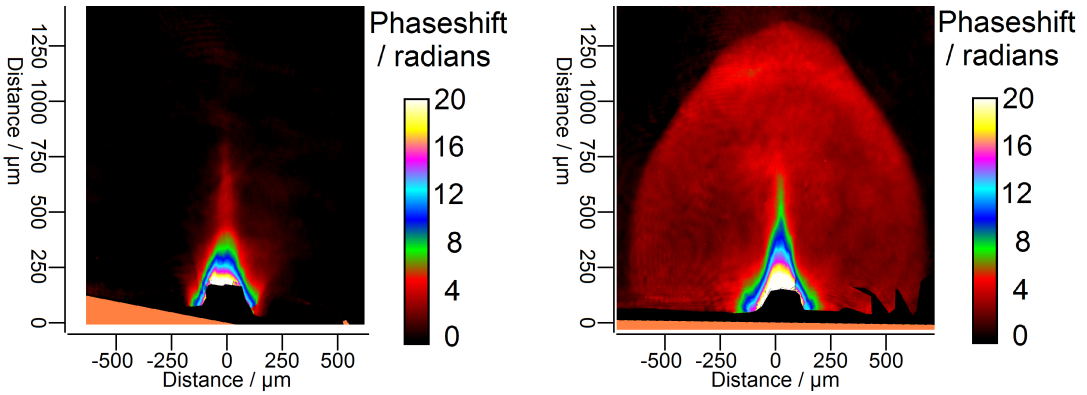

(a) (b)

Figure 33: A particularly striking comparison of jets in vacuo and in gas. The two images are phasemaps for Au jets propagating in (a) a vacuum (b) 50 mb He. Both images were taken at +10 ns. The electron density maps for these jets are shown in figure 32.

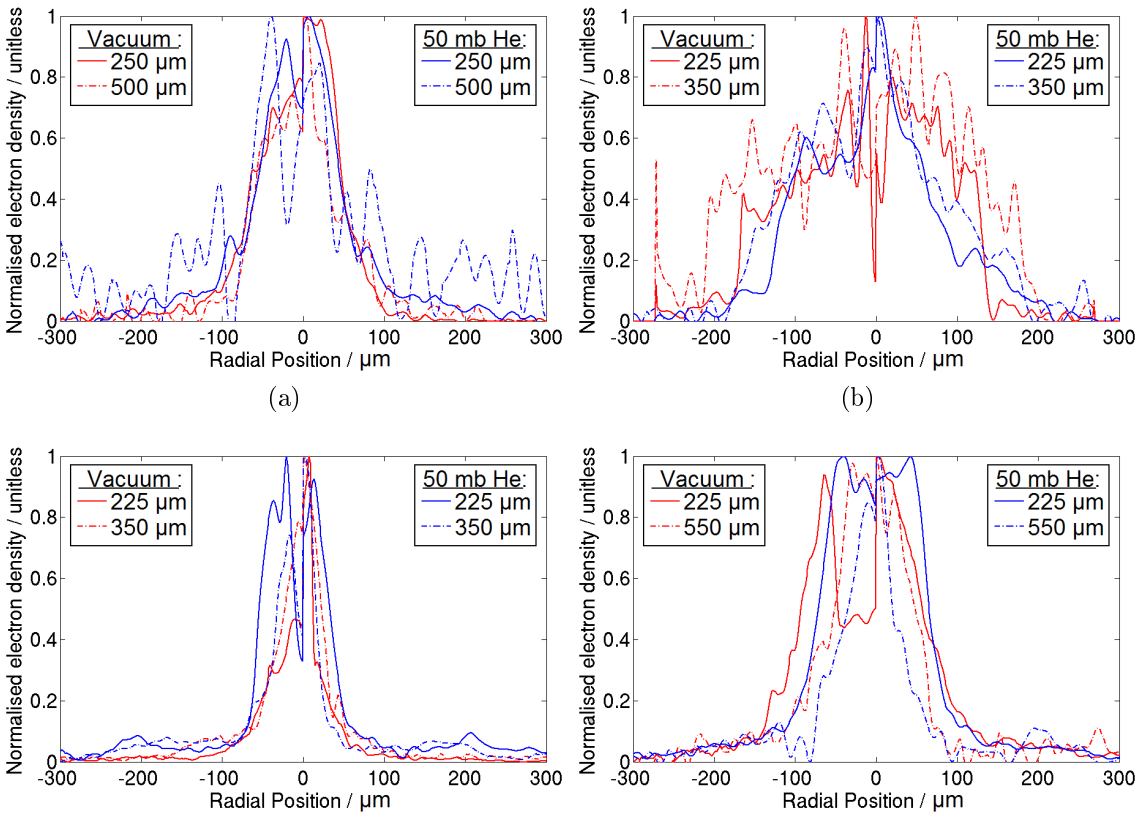

(a) (b)

(c) (d)

Figure 34: Normalised electron density plots comparing jets in vacuum with jets in gas. (a) Cu, +5 ns, lineouts at + 250 and +500 µm (b) Cu, +10 ns, lineouts at + 225 and +350 µm (c) Au, +5 ns, lineouts at + 225 and +350 µm (d) Au, +10 ns, lineouts at + 225 and +550 µm.

density in this region. At +10 ns, 225 μm from the target the jet in the gas is slightly narrower. Further from the target at +550 μm, which is inside the tip of the jet, the difference in the calculated width is more pronounced, with the jet in the gas again being the narrower.

Only one image was taken for Au in 50 mb of He gas at this time. Considering that the illumination of the target appears to have been more symmetrical for this shot than for the shot in vacuum, and also the uncertainty in the calculated electron density values, it is not possible to draw a firm conclusion as to the extent of the improvement in the collimation that was achieved when using the gas. Both Cu and Au results are, however, consistent with an improvement having taken place, at least at times greater than +5 ns.

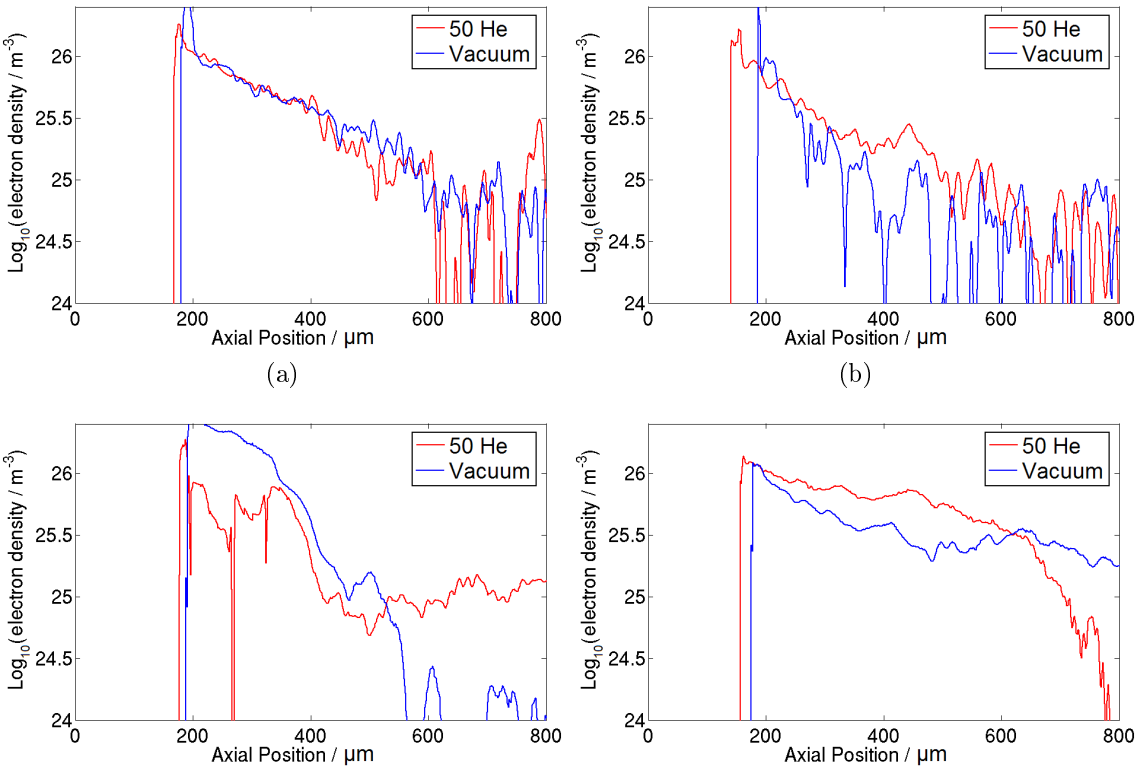

Figure 35: Axial electron density lineouts for Cu and Au jets in vacuum and in 50 mb He. (a) Cu, +5 ns, (b) Cu, +10 ns, (c) Au, +5 ns, (d) Au, +10 ns.

Figure 35 shows a comparison of the variation of the electron density along the Cu and Au jets for shots into vacuum and into the gas. The lineouts are averaged over 21 pixels (30 μm) in the radial direction, 10 on either side of the axis. The vertical lines near 200 μm in each image mark the edge of the fringe-free region in the interferograms.

At +5 ns, the two lines for the Cu jets are almost identical, and are nearly straight until near the end of the jets; taking the gradient gives an approximate form for the

electron density along the parts of the jets for which there is data of

$$n_e(\mathrm{m}^{-3}) \approx (3 \times 10^{26}) \times 10^{-z/410}$$

where z is the axial position in μm. The rise near 800 μm for the 50 He line marks the inner edge of the shock. For the Au at +5 ns, the 50 He line is affected by fringe-splitting until about 350 μm from the target. After this, it agrees in shape with the vacuum line fairly well up to 400 μm, though the vacuum line is slightly higher. The vacuum line then falls off, while the line for the He grows slightly out to the position of the shock, which is again at about 800 μm.

At +10 ns, for both Cu and Au there is a position between 200 and 300 μm from the target at which the electron densities in the vacuum and the gas are equal. After this, the electron density for the jet in the gas remains higher until the jet terminates. This is consistent with the picture which was obtained from the qualitative observations of the electron density maps and from the radial lineouts, in which the gas confines the jets at later times, and thereby maintains their electron densities over a longer distance.

4.5.3 Shock features and working surfaces

Figure 36a on the next page shows a time series for jets from Cu cones in a higher pressure of He, 100 mb He. Images are shown at times of +1, +2, +3, +4, +5, +10 and +20 ns. At +1 ns it is too early for the structure of the plasma to have become clear. However, in each of the subsequent images it can be seen that the plasma has at least two components, an axial jet and a shock, just as with the 50 mb He. The bubble-like shocks appear to have two distinct components: at large angles to the axes of the jets the fronts are approximately (hemi)spherical, while in the axial region they have a "nosecone" shape. The axial plasma flows inside the shocks all have a high degree of symmetry. The same is also true of the shocks, with the exceptions of the nosecone parts of the shocks at late times (+10, +20 ns); the behaviour in these regions is discussed later on in this sub-section.

Figure 36b shows the results of two additional shots taken at +4 ns. Only three shots were taken at this probe timing, and hence comparison of the two images in figure 36b and the +4 ns image in figure 36a gives a realistic impression of the shot-to-shot variability. The images are fairly similar, though some variation can be seen. The most pronounced difference is in the shock: the nosecone in the right hand image of

figure 36b is much more pronounced than that in the left hand image and extends considerably further from the target surface. Correlated with this, the diameter of the spherical part of the shock, measured perpendicular to its axis of symmetry, is reduced.

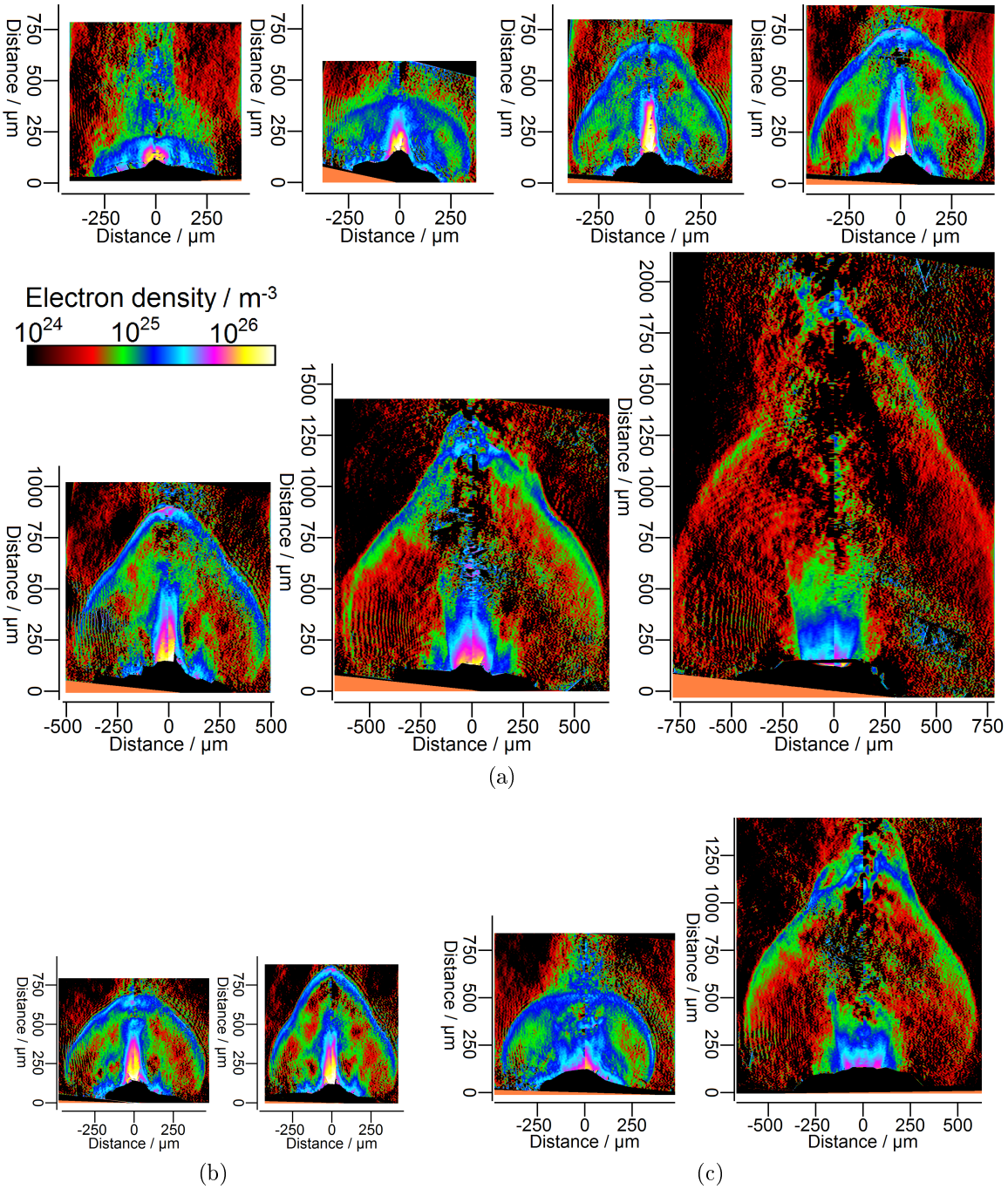

Figure 36: Electron density maps for plasmas created from Cu-coated targets in 100 mb He. The images in (a) are for shots onto conical targets at times of +1, +2, +3, +4, +5, +10 and +20 ns. (b) shows a pair of repeat shots taken onto cone targets at +4 ns, while (c) shows shots onto flat targets at +3 and +10 ns.

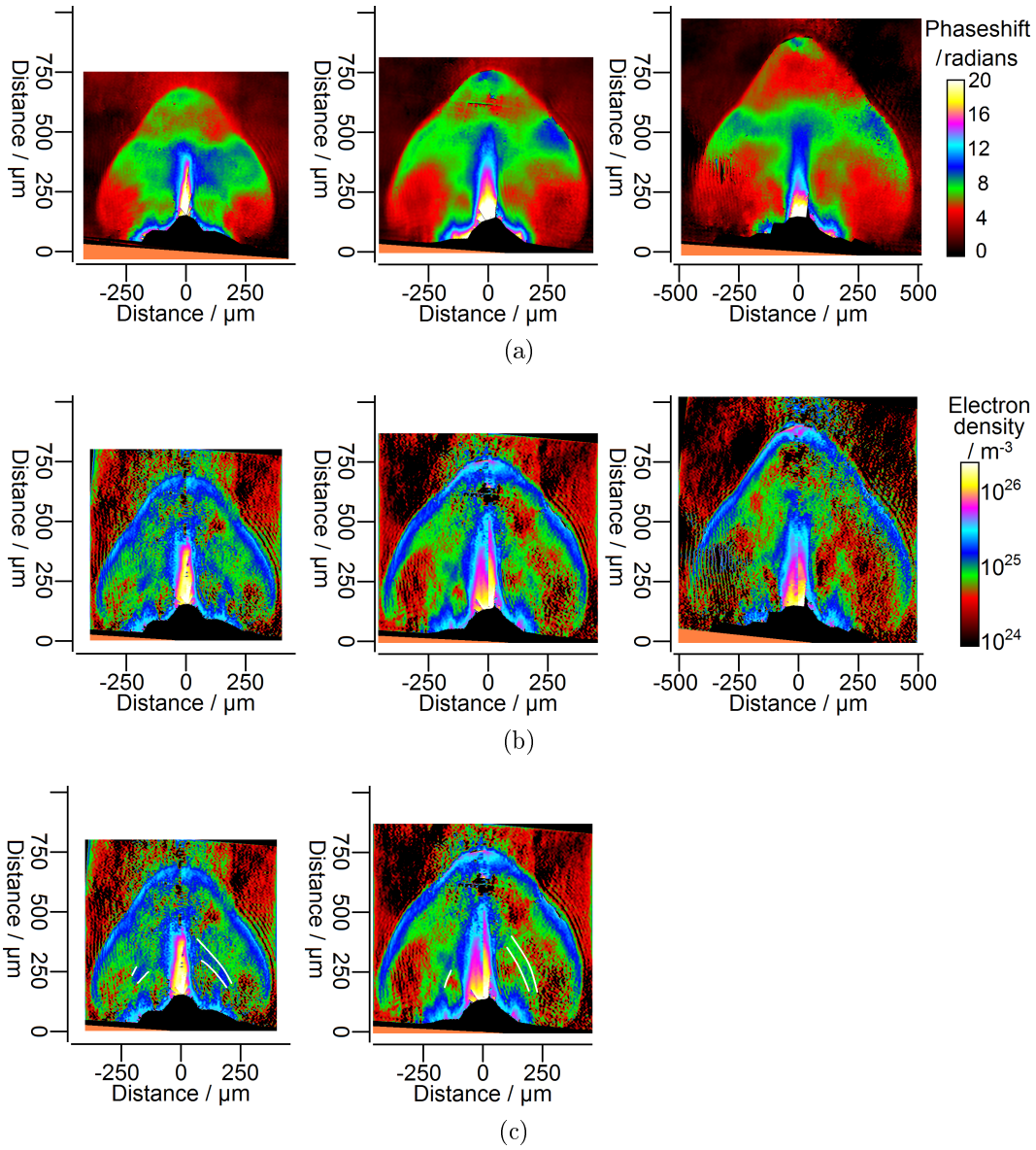

Figure 37: Jets from Cu cone targets in 100 mb He at +3, +4 and +5 ns. (a) phasemaps (b) electron density maps (c) electron density maps with positions of faint arcs indicated in white.

The electron density maps for times of +3 to +5 ns look very different from the phasemaps from which they are derived, as can be seen from figure 37. In the discussion of astrophysical jets in chapter 2, it was described how YSO jets terminate in a working surface structure (see section 2.4). At the front of the working surface is a bow shock, where the interstellar medium is accelerated. Behind this there is a jet shock where the material in the beam of the jet is decelerated. Between the two shocks lies the contact discontinuity, the surface where the shocked interstellar medium and shocked jet beam material are in contact. In the +3 to +5 ns phasemaps there is a green/blue region, corresponding to a phaseshift of between 7 and 11, which extends more or less continuously across the width of the shock bubble in line with the tip of the jet. It could be supposed that the shock front in the phasemaps corresponds to the

bow shock in the astrophysical case, and that the green region corresponds to plasma from the beam of the jet that has been decelerated at the jet shock and forced out sideways. The plasma in the nosecone, where no jet is seen to propagate, would then correspond to the shocked interstellar medium.

However, such an interpretation would not be correct. The electron density maps do not show an extended region of electron density extending across the shock bubble in line with the jet tip. Instead, there is a high electron density at the edges of the shock, and the jet has a high electron density, but the jet and the shock do not appear to be connected. The apparent extended region between the jet and the shock in the phasemaps results from phaseshift being a line-integrated quantity: as the probe beam passes all the way through the bubble on its way to the detector, the phaseshift in the region "between" the jet and the shock in the phasemaps contains contributions from the high electron density regions at the edges of the shock bubble.

While a feature connecting the jet to the shock is not seen, some faint blue/green arcs can just be resolved in the electron density plots, as indicated in figure 37c. These arcs appear to proceed from relatively near the tip of the jet back towards the target, and could correspond to the reverse shock of a working surface. This explanation would not only fit well with what is expected from astrophysics simulations, but would also fit with the experimental and simulation results reported by Nicolaï *et al.* in [2]. In their figures 2, 4 and 9 they show images of jets from flat Cu targets propagating in He or Ar gas columns created using a gas jet. The jets propagated along target normal and, as with the Astra results for Cu cone targets in 100 mb He, the bowshocks had a two-component structure with the shape of the shock in the axial region differing from that far from the axis, where it was approximately (hemi)spherical. Within their shock bubbles reverse shocks can be clearly seen, appearing as pairs of lines extending back from the axis; the interpretation of these lines as reverse shocks is supported by simulation results, specifically their figures 19 and 23. In their figure 9 (b), it is seen that for a low pressure of He the reverse shock can appear significantly fainter than the bowshock, in agreement with the faintness of the arcs in the Astra data compared to the bow shocks.

The third set of images in figure 36, figure 36c, shows two phasemaps for shots onto flat targets at the same gas pressure. It can be seen that at +3 ns the axial jet from the flat target is much wider than that from the conical target. Additionally, the shock lacks the "nosecone" seen with the conical target. This suggests there is a connection

between the shape of the nosecone bump on the otherwise hemispherical shock front and the collimation of the plasma flow from the target. However, other data seems to make this conclusion less certain. First, at +10 ns the nosecones for the flat and the cone shots are virtually identical even though the electron density of the axial flow is strongly peaked on-axis for the conical target, but not for the flat target. Second, a nosecone is not seen in the +2 ns conical target image in figure 36a and the nosecone in the left of the two +4 ns conical target images in figure 36b is not very pronounced. Hence, it is possible that the lack of a nosecone in the +3 ns flat target image is the result of shot-to-shot variability. From comparing the flat and cone target data it can be concluded that, at least for high gas pressures, the conical target geometry is important for creating a jet with a high aspect (length to width) ratio.

Figures 38a and 38b on the following page show a pair of time series for jets produced from Cu and Al groove targets. Two sets of units are given for the scale bars. The first of these is phaseshift, in radians, and the second is line-integrated electron density, in $m^3 \cdot m$. Using equation 20, these quantities are related by $\int n_e dy = 8.87 \times 10^{20} \Delta\phi$, where $\Delta\phi$ is the phaseshift.

For this target geometry, one would expect to observe different behaviour in the directions along and transverse-to the groove. Transverse to the groove, plasma ablated from the sides converges on the axis, and hence one would expect a collimated flow to form, while in the along-groove direction there is no plasma convergence. In all of the images in the two figures the groove has the same orientation, going into the page, and hence the images show the convergence of the plasma.

The plasmas produced from the Cu groove targets all show a high degree of symmetry: the laser focal spot was well aligned with the centre of the groove, resulting in the formation of a jet that propagated away from the target in the plane of symmetry of the groove. To either side of the central jet a small secondary jet can be seen. While most of the laser energy would have been contained within the central 100 μm of the focal spot, some of the energy would have fallen outside this. The secondary jets are produced where radiation from the main laser, and also radiation emitted by the plasma in the jet, ionises the flat surfaces to the sides of the groove.

The plasmas from the Al groove targets are considerably less symmetrical than those from the Cu. In each case, the laser pulse has struck the target to the left of the centre of the groove. This has several consequences. First, the main jets propagate to the right of target normal. Second, the amounts of energy falling on the flat parts of the

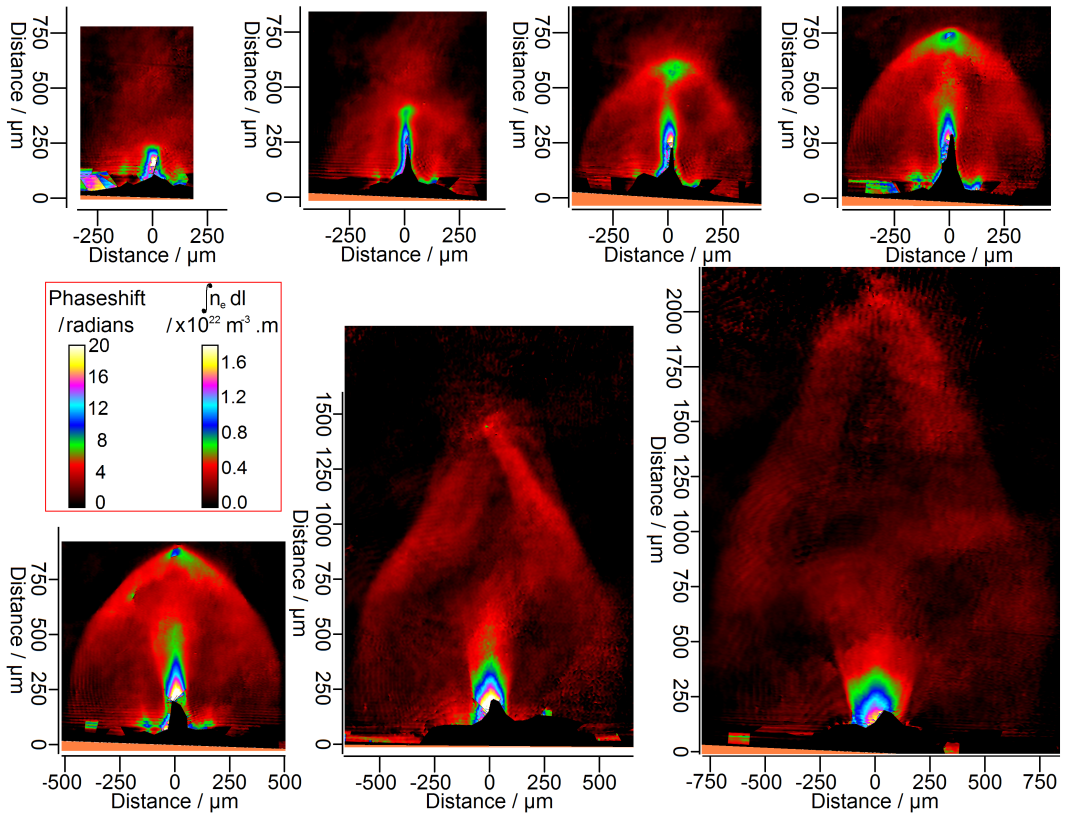

(a)

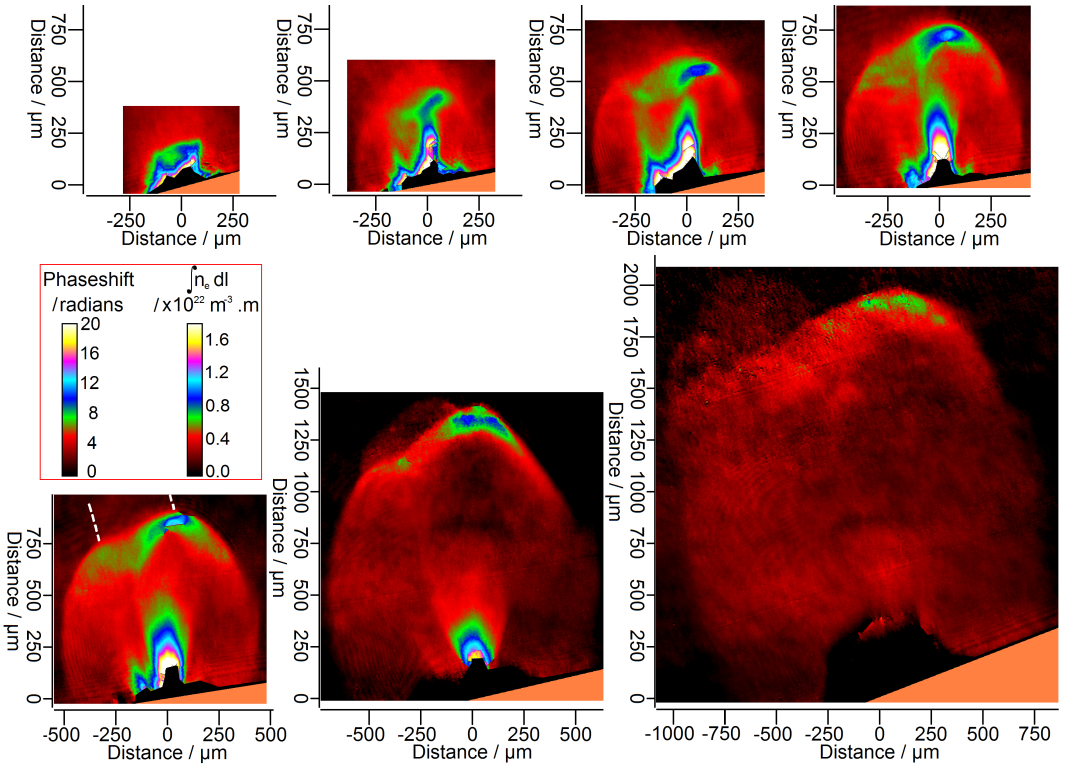

(b)

Figure 38: Results for (a) Cu and (b) Al groove targets in 50 mb He gas at times of +1, +2, +3, +4, +5, +10 and +20 ns. Two equivalent sets of units are given for the scale bar, phaseshift (in radians) and line-integrated electron density (in $m^3 \cdot m$). The dashed white lines in the +5 ns Al image indicate the approximate position of the laser channel.

targets to the left of the grooves are enhanced; it is the flat-surface plasmas that are visible as the sizable secondary jets to the left of the primary jets. The secondary jets, being created from a flat surface, propagate in a direction close to target normal, though in fact slightly to the left of it, possibly as a result of hydrodynamic pressure exerted by the plasmas leaving the grooves.

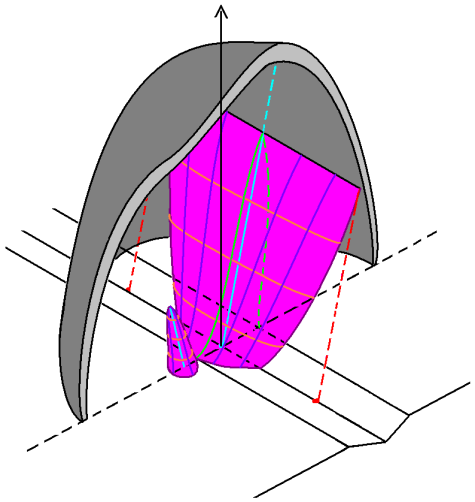

Figure 39: Cartoon to illustrate the geometries of the jets and shock for an Al groove shot at +5 ns. The primary and secondary jets are shown in pink and the shock in grey.

For a Cu jet, the shock can be expected to be roughly cylindrically symmetric at a large distance from the axis. The jet inside the shock is not cylindrically symmetric: perpendicular to the groove there is convergence like that for a cone target, while along the groove there is no convergence and the jet behaves like that from a flat target. For an Al groove the situation is similar, though the primary jet does not point along target normal. Figure 39 shows a cartoon to illustrate the geometry of the jets and the shock for an Al groove at +5 ns. Although it is desirable to process phasemaps to estimate values of electron density, these considerations suggest that, due to its reliance on cylindrical symmetry, Abel inversion is not an appropriate technique to use for the jets from groove targets: it cannot be expected to estimate well either the form of the electron density, or its peak value in the centre of the primary jet.

An approach which can be used to estimate mean values of electron density along lines through the jets, parallel to the grooves, is as follows. The first step is to estimate the contribution of the shock to the phaseshift values in the jet regions of the phasemaps. This contribution arises as the probe passes through the shocks both on its way to the jets and also in travelling from the jets to the detector. The shock contribution can be estimated by taking lineouts across the phasemaps, perpendicular to the jets. At large distances from the plane of symmetry, the only contributions to the phaseshift come

from the shock. If a curve is plotted on each lineout to connect the regions on either side of the plane of symmetry for which the phaseshift value is determined solely by the shock, then the value of the curve at each point between the regions is an estimate of the contribution of the shock to the phaseshift at that point. The estimated values for the shock contributions can be subtracted from the phaseshifts in the phasemap to leave only the parts of the phaseshifts that are due to the jets.

Having subtracted the shock contribution, the relation $\int n_e dy = 8.87 \times 10^{20} \Delta\phi$ from sub-section 4.3.2 can be used to convert the shock-corrected phaseshifts to corrected values of line-integrated electron density, where the integration is along lines through the jets parallel to the grooves. To convert a line-integrated value to an electron density requires, at a minimum, knowledge of the width of the jet in the along-groove direction at the position of the line-integrated value. Dividing the line-integrated value by the width of the jet then yields the mean value of the electron density in the along-groove direction at that location.

Here, for simplicity, a single average value is estimated for the shock contribution to the phaseshift for the jet when it is taken as a whole. For each jet this value is calculated by using a single lineout perpendicular to the jet and averaged over its entire length. An example of this is shown in figure 40a on the next page for the +4 ns Cu groove in figure 38a. In the left of the two images is the phasemap, with a yellow box indicating the region used in producing the average lineout shown on the right. A curve linking the two parts of the lineout contributed to solely by the shock is shown in red. This curve is flat across the width of the central jet, indicating that the shock contribution to the phaseshift has a uniform value across the width of the jet. The size of the contribution is about 2.6 radians. Using a single value for the shock contribution in this manner is a significant simplification. It is an underestimate far from the target, where the shock front has a high electron density and lies near to the axis, and an underestimate nearer to the target. Figure 40b shows the shock-corrected phasemaps for the central jets in the +2 to +20 ns images in figure 38a.

Having estimated the shock contribution to the phaseshift in the jet region, the next step is to estimate the widths of the jets in the along-groove direction. As shots were only taken looking along grooves, these widths were not directly measured. In the along-groove direction, there is no plasma convergence. The same is true for flat targets, and consequently the widths of plasmas from flat targets will be used as an estimate of the widths in the along-groove direction. These widths can be expected to

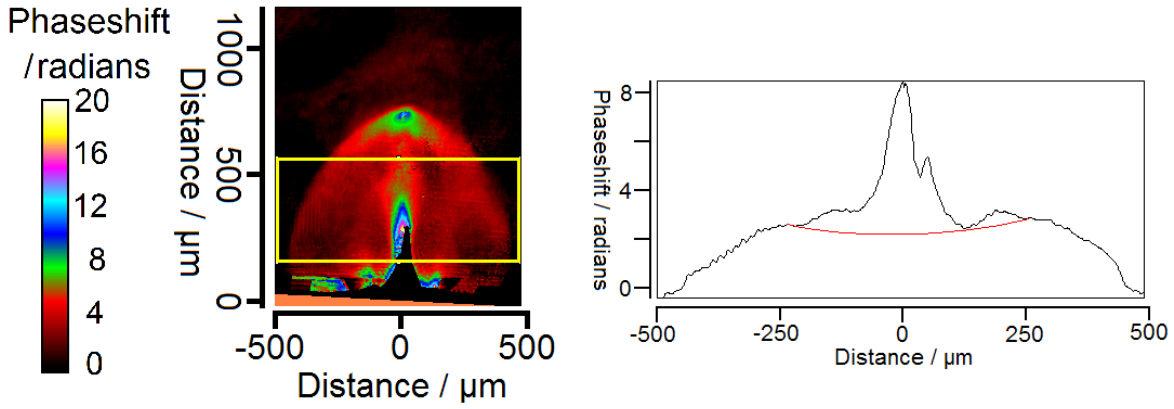

(a)

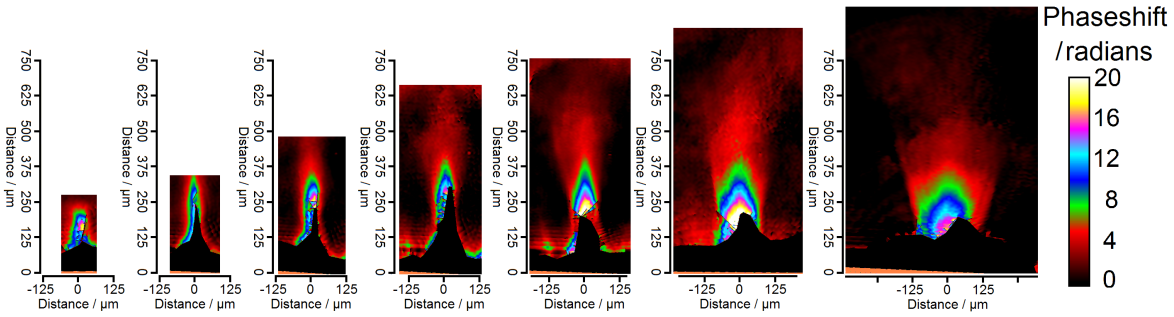

(b)

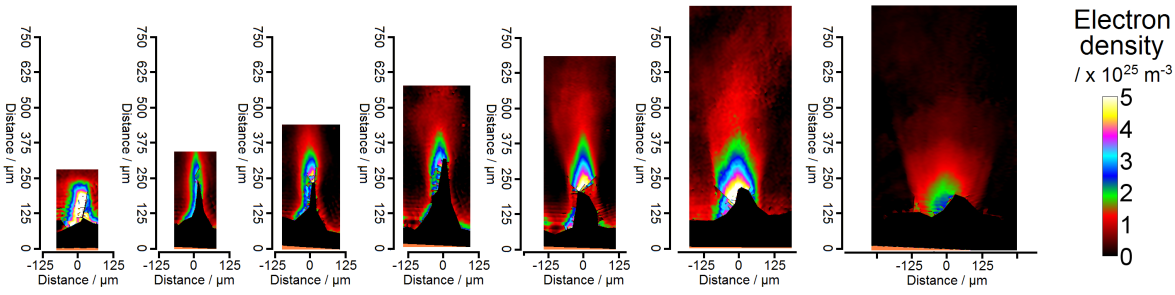

(c)

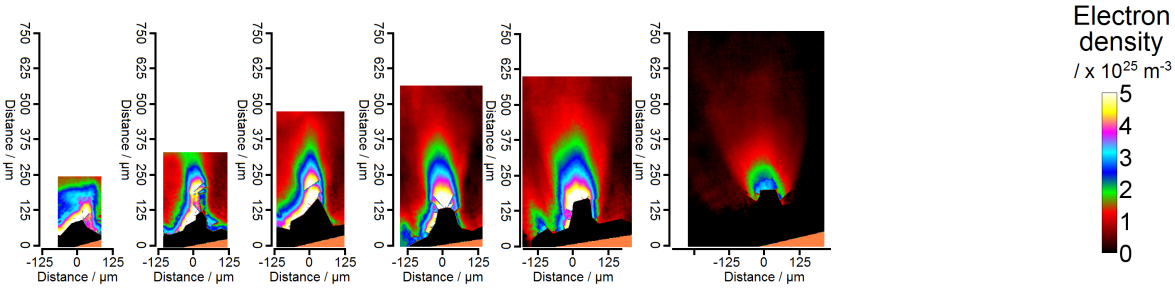

(d)

Figure 40: Estimation of values of mean electron density for along-groove paths through Cu and Al groove jets. (a) Images illustrating the estimation of the contribution of the shock to the phaseshift at the position of the central jet. On the left is a phasemap for a Cu jet at +4 ns, with the yellow box marking the region used to take the lineout shown on the right, which is averaged over the length of the jet. (b), (c) and (d) show shock-contribution-corrected phasemaps for Cu and the mean electron density in the along-groove direction for Cu and Al at times of +2, +3, +4, +5, +10 and +20 ns.

be an under-estimate due to the along-groove direction acting as a release for pressure built up in the convergence of plasma onto the plane of symmetry.

For each jet a single representative value for the width is chosen. As with the use of a single value to represent the contribution of the shock to the phaseshift in the jet region, the use of a single value to represent the width of a jet is a significant simplification of the situation, as in practice the width of a jet varies both with distance from the target and also with distance from the plane of symmetry. In the Astra experiment only a few shots were taken using flat Cu targets. One shot was taken in 50 mb He, two in a vacuum and three in 100 mb He. Three of these, one at each gas pressure, were taken at +3 or +5 ns, and the widths of the flows are similar in all three cases, all being around 230 μm. Hence, this value is taken for the representative widths of the groove jets at times of +2 to +5 ns. At later times the only flat target shots were either in vacuum or in 100 mb He, and so the representative values chosen for the widths of the +10 and +20 ns flows are very rough. Shots in 100 mb He yielded widths of 310 μm at +10 ns and 410 μm at +15 ns. As the widths of flows in a lower He pressure should be greater, representative widths of 350 and 600 μm are chosen for the times of +10 and +20 ns.

In the case of Al, there is a lack of data for flat targets in 50 mb He. However, there is data for flat targets in a N_2 atmosphere with a similar density. Using measurement from images taken at +4.6 and +10 ns, representative width values of 280 μm at +2 ns, 350 μm at +3, +4 and +5 ns, and +450 μm at +10 ns are chosen. The central jet in the +20 ns Al groove image in figure is barely discernable. Hence, this shot is ignored. For Cu and Al, plots of the mean electron densities in the along-groove direction estimated using the representative widths are shown in figures 40c and 40d.

The reason for introducing the groove time series at this point is that the connection between the shape of the shock front and the position of the jets is very clear in the Al groove images. Picking out the +5 ns image in figure 38b as an example, a pair of edges can be made out linking the primary jet directly to the most advanced part of the shock front, which lies to the right of target normal and in line with the jet. The position of the edges of the laser channel are indicated in white, and the advanced part of the shock front is not contained within this channel. From these observations it is concluded that the jet has acted like a piston, driving the gas ahead of it.

The shock structure seen in the +10 ns image of figure 38b is more complicated than that at +5 ns. At +5 ns, the top of the shock has a double-bump structure. The bump

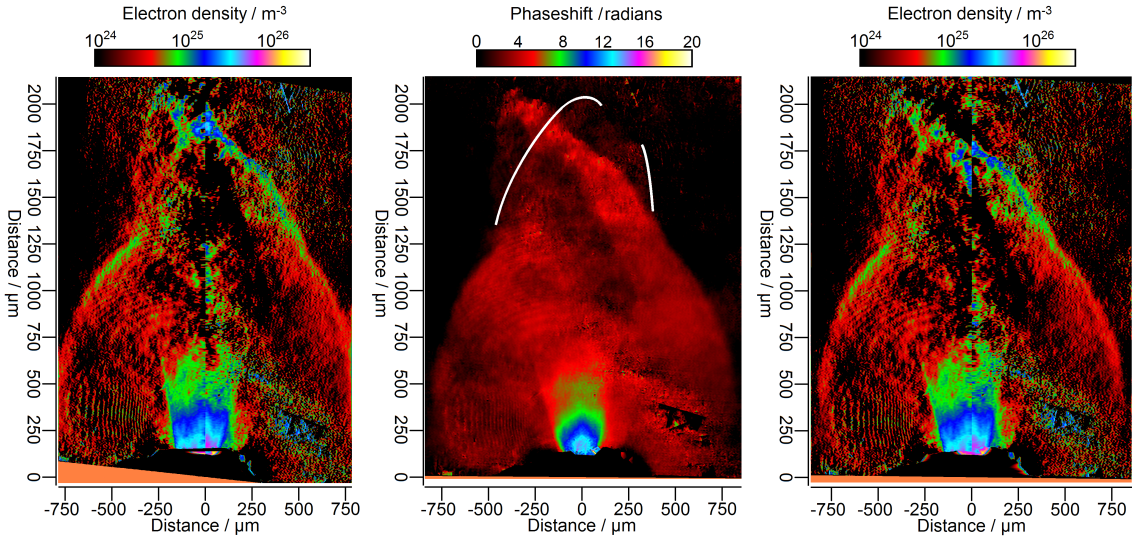

Figure 41: Comparison of electron density maps for a Cu cone target in 100 mb He with the phasemap from which they are derived. The electron density map in (a) is oriented with the axis of the jet vertical, the phasemap in (b) is oriented such that target normal is vertical, and the electron density map in (c) is oriented with the axis of the outer parts of the shock vertical. White lines have been added to (b) in order to clearly distinguish the two components of the shock in the axial region.

to the right of target normal is, as discussed in the previous paragraph, caused by the driving of the primary jet. The lesser bump to the left of this, on the left of target normal, can be associated with the driving of the weaker secondary jet. At +10 ns, there are three features at the top of the shock: the bumps attributed to the jets are accompanied by a third feature aligned along target normal. Later, at +20 ns, the shock is again seen to have multiple bumps.

Figure 41a shows the +20 ns electron density image from figure 36, the time series for Cu cones in 100 mb He, oriented such that the axis of the jet is vertical. In the axial region, it appears on first inspection to have a single asymmetric feature. However, there are actually two features here, though the second is fainter and at an angle to the first. Figure 41b shows the phasemap from which the electron density plot is derived, oriented such that target normal is vertical rather than the axis of the jet. In the axial region the shock has two features, one to the left of target normal and one aligned with it. The feature on the left is aligned with the jet and can be associated with it, leaving the feature along target normal, the edges of which are highlighted in white, unaccounted for, just as with the third of the bumps for the Al groove target.

In all of the Abel-inverted electron density maps shown previously, the axis chosen for the Abel inversion has been that line which, as judged by eye, is the best axis of symmetry when considering both the jet and the part of the shock which the jet drives

hydrodynamically. However, this is not the only choice that could have been made. The best axes of symmetry for the parts of the shocks away from the axial nosecone regions are usually roughly aligned with target normal. However, as there is usually a measure of asymmetry in the illumination of the targets, the axes of the jets are usually inclined with respect to target normal. If the best axes of symmetry for the shocks were used as the axes for Abel inversion, instead of those of the jets, more accurate values for the electron densities in the outer parts of the shocks would be obtained. Figure 41c shows an example of Abel-inverting using this approach for the Cu cone in 100 mb He at +20 ns; as it lies along target normal, the additional shock feature is more prominent in this image than in figure 41a.

The multi-bump nature of shock fronts for cone and groove targets is only readily apparent in cases where jets propagate to one side of target normal (as otherwise features on the shock front are overlapped along the line of sight), and even then often only at times of +10 ns or later. Where multiple bumps are seen, in each case one of the bumps of the shock front can be directly attributed to the primary jet, leaving an additional feature near target normal. A fully satisfactory explanation of the additional features is hard to pin down. In the case of cone targets, it is relatively easy to provide a possible explanation for an additional target normal component. While most of the laser energy falls into the cone, some always falls onto the flat surface around the edges. If a cone is illuminated asymmetrically, the resulting jet leans to one side, overshadowing part of the flat surface around its edge. While the plasma from this part of the flat surface becomes deflected by the jet, the plasma from the rest of the flat surface need not be deflected; this plasma will primarily propagate normally to the target, and could therefore contribute to an axial shock feature.

There are potential difficulties with this theory, however. First, the energy falling on the flat part of the target that could contribute to the shock driving is much smaller than the energy deposited into the cone. Consequently, one would expect the driving of the shock by the primary jet to be far stronger than that from the flat part of the target, and hence that the tip of the bump due to the primary jet would be far in advance of the tip of the axial bump. The Al groove data effectively demonstrates this principle: the bump associated with the secondary jet, produced by the illumination of the flat target to the left of the groove, lies far behind the bump due to the stronger primary jet. However, looking at the +20 ns cone target image in figure 41b, the tip of the feature on the axis is seen to lie at a similar distance from the target to the feature produced by the primary jet. Second, it is hard to see how the theory could explain the

additional axial bump seen with the Al groove targets. In this case, the jet overshadows the flat part of the target to the right of the groove which gets irradiated by the laser. The flat part of the target to the left of the groove contributes to the shock bump associated with the secondary jet. There is therefore little flat-target plasma that can contribute to the strong axial shock feature that is seen.

In the experiment the laser beam was incident on the target along a line at 8° to target normal. However, due to the angle at which the probe beam passed the target, the laser channel appears aligned with target normal in the interferometry data. It is possible that the additional shock feature also has a component of motion into/out of the page, and further that the additional feature is connected with the laser channel. In [71] by Edens *et al.* and [102] by Hansen *et al.* experiments are described in which shock waves were produced by illuminating the tip of a pin immersed in a gas, either N_2 or Xe, with an intense laser. In the results presented by Edens *et al.* the path taken by the laser through a Xe background can easily be made out at +300 ns, long after the end of the 1 ns, 10 J laser pulse (see their figures 3 and 4).

In both N_2 and Xe gases the blast waves were seen to be aspherical, being more extended on the side of the pin from which the laser was incident. Several factors contributed to this. The side of the pin heated directly by the laser would have emitted a lot of X-rays, resulting in ionisation and heating of the gas on the laser-entry side, and hence the blast waves would have had an anisotropic medium to propagate into. Second, the plasma generated from the pin would have moved away from the pin into the gas on the laser entry side, driving the gas on this side strongly. Hansen *et al.* state that it is this hydrodynamic motion of the gas that launches the shock, and so one would expect the shock to propagate faster on the laser entry side than at the rear. Third, there is an additional source of inhomogeneity in the gas on the laser-entry side: the laser pulse ionised and heated the gas it passed through on the way to the pin. Assuming that the shock in the Astra experiment was launched in a similar manner, these comments apply equally to the Astra experiment, explaining why the shocks launched in the gas are not (at a sufficiently large distance from the target) hemispherical, which would be the case if the driving of the shocks and the ambient medium were both isotropic.

For laser pulse energies of 10-1000 J, the blast waves in N_2 in the experiment of Edens *et al.* were seen to have a smooth surface except around the position of the laser entry channel, where they appear turbulent. In Xe the behaviour was somewhat different. The shock front, particularly on the laser-entry side of the pin, was seen to

be covered in small-scale perturbations. In addition, for 10 J laser pulses in both N_2 and Xe close inspection of the data shows the presence of additional features at the heads of the shocks in the regions of the laser channels. In N_2, a single bump in the shock front is seen within the laser channel slightly below its axis. In Xe, a large-scale perturbation is seen, co-axial with the laser channel and of approximately equal width at the times shown. There is at least one small bump ahead of this in the laser channel which, as with the N_2, lies slightly below its axis.

The large scale perturbation in the Xe was replicated in a simulation (see figure 4 of [71]) in which it appears qualitatively similar to the nosecones seen in the Astra data. The explanation given by Edens *et al.* is that the part of the blast wave travelling along the laser channel encounters gas that has been heated and ionised and has expanded hydrodynamically to a lower density than the surrounding gas. The blast wave is slowed down less in accelerating this medium and consequently the shock front in the laser channel runs ahead of the shock front in the rest of the gas, gaining a nosecone-like appearance. The small bumps slightly below centre in the laser channels, which are the most advanced parts of the shocks, could result from intensity non-uniformities in the beam. However, the other factors identified as producing anisotropy in the shocks, specifically X-ray radiation from the target and hydrodynamic driving, would have produced effects approximately co-axial with the laser channel. It could be, then, that hydrodynamic driving plays a significant part in the formation of the bumps, just as hydrodynamic driving was identified as directly related to the most advanced parts of the shocks in the Astra Al groove data.

To conclude this part of the discussion, it has been seen how some, but not all, of the features of the bowshocks in the Astra data can be directly related to hydrodynamic driving by flows from the target. For both cone and groove targets, at sufficiently late times the shocks have an additional axial feature. In addition to the hydrodynamic driving, there are at least two factors that contribute anisotropy to the gas in front of the target, specifically the X-ray emission from the target and the ionisation of gas by the laser on its way to (and partial reflection from) the target. It is possible that the additional axial feature of the shocks could be a result of the shock being slowed down less in passing through the ionised, heated material in the laser channel than in passing through the rest of the gas. In order to pin down whether this is the correct explanation, in a future experiment a second probe beam could be used, again passing parallel to the target, but travelling orthogonally to the first. Whereas the projection of the laser entry channel in the first probe system is along target normal, the laser

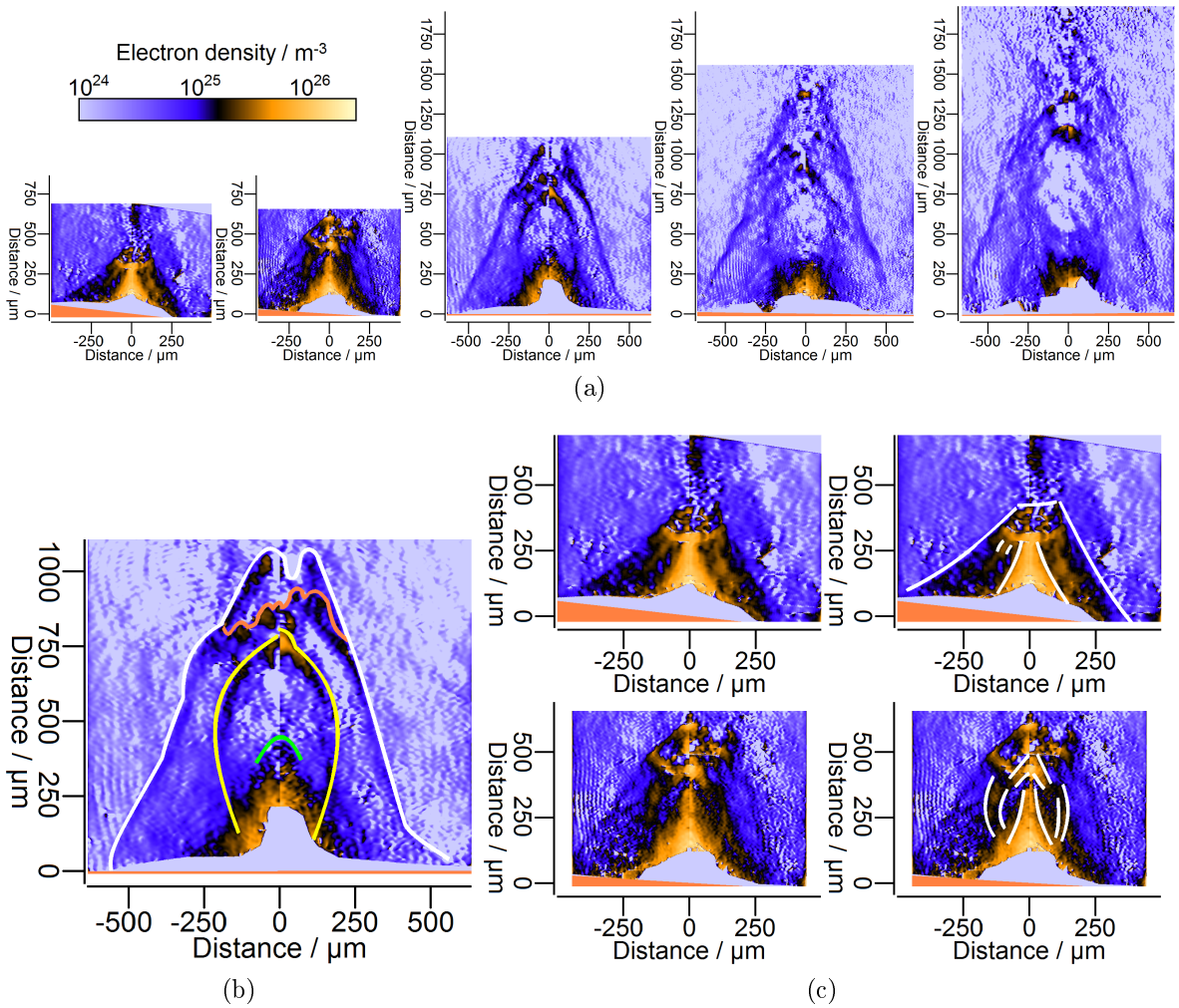

Figure 42: Images for jets from Cu cone targets in 11 mb Xe. (a) Electron density map time series showing images at +3, +5, +10, +15 and +20 ns. (b) Repeat of the +10 ns image from the time series, annotated to indicate the positions of key features. (c) Close-ups of the +3 and +5 ns electron density images with and without the edges of the features picked out.

channel would lie at 8° to target normal in the second. If the additional shock feature is associated with the laser channel, one would expect to see it similarly offset from target normal.

4.5.4 Shots in Xe

Figure 42a shows a time series for Cu jets in 11 mb Xe. The morphology seen in these images is very different from that seen in 50 or 100 mb He. Figure 42b shows the +10 ns image from the time series with the edges of the features picked out. In the series the outer shock appears conical, in contrast to the bubble-like shocks seen in He. Within the outer shock is an ovoid feature. This outer shock-ovoid structure bears a striking resemblance to the simulation results published by Nicolaï *et al.* in [2], specifically their figures 19 and 23. Using the CHIC [103] code they simulated a jet created by

laser-ablation of a flat Cu target, and the subsequent interaction with a plume of gas from a gas jet. They found that this results in the creation of a roughly ovoid feature inside a conical outer shock. They identified the outer shock-ovoid structure with the triple-discontinuity working surface structure seen in astrophysical simulations: the outer shock is the bowshock propagating in the ambient gas, the outer surface of the ovoid is the contact discontinuity separating the shocked ambient gas from the shocked jet material, and the jet shock where the jet material is decelerated is located on the inner surface of the ovoid.

This explanation seems plausible for the structure seen in the 11 mb Xe images. Figure 42c shows close-ups of the images taken at +3 and +5 ns. At these early times, some of the features of the plasma are hard to resolve. At both times the outer shock can be made out and also parts of the edges of an oval. In addition, axial flows are seen. The presence of an axial flow can barely be made out at +10 ns and is missing after this. This correlates well with what has previously been seen of axial flows from Cu cones in a vacuum and in 50 mb He. In these two cases, at +5 ns the axial flow is conical. By +10 ns it has either already become fully divergent, or started to diverge, becoming fully divergent by +20 ns. The axial flow in the simulations of Nicolaï *et al.* develops in a similar manner, as shown in their figure 19, which is a time series for a jet in He gas.

In the +5 ns electron density map, above the axial flow the image shows an arrowhead above which there is a further yellow/black region. Given its position relative to the axial flow, and its similarity to the jet shock in the experimental data of Nicolaï *et al.*, it seems likely that the arrowhead corresponds to the jet shock. Interpreting the rest of the structure in the phasemap between the arrowhead and the outer shock is more difficult. This region is small, and features are close together, and the electron density values there are affected by a fringe-splitting event.

The +10, +15 and +20 ns images clearly show the presence of a feature between the oval of the jet shock and the outer bow shock. This feature, not seen in the simulation data or experimental results of Nicolaï *et al.*, is indicated in orange in figure 42b. The cause of this feature is uncertain; it could perhaps be related to an interaction between the shock front and the ionised gas in the laser channel. The shape of the bowshock at +10 ns is also not understood. One would expect a bowshock to be most pointed on its axis. However, in the image it appears that the bowshock has a V-shape in this region. It could be suggested that the edges of the white and orange regions are mis-identified,

with the point of the bowshock on the left of the V corresponding to the tip of the bowshock associated with the jet, and the tip of the shock on the right of the V being associated with a second feature. However, this suggestion seems unlikely to be true as the jet and oval are well aligned with target normal, and there is no obvious reason for the appearance of an additional, off-axis component to the bow shock.

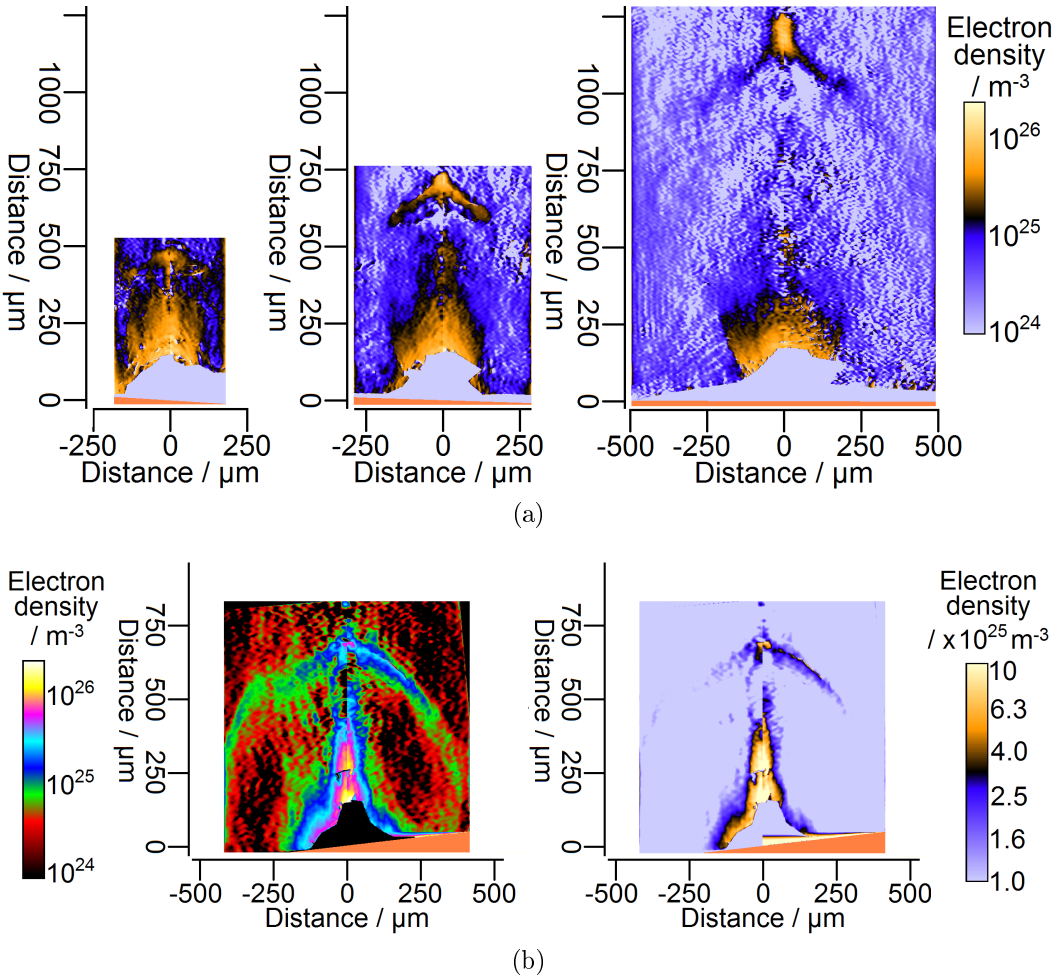

Figure 43: Electron density maps for conical Cu targets in (a) 4 mb Xe at times of +3, +5 and +10 ns (b) 50 mb He at +4 ns. In (b) the same image is shown in two different colour schemes in order to bring out the structure at the top of the shock.

When using a lower pressure of Xe, the observed structure was very different. Figure 43 shows a time series for Cu jets in 4 mb Xe. The axial flows are similar to those in 50 mb He. The only feature seen in addition to these is a "hat" on the axis, the shape of which changes with time. To the sides of the axial flow, no shock edges are seen: at +10 ns it appears that there is a faint edge on the far left of the image, but this turns out to be an artefact.

The front edge of the hat is sharp, suggesting it could correspond to a discontinuity of some kind. In the +3 and +5 ns images its width is seen to match that of the flow. A reasonable first hypothesis is thus that the hat corresponds to the reverse shock of

a working surface. In figure 4 of [2], Nicolaï *et al.* show a set of four shadowgrams of Cu jets propagating into Ar. Each of the shadowgrams was taken at the same time after the laser pulse, but with a different pressure of Ar. When the Ar pressure is high, both the reverse shock and bow shock can be made out clearly. At a lower pressure these shocks are harder to see, with the bow shock fainter than the reverse shock. The Astra data for 4 and 11 mb Xe, though in the form of interferometry rather than shadowgraphy, is consistent with these observations if the hat is identified as a reverse shock.

Examination of the Astra data for shots onto Cu cones in 50 mb He (figure 26) initially suggests that this interpretation may need to be modified. Figure 43b shows, in two colour schemes, the +4 ns image previously shown in figure 26. The first colour scheme is that used in figure 26. The second scheme was produced by raising the minimum electron density value for which pixels appear coloured in the image, lowering the maximum value and using a different look-up table for the false-colouring. In the second colour scheme, a hat-like feature in seen in front of the jet. The position of the off-axis part of the bow shock in the first colour scheme suggests that the outside edge of this hat corresponds to the bow shock driven by the jet. However, examination of figure 4 of [2] argues against interpreting the edge of the hat in the 4 mb Xe data, figure 43, as a bowshock. In that paper, the relative visibilities of jet and bow shocks in Ar and in He are different. Whereas in a low pressure of Ar the bow shock can appear fainter than the reverse shock, in a low pressure of He (their figure 9 (b)) the reverse shock can be the fainter.

The change of shape of the hat in figure 43a from an inverted-V shape at +3 ns to an inverted-Y shape at +10 ns could potentially be ascribed to uneven driving of the gas by the jet: the jet is strongest on the axis, and hence the central part of the hat runs ahead of the edges. Other factors may also play a part. The hat moves in the vicinity of the laser channel, within which the ionisation of the gas and the temperature peak on axis. Additionally, as the region driven by the axial flow is of finite width, and the driving is strongest on the axis, the radiative emission from shocked Xe gas, and shocked Cu from the jet, might be expected to be stronger nearer the axis. This could result in the gas ahead of the shock being heated fastest on the axis, furthering the inhomogeneity of the medium into which the hat advances.

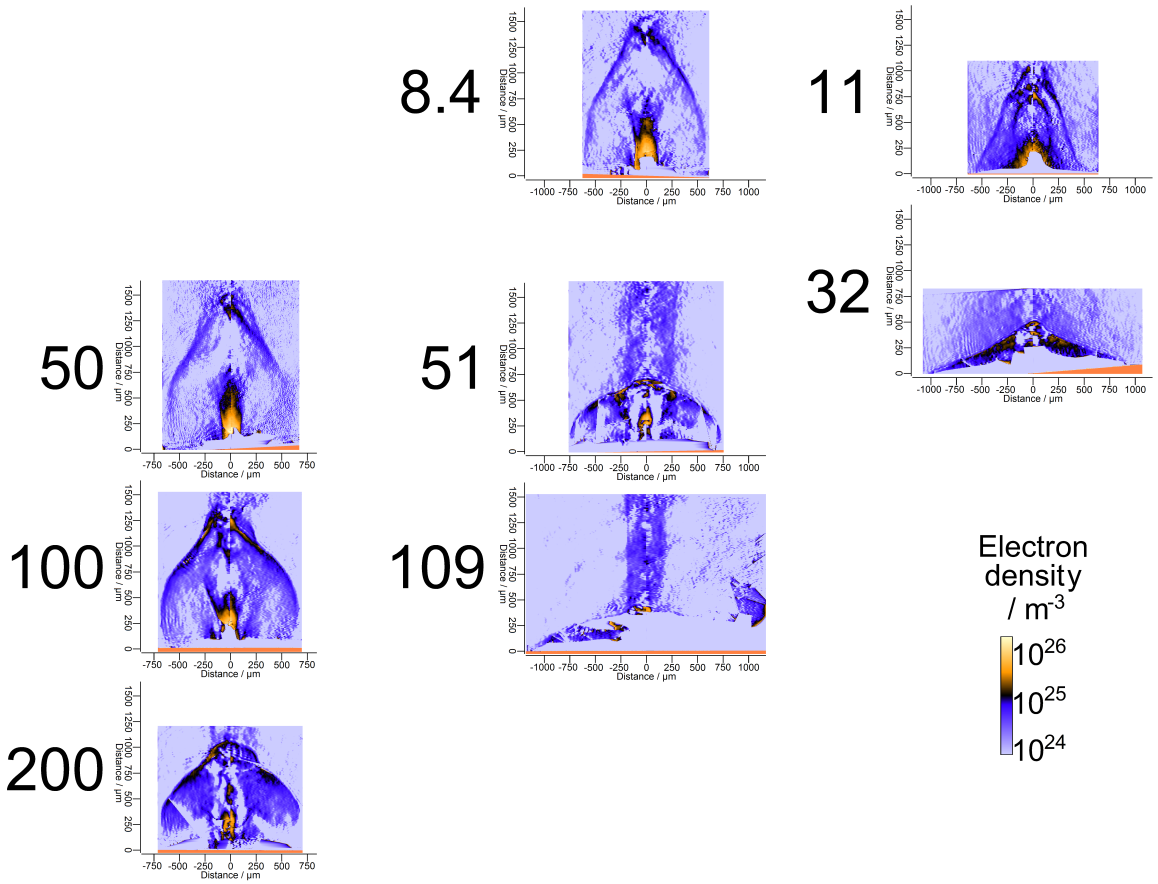

Figure 44: Comparison of shock shape and size at +10 ns as a function of gas pressure. Each image corresponds to a different combination of target, gas type and gas pressure. The target and gas types were: (a) Cu groove, He (b) Cu groove, N_2 (c) Cu cone, Xe. The numbers indicate the gas pressures in units of mb.

4.5.5 Shock radii in gases of different type and density

Figure 44 shows the dependence of bowshock shape on gas pressure at a time of +10 ns for three gases, He, N_2 and Xe. The images all correspond to shots onto Cu targets, with the He and N_2 images coming from shooting groove targets, and the Xe images from shooting cone targets. Even though the He and N_2 images are for groove targets, Abel-inversion has been performed in all cases using the axis of the shock as the axis for the Abel inversion. For the groove targets, the calculated values are reasonable estimates for the parts of the shocks far from the axis, but are not reliable near the axis; the central regions of the plots have not been masked in these cases as they still give a qualitative picture of the structures present.

In all three gases the axial size of the bowshock is seen to be smaller when the gas pressure is higher. This behaviour, corresponding to shocks propagating more slowly in higher density gases, is intuitively sensible. The behaviour in the radial direction is counter-intuitive. It might be expected that the diameters of the shocks would

behave in the same way as their axial extent, with diameters being smaller at higher gas pressures due to the shocks having a slower radial propagation speed. However, this is seen not to be the case. For both N_2 and Xe the shock diameter is seen to be significantly larger at a higher gas pressure. For He the diameters at pressures of 100 and 200 mb are similar, both being larger than the diameter at a pressure of 50 mb.

Re-plotting the data shown in figure 44 as a function of gas mass density rather than gas pressure is informative. As can be seen from figure 45 on the following page, the shocks in He and N_2 have a similar size and shape at an equivalent gas pressure. This result seems reasonable if the shocks in the He and N_2 are purely hydrodynamic phenomena, in which case it is only the density of the gas, a macroscopic property, and not the masses of individual particles, that is important. In the one case where a direct comparison can be made, the bow shock in Xe is not similar in either size or shape to the bow shocks in the He and N_2.

4.6 Summary

The high-repetition rate of the Astra laser system, and the long run-time of the experiment (6 weeks) meant that a considerable volume of data was gathered, with over 250 shots being taken in total. The data presented in this chapter, which comes from many but not all of these shots, is summarised in table 3.

Figure	Target		Gas		Image Times	Minor figures
	Geometry	Coatings	Type	Pressure / mb	/ ns	
22	Cone	CH, Cu, Cu-smoke, Au	-	-	1-5, 10, 20	18, 19, 21-25,32, 34
30	Cone	CH, Cu, Cu-smoke, Au	He	50	5, 10	25, 32-35
29	Flat	Al	N_2	50	4.6	-
38b	Groove	Al	He	50	1-5, 10, 20	39, 40
24	Flat	Cu	-	-	5, 10	20,24
26	Cone	Cu	He	50	2-5, 10, 20	25,27,2831, 43
38a	Groove	Cu	He	50	1-5, 10, 20	40
36	Cone / Flat	Cu	He	100	1-5, 10, 20	37, 41
43	Cone	Cu	Xe	4	3, 5, 10	-
42	Cone	Cu	Xe	11	3, 5, 10, 15, 20	-
44, 45	Cone / Groove	Cu	He, N_2, Xe	50-200, 8.4-110, 11-32	10	-

Table 3: A summary of the data from the Astra experiment presented in the results sections of this chapter. For the figures listed in column one, columns two to five list the target geometries and coatings, gas types and pressures, and times for which figures are shown. The "minor figures" listed in the seventh column contain subsets of the data within the figures listed in column one.

Two factors affecting jet collimation were looked at in the experiment. First, the target material was varied in an attempt to vary the importance of radiative emission for the

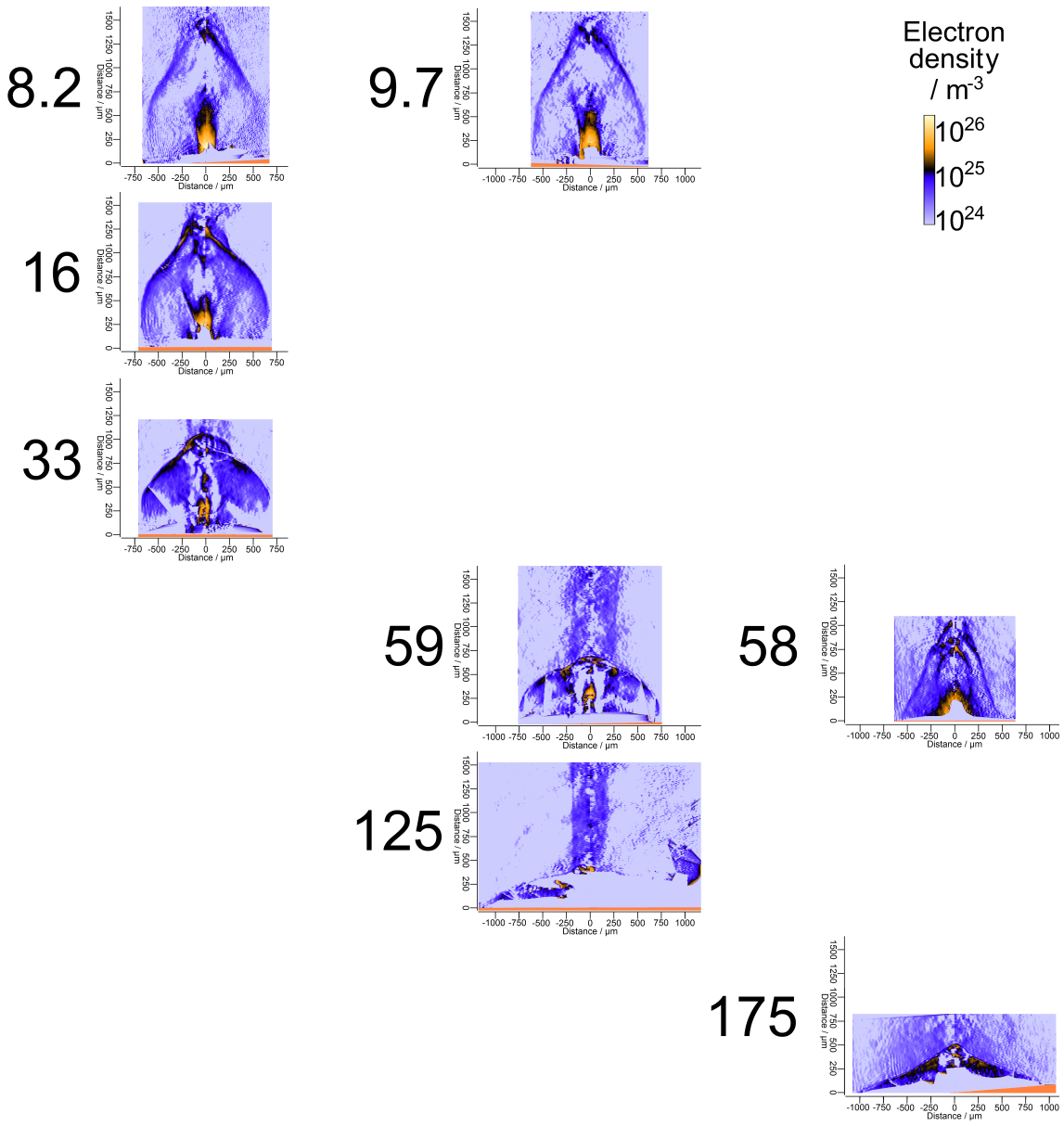

Figure 45: Comparison of shock shape and size at +10 ns as a function of gas density. Each image corresponds to a different combination of target, gas type and gas density. The target and gas types were: (a) Cu groove, He (b) Cu groove, N_2 (c) Cu cone, Xe. The numbers indicate the gas densities in units of 10^{-3} kg m^{-3}.

plasma dynamics. When using Au cone targets in a vacuum, at both +5 and +10 ns the flow near to the target was conical, with plasma from the cone converging towards the axis. By +5 ns a narrow jet was starting to emerge from the tip of the conical flow. At +10 ns this jet extended to over 800 from the target. At +20 ns the remnants of the convergence cone could still be seen but the narrow flow was not seen; however, the data in the +20 ns image was of low quality. The behaviour of the plasma from a Cu cone was markedly different. At +5 ns, a narrow flow was seen extending beyond the end of the convergence cone. However, by +10 ns there was no evidence of a narrow flow, with the plasma coming from the target being fully divergent and resembling that from a flat target. For CH, a narrow flow was not seen at +5 ns.

The results at +5 ns are consistent with higher atomic number, more radiative materials making narrower, longer lasting jets. This has been seen previously in experiments using both high-intensity lasers and Z-pinches (see sub-sections 3.3.1 and 3.3.2). In the axial convergence of a radiative plasma, at least early on, the density on the axis rises as a result of a positive feedback loop. The radiative emission is a non-linear function of the electron density and is strongest from the core of the jet, where the density is already high. This tends to promote pressure loss in the core, and the plasma collapses onto the axis under the pressure of the surrounding converging material [1]. Hence, one would expect narrower jets to form from more radiative plasmas. Outside a convergence region, radiative emission results in a loss of the pressure which drives radial expansion, and one would expect jets from more radiative plasmas to have a smaller angle of divergence.

The second factor affecting collimation studied in the experiment was the effect of an ambient medium. The combined effect of radiation and an ambient medium for jet collimation is expected to be greater than either of these in isolation [101], as the confining effect of the ambient medium keeps the density in the jet higher, enhancing the effect of the radiative cooling, which depends non-linearly on the electron density. When jets were created within a 50 mb He background, jets from targets made from a higher atomic number, and therefore more radiative, material were again seen to produce narrower axial flows. When making a direct comparison of the collimation of CH, Cu and Au jets produced in vacuum and in 50 mb He, no major improvement was seen at the early time of +5 ns. However, at +10 ns the widths of Cu and Au jets were smaller, consistent with the gas improving the collimation. The most interesting result was seen when comparing the images for Au at +10 ns: the flow protruding from the tip of the convergence region in the gas appears to be much narrower than that in a

vacuum. As only one shot was taken using an Au cone at this gas pressure and time, it is not possible to decide to what extent the improvement in the collimation is a result of the presence of the ambient medium, and to what extent the result of shot-to-shot variation.

While several studies have explored the variation between jets made from materials with a different atomic number in a vacuum (e.g. [1, 72]), and while studies have been done showing how the behaviour of a jet made from a specific material changes when the gas it propagates into is varied (e.g. [2]), few, if any, experimental studies have previously been published for work done using either lasers or Z-pinches which show how the collimation of supersonic jets propagating into ambient media varies as the atomic number of the plasma is changed. As far as the author is aware, the nearest experimental work to this which has been carried out is by a group from LULI, in which foams doped with varying percentages of a heavier element were used to make jets that propagated into a gas (see, for example, the paper [5] for an example of work by this group). An experimental demonstration of the non-linear combined effect on the collimation of a jet of radiative cooling and the presence of an ambient medium is a potential avenue for further research.

For jets in ambient media it is not only the collimation of the jet that is of interest but also the shock structures formed at the head of the jet where the ambient medium is being displaced. Astrophysical simulations predict the existence of a three-discontinuity "working surface" in such a case: the jet shock, where the material in the jet is decelerated, the bowshock ahead of this where the ambient medium is accelerated, and between the shocks the contact discontinuity, the surface where the shocked jet and ambient medium material meet. Such a structure has previously been seen in laboratory experiments by a group using the PALS laser, as discussed in section 3.3.1. In the Astra experiment, a working surface was seen when using 11 mb Xe, with the structure resembling closely simulations results published by the group using PALS, in particular those in figures 19 and 23 of [2].

The visibility of the parts of the working surface in the Astra data was seen to change with gas type and pressure. It is suggested that the data shows that the relative visibilities of the jet and bow shocks, particularly at lower gas pressures, were reversed when He was used instead of Ar. This is consistent with the data published by Nicolaï *et al.* in [2]. Whereas both the bow and jet shocks were clearly defined when using 11 mb of Xe, when using 100 mb of He the outer bow shock was easy to see but the jet shock

was hard to make out: faint arcs reaching back from the jet towards the target were seen which could correspond to this. When a lower Xe pressure of 4 mb was used, in addition to the axial flow the only feature that was seen was a hat-like structure on the axis which, it was hypothesised, corresponded to the jet shock. In contrast, when using a lower pressure of He, 50 mb, the bow shock was visible but there was no evidence of an independent jet shock.

The experimental observation of the effects of radiation on the formation and propagation of jets in a vacuum, and the experimental observation of working surface structures in the interaction of a jet with an ambient medium, are not in themselves new. However, previous laser experiments involving cylindrically-symmetric jets in which such observations have been made have all used much higher laser energies, extending upwards from 13 J (e.g. [67]) to over 1 kJ (e.g. [58]). The only experiments using a pulse energy similar to the 0.5 J used in the Astra experiment have involved the creation of two-dimensional jets from flat or grooved targets in a vacuum ([68, 69, 70]); these jets were observed to exhibit the same behaviour under change of target material as their three-dimensional, higher energy counterparts.

The significance of extending jet experiments to lower energies is three-fold. First, it shows experimentally that the same physical processes govern the behaviour of plasmas with overall energy contents differing by a greater number of orders of magnitude. This is true irrespective of whether the plasma within the jets is suitable for the scaling relations discussed in chapter 3 to be applied, either to scale between laboratory plasma experiments or to scale up from the laboratory to the astrophysical case. Second, the demonstration that useful jet experiments can be performed at lower energies is of research and educational value as it brings laboratory jet experiments within the reach of university-scale laser facilities. Third, the higher repetition rate of smaller lasers enables larger scans of parameter space than is possible with high-energy facilities.

In terms of quantitatively assessing the applicability of the scaling relations, it is necessary to estimate values for six dimensionless parameters, three of which are related to whether the plasma within the jets can be modelled using the equations of ideal hydrodynamics, while the other three are used to establish whether the laboratory jets are similar to their astrophysical counterparts (see 3.2). Analysis of experimental data for a Cu jet from a flat target in a vacuum, at a time of +5 ns, suggested a rough estimate for the Mach number of 3, where the estimate was made at about 250 μm from the target. Assessment of the other scaling parameters requires an estimate of

the ionisation of the plasma and a knowledge of how quantities such as velocity and ionisation vary within a jet. In the absence of experimental measurements of these parameters, further discussion of the scaling of the Astra experiment is deferred until section 5.4 of chapter 5, after numerical simulations of aspects of the experiment are presented.

As well as the results that were of direct astrophysical interest, the experiment produced other results that are of interest from an experimental perspective in their own right. In sufficiently high pressures of He, N_2 and Xe gases the channel ionised and heated by the laser on its way to the target could be made out in the interferometry data. For a shot into 52 mb of N_2 an electron density map was presented showing that the ionisation within the centre of the channel was still above 30% of its maximum value 4.6 ns after the end of the laser pulse.

With regard to the bowshocks ahead of jets in gas, two aspects have been discussed in detail. It was observed that the bowshocks from cone and groove targets were not simple arcs. In the case of Al groove targets, for which the plasmas showed considerable asymmetry due to the targets having been hit off-centre, the shock at early times was observed to have two features, one either side of target normal. The larger of these was produced as a result of hydrodynamic driving by the jet from the groove, while the smaller was driven by a secondary jet coming from a flat part of the target. In the case of Cu cone targets in 100 mb He, the bowshocks had a two-component structure at early times: to the sides, far from target normal, the shocks were approximately spherical, while on the axis the shock had a "nosecone" shape. For both these Al groove and Cu cone targets, at times of +10 ns or later the shock was seen to have an additional, axial component. By reference to [71] it was discussed how both the X-ray emission from the target and the ionisation of the gas by the laser contribute anisotropy to the ambient medium, and it was speculated that the additional component of the shocks could be the result of the shocks slowing down less in passing up the ionised, heated laser channel than in passing through the rest of the gas. It was suggested that in future experiments the addition of a second probe line orthogonal to the first could be used to help resolve this question: as the projection of the laser entry cone in this system would lie at 8° to target normal, if the shock feature is associated with the laser channel, it would be expected to lie at a similar angle to the normal.

The second aspect of the bowshocks to be discussed was their overall size in both the axial and radial directions. At +10 ns, it was found that the diameters of shocks in

denser gases was larger. This is a counter-intuitive result as one would expect shocks in higher density environments to be smaller in diameter due to their slower propagation speed. The correct explanation of this observation is not known to the author.

5 Simulations

In chapter 4, two experiments to create plasma jets have been outlined. In the first of these, the Astra experiment, the majority of the data was obtained using optical interferometry. While this has been used to provide information on the electron density distribution within the jets, it does not provide information on other plasma properties of interest such as the mass density and the electron and ion temperatures. This gives a motivation for attempting to simulate the Astra experiment numerically: the output from a simulation can give information on all these properties of a plasma simultaneously.

In order to produce a simulation that can be completed in a reasonable amount of time, say a week at most, with the computing resources currently available, simplifying assumptions are made in the construction of numerical codes. These assumptions, and the numerical algorithms used in the codes, limit both their accuracy and the range of experiments which each code can model. This means that in practice experiments and simulations are complementary, rather than simulations simply replacing experiments.

In this chapter, simulations of aspects of the Astra experiment using the radiation-hydrodynamics codes HYADES [3] and h2d [3] are presented. HYADES is used for simulations in one dimension, while h2d is used to simulate cylindrically-symmetric situations; even though objects with cylindrical symmetry occupy a volume of three-dimensional space, h2d can still be classed as a two-dimensional code as only two position coordinates, radial and axial, are used.

Simulations of experiments such as the Astra experiment are not straightforward. A full simulation of the experiment has to model the effects of the laser on the solid target, and later in time its interaction with the plasma ablated from the surface. It also has to model the propagation of a shock wave into the target, the hydrodynamic flow of plasma away from the target, and the interaction of this plasma with the surrounding ambient medium, including modelling any shock structures generated. The time and length scales of these processes differ by several orders of magnitude. For example, the Astra pulse was only 2 ps long, so to resolve the laser-target interaction requires modelling processes occurring on a timescale of picoseconds or shorter. The hydrodynamic flow, on the other hand, evolved on a timescale of 100 ps, and was observed with interferometry as late as +20 ns. Also, whereas the widths of shock fronts in the gas were much less than 20 μm, at +20 ns the hydrodynamic flow extended to a distance of about 2 millimetres from the target. Differences such as these make

it difficult to create a simulation that has sufficient spatial and temporal resolution to resolve those processes with small time and length scales, yet which runs sufficiently quickly to model behaviour on larger scales.

The modelling of radiation transport, even in the absence of hydrodynamics, is very demanding. Radiative emission and absorption within a plasma occurs via several different processes (free-free, bound-free, etc.), each of which has a different dependence on the local composition of the plasma, the ionisation and excitation state(s) present and their populations, and the density and temperature. Also, not only does each part of a plasma emit radiation in all directions, and over a wide range of wavelengths, but radiation transport is non-local: radiation emitted at one location can potentially travel some distance before being re-absorbed.

Another difficulty arises in including both a solid target and a low-density gas in a simulation simultaneously. The densities of these media, of order 1 g cm^{-3} [13] and 10^{-5} g cm^{-3} respectively, differ by a factor of 10^5. This can prove problematic for obtaining stable hydrodynamic calculations when modelling the interaction between a flow of material ablated from a target and a gas. In the HYADES and h2d codes used for the simulations in this chapter, the materials being simulated are split into regions, each of which is sub-divided into a mesh of smaller zones. If one attempts to model the interface between a solid target and a gas, then, in order for the adjacent solid and gas zones at the interface to have approximately the same mass, which is desirable for hydrodynamic calculations to be stable [106], their volumes would have to differ by a factor of about 10^5. This means that even if the spatial resolution of the mesh in the solid is high, the resolution in the gas is very poor. As a consequence of this, in this chapter results are presented for simulations of the laser ablation of a solid target in a vacuum, but no results are presented showing the ablation of a solid target in an ambient medium.

The structure of this chapter is as follows. In section 5.1 the numerical codes HYADES and h2d are introduced and their use is discussed. There then follow two sections for simulation results, first section 5.2 for those obtained using HYADES and then section 5.3 for those obtained using h2d. After this, in section 5.4, the possibility of scaling between some of the jets created in the laboratory and YSO jets is analysed by using a combination of experimental and HYADES values for the plasma properties to make numerical estimates of the scaling parameters discussed in chapter 3. Finally, in section

[13] 1 g cm^{-3} = 1000 kg m^{-3}

5.5 there is a summary and discussion of the results presented in the chapter.

5.1 Description of HYADES and h2d and their use

Using HYADES or h2d is essentially a three step process. First, an input file is written defining the problem to be simulated. Second, the code is run using the input file. Third, the results produced by the code are post-processed, either immediately being displayed graphically or used as input data for other programs. In this section, each of these steps will be examined in turn. First, the creation of input files is described. This is followed by a sub-section discussing difficulties encountered in running h2d and limitations of 2-D, Lagrangian radiation-hydrodynamics codes for simulating experiments like the Astra experiment. Last, there is a sub-section commenting briefly on the post-processing of the simulation results that has been carried out in order to present them in the form shown in this chapter.

5.1.1 Input file creation

The simulations discussed in this thesis are all simulations of the interaction of a laser with a target and the subsequent evolution of the system. A separate input file had to be written for each simulation. It had to contain information on the initial conditions of the target, a specification of the laser pulse parameters, and code control statements (for example, the desired simulation length). Also required were statements specifying the physical processes to be included within the simulation, the numerical models to be used to model these processes, and the values of some of the numerical constants within these models. While HYADES and h2d input files are very similar, for simplicity they will be discussed separately. The creation of a HYADES input file will be discussed first, and the creation of an h2d input file second.

5.1.1.1 HYADES input files

In HYADES the target is split into a mesh of zones. As the code is one-dimensional, all that has to be specified in the input file is the positions of the mesh points, which lie along a straight line. Having defined the mesh, statements are used to split the mesh into regions and then to specify the material within each region and its initial density and electron, ion and radiation temperatures. In the simulation results presented in this thesis, targets always started in thermodynamic equilibrium at room temperature, which was taken to be 2.5 x 10^{-5} keV (= 290 K). Next, the equation of state and the

model used to calculate the ionisation in each region are specified. In all the simulations carried out tabulated SESAME equations of state [107] were used. SESAME tables give tabulated values of the specific[14] pressure and energy of a material as functions of density and temperature ([23], chapter 3, p.94). It was found when performing one-dimensional simulations containing Au targets that the choice of ionisation model strongly affected the length of time a simulation took to run. Using the Thomas-Fermi ionisation model simulations could be completed within a reasonable amount of time, while use of the "average-atom, local thermodynamic equilibrium" model took prohibitively long. As a result, the Thomas-Fermi ionisation model (see [23], chapter 3, pp. 91-93 for details) was used in all of the simulations for which results are presented.

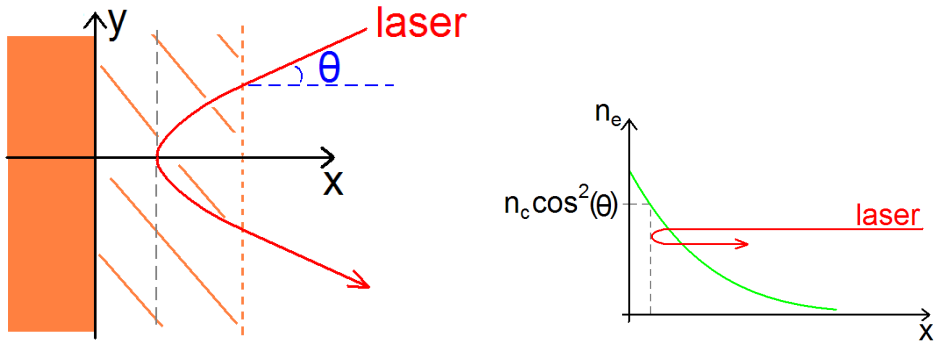

Figure 46: Cartoons to illustrate the ray-trace laser-target interaction model used in HYADES. Laser rays propagate through the sub-critical electron density plasma in front of a target until they reach a surface of electron density $n_c \cos^2(\theta)$, where n_c is the critical electron density and θ the angle of incidence. Energy absorption from the rays is calculated as they propagate.

Within HYADES there are two ways of modelling the interaction between a laser and a planar target. In both cases, the laser wavelength and the variation in intensity with time have to be specified. Additionally, as the angle at which a laser beam strikes a planar target significantly affects both the absorption of energy from the beam and the maximum electron density up to which the beam can penetrate, both of the laser interaction models allow the angle that the incident beam makes with target normal to be specified; even though the code is one-dimensional, the plasma produced by a beam obliquely incident on a planar target can be modelled. The difference between the laser models is as follows. The first interaction model traces rays as they propagate through sub-critical electron density plasma up to the point of reflection, reflect and travel back out of the plasma. This is illustrated in the cartoon in figure 46. This figure, with a different caption, has previously been shown in the discussion of probe beam

[14]"specific" in this context means "per unit density" ([23])

refraction in section 4.3.2 of chapter 4. The energy the plasma gains from the rays via inverse Bremsstahlung absorption is calculated during the ray-tracing. In the second interaction model the Helmholtz wave equation is solved in the interaction region (see, for example, [109]). The second model is important for modelling the interaction of short-pulselength, high-intensity laser pulses with solid targets. In such a situation the laser-target interaction finishes before a sizable region of sub-critical electron density plasma has had time to form in front of the target.

Mourou and Umstadter [108] estimate that a lack of sub-critical electron density plasma needs to be considered for a laser pulselength of a few hundred femtoseconds. At 2 ps, the pulselengths used in the Astra experiment are not too much greater than this. However, in the experiment the contrast of the pulse was poor: the main part of the pulse was preceded by a lower-intensity pre-pulse which would have created a sub-critical electron density plasma in front of the target before the arrival of the main part of the pulse. In the HYADES simulations, only the main part of the pulse was modelled. Simulations were run using both of the laser interaction models, hereafter referred to as the ray-trace and Helmholtz models, and the results are compared in section 5.2.

Within the simulations, radiation transport was modelled using multi-group diffusion, with radiation divided into 40 energy groups up to a maximum photon energy of 20 keV. Electron thermal conduction was flux-limited to 0.06 of the free-streaming flux.

5.1.1.2 h2d input files

The structure of an h2d input file is very similar to those for HYADES. First, a mesh is defined. When using h2d a two-dimensional mesh of quadrilaterals has to be described, and this is done by specifying the initial positions of the corners of the zones in the input file. Once the mesh has been defined, it is then divided into regions. For each of these, the material and its initial density and electron, ion and radiation temperatures are then specified, along with the equation of state and ionisation model to be used. This is done exactly as in HYADES, and just as with HYADES the simulations presented in this chapter used initial target temperatures of 2.5 x 10^{-5} keV and the Thomas-Fermi ionisation model.

When using h2d, the laser pulse is modelled as a set of rays, each of which had its path ray-traced during the simulation. In modelling the Astra experiment, a single, converging cone of rays was used, with the intensity either uniform across the cone or

decreasing towards the edges. When the intensity was uniform, a single statement was required in the input file listing the half-angle of the cone, the number of laser rays, and the position of the tip of the cone. When the intensity was lower at the edges of the beam, a separate statement was required for each ray giving a position on its path, its direction of motion, and its intensity relative to the pulse as a whole. The maximum number of laser rays one can choose is limited to 500. This ends up imposing a restriction on the mesh for the following reason. In order for the interaction of the laser with the target to be modelled properly, the number of rays striking each zone at the front of the target needs to be relatively large, about 10. If the zones at the front of the target are of too small a size in the radial direction, few rays strike each zone. As adjacent zones are struck by different numbers of rays, this has the result that, in regions where target illumination should be uniform, adjacent zones receive significantly different amounts of laser energy - if adjacent zones each only receive a few rays, the arrival of a single additional ray represents a large fractional difference in laser intensity received. The limit on the number of rays effectively limits the maximum number of zones in the radial direction to 40-50 within the radius of the laser beam.

The radiation transport modelling and the electron flux limiting were the same as those for the HYADES simulations.

5.1.2 Difficulties encountered in using h2d and limitations of 2-D, Lagrangian simulations for simulating experiments such as the Astra experiment

HYADES and h2d are both Lagrangian radiation-hydrodynamics codes. The term "radiation-hydrodynamics" implies that radiation transport is included in a simulation and that all plasma material is treated within the fluid approximation (see section 3.1.3 of chapter 3). "Lagrangian" is a term used to describe the behaviour of the mesh when plasma moves. In an Eulerian simulation, the mesh remains fixed in place and the plasma flows through it. Consequently, the material and the amount of mass within any zone of the mesh can change with time. In a Lagrangian simulation, the mesh moves with the plasma and both the composition and mass within each zone is therefore fixed. This approach has definite advantages, such as the automatic conservation of mass density and the automatic maintenance of the boundaries between regions of different materials. However, for the kind of hydrodynamics simulations being performed in this thesis there are also two big disadvantages.

The first problem, bow-tying, is an issue for a 2-D code such as h2d, but not for a 1-D code such as HYADES. In a 2-D simulation the mesh, moving as it does with the plasma, becomes increasingly distorted with time. The code is able to handle this distortion until a bow-tying event occurs. A bow-tying event is where one of the quadrilateral zones of the mesh either becomes triangular or bow-tie shaped. When such an event occurs, the code stops and it requires the user to re-assign the mesh points in the region where the bow-tying event has occur ed in order that the bow-tying is removed. The user can then generate a restart file and restart the code. The requirement for a user to untangle the mesh, an occurrence which can happen regularly when running a hydrodynamics problem for a long time (several nanoseconds), is a significant drawback, as it means that the time available for code execution is reduced and the time of the user taken up. The current version of h2d does contain a basic automatic rezoning tool which users can instruct to automatically re-zone areas of a mesh prone to bow-tying in an attempt to prevent some of the bow-tying events. For the solid target simulations discussed in section 5.3, the auto-rezoner has been found to be capable of preventing bow-tying events on the axis early in the simulation. However, less success has been found in preventing bow-tying in other parts of the mesh.

The second problem in using a Lagrangian approach is resolution. At the start of the simulation of the laser-ablation of a solid target, a mesh is defined with adjacent zones containing approximately the same mass and having approximately the same size. When a laser strikes the surface of the target, the zones start to move. The plasma at the head of the expansion is low density and fast moving, with the plasma following behind being denser and slower. As the mesh points move with the flow in a Lagrangian code, the mass within each zone remains constant as the flow progresses: at the head of the ablating plasma, where the flow has a low density, the zones are very large and the spatial resolution of the hydrodynamics is poor. It will be seen in the results presented later in this chapter that this proves very limiting when trying to model an experiment such as the Astra experiment, for which the experimental data consists of interferograms of the plasma in the "far from the target" region.

Another of the limitations of using hydrodynamics codes to model plasmas is found in modelling the initial interaction between two colliding plasmas. Within each of the plasmas the fluid approximation may be comfortably satisfied: the timescales for collisions between particles may be much shorter than the timescale for their hydrodynamic evolution, and the mean free paths for collisions between ions may be much shorter than the lengthscales over which the plasma changes significantly. In such

a case, treatment of either of the plasmas on its own as a fluid would be perfectly satisfactory. However, when two fluid plasmas approach each other very quickly, the mean free paths for collisions between ions from opposing plasmas can be much larger than the lengthscales in the individual plasmas. The result of this is that the plasmas interpenetrate rather than collide. The fluid approximation is not satisfied in such an interaction, and the use of a hydrodynamics code is consequently not a valid way of modelling it.

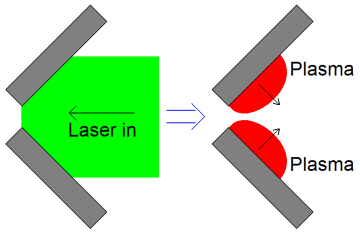

Figure 47: Cartoon illustrating the interaction between plasmas from a pair of planes in an experiment by Wan *et al.* [109]. Two plane foils, shown end-on in grey in the image, were illuminated simultaneously using a single, wide laser pulse, indicated in green. This resulted in the generation of a pair of plasmas, indicated in red, on the front sides of the foils. These plasmas propagated into the gap between the foils, where they could interact.

An example of this behaviour is reported by Wan *et al.* [109]. Figure 47 shows a cartoon of their experiment. The surfaces of a pair of planar foils, shown end-on in the figure in grey, were illuminated using a single, wide laser pulse indicated in green. This resulted in the creation of ablation plasmas on the front surfaces of the foils, indicated in red. These plasmas moved into the gap between the foils, where they could interact. Wan *et al.* explain the interaction as follows. When the plasmas initially meet, the flows interpenetrate. Later in time, stagnation of the flows on the axis occurs, leading to an increase in density and temperature on the axis. This leads to shocks propagating away from the axis into the incoming flows and the appearance of a pair of off-axis density peaks instead of a single on-axis peak. Wan *et al.* discuss how single-fluid codes do not capture the initial interpenetrative nature of the plasma collision, instead predicting that stagnation should occur as soon as the colliding plasmas first meet: this has the result that the shocks that lead to the off-axis density peaks, and the peaks themselves, are produced earlier than seen in the experiment.

In the Astra experiment, jets were created via the on-axis convergence of plasmas generated by the laser-ablation of conical and grooved targets. As has already been stated, the plasma at the head of laser-ablation plumes is fast moving and low density, with slower, denser plasma following behind. Early on in the jet formation process

one might therefore expect a degree of interpenetration in the on-axis convergence as low density plasma volumes arriving at the axis from opposite sides will have a high relative radial velocity. Only later in time, as slower, denser plasma arrives at the axis would the interaction become fully collisional. The significance of interpenetration is analysed for Al, Cu and Au cone targets in sub-section 5.3.1 using the results of HYADES simulations.

It has previously been stated that the h2d code is written to simulate situations with cylindrical symmetry. A consequence of the assumption of perfect symmetry in a radiation-hydrodynamics code is that the predicted on-axis behaviour can be more extreme than is encountered experimentally, where symmetry is imperfect. There are two related effects that contribute to this. In an experiment the lack of perfect symmetry in the convergence of a fluid onto an axis has the result that fluid gets squeezed out sideways in the directions from which the incoming flow is weakest. This results in the density on the axis being lower than would be seen in the case of perfect symmetry, where squeezing out is impossible. The second effect occurs in plasmas for which radiative emission is important. The strength of the radiative emission depends on local values of density and temperature. In the case of perfect symmetry, over-estimation of on-axis density and temperature leads to over-estimation of the radiative emission. This then results in an over-estimate of the pressure reduction in the axial region, and can lead to the on-axis density rising even further as the plasma flows to equilibrate the pressure.

In addition to what has already been said in this sub-section about difficulties with two-dimensional simulations, it needs to be stated here that there is a known bug in the h2d code relating to the transport of mesh points lying on the axis of the simulation. The result of this is that values of plasma parameters on or close to the axis are incorrect. This can be clearly seen in the simulation results in section 5.3 and it is pointed out there.

5.1.3 Simulation results post-processing

After running a simulation, the results were plotted using the programs hyadplot (for HYADES) and h2dplot (for h2d). The h2d output was also post-processed into sets of simple text files using the program h2dpost. The hyadplot, h2dplot and h2dpost software was supplied with the HYADES and h2d codes. The HYADES output files and the sets of text files from the h2d simulations were subsequently used as inputs

to Matlab programs written by the author. Matlab was useful for two reasons. First, it has an extensive range of graphical tools for plotting data; the programs hyadplot and h2dplot are useful for getting a first look at simulation results, but have limited flexibility. Second, Matlab could be used to manipulate the data produced by HYADES and h2d in order to generate plots of additional plasma properties such as the internal Mach number. Many of the plots of HYADES results within this chapter, and all of the plots of h2d results, were generated using Matlab. Most of the h2d results are plotted as contour plots: they were generated by re-gridding the raw h2d data onto a regular, rectangular mesh using linear interpolation and then using Matlab's standard contour plotting routine.

5.2 1-D simulations using HYADES

5.2.1 Motivation - what are 1-D simulations useful for?

To fully simulate the creation of jets from the conical targets used in the Astra experiment requires either a fully three-dimensional simulation or a two-dimensional simulation with cylindrical symmetry. The use of a 1-D code such as HYADES is limited. However, 1-D simulations are important for confirming the accuracy of more complicated 2-D or 3-D simulations and, where they can be used, they can be preferable to their 2-D or 3-D counterparts as they are typically much quicker to perform.

One situation in which 1-D simulations can be useful is in modelling the effects of a laser pulse on a flat target in the case that the intensity of the laser pulse is uniform across the beam. The laser-target interaction creates a plume of plasma which ablates from the target surface. Within the centre of the plume, and close to the target, the plasma is uniform and moves perpendicular to the surface: it behaves in a 1-D manner, and hence can be modelled with a 1-D simulation. Only when sufficient time has passed for information about the vacuum at the edge of the plume to propagate from the edge of the plasma into the centre does the plasma at the centre of the plume cease to behave in 1-D. This propagation of information happens at the sound speed.

For a laser pulse illuminating a conical target, the situation is more complicated than in the flat target case. Near the apex of the cone, the 2-D nature of the problem cannot be neglected; cylindrical convergence of plasma onto the axis cannot be approximated as 1-D. However, further out from the axis, the plasma near the target can be modelled in 1-D, though only over distances from the surface that are small compared with the

surface's radius of curvature.

The 1-D simulations discussed in this thesis are used in two ways. First, they are used for learning about the ablation of material from the surface of a target, providing information on how far from the original target surface the interface between the coating layer and the substrate would have moved during the Astra experiment. This is useful for assessing whether the plasmas seen in the interferometry data from this experiment were composed solely of coating layer material, or whether substrate material would also have been present. The second use of 1-D simulations occurs later in this chapter in sub-section 5.3.3, where 1-D simulation results are compared with the results of 2-D simulations of flat targets. This comparison is useful as where results obtained using different codes are seen to be in agreement one is more confident in the reliability of the simulations.

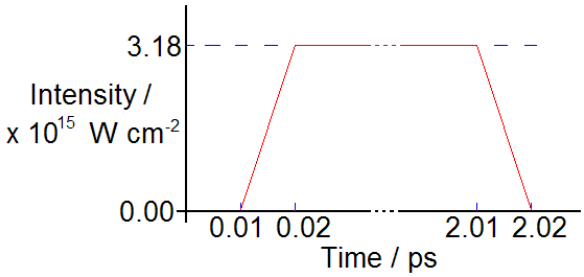

Figure 48: Astra pulseshape

5.2.2 Simulation initialisation

The simulations in this section used two different models for the target. In the first, the target was modelled as a 50 μm thick, homogeneous slab of either Cu or Au. In the second, the target was modelled as a 50 μm slab of Cu with a 1 μm coating of Cu or Au on the surface; this latter model more accurately represents the targets used in the Astra experiment. In both cases the simulations were done in planar geometry with the mesh in the 50 μm region "feathered" such that the zones at the front of the target were smaller than those further back. This was useful for obtaining a high spatial resolution in the region near where the laser-target interaction occurred and in the plume of ablated plasma without using an unnecessarily large number of mesh points. The mesh in the coating layer was not feathered, and the rear surface of the mesh was not kept fixed.

The Astra laser pulse was modelled as a top-hat function in time with a peak intensity of 3.18 x 10^{15}W cm^{-2}. This value comes from assuming that a pulse energy of 0.5 J was distributed evenly in time over the pulse length of 2 ps, and evenly in space throughout a 100 μm diameter focal spot. The pulseshape is shown in figure 48. As mentioned in

section 5.1, there are two models for the laser-target interaction in HYADES, referred to in this thesis as the ray-trace and Helmholtz models. Both of these were used, and a comparison of the results is presented in the next sub-section. In the Astra experiment, the laser arrived at the target along a line 8° from target normal. It was found that when this angle was included in simulations (instead of assuming a normally incident beam) the change in the results was insignificant; this was found to be true for both laser-target interaction models.

When using the ray-trace model, the default absorption of laser energy occurs via Fresnel absorption where the laser interacts directly with a region of above-critical electron density. Such a scenario occurs in the simulation of the laser-ablation of a solid target, where at early times the laser interacts directly with solid density material [106]. Where a laser interacts with ablation plasma below the critical electron density, the default absorption mechanism is linear inverse Bremsstrahlung [106]. Simulations were carried out including models of three additional processes, specifically resonance absorption, non-linear inverse Bremsstrahlung absorption and ponderomotive effects. The mass density and electron temperature results at +5 ns with and without the additional processes were compared and the difference was negligible, showing that these processes were not important for these simulations.

The simulations were typically run for 5 ns. The maximum time step was limited to 5 fs during the laser pulse in order that the interaction between the laser and the target was well resolved. After the end of the laser pulse, the size of the time step was limited to 1 ps. The results presented in the rest of this section are divided into three sub-sections. In the first, sub-section 5.2.3, the simulation of a homogeneous Cu target is outlined. The effects of changing the mesh and changing the model used for the laser-target interaction are discussed. In the second sub-section, results for homogeneous Cu and Au targets are compared. Finally, in sub-section 5.2.5 results for coated targets are presented and comparisons are made with experimental data.

5.2.3 Effects of changes in the mesh and choice of laser-target interaction model on homogeneous Cu target results

Figure 49 on the following page shows results which were obtained when simulating the laser-ablation of a homogeneous Cu block using the Ray-trace model of the laser-target interaction. The two plots in the figure show the spatial variation of the mass density and the electron temperature at +1 ns. At the start of the simulation the Cu block

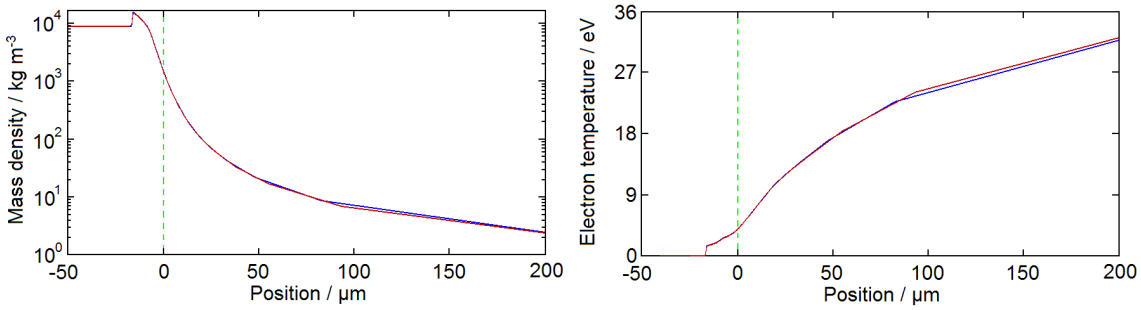

(a) (b)

Figure 49: Results for simulation of a Cu target at +1 ns using meshes containing 124 mesh points (red lines) and 247 mesh points (blue lines). The dashed green line indicates the position of the front of the target at the start of the simulation. The quantities plotted are (a) mass density (b) electron temperature.

lay within the region -50 µm to 0 µm. The laser pulse came in from the right hand side and struck the front face of the target, generating a plasma that moved away from the target from left to right. In addition, the incidence of the laser pulse generated a shock wave that propagated from right to left through the target: it is this that is responsible for the spike in mass density at about -17 µm. For convenience, the same target orientation is used in all of the remaining HYADES plots in this chapter. In these plots, a dashed green vertical line will be used to indicate the initial position of the front of the target.

There are two lines, one red and one blue, in each of the plots in figure 49, corresponding to simulations done with meshes containing 124 and 247 points. The feathering factor (the ratio of the size of adjacent zones at the start of the simulation) was different in the two cases. For the 124 point simulation this factor was 1/1.03, while for the 247 point simulation it was 1/1.01. The reason for using a different feathering factor was to control the sizes of the zones at the fronts of the targets. This was roughly the same in the two simulations, being 41 nm and 47 nm for the 124 and 247 point meshes.

It can be seen that the red and blue lines overlap up to about 85 µm from the original target position. Beyond this point the curves become straight, slightly separated lines as the spatial resolution in this region is very poor: there are few mesh points beyond 85 µm and so the fact that the results for each mesh point are joined by straight lines becomes apparent. The near-perfect overlap below +85 µm when doubling the number of points in the mesh implies that the spatial resolution of the mesh was sufficiently high to resolve the details of the plasma ablation. However, it does not give information on whether the spatial resolution of the laser-target interaction at the front of the target was adequate as the zones in this region were roughly the same size in both simulations.

To investigate this, the results for 247 point meshes with feathering factors of 1/1.01 and 1/1.013 were compared. For these meshes, the sizes of the zones at the fronts of the targets differed by nearly a factor of 2, being 47 and 28 nm respectively. It was found that there was no significant difference in the results within 100 μm of the target at +5 ns, indicating that the spatial resolution of the mesh in the region near where the laser-target interaction occurred was high enough not to affect the result in this region.

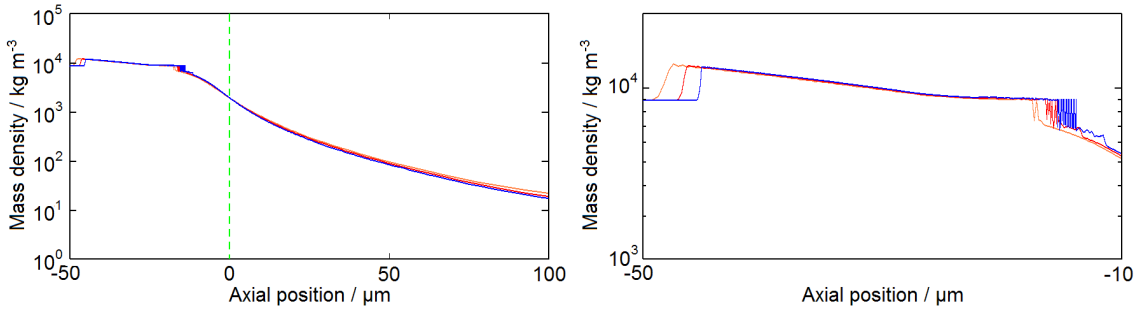

(a) (b)

Figure 50: Results for a 50 μm Cu target calculated using the Helmholtz laser-target interaction model. (a) shows the mass density at +5 ns for three different meshes, while (b) shows a close-up of the ablation front and the shock in figure (a). The orange, red and blue lines correspond to meshes with 247, 493 and 985 mesh points, with feather factors of 1/1.01, 1/1.005 and 1/1.0025 and zone sizes at the front of the target of 47, 24 and 12 nm.

Simulations were also carried out using the Helmholtz laser-target interaction model (see section 5.1 for a discussion of the difference between these models). As with the ray-trace model, the number of zones in the mesh and the feathering factor were altered in order to determine the stability of the results with respect to changes in the mesh. It was found that if the number of zones in the simulation was doubled from 246 to 492, with the feather factor adjusted so that the size of the zones at the front of the target was kept roughly constant, the change in the results was negligible. A greater difference was seen when the size of the zones at the front of the target was allowed to vary. This can be seen in the images in figure 50, which shows the mass density results at +5 ns for three different meshes. The orange, red and blue lines correspond to meshes with 247, 493 and 985 mesh points. They had feather factors of 1/1.01, 1/1.005 and 1/1.0025, respectively, giving zone sizes at the front of the target of 47, 24 and 12 nm. Figure 50a shows that as the front zone size is reduced simulations predict that at +5 ns the shock has propagated less far into the target and the mass densities in the plume in front of the target are lower.

Figure 50b shows a close up of the part of figure 50a which shows the behaviour within

the target. On the extreme left of this image, near -50 μm, the mass density curves are flat; the shock, which propagates from right to left, has not yet reached this region. Slightly further to the right is the shock front, where the mass density rises above its value in the unshocked material. For the higher resolution simulations the shock front is steeper, better resembling a discontinuity. On the right hand side of the image is the ablation front where material leaves the target and enters the plume. As the size of the zones at the front of the target is reduced (orange to red to blue), it can be seen that the ablation front appears structured. The change in the position of the shock and ablation fronts in halving the front zone size from 47 nm to 24 nm (orange to blue) is roughly the same as that found when halving again from 24 nm to 12 nm (blue to red). This is an unwanted result, as one would hope that the positions of the shock and ablation fronts would converge as the front zone size is reduced.

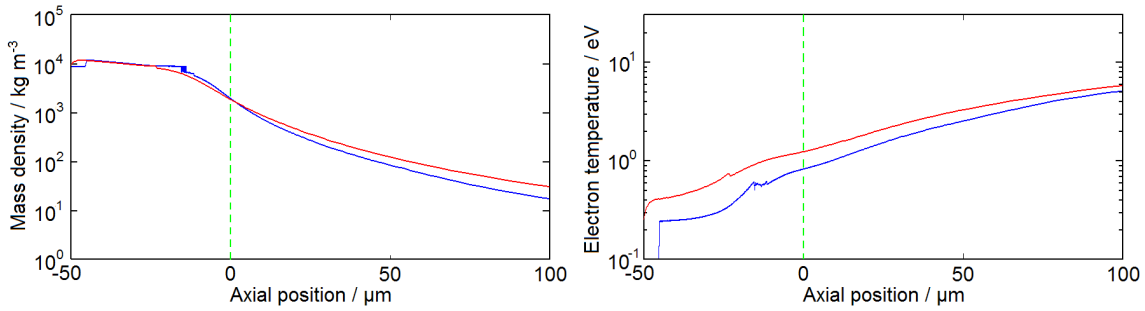

(a) (b)

Figure 51: Comparison of (a) mass density and (b) electron temperature results at +5 ns for simulations of the ablation of a 50 μm Cu block using the ray-trace (red) and Helmholtz (blue) laser-target interaction models.

While the behaviour inside a target is interesting, the behaviour in the plume is more directly relevant to the Astra experiment. As with the positions of the shock and ablation fronts, it was found that the behaviour in the plume did not converge. Figure 51 shows a comparison of the results obtained using the ray-trace (in red) and Helmholtz (in blue) models for a 50 μm Cu target at +5 ns. The ray-trace curve corresponds to a simulation using a 247 point mesh with a feathering factor of 1/1.01, while the Helmholtz curve corresponds to a 985 point mesh with feathering factor 1/1.0025. As before, the initial target position is indicated in green and the laser entered from the right hand side. The results are similar, but by no means identical. As the results of the Helmholtz model have been found not to converge, only results obtained using the ray-trace model will be presented from here on.

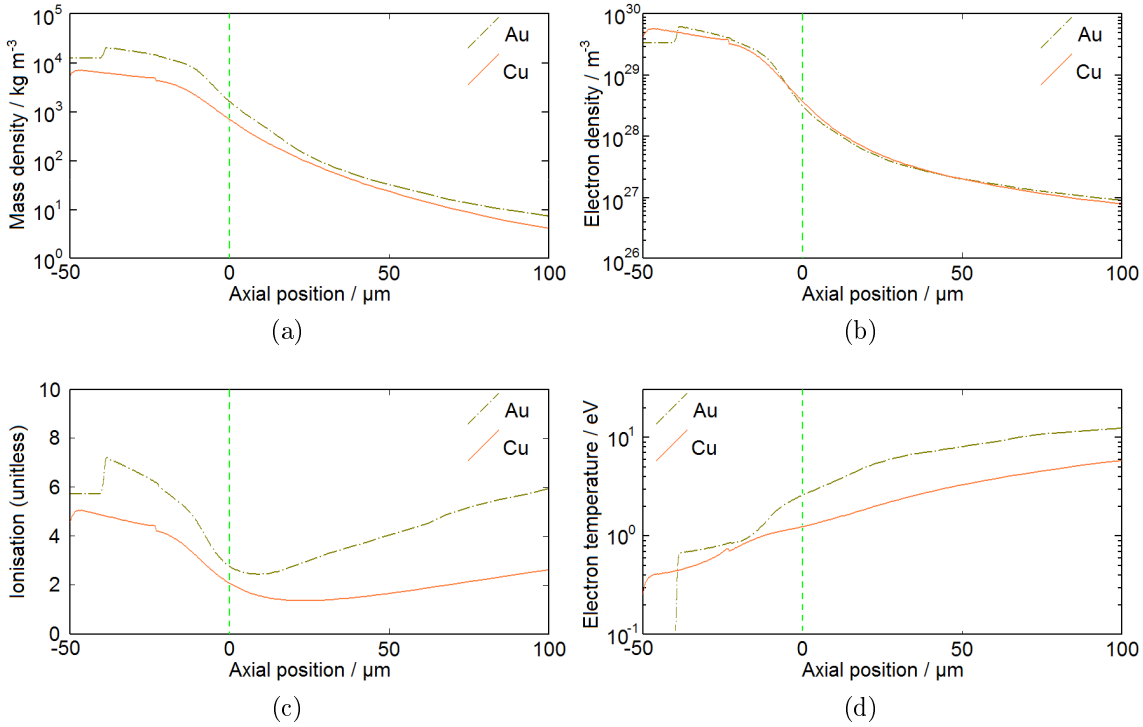

Figure 52: HYADES simulation results for homogeneous, 50 μm Cu and Au targets at +5 ns obtained using the ray-trace laser-target interaction model. The laser approached the target from the right hand side and the original position of the target front surface is indicated with a dashed green line. (a) Mass density (b) Electron density (c) Mean ionisation (d) Electron temperature.

5.2.4 Results for homogeneous Cu and Au targets

The analysis for a Cu target shown in the previous sub-section was also carried out for an Au target, both of these being materials used in the Astra experiment. Figure 52 shows plots of the mass and electron densities, the mean ionisation and the electron temperature at a time of +5 ns. In each plot the Cu results are plotted using solid orange lines, the Au results using a dot-dash olive line, and the initial position of the front of the target is indicated with a dashed green vertical line.

It can be seen from figure 52a that the shock in the Cu target has travelled all the way through the 50 μm block, while the shock in the Au target has only penetrated about 40 μm. Between -50 and -40 μm the properties of the Au are those of solid, unshocked Au. The electron density and the ionisation in this region take a non-zero value due to the way HYADES assigns a non-zero ionisation to the material in the target at the start of the simulation.

Figure 52a shows that the mass density in the Au plume is higher than that in the Cu plume. However, for the Au the ion number density is lower due to Au having a higher mean mass per ion than Cu (Au and Cu have mean atomic masses of 196.97

and 63.55). Figure 52b shows that the electron number densities in the two plumes are almost identical, with the lower ion number density for the Au being compensated for by a higher mean ionisation (figure 52c).

Figure 52d shows a plot of the electron temperature. At this time, a plot of the ion temperature is identical to that of the electron temperature. In general, electron and ion temperature values in HYADES simulations are not identical as the code uses a two-fluid, two-temperature model. ([106], p. 5). Examining the simulation results (not shown) at the end of the laser pulse, +2 ps, differences in the electron and ion temperatures are apparent. However, equilibrium is rapidly established, so that by +0.5 ns the ion and electron temperatures are virtually identical.

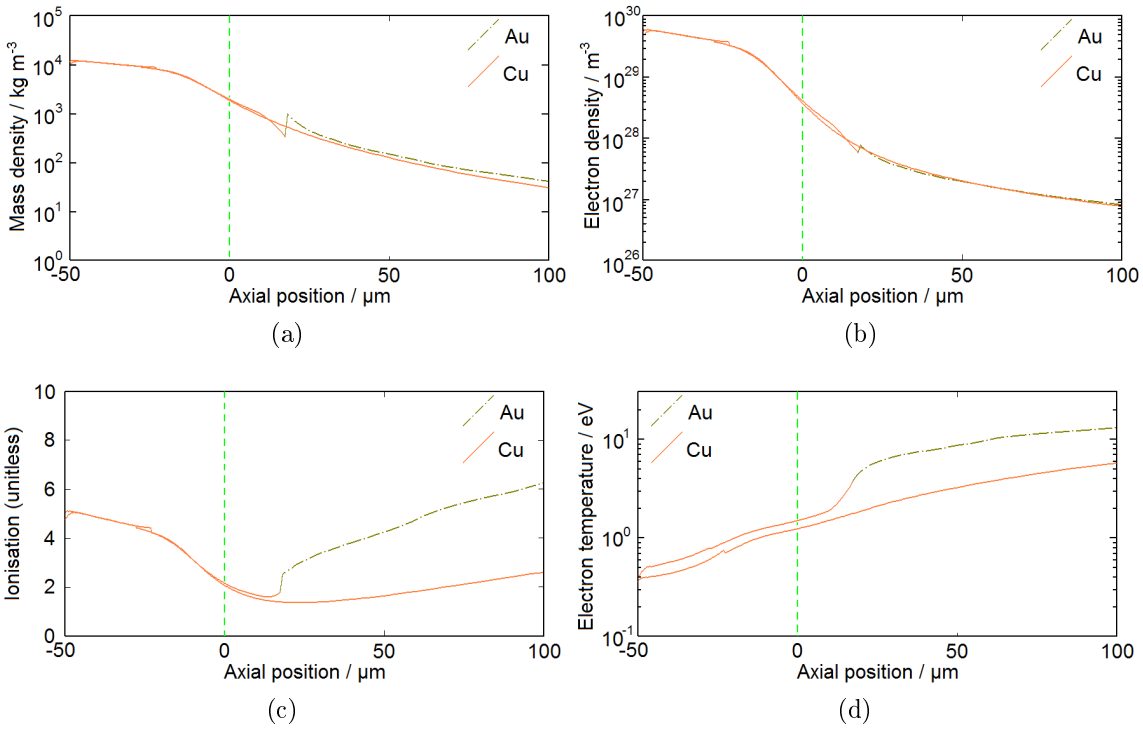

Figure 53: HYADES simulation results for coated Cu-substrate targets for the coating materials Cu and Au. The results shown are for a time of +5 ns and were obtained using the ray-trace laser-target interaction model. The original target front surface position is indicated with a dashed green line. (a) Mass density (b) Electron density (c) Mean ionisation (d) Electron temperature.

5.2.5 Results for coated targets

Figure 53 shows the results of simulating the laser-ablation of 50 µm Cu blocks with a 1 µm Cu or Au surface coating. The Cu-on-Cu results act as a test of how well the code treats the interfaces between different regions of a target. At the interface between two regions of identical composition one would not expect to see any discontinuities in the calculated properties of the plasma, and indeed no discontinuities are evident in the

Cu-on-Cu curves in figure 53. For the Au-on-Cu target, discontinuities are seen in the mass density, electron density and ionisation plots at the interface between the Au coating and the Cu substrate. It can be seen that the interface lies about 20 μm in front of the target. This information is useful in interpreting the data from the Astra experiment which was presented in sections 4.4 and 4.5 of chapter 4. In those sections, it was assumed that the plasmas seen in the interferometry data were composed solely of coating material. The HYADES results suggest that at +5 ns this would indeed have been the case except within a few tens of microns from the target surface: this is a small distance when compared with the sizes of the plasmas seen in the interferometry data, which were an order of magnitude larger.

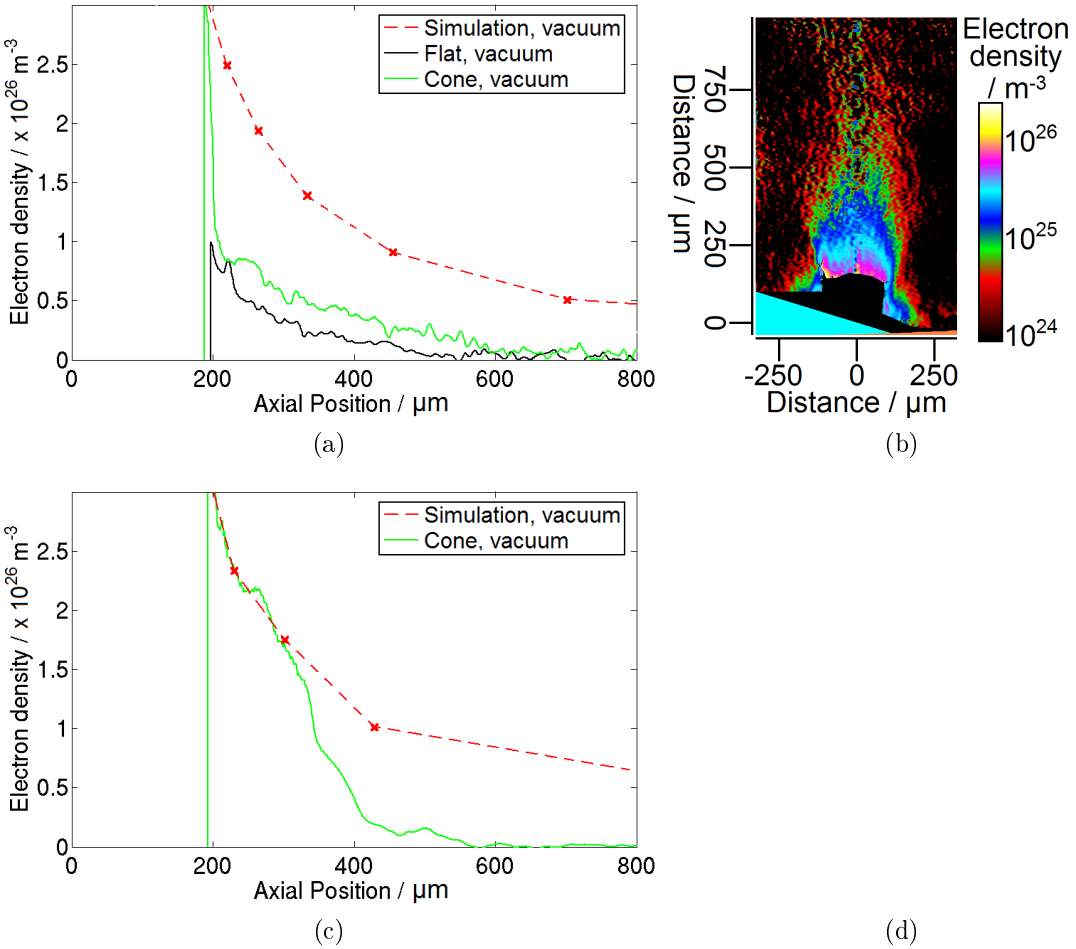

Figure 54: Comparisons between HYADES simulation results and Astra data at +5 ns. In (a) and (c) the HYADES results for Cu and Au are plotted together with axial lineouts from the experiment. (b) shows the experimental electron density map for a flat Cu target at +5 ns.

Figure 54 shows a comparison between the HYADES results and the experimental electron density data. In figures 54a and 54c, the HYADES results are plotted as dashed red lines, with small crosses marking the positions of the centres of the zones. The experimental lines are lineouts taken down the axes of the jets. In the Cu plot,

figure 54a, lines are plotted for both flat and cone targets, while for Au, figure 54c, there is only a single line for a cone target due to an absence of flat target data. To reduce noise, the line for the flat Cu target has been averaged over 51 pixels. The lines for the cone targets have been averaged over only 21 pixels due to the smaller radii of jets from targets with this geometry.

Comparing the simulation and flat target lines for the Cu, it can be seen that the electron density in the simulation is larger than that of the experimental jet over the range for which data is available. The cut-off at an axial position of about 200 μm corresponds to the edge of the data-free region in the interferogram. At the position of the cut-off, the experimental value is about one third of the simulated value, while further from the target this ratio is smaller; between 200 μm and 450 μm from the target it falls off with distance as roughly $1/z^{0.7}$.

A significant contribution to the difference in simulated and experimental values comes from radial expansion, which is not modelled by HYADES as it is a 1-D code. In figure 54b, which shows the 2-D electron density plot from which the flat target lineout was taken, it can be seen that the width of the jet increases with distance from the target. This has the effect of reducing mass and electron densities within the jet. The opposite effect occurs near to the surface of a cone target, where plasma is converging onto the axis, and hence one would expect mass and electron densities to be higher than in a 1-D simulation. Radial expansion would, however, become dominant sufficiently far from the target, and the experimental electron densities would fall below the simulated values. In the comparison of the experimental and simulated values for Au in figure 54c, between 200 and 300 μm from the target the experimental and simulated values are comparable, while after 300 μm the experimental value rapidly drops below the simulated value; if the convergence does raise the electron density above the simulated value, this occurs in the region closest to the target, from which data was not obtainable. For the Cu cone jet in figure 54a, the experimental value is only close to the simulated value near the edge of the cut-off, suggesting that radial expansion becomes dominant nearer to the target than for Au. The effect of the initial convergence can be seen down the length of the jet, however, as the line for the cone target lies above that for the flat target.

5.3 Simulation of flat and conical targets in a vacuum in 2-D

5.3.1 Interpenetration on the axes of the cone targets

In the description of the h2d code in sub-section 5.1.2, it was mentioned how one of the limitations in the use of a hydrodynamics code is found in modelling the initial interaction between colliding plasmas. The plasma at the head of a plume produced in the laser-ablation of a solid target is fast-moving and has a low density. When two such plumes collide head-on, at first the mean free paths for collisions between particles from the two flows are large and the plasmas interpenetrate. Later in time, as slower, denser material arrives at the interaction region the mean free paths become small compared to the lengthscale of this region. Once this occurs, the fluid approximation is satisfied throughout the system. As a hydrodynamics code has as one of its fundamental assumptions the satisfaction of the fluid approximation, it cannot model the initial interpenetration.

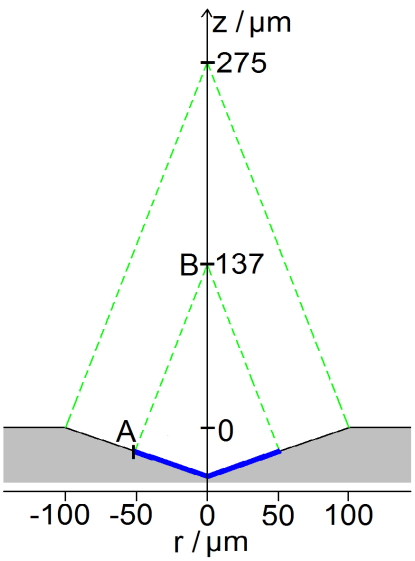

Figure 55: Cartoon illustrating the geometry of plasma convergence for a groove with an opening angle of 140°.

In the simulation of the ablation of a flat target, interpenetration is not a concern as there is no place within the system where a collision of two plasmas might occur. However, for cone and groove targets there is an interaction on the axis/plane of symmetry as plasma volumes converge onto it from opposite sides. Using the results of HYADES simulations, the collisionality of the convergence of plasma onto the plane of symmetry of an infinite groove target can be analysed. The geometry of this situation is shown in the cartoon in figure 55. A laser with a FWHM of 100 μm illuminates the inner part of the groove, along the length of which the laser intensity is assumed to be uniform.

Plasma leaving the target surface initially moves along the local surface normal. The dashed lines in the figure extending from the surface of the target indicate the paths that plasma volumes would follow if they continued to move along the surface normal until reaching the plane of symmetry. Plasma ablating from the edge of the FWHM at position A would converge at position B, about 140 μm from the front of the target.

The analysis of the interpenetration at point B proceeds as follows. A HYADES simulation is used to model the plasma ablated from one side of the groove as if it were in isolation. It is assumed that the laser intensity on the surface is uniform within the focal spot, and that it approaches the target parallel to the z-axis, striking the surface at an angle of 20° to the normal. It is assumed that plasma travels uninterrupted from A to B, a distance of about 150 μm, and thus plasma volumes arriving at B have the temperature, ion density and ionisation values from the HYADES simulation at 150 μm from the target. Volumes from opposite sides of the groove approach one another with a relative velocity of $2v\cos(70°) \approx 0.7v$, where v is the bulk flow speed from the simulation. Using a code written by M. Sherlock which implements formulae from Spitzer [111], the average times between collisions for individual electron and ion test particles from one plasma as they interact at B with the opposing plasma are estimated. It is assumed that the test particles from the first plasma approach the second plasma at the relative speed of approach of the two plasmas, i.e. $\sim 0.7v$, and in the calculations the ionisations of both the test ions and the ions in the second plasma are assumed to be equal to the mean ionisation in the simulation.

Table 4 on the following page shows the results of the analysis for Al, Cu and Au targets, each at three different times. For each material and time both mean times between collisions and mean free paths in the lab frame are listed for ion-ion and electron-electron collisions. For the ion-ion collisions the mean free paths at times of 0.5-1.0 ns are typically a couple of microns. Electron-electron collisions occur rapidly, and at 0.75 ns the mean free paths are all below 10 nm. As the mean free paths are larger for the ions, they determine the distance over which the motion perpendicular to the plane of symmetry is brought to rest in the collision at B for the plasma as a whole. After a particle has scattered three of four times, knowledge of its original direction of motion is lost. Hence, the distance over which interpenetration is significant is a few times the mean free path, which for the values in the table is roughly 2-10 μm. This is comparable to the lengthscale of the flow perpendicular to the plane of symmetry. At +3 ns the mean free paths are an order of magnitude lower, and radial stagnation occurs over a distance of order 1 μm or less.

Material	Time / ns	Mean time between collisions / ps		Mean free path / μm	
		τ_{ii}	τ_{ee}	λ_{ii}	λ_{ee}
Al	0.5	30	0.04	3	0.004
	0.75	10	0.04	1	0.003
	3.0	1	0.009	0.04	0.0003
Cu	0.5	30	0.06	3	0.005
	0.75	20	0.04	2	0.004
	3.0	3	0.006	0.100	0.0002
Au	0.75	30	0.04	1	0.007
	1.0	10	0.04	0.5	0.003
	3.0	0.8	0.003	0.02	8×10^{-5}

Table 4: Estimates of mean times between collisions and mean free paths in the lab frame for collisions between ions/electrons in plasma volumes arriving at point B in figure 55 from opposite sides of the groove.

The ion-ion mean free path is inversely proportional to the density, and depends on the fourth power of either the relative bulk flow velocity of the colliding plasmas or the ion thermal velocity, whichever of the two is the larger. For a conical target, the cylindrical convergence means that a higher number density is reached on the axis than on the plane of symmetry of a groove. Also, any plasma volume arriving at the axis of a cone simultaneously interacts with other plasma volumes with a whole range of radial velocities, only the most extreme of which is exactly opposite to its own. As a result of these two factors, the collisional mean free paths on the axis of a cone can be expected to be significantly shorter than those estimated above for a groove. Hence, the lengthscale over which interpenetration is significant can be expected to be a few microns or less for times below +1 ns, and much less than 1 μm at +3 ns. Hence, after a few nanoseconds the interpenetration occurs over a distance that is small compared with the radial lengthscale of the flow, and the interaction between the plasma volumes arriving at the axis can be approximated as collisional and modelled with a fluid code. In the h2d simulations in the following sub-sections results are presented only for a time of +5 ns, when this condition is met.

5.3.2 Simulation initialisation

In the experiment, the targets were illuminated by ~ 0.5 J pulses of 800 nm laser light, focused down using an f/6.5, 8° off-axis parabola to produce a focal spot of 100 μm FWHM. In the simulations, the slightly off-axis arrival of the beam in the experiment

was neglected to leave the situation being modelled with perfect cylindrical symmetry.

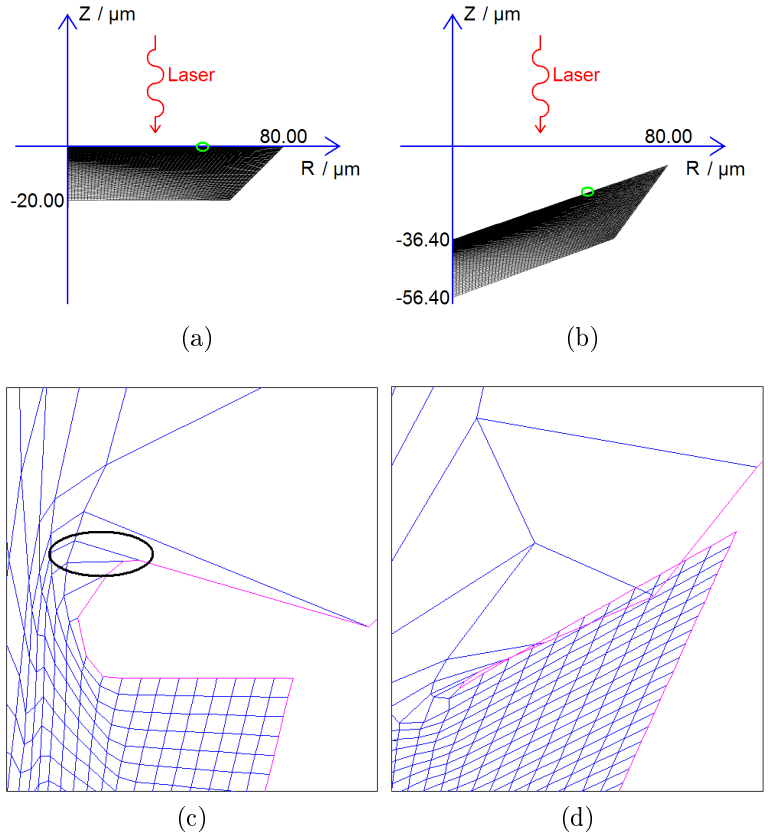

Figure 56: Bow-tying events. (a) and (b) show meshes used when simulating flat and conical targets using the top-hat intensity model. The green circles in these images indicate the positions of the edges of the laser pulses, where bow-tying events were common. (c) and (d) show examples of bow-tying events; the axial and radial scales are not the same in (c) and (d) as in (a) and (b).

Simulations were attempted with both top-hat and super-Gaussian functions used to model the radial intensity distribution of the laser pulse. Figure 56 shows examples of the meshes used in simulations of flat and conical targets when using the top-hat intensity model. For clarity, only the halves of the targets to the right of the axes are shown. Both of the target types were modelled as 20 μm thick shells. In the Astra experiment, the conical targets had a radius of 100 μm and a full opening angle of 140°. In the simulations, only the inner 80 μm of the cones was simulated. Cylindrical polar coordinates were used, with the axial coordinates chosen such that 0 μm corresponds to the front of a 100 μm cone. The laser was incident on the target from above. Geometrically, the pulse was modelled as an f/6.5 conical bundle of converging rays with 500 rays included in the bundle. The bundle had a radius of 50 μm at $Z = 0$ μm, giving a FWHM of 100 μm, and it had its tip behind the target at $Z = -650$ μm. As with the 1-D simulations, a top-hat function was used for the temporal shape of the pulse implying that the arrival of energy at the target was evenly distributed in time.

When running a simulation using a laser pulse with a top-hat intensity distribution, bow-tying was a significant problem for both flat and conical targets, with the mesh having to be untangled and the code restarted frequently during a typical 5 ns simulation. Certain regions of the mesh were particularly prone to bow-tying. One of these is indicated in figure 56a and 56b. It is located at the edge of where the laser pulse illuminated the target. Zones lying inside the laser focal spot ablated away from the target while the neighbouring zones just outside the focal spot remained stationary, leading to severe distortion of the mesh. Figures 56c and 56d show two examples of bow-tying at this location: in figure 56c one of the zones, circled in black, has become triangular rather than quadrilateral, while in figure 56d a slightly different problem, that of one region of the mesh overlapping another, has occurred.

The black lines within the target in figure 56a indicate the geometry of the mesh within the target. The rear of the mesh extended radially out to 60 μm, while the front extended to 80 μm. It was found that using a mesh such as this, in which the lines of mesh points slope radially outwards at the edge of the laser pulse, was useful in easing bow-tying problems.

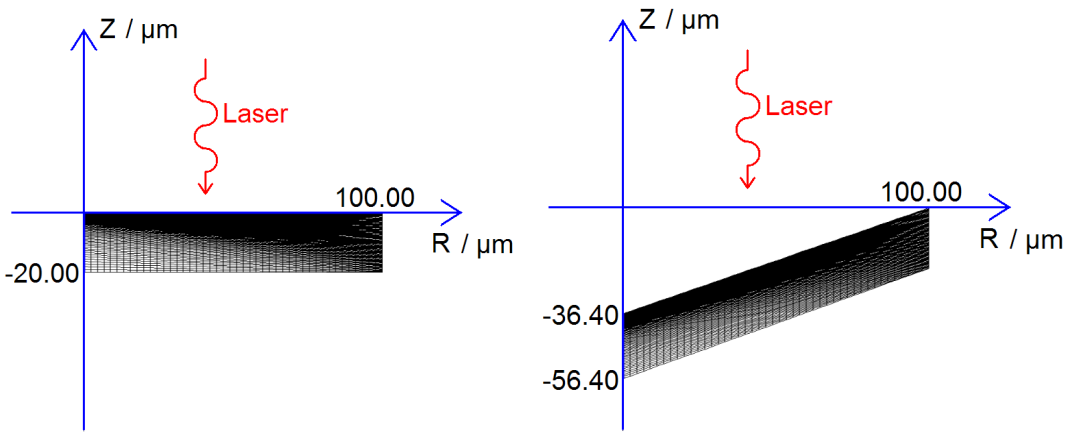

(a) (b)

Figure 57: The initial meshes for h2d simulation of (a) flat and (b) conical Astra targets in a vacuum.

Figure 57 shows a sketch of the flat and conical target geometries employed when using a super-Gaussian model for the radial distribution of intensity within the laser pulse. Both the flat (figure 57a) and conical (figure 57b) targets were modelled as 20 μm thick shells extending radially out to +100 μm, and the full opening angle of the conical target was again 140°. The positions of the bottom and outer edges of the targets were kept fixed in order to minimise the time taken up in simulating these regions; as the Astra targets were much thicker than 20 μm, the behaviour in these

regions is not of interest.

Just as when using a top-hat intensity distribution, the pulse was modelled as an f/6.5 conical bundle of converging rays, with 500 rays included in the bundle and the FWHM of the intensity distribution set at 100 μm. However, the tip of the bundle was located further behind the target, at $Z = -1300$ μm, giving the bundle a radius of 100 μm at $Z = 0$ μm rather than the 50 μm with the top-hat model. In this case, the zones lying at radial distances of more than 50 μm from the axis received some illumination rather than none. The result was that the bow-tying problems encountered at the edge of the laser pulse with the top-hat intensity distribution were nearly eliminated. This had two advantages. First, the simulations were much quicker to run. In addition to the reduction in the time taken up in manually untangling a mesh and restarting a simulation, the lack of small zones with very irregular shapes at the edge of the laser focal spot meant that the time step within the simulations could sometimes be larger. Second, the results of the simulations were greatly improved. The repeated manual untangling of the mesh at the edge of the laser pulse when using the top-hat intensity profile meant that by the end of a simulation the values of the properties of the material in this region were visibly incorrect. As a result of the better performance obtained when using the super-Gaussian intensity model, only results obtained with it are presented in this chapter.

The black lines within the targets in figures 57a and 57b show that the lines of mesh points were initially vertical. In the radial direction the meshes had 46 zones, each with a radial size of 2.17 μm. The maximum number of zones within an h2d mesh is limited to 25,000. Consequently, for a mesh with 46 zones in the radial direction the number of zones in the axial direction is theoretically limited to 543. However, in practice this limit was not approached as simulations with this many zones would have been far too slow. Meshes with 100 and 125 zones in the axial direction were used in order to establish whether the results of simulations were stable with respect to increasing the number of mesh points; this is discussed further in the next sub-section. The zones were "feathered" in the axial direction, with adjacent zones initially differing in size by a ratio of 0.97. As in the 1-D simulations, this meant that the zones were smaller towards the front of the target, and hence that the spatial resolution of the mesh was higher where the laser-target interaction occurred and the first ablation plasma was generated. In the 1-D simulations, the mesh was divided into two regions, one for the alloy substrate and one for the coating material. However, in the 2-D simulations, the targets were modelled as blocks of a single material for simplicity: results for Al, Cu

and Au targets are presented in this chapter.

In the next three sub-sections results of flat and conical target simulations are presented. First, in sub-section 5.3.3, results are presented for a flat Cu target. Using this as a basis for comparison, results for a conical Cu target are presented in sub-section 5.3.4. After this, the Cu results are compared with results for Al and Au targets in sub-section 5.3.5.

5.3.3 Simulation of a flat Cu target

On the next page figure 58 shows results at a time of +5 ns for simulations of a flat Cu target. The initial position of the boundary of the mesh is indicated in red. Figure 58a shows the positions of the mesh points for a simulation using 100 zones in the axial direction. Close to the target surface, the density of mesh points is high out to a radial position of about 80 μm. At an axial position of +300 μm, the mesh point density on the axis is still significant, but away from the axis it is very low, indicating that the spatial resolution in the plume is poor. The third line of mesh points in from the edge of the simulation roughly corresponds to the boundary of the well-resolved region.

Figure 58b show contour plots of the mass density for this simulation. The contours are smooth except in two places. Within about 15 μm of the axis they have sharp spikes resulting from a bug in the code relating to the transport of mesh points along the axis. Far from the axis, the contours are seen to suddenly reverse direction. Comparing the mass density figure with the mesh point position figure, this unphysical behaviour is seen to occur at the position of the second line of mesh points in from the edge of the simulated region. The density of the mesh points is very low here and the plasma is not well modelled.

Figures 58c and 58d show the mesh point positions and the mass density for a simulation with 125 zones in the axial direction. The 100 and 125 zone mesh point plots are very similar, though a close comparison shows that for the 125 zone simulation the well-resolved region extends out to slightly larger radii within 200 μm of the target. Comparing the 100 and 125 axial zone mass density plots, the contours within the region for which the mesh point density is high lie in similar positions, with the degree of similarity being higher where the density is higher except on the axis, where the bug operates.

In general, when using h2d to simulate the ablation of a solid target it was found that the results of 100 and 125 axial zone simulations were similar within the region that was

well resolved in both simulations. Outside the well resolved region, the differences could be significant. This shows that the simulation results within the well-resolved region were stable both with respect to an increase in the number of axial mesh points and, as the sizes of the zones at the fronts of the targets were different in 100 and 125 zone simulations, with respect to an improvement in the spatial resolution of the laser-target interaction. In the figures following this, either only the well-resolved region is shown or the edge of this region is indicated using a thick black line.

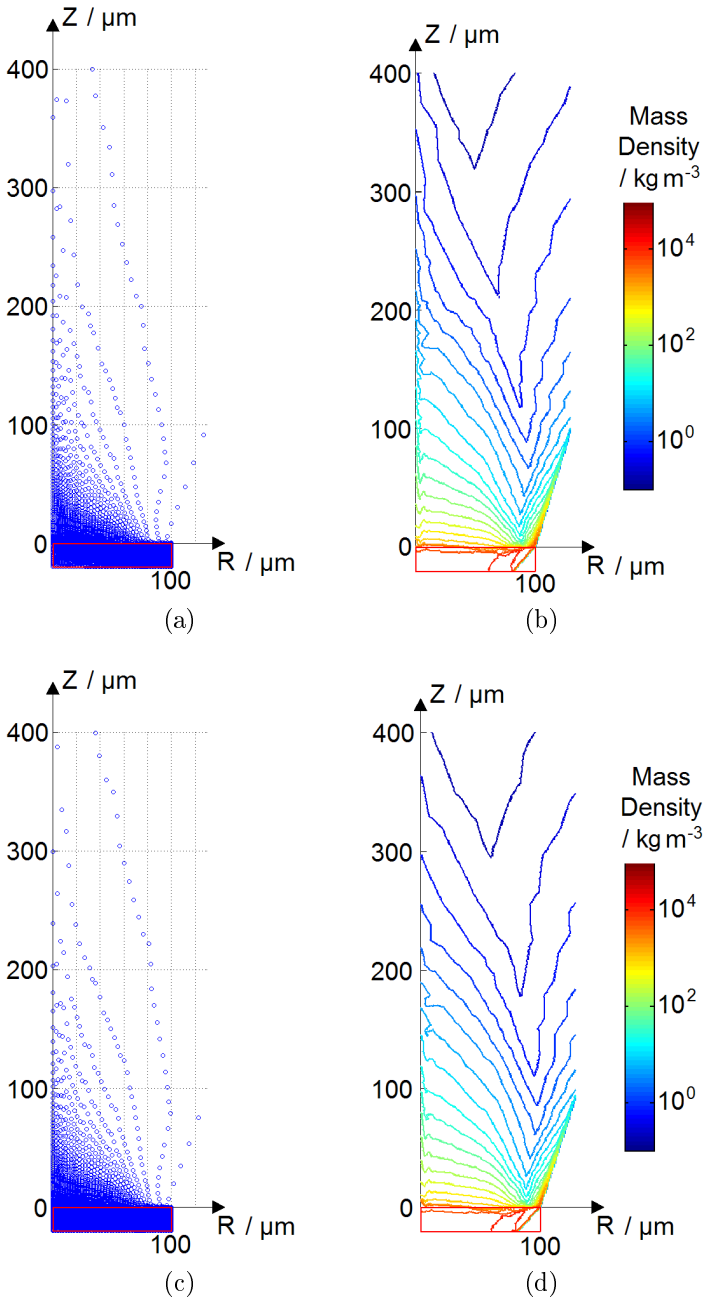

Figure 58: h2d results at a time of +5 ns for simulations of a flat Cu target using 100 ((a),(b)) and 125 ((c),(d)) zones in the axial direction. Figures (a) and (c) show the mesh point positions and figures (b) and (d) are contour plots of the mass density. The initial position of the boundary of the mesh is indicated in red.

In sub-section 5.2.1 it was stated how one of the motivations for performing 1-D simu-

lations using HYADES was that their results could be compared with those obtained using h2d in order to give a measure of its reliability. In the centre of the plasma plume created when a laser pulse with a super-Gaussian intensity profile ablates a flat target, the illumination of the target is fairly even. The plasma in this region moves away from the target roughly normally to the surface, and is effectively 1-D. The 1-D approximation breaks down further from the target where sufficient time has elapsed for information about the presence of the vacuum at the edge of the plume to propagate in as far as the centre of the plasma.

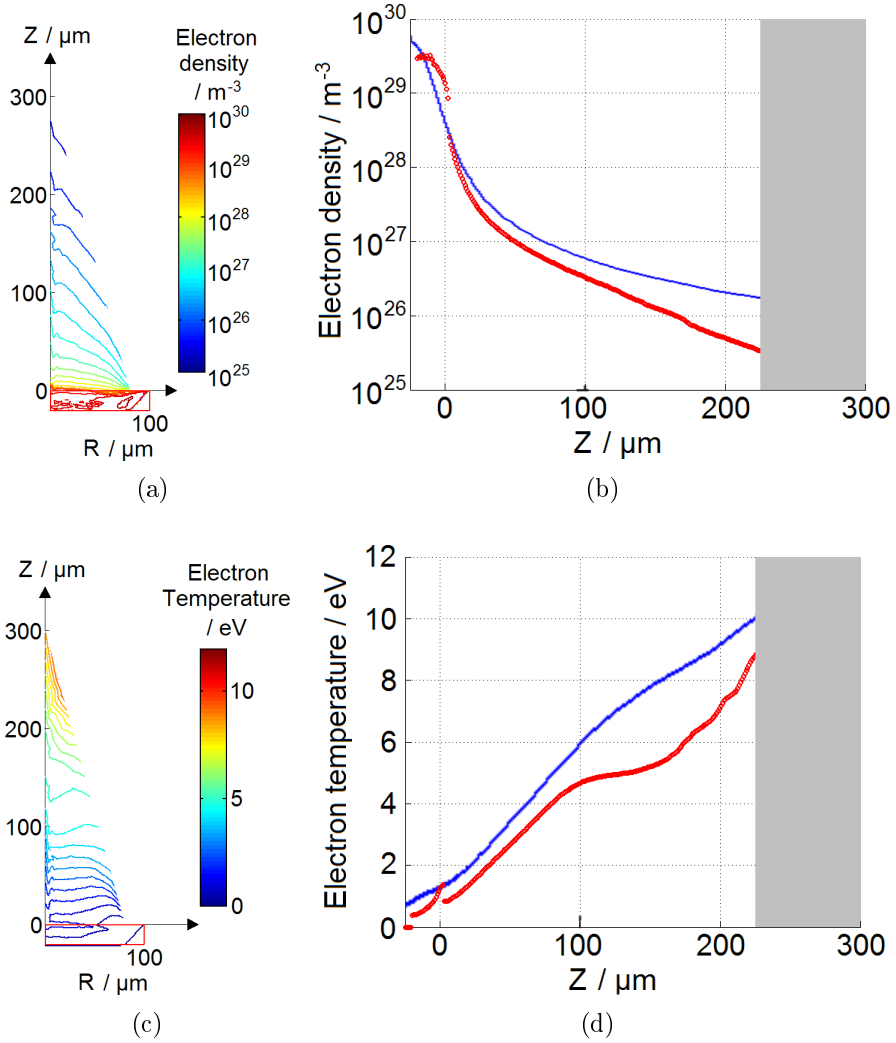

Figure 59: Comparison of results from HYADES and h2d simulations at +5 ns. (a) and (c) show plots of electron density and electron temperature obtained from h2d simulations of a flat Cu target. (b) and (d) show comparisons between the results of HYADES simulations of a Cu target and lineouts taken from the h2d simulations at a radial position of +20 μm. The h2d results are in red, and the HYADES results, calculated using the ray-trace laser-target interaction model, are in blue.

In figures 59a and 59c above, which show the electron density and electron temperature from an h2d simulation of a flat Cu target, the contours close to the target surface are approximately parallel to the surface of the target, demonstrating the approximately

1-D nature of the flow. Towards the edges of the target, and in the axial region further from the target surface, the contours are not roughly parallel to the surface. There, the radial variation in the intensity of the laser pulse and the effects of radial expansion into the vacuum cannot be neglected.

In the images in figures 59b and 59d HYADES results and lineouts from the h2d simulations are plotted together. Due to the axial bug in the code, the h2d lineouts were not taken along the axis but instead at a radial position of +20 μm. Near the target the electron density falls more steeply in the h2d results, but between where the lines cross and an axial position of 100 μm the difference is limited to a factor of about 2. Far from the target, the electron density lines are seen to diverge; over large distances, the behaviour of the plasma in the plume cannot be approximated as 1-D.

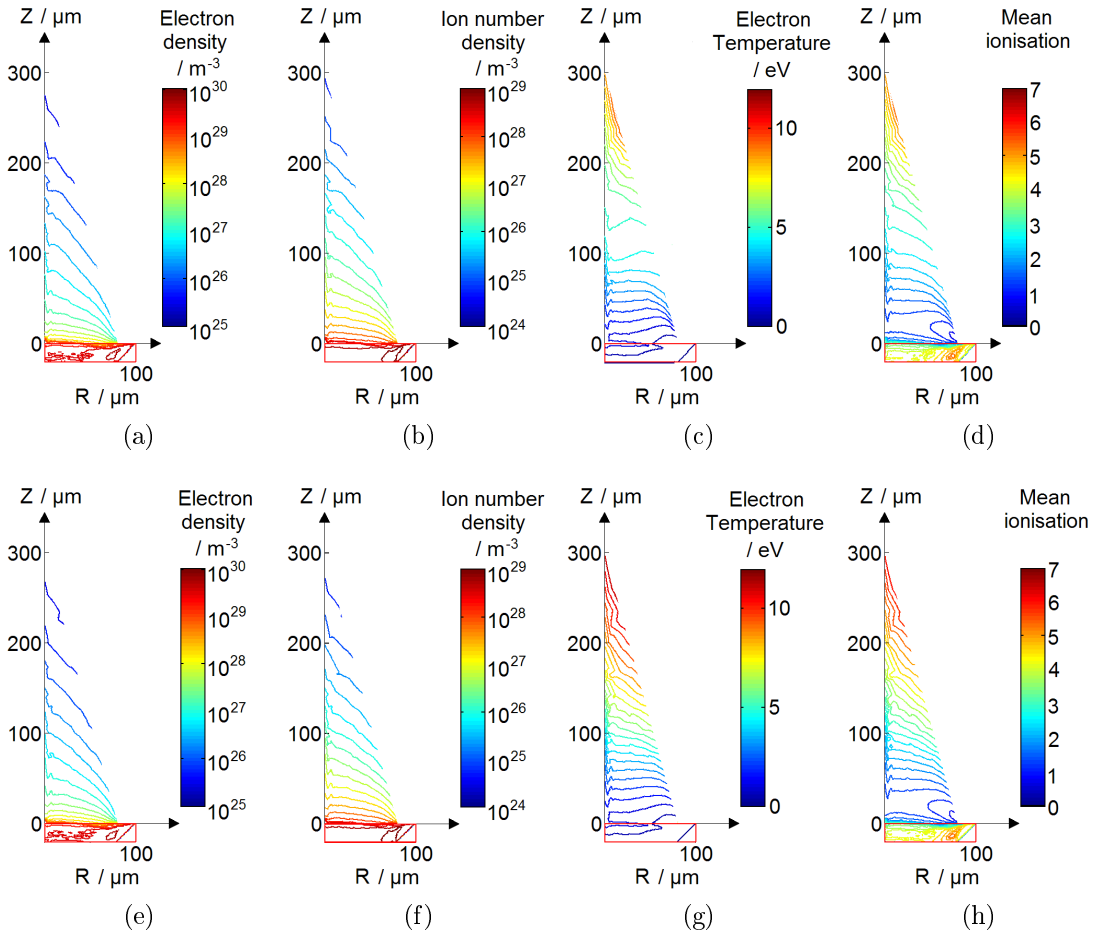

Figure 60: h2d results at a time of +5 ns for simulations of a flat Cu target with the radiation transport routines in the code switched on (top row) and switched off (bottom row). Plotted plasma properties are: (a),(e) electron density (b),(f) ion number density, equivalent to mass density (c),(g) electron temperature (d),(h) mean ionisation.

Figure 60 shows plots of four properties of the plasma from a Cu target at a time of +5 ns. The plotted plasma properties are the free electron number density, the ion number density (equivalent to mass density), the electron temperature and the mean

ionisation state. Plots are shown for simulations done with the radiation transport routines in the code both switched on and switched off in order to assess the importance of radiative processes for the plasma dynamics. Within 100 μm of the target, where the modelling of the plasma is at its best, the values of all four properties are similar with or without radiation transport, showing that it is not significant in this region. Beyond 100 μm from the target, the plasma is seen to be hotter and more highly ionised in the absence of radiation transport, a result which makes physical sense as when radiation transport is active the plasma loses some of its energy content through radiative emission.

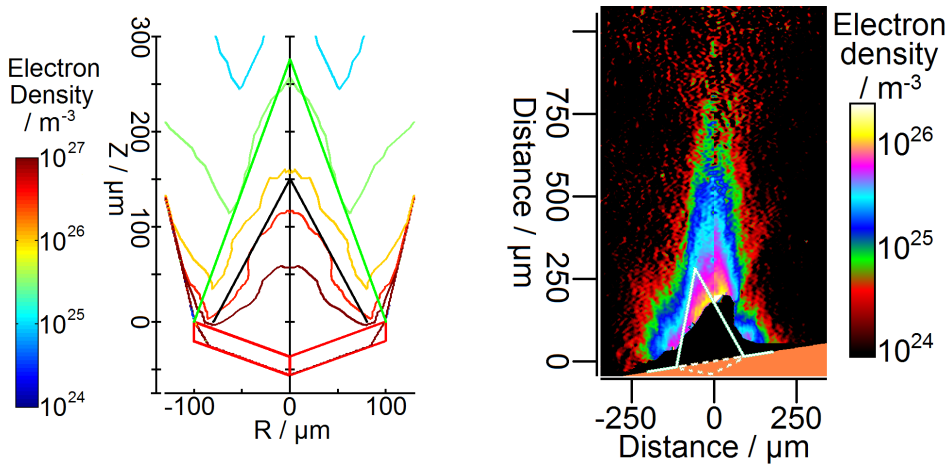

(a) (b)

Figure 61: Comparison of simulated and experimental results for a Cu cone target at +5 ns. (a) is an electron density plot simulated using h2d, while (b) is an electron density plot from the Astra experiment. In (a) the black line indicates the position of the edge of the well-modelled region. In both (a) and (b) the edge of the convergence cone is marked, with straight green lines being used in (a) and white in (b).

5.3.4 Simulation of a conical Cu target

Figure 61a shows a contour plot of the electron density at +5 ns for a simulation of a Cu cone target. The edge of the well-resolved region is marked with straight black lines. To first approximation, plasma ablating from a solid target moves away along the local surface normal. The straight green lines, which makes right angles with the initial front surface of the cone, marks the edge of the convergence cone. This is the region within which plasma leaving the target along the local surface normal would move if it travelled to the axis without deviation. It can be seen that the plasma from the Cu cone target is only well modelled in the innermost region of the convergence cone. This means that the simulation result is only useful for learning about the formation of Cu jets close to the surface of a target, and not the propagation of jets once they leave

the convergence region. As such, it shows a serious limitation of using codes which employ a Lagrangian method for simulating plasma hydrodynamics when modelling the ablation plume from a solid target. This is further brought out by a comparison of the simulated electron density plot in figure 61a with figure 61b, an electron density plot from the Astra experiment taken at an equivalent time. The convergence cone is here indicated using a white line. It can be seen that the simulated and experimental results are complementary. Far from the target, where the plasma is not well modelled in the simulation, the experimental data is of high quality. Close to the target surface, where the plasma is well modelled, there is a dark region from which experimental data could not be obtained.

The critical electron density for the Astra probe beam, which had a wavelength of 400 nm, is 6.97×10^{27} m^{-3}. The simulation results suggest that, at +5 ns, the plasma above the critical electron density was mostly limited to the interior of the cone. This suggests that the data-free region near to the target in the experimental data is not caused by the probe beam encountering plasma at the critical electron density, through which it would have been unable to propagate, and consequently never making it to the detector. Instead, as discussed in section 4.3.3 of chapter 4, the preferred explanation is that the probe beam was refracted by electron density gradients in the plasma through a sufficiently large angle that it did not pass through the collecting lens and become focused onto the detector.

When simulating a Cu cone target, the convergence of mesh points onto the axis led to bow-tying of the zones at the front of the plume early on in the simulation. This is illustrated in figure 62a on the following page. As described in section 5.1, when a bow-tying event occurs while using h2d it is required that the user manually remove the bow-tie events from the mesh and restart the code. Several methods are available for performing the untangling, for example dragging mesh points into new positions using the mouse or specifying that the spacing of the points along a section of a particular line of mesh points be made even. Figures 62b to 62f show contours plots of the electron density at +5 ns for five 125 axial zone simulations differing only in how the bow-tying events were handled. Comparing the five images, significant differences in the shapes of the red (3×10^{26} m^{-3}) contour are apparent not only near the axis, where the bug in the code operates, but also further out. In figures 62b and 62c this contour appears rounded, while in figures 62d to 62f it has distinct "shoulders" at a radial position of about 40 μm. The shape of the green (3×10^{25} m^{-3}) and yellow (1×10^{26} m^{-3}) contours in figure 62e shows how the untangling of the mesh in this case led to a serious distortion

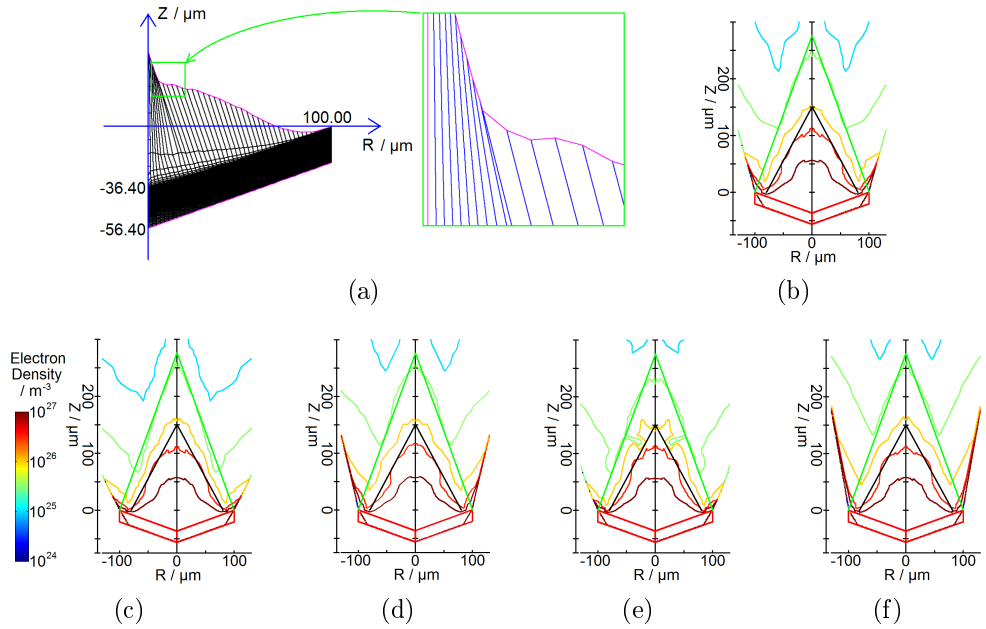

Figure 62: Demonstration of the effects of bow-tying on the results of h2d simulations. (a) shows the location where bow-tying events occurred early in the simulations. (b)-(f) show contour plots of the electron density for five h2d simulations of a Cu cone target differing only in the handling of bow-tying events. The straight black and green lines indicate the positions of the edges of the well-resolved regions and the edges of the convergence cones, respectively. The initial position of the boundary of the mesh is indicated in red.

in the calculated plasma properties at the edge of the well-resolved region. Of the five plots, figure 62d seems to be an "average" result and consequently it was this figure that was chosen for the comparison with the experimental data in figure 61.

On the next page figure 63 shows a comparison of the results of simulations of flat and conical Cu targets, with the radiation transport routines switched on in both cases. The size of the well-resolved region for the flat target is appreciably larger than that for the conical target. The flow leaving the surface of the conical target is directed in towards the axis. As a result, the mesh points, which move with the flow, become more clustered in towards the axis than in the case of a flat target and the well-modelled region consequently extends less far in the radial direction. In addition, the axial component of the flow velocity for plasma leaving the surface of a conical target is less than that for a flat target and as a result mesh points move less far in the axial direction, also resulting in a lower size for the well-modelled region.

As with the flat targets in sub-section 5.3.3, simulations of conical targets were run both with and without use of the radiation transport routines in the code. In the absence of radiation transport, the agreement between simulations using 100 and 125 axial zones was seen to break down at an axial position of around +50 µm. Due to the small size

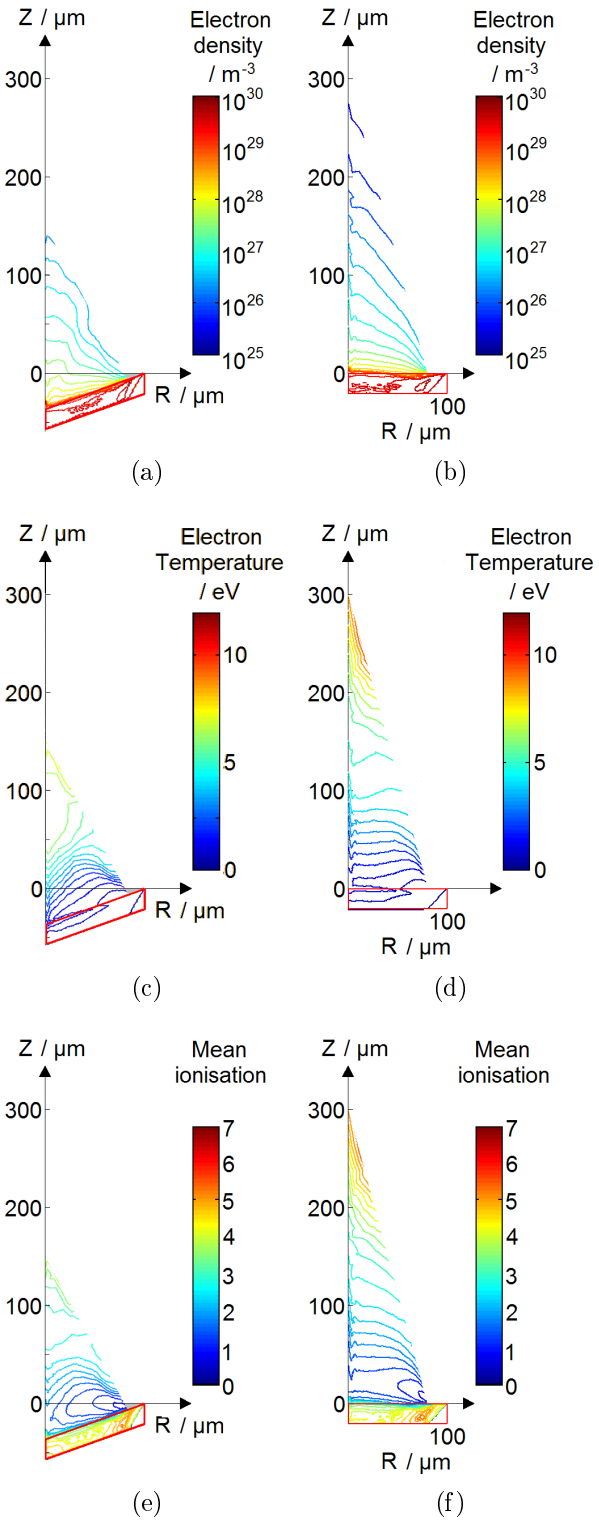

Figure 63: h2d results showing a comparison between simulations of conical and flat targets. Plotted plasma properties are: (a),(b) electron density (c),(d) electron temperature (e),(f) mean ionisation.

of the well-modelled region and the presence of the axial bug there is little that can be learnt in this case.

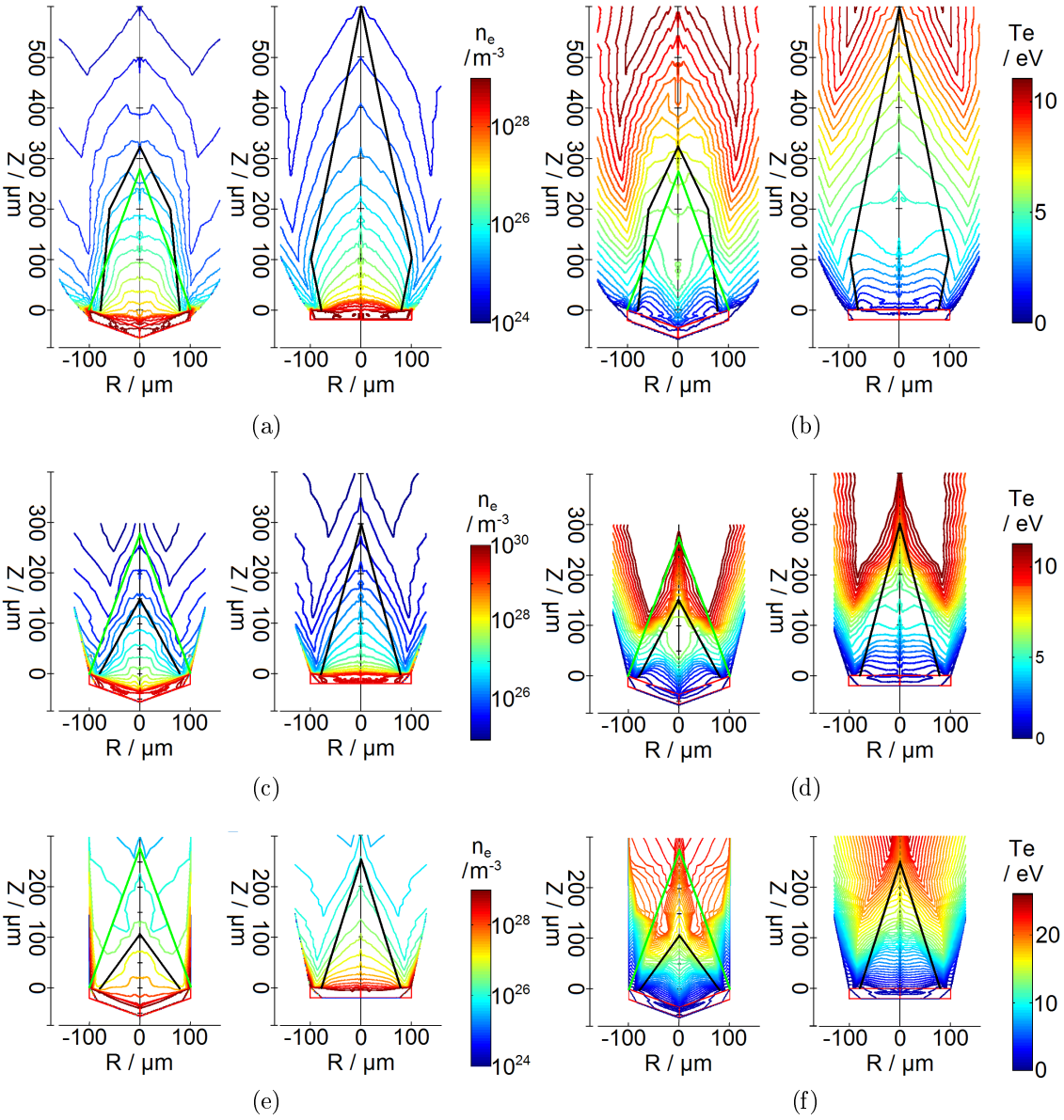

Figure 64: Comparison of simulation results at +5 ns for three target materials. These are: (a),(b) Al (c),(d) Cu (e),(f) Au. Figures (a),(c) and (e) show electron density and figures (b),(d) and (f) electron temperature. Each of the six pairs of images contains one plot for a cone target and one for a flat target. The black lines mark the edges of the well-resolved regions and the straight green lines indicate the positions of the convergence cones.

5.3.5 Comparison of results for Al, Cu and Au targets

In addition to the simulations of flat and conical Cu targets presented in the previous two sub-sections, simulations were also run for Al and Au targets. Figure 64 above shows a comparison of the electron densities and temperatures for the three materials at +5 ns. Results are shown for both flat and conical targets. The size of the well-modelled region is much larger for Al than it is for Cu and Au: it is axially slightly

longer than the convergence cone, though not enough to study the propagation of the jet after leaving this region. A physically intuitive explanation for the size of the well-modelled region would be that it is determined by the speed of the ions in the plasma, which could be expected to be higher for Al than for Cu and Au due to the atomic masses of these elements being 27.0, 63.5 and 197.0, respectively. However, the speeds predicted by the simulations are in fact similar for all three materials. Hence, as the spatial resolution of an h2d simulation is determined by the local ion density, the differences in the sizes of the well-resolved regions may result more from the rates at which ions are ablated from the targets than from the masses of these ions.

5.4 Assessment of the possibility of scaling the Astra experiment

In the analysis of the data from the Astra experiment in chapter 4, a rough estimate of 3 was obtained for the Mach number of a Cu plasma from a flat target at +5 ns. This is one of the parameters which are needed to assess whether the jets created in the experiment scale to YSO jets, as discussed in section 3.2 of chapter 3. In this section the experimental data set is supplemented by values of quantities such as mean ionisation from HYADES simulations in order to estimate values of the other scaling parameters for jets from Cu and Au cone targets propagating into 50 mb of He, at a time of +5 ns.

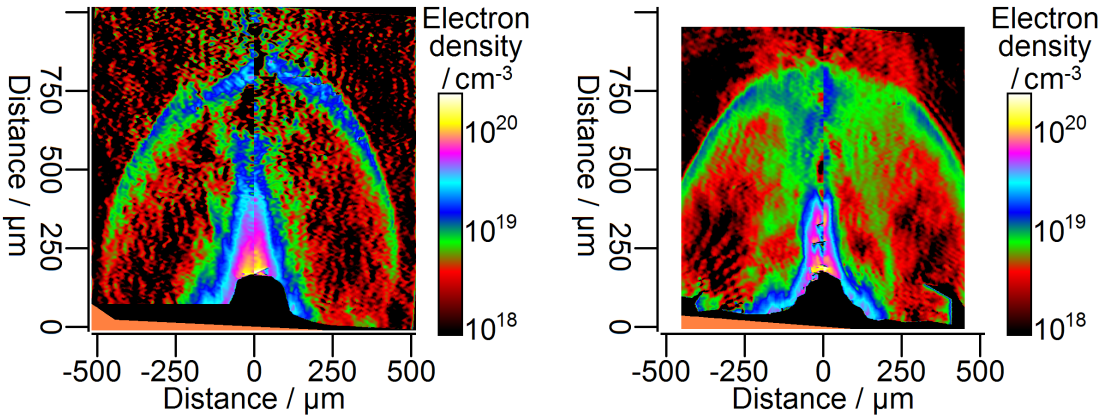

Figure 65: Electron density maps for (a) Cu and (b) Au cone targets in 50 mb He at a time of +5 ns.

The electron density maps for the Cu and Au jets are shown in figure 65. These images were previously shown in section 4.5 of chapter 4, though the units have been changed

from SI units to cgs units (m^{-3} to cm^{-3}) as the formulae used in this section are in cgs units.

Near the target, the Cu plasma has a width in excess of 250 μm. The plasma is conical in shape, narrowing down to a width of about 100 μm at 500 μm and giving a radius of 50 μm for the tip of the jet. Further back near the target at an axial position of 150 μm, near the edge of the dark region, the width of the jet is about 250 μm and the radius therefore about 130 μm. The electron density varies down the jet from about 1.5×10^{20} cm^{-3} at 150 μm to about 1.5×10^{19} cm^{-3} at 500 μm. These values differ by a factor of about 3 and 6 from the values in HYADES simulations; a comparison between experimental and simulated electron density values has previously been presented in sub-section 5.2.5. As with Cu, near the target the Au plasma has a width in excess of 250 μm. At around 440 μm the diameter is about 80 μm, giving a jet radius of 40 μm, and the electron density at this position is about 1.5×10^{19} cm^{-3}.

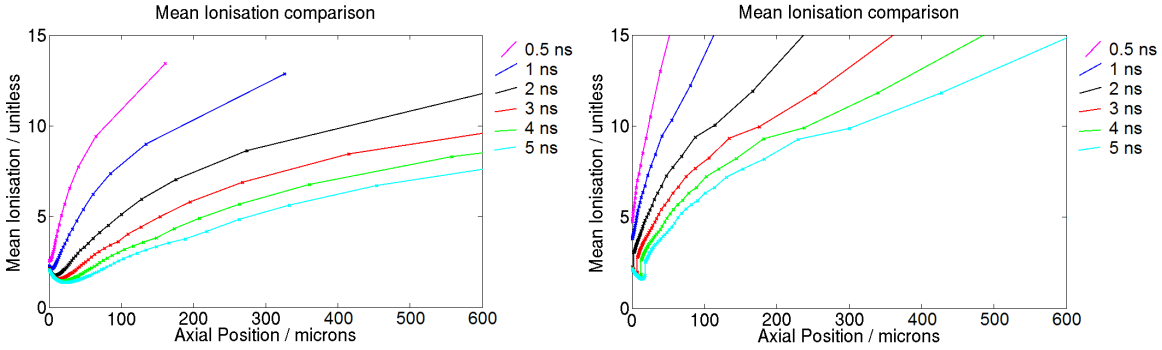

(a) (b)

Figure 66: Ionisation plots for HYADES simulations of (a) Cu and (b) Au targets.

5.4.1 Estimation of η, the mass density ratio

The mass density of the material in a jet is related to the electron density by $\rho_{jet} = m_i n_i = (m_i n_e / \overline{Z})$, where $\overline{Z}$ is the mean ionisation. In the absence of experimental measures of ionisation, values from HYADES simulations will be used. Plots of this quantity are shown in figure 66 for both Cu and Au. For Cu, it can be seen from figure 66a that at +5 ns the ionisation varied from about 3 at 150 μm from the target to 7 at 500 μm, giving mass densities of about 5×10^{-3} g cm^{-3} at 150 μm and 0.2×10^{-3} g cm^{-3} at 500 μm. The mass density of He gas at a pressure of 50 mb, assuming a room temperature value of 20°C, is 8.4×10^{-6} g cm^{-3}. Consequently, for the Cu jet the scaling parameter η, which is the ratio of the mass densities in the jet and in the ambient medium, takes values of $\sim$ 600 at 150 μm and $\sim$ 30 at 500 μm. For Au,

the HYADES simulation gives a value of 12 for the ionisation (figure 66b) at 440 μm, yielding a mass density of 0.4×10^{-3} g cm^{-3} and a value for η of 50.

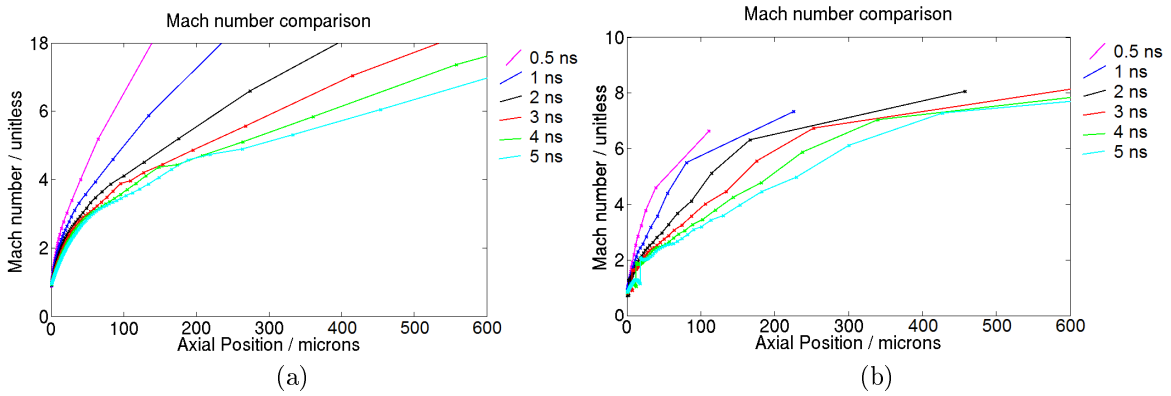

(a) (b)

Figure 67: Mach number plots for HYADES simulation of (a) Cu and (b) Au targets.

5.4.2 Comparison of the estimated Mach number with HYADES results

In sub-section 4.4 of chapter 4 the internal Mach number was estimated at + 5 ns for a Cu jet from a flat target propagating into a vacuum. The measurement was made by taking the gradient of edges in the flow at around 250 μm from the target, and yielded a value of 3. In the HYADES simulation for the Cu target, the Mach number increases from 3.4 to 6.3 over the range 150 to 500 μm, as shown in figure 67a, and hence at 250 μm the experimentally inferred and simulated Mach numbers differ by about 1-2. It will be assumed that the Mach number of a jet from a cone target is comparable to that from a flat target.

Ideally, it would be possible to estimate from the experimental data how the Mach number varies with distance from the target. However, this cannot be done using the estimation technique employed in chapter 4. In the absence of such information, and considering both the experimentally estimated value of the Mach number and the way the Mach number varies with axial position in the HYADES simulations, values of 2 and 4 will be used at axial positions of 150 and 500 μm. For the Au jet, no flat target was shot in a vacuum and imaged at +5 ns, and so the Mach number of 7 at 440 μm in the HYADES simulation results in figure 67b will be used.

In sub-section 4.5.1 of chapter 4, the speed of the bowshock for jets from Cu cone targets in 50 mb He was estimated at 120 km s^{-1} at +5 ns. For an overdense jet, the on-axis bowshock speed is of the same order as the speed of the material within the jet beam. As a result, a speed of 1.2×10^7 cm s^{-1} will be taken for the speed of the plasma in the Cu jet at the position of the jet shock, where it interacts with the ambient medium.

For an Au cone target, plotting the position of the tip of the bowshock as a function of time gives a speed of 1.3×10^7 cm s^{-1}, and hence this value will be taken for the speed of the plasma in the Au jet at the jet shock. Inspection of the electron density maps in figures 65a and 65b suggests that rough values for the axial positions of the jet shocks for the Cu and the Au are 550 and 650 μm. At these positions, the electron density takes its highest value between the convergence region nearer to the target and the bowshock. There are also faint arcs visible which link these regions to the bowshock and, in the case of Au, there are faint arcs heading back towards the target, as one would expect to see for a reverse shock. (Similar arcs thought to correspond to the reverse shocks for Cu jets in 100 mb He are discussed in section 4.5.1 of chapter 4.)

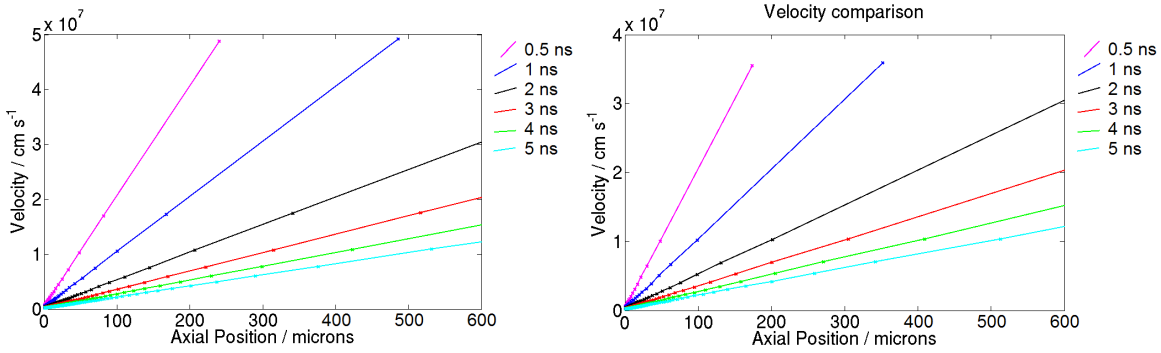

Figure 68: Velocity plots for HYADES simulations of (a) Cu and (b) Au targets.

Looking at the HYADES results for the jet velocities in figure 68, it can be seen that the velocities in the plumes increase roughly linearly with the distances from the targets. As the speed of the Cu plasma at 550 μm, the position of the jet shock, has been taken to be 1.2×10^7 cm s^{-1}, the speeds at 150 μm and 500 μm are therefore 0.3×10^7 cm s^{-1} and 1×10^7 cm s^{-1}. For the Au, the speed at 440 μm is estimated at 0.9×10^7 cm s^{-1}. From these speeds and the previously estimated Mach numbers it is possible to estimate sound speeds using the relation $c_s = (V_j/M)$, which gives values of 2 x 10^6 and 3 x 10^6 cm s^{-1} for Cu at 150 μm and 500 μm, and 1 x 10^6 cm s^{-1} for Au at 440 μm.

5.4.3 Estimation of the temperature in the plasma

The electron temperature of the plasma can be estimated from the ion sound speed. A formula relating these can be found on page 29 of the NRL plasma formulary [112]:

$$c_s = \sqrt{\frac{\gamma Z k_B T_e}{m_i}} \quad \Rightarrow \quad T_e = \frac{m_i c_s^2}{\gamma Z k_B}$$

where γ is the polytropic index and Z and m_i are the charge and mass of the ion. The estimated temperature depends on the square of the sound speed and is therefore quite sensitive to the values estimated for the jet velocity and the Mach number because the sound speed is the ratio of these quantities.

The polytropic index γ for a fluid is related to the number of degrees of freedom the fluid possesses. The value of γ is close to 1 where this is large, and $\gamma = 5/3$ where the only degrees of freedom are the three directions of (3-D) translational motion. This latter value is the case for an ideal gas and also for fully-ionised plasmas. Plasmas which are not fully ionised can also have an effective γ of $5/3$ if their temperature is sufficiently low that excitation of the ions can be neglected, and the recombination rate is sufficiently small. The Cu and the Au in the experiment are nowhere near fully ionised, with the mean ionisations being only about 5 and 12 at +5 ns. However, as the range of values γ takes is small, and here only order-of-magnitude estimates for the scaling parameters are being calculated, a value for γ of $5/3$ will be used.

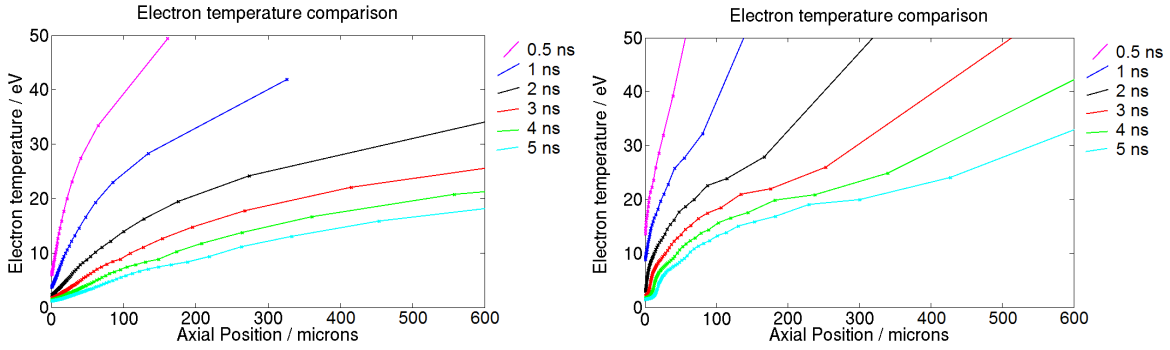

(a) (b)

Figure 69: Temperature plots for HYADES simulation of (a) Cu and (b) Au targets.

Using the sound speed and ionisation values estimated previously, for Cu the electron temperature is estimated at 36 and 42 eV at 150 and 500 μm. These values are much higher than the HYADES values of 8 and 17 eV in figure 69a, and this is due primarily to the small size of the experimentally estimated Mach number. The difference in the geometry of the cone targets from the 1-D geometry of the simulations has several competing effects on the temperature. In the initial convergence of plasma onto the axis of the cones, kinetic energy of the bulk flow is converted to thermal energy, which raises the plasma temperature. However, the rate of radiative energy loss, which acts to lower the temperature, also rises as the density and ionisation increase in the convergence. Furthermore, the 3-D nature of the experiment allows energy to be lost from the system in the radial direction, which is not taken into account in the HYADES simulation. Due to the estimated values of the temperature being so much higher than the HYADES

estimates, the HYADES estimates will be used in the calculations in the following subsections. For Au, the estimated temperature is 16 eV. The only experimental parameter used in obtaining this value is the plasma speed, which agrees well with the HYADES value, and hence it is not surprising that the temperature estimate is similar to the value of 25 eV in the HYADES simulation.

5.4.4 Estimation of δ, the collisionality parameter

The scaling relations discussed in chapter 3 are based on the equations of ideal hydrodynamics. In order for these equations to be applicable, it is necessary that the fluid approximation be satisfied. As discussed in section 3.2 this can be judged using the collisionality parameter, denoted δ [15], which is the ratio of the mean distance particles travel between collisions to the characteristic lengthscale of the system. For an experimental jet there are two possible lengthscales, jet radius and jet length; as the fluid approximation must be satisfied in both the radial and longitudinal directions, the smaller value is chosen, which for the Cu and Au jets is the radius.

Following [57], the mean free paths for collisions between ions can be estimated using the formula

$$\lambda_{ii} = \frac{(k_B T)^2}{4\pi e^4 \overline{Z}^4 n_i \ln\Lambda_{ii}} \tag{22}$$

from [113], where T is in Kelvin and the charge of the electron and the ion density are in cgs units. The quantity $\ln\Lambda_{ii}$ is the ion-ion Coulomb logarithm. Calculation of Coulomb logarithms for plasmas in the electron density and temperature regime of the experimental jets is not straightforward. This subject is treated in detail in [116], particularly pages 12-15 and 19-20, and using formulae therein the ion-ion Coulomb logarithm is estimated to be 2 for both of the Cu positions and also for the Au.

For the Cu plasma, the formula for the ion-ion mean free path gives values of $\sim 10^{-7}$ cm at both 150 and 500 μm. Dividing by the estimated jet radii at these locations, 130 μm and 50 μm, gives values for the ion collisionality parameter of $\delta_{ii} \sim 10^{-6}$ at 150 μm and $\sim 10^{-5}$ at 500 μm. For the Au jet, the formula yields a value of $\sim 10^{-6}$ at 440 μm. In all cases, the ratio of the mean free path to the jet radius is several orders of magnitude less than 1, suggesting that the ions can be treated as a fluid.

For electrons there are two possible lengths that govern the collisionality, the mean free path for electron-electron collisions and the mean distance an electron travels

[15] ζ is sometimes used for the collisionality parameter rather than δ.

between successive collisions with ions. Inspection of equation 22 suggests that the ratio of the electron-electron and ion-ion collisional mean free paths is roughly $\overline{Z}^3$, where use has been made of the relation $n_e = \overline{Z} n_i$; the Coulomb logarithm values differ only by a factor of a few, and so have been neglected. From the discussion of momentum relaxation timescales in [20], the ratio of the mean distance an electron travels between collisions with an ion to the ion-ion mean free path is roughly $\overline{Z}^2$. Hence, for the Cu and Au jets the smaller of these ratios is that for electron-ion collisions, and these determine the lengthscale over which the fluid approximation is satisfied for the electrons. Estimates of the collisionality parameter for the electrons are $\delta_{ei} \sim 10^{-5}$ for Cu at 150 μm, and $\sim 10^{-3}$ for both Cu at 500 μm and Au at 440 μm. Consequently, the fluid approximation is satisfied for the electrons, though not as well as for the ions.

(For both electrons and ions the timescale over which collisions occur is of order 1 ps or below, smaller than the hydrodynamic timescale, which is above 10 ps.)

5.4.5 Estimation of Re and Pe, the Reynolds and Peclet numbers

The Reynolds and Peclet numbers are discussed in section 3.1.3. The Reynolds number is the ratio of the magnitudes of the advective and viscous terms in the fluid momentum conservation equation. If the value of the Reynolds number is much greater than 1, viscosity is negligible. Similarly, the Peclet number gives the ratio of the advection and thermal conduction terms in the energy conservation equation. When the Peclet number is much larger than 1 thermal conduction can be neglected. The Reynolds and Peclet numbers are given by

$$Re = \frac{LU}{\nu} \quad , \text{ and } \quad Pe = \frac{LU}{\kappa} \tag{23}$$

where L is a characteristic lengthscale over which the hydrodynamic properties of a fluid vary, and U is a characteristic value of the speed within the flow. The quantities ν and κ are the kinematic viscosity and thermal conductivity.

Within the plasma of a jet, there are two possible choices for both L and U. For the lengthscale, there are the radius and length of the jet, and for the speed there are the speed of the material along the jet and the sound speed, which is the maximum speed at which material moves transverse to the axis. The plasma within the experimental jets

is distinctly anisotropic: the speed along the jets is greater than the speed transverse to the jets by roughly the Mach number, which was about 5, and the lengths of the jets are an order of magnitude larger than their width. Consequently, the choice of values of L and U can have a significant effect on the calculated values of Re and Pe.

In a flow for which L and U are of a similar order of magnitude in all spatial directions, it is appropriate to assess the significance of viscosity for the flow as a whole by calculating a single value for Re. However, in the highly anisotropic flow of a jet the assessment is not as straightforward, as the components of the momentum transport along the jet and transverse to its axis differ significantly. For viscosity to be negligible, advective transport needs to dominate viscous transport in both radial and axial directions. In this case, values of Re could be calculated for the two directions separately. The lower of the two values would then set the limit on the importance of viscosity for the flow as a whole.

Consideration of the momentum and energy conservation equations suggests that, for the jets in the Astra experiment, for both Re and Pe the appropriate combination of L and U to use for assessing the importance of viscosity and thermal conduction for the flow when taken as a whole are the radius of the jet and the sound speed. In the literature the jet velocity is usually used, possibly due to it being easier to (accurately) infer a value for this quantity from experimental data. For consistency with the literature the jet velocity will be used, giving

$$Re = \frac{r_j v_j}{\nu} \quad , \text{ and } \quad Pe = \frac{r_j v_j}{\kappa} \, . \tag{24}$$

Referring to [114], Ryutov *et al.* [34] give the formulae

$$\nu = \frac{3.3 \times 10^{-5} T^{5/2} m_i^{1/2}}{\rho \overline{Z}^4 \ln\Lambda} \quad , \text{ and } \quad \kappa = \frac{\alpha(\overline{Z}) T^{5/2} m_i}{\rho \overline{Z}(\overline{Z}+1)\ln\Lambda} \tag{25}$$

for the viscosity and thermal conductivity, where the temperature is in units of eV, the ion mass is in proton masses, and the mass density is in g cm^{-3}. The formula for ν above is only valid for $\overline{Z}$ below about 6, for which the viscosity is dominated by the ions ([34]). Where $\overline{Z}$ is higher, the electron contribution also needs to be considered.

Using [117] (p. 21, formulae D.50 and D.51), which refers to [114] , a formula for this is

$$\nu_e = \frac{4.0 \times 10^{-7} T^{5/2} m_i^{1/2}}{\rho \overline{Z}^3 \ln\Lambda} \tag{26}$$

The ν that will be used in calculating the Reynolds number where $\overline{Z} \geq 6$ is the sum of the ion contribution from equation 25 and the electron contribution from equation 26. The expression for κ in equations 25 is the electron contribution to the thermal conduction, which dominates the ion contribution in the plasma regions being considered. $\alpha(\overline{Z})$ is a coefficient that depends on the ionisation, taking values of 4.1 x 10^{-3}, 5.7 x 10^{-3} and 6.6 x 10^{-3} for $\overline{Z}$ values of 3, 7 and 12 ([116], pp. 5-6). Using the formulae on pages 19 and 20 of [116], the electron-ion Coulomb logarithm is estimated at 2 and 3 for Cu at 150 μm and 500 μm, and 3 for Au at 440 μm, and these values are used for $ln\Lambda$ when substituting into equations 25.

Applying these formulae yields $Re \sim 10^6$ and $Pe \sim 100$ for Cu at 150 μm, $Re \sim 10^5$ and $Pe \sim 1$ for Cu at 500 μm, and $Re \sim 10^6$ and $Pe \sim 1$ for Au at 440 μm. In all three cases the estimate for the Reynolds number is much greater than one, indicating that viscosity within the plasma is negligible. The value of the Peclet number is much lower. For Cu at 150 μm it is still greater than one, but for Cu at 500 μm and Au at 440 μm it is of order 1. It is concluded that thermal conduction may play a significant role in the plasma dynamics, particularly in the narrow parts of the jets far from the targets.

5.4.6 Estimation of χ, the radiation cooling parameter

The last of the scaling parameters to estimate is that which is used to assess the importance of radiation for the hydrodynamics. In [1] the following formulae are used:

$$\chi = \frac{v_j \tau_{rad}}{r_j} \quad , \qquad \tau_{rad} = \frac{\frac{3}{2}(\overline{Z}+1) n_i k_B T}{\Gamma' n_i} \; . \tag{27}$$

Here, the radiation cooling parameter χ is the ratio of the radiative cooling timescale to the hydrodynamic timescale. Where χ is less than or comparable to one, the emission of radiation is sufficiently rapid to affect the hydrodynamics of the plasma. The radiative cooling timescale, denoted τ_{rad}, is the ratio of the thermal energy density of the plasma, which is equal to $\frac{3}{2}(\overline{Z}+1) n_i k_B T$, to the rate at which radiation is emitted per unit

volume, which is given by $\Gamma' n_i$.

Material	Electron density	Temperature	Γ'/ ergs s^{-1} $atom^{-1}$		
	/ g cm^{-3}	/ eV	0 μm	10 μm	100 μm
Cu	1e19	17	0.2	0.05	0.03
Cu	1e20	8	0.05	0.01	0.009
Au	1e19	16	0.4	0.1	0.07

Table 5: Table showing estimates of the average power radiated per ion taken from simulations of Cu and Au plasmas with particular combinations of density and temperature. For each combination a separate calculation was done for plasmas with three thickness, 0, 10 and 100 μm.

The quantity Γ', which has units ergs s^{-1}per ion, is the average power radiated by the plasma per ion within it. The value of this quantity was estimated by N. C. Woolsey using FLYCHK [115], a zero-dimensional, collisional-radiative, non-LTE model of atomic kinetics. Values of Γ' were calculated for Cu at electron densities of 10^{19} cm^{-3} and 10^{20} cm^{-3}, and for Au at 10^{19} cm^{-3}, and are summarised in table 5. For each combination of material, density and temperature calculations were done for plasmas with three different depths, 0, 10 and 100 μm. The 0 μm calculations were done ignoring opacity effects, which the 10 and 100 μm calculations attempt to model using an escape factor approximation.

For the Cu and Au jets at 500 and 440 μm from the target, the diameters of the jets are about 100 μm and 80 μm, while for Cu at 150 μm the diameter is greater at over 250 μm. In all three cases, the values of Γ' for a plasma depth of 100 μm are more appropriate as estimates than the values for the lower plasma depths. Substituting the estimates for Γ' for a depth of 100 μm into formulae 27 yields values for the radiative cooling parameter of ~ 1 and ~ 10 for Cu at 150 and 500 μm, and ~ 10 for Au at 440 μm.

5.4.7 Scaling summary

The values calculated for the scaling parameters for the Cu and Au jets are summarised in table 6 on the following page. Given the large number of assumptions and approximations made in arriving at these values, the mean free paths, collisionality parameters, Reynolds numbers, Peclet numbers and radiative cooling parameters are only order-of-magnitude estimates at best, and hence are given as powers of 10.

For both Cu positions and for the single Au position the estimated values of the collisionality parameters differ from one by several orders of magnitude, and it is concluded

		Cu jet		Au jet	
Quantity	Units	Value at 150 μm	Value at 500 μm	Value at 440 μm	Value for a YSO jet
ρ	g cm^{-3}	5×10^{-3}	0.2×10^{-3}	0.4×10^{-3}	
n_e	cm^{-3}	1.5×10^{20}	1.5×10^{19}	1.5×10^{19}	10 - $> 10^5$
n_i	cm^{-3}	0.5×10^{20}	0.17×10^{19}	1.3×10^{18}	
T	eV	8	17	16	0.1
$\overline{Z}$	-	3	6	12	0.05 - 0.4
v	cm s^{-1}	0.3×10^7	1.0×10^7	0.9×10^7	$\sim 10^7$
c_s	cm s^{-1}	0.2×10^6	3×10^6	1 x 10^6	
γ	-	5/3	5/3	5/3	
λ_{ii}	cm	10^{-7}	10^{-7}	10^{-8}	
λ_{ei}	cm	10^{-7}	10^{-5}	10^{-6}	
δ_{ii}	-	10^{-6}	10^{-5}	10^{-6}	10^{-7}
δ_{ei}	-	10^{-5}	10^{-3}	10^{-3}	
Re	-	10^6	10^5	10^6	10^7
Pe	-	100	1	1	10^6
η	-	600	30	50	1-10
M	-	2	4	7	10-40
χ	-	1	10	10	0.1-1

Table 6: Summary of the scaling parameter calculations for Cu and Au jets from cone targets propagating into 50 mb of He gas at a time of +5 ns. The top part of the table shows the values of temperature, density etc. used in calculating the scaling parameters, which are grouped together in the lower part of the table. Values for a YSO jet, included for comparison purposes, are taken from [1, 14, 16, 25, 44].

that both the ions and electrons can be treated as fluid. By +5 ns the temperatures of the electron and ion populations have equilibrated, and hence it is appropriate to model the hydrodynamics of the plasma using single-fluid, single-temperature equations. The high values of the Reynolds numbers, above 10^5 in all cases, indicate that viscosity is negligible. However, the estimates for the Peclet numbers in the narrow parts of the jets are of order 1, and hence, in contrast to the astrophysical case, thermal conduction may play a significant role in the plasma dynamics.

The use of the Mach number, density ratio and cooling parameter to characterise an astrophysical jet comes from astrophysical simulations in which a jet moves through an initially uniform volume of ambient gas contained within a computational box, with the density and speed of the jet where it enters the box remaining constant in time. In such a simulation, the ratio of the density of the jet as it enters the computation to that of the ambient medium, and the values of the cooling parameter for the shocked jet and ambient medium material in the shock structure at the head of the jet are useful parameters for characterising the morphology of the structure where the jet is interacting with the gas. The structure is less dependent on the value of the Mach number, as long as it is above a few.

For the experimental Cu and Au jets, the Mach number estimates are greater than 4 in the region where the interaction with the ambient medium occurs, though they are less than that of a YSO jet, and it is concluded that the value of this scaling parameter is acceptable when considering scaling. The estimate for the density ratio for the Cu jet at 500 μm is made near to the region believed to correspond to the jet shock, which is at about 550 μm, and hence the value of this parameter can be compared directly with those of YSOs. Both the Cu jet and YSO jets are overdense, though the ratio of 30 for the Cu jet is larger than that for a YSO jet. The estimate for the Cu jet relies on the value of 7 for the ionisation taken from the HYADES simulations; an error of ±1 in this quantity changes the result by ±20%. For the Au jet, the estimate of the density ratio is made at 440 μm, the tip of the region near to the target that has a qualitatively jet-like appearance. This is relatively far from the region believed to correspond to the jet shock, which is at about 650 μm, and the value of the density ratio is therefore likely to be an overestimate of the ratio nearer to where the interaction with the ambient medium is occurring. The HYADES simulation indicates that the ionisation could increase by about 3, equal to 25%, over this distance, while the electron density map in figure 65b suggests that the electron density remains roughly constant, at $\sim 0.8 - 1.5 \times 10^{19}$ cm^{-3}. Overall, the density ratio might reduce by a factor of up to ~ 2, making it comparable to that of the Cu jet, and still over twice that of the upper end of the YSO range.

Within both laboratory and astrophysical jets, the value of the cooling parameter is position-dependent. Due to differences in composition, density, ionisation and temperature it takes different values in the beam of the jet and the ambient medium ahead of it, and also in both the shocked beam and shocked ambient medium plasmas between the jet and bow shocks. For the experimental jets the cooling parameter has been estimated within the beam of the jet. Close to the surface of the Cu target the radiative cooling and hydrodynamic timescales are roughly equal, while far from both the Cu and Au targets the hydrodynamic timescales are shorter than the radiative timescales by an order of magnitude. After the jet shocks the ionisations, temperatures and densities will be larger than their pre-shock values, and both the thermal energy densities and the mean powers radiated will be larger. Making the rough approximations that the dependencies of the radiated powers on electron density and temperature are linear, and noting that for Cu the electron density value is roughly the same at 500 μm and at the estimated position of the jet shock, and likewise for the Au at 440 μm and at the jet shock, equations 27 suggest that the cooling parameter might be larger in the shocked

beam material, though only by a factor of a few. Due to its low atomic number, the value of the cooling parameter for the He gas both before and after passing through the bow shock should be much larger than for Cu or Au. Comparing the estimated cooling parameter values with the range for a YSO jet, the values of which are appropriate to the cooling of at least part of the shocked material between the jet and bow shocks, suggests that radiation is more significant for the hydrodynamics in the astrophysical case.

5.5 Chapter summary and discussion

In this chapter 1-D and 2-D simulations using the codes HYADES and h2d have been presented which model aspects of the Astra experiment described in chapter 4. 1-D simulations of a Cu target with a 1 μm Au coating show that at +5 ns the interface between the coating and the substrate would only have been about 20 μm in front of the target. At this time the plasmas observed in the interferometry data in chapter 4 were an order of magnitude larger than this, and the approximation made in that chapter that they were composed solely of coating material is justified.

In the Astra experiment, a full shot using a conical target consisted of a laser pulse striking the target and generating a plasma, the convergence of this plasma onto the axis of the cone to form a jet, and, if a gas was present, the interaction of the jet with the gas surrounding the target. While the density difference between the solid target and the gas prevented modelling of the jet-gas interaction with h2d, simulation of jets propagating into a vacuum was possible. For Cu cone targets it was found that the position of the critical electron density surface for the probe beam was located close to the front edge of the cone at +5 ns, suggesting that the fringe-free regions near the targets in the data presented in chapter 4 were not the result of the probe beam encountering plasma above the critical density; in section 4.3.3 of chapter 4 it is shown that these regions can be accounted for by refraction.

Due to the Lagrangian nature of h2d the spatial resolution of the simulations was high close to the target and lower further out. For both flat and conical targets the size of the well-resolved region varied with the atomic number of the target material. In front of a conical Cu or Au target it extended 150 μm or less. The axial extent of the convergence cone, at 275 μm, is much larger than this, and consequently only the inner part of the convergence region was modelled. For Al, a less massive element, the well-resolved region was slightly larger than the convergence cone at +5 ns. The simulation results

were complementary to the experimental data, providing information on the part of the plasma close to the target that could not be accessed with the optical probe beam. In order to model the behaviour of the jets far from the target, a code such as CHIC [103] could be employed. This has been used previously by Nicolaï *et al.* [2] to simulate the interaction of higher-energy jets from solid targets with a gas. Another option is to use a laser-plasma code such as HYADES to simulate the initial interaction between the laser and the target, and then to use the results of this preliminary work as inputs to a simulation using a modified version of a code used for astrophysical simulations such as ZEUS-2D [118]; using these codes such an approach has been taken previously by Leibrandt *et al.* [119].

In the last section in the chapter, the results of HYADES simulations were combined with the experimental results from chapter 4 to obtain order-of-magnitude estimates for the scaling parameters for Cu and Au jets from cone targets in 50 mb He. It was concluded that the plasmas could be modelled using inviscid, single-temperature fluid equations. However, in contrast to the astrophysical case thermal conduction may play a significant role. This result is usually the case for both laser and Z-pinch experiments, and represents one of the limitations of using these devices to model YSO jets. Near the heads of the experimental jets the estimates of the internal Mach numbers were low compared to the values for YSOs, while the jet beam-ambient medium mass density ratios in this region were estimated to be roughly three times the upper limit for a YSO. The estimate of the cooling parameter for the shocked material in the experimental jets suggests radiation was less important for the hydrodynamics of the working surface than in the astrophysical case.

6 The ILE Experiment

In this chapter the second of the two experiments, the ILE experiment, is described and its results discussed. The overall scope of the ILE experiment was wider than the Astra experiment, though still confined to laboratory astrophysics, and a wide variety of targets were shot. In this chapter the discussion of experimental details and results is limited to the 10 shots involving targets with a similar design to those used in the Astra experiment. The details of the experimental set-up are provided in section 6.1. In section 6.2 a selection of the data is presented, focusing mainly on the data obtained using a time-resolved optical self-emission imaging diagnostic. Finally, the chapter is summarised in section 6.3.

6.1 Experimental details

6.1.1 The main laser beams

The GEKKO XII laser system [7] has twelve separate beamlines, each using Nd-glass for the gain medium. In the ILE experiment, the second of the two target areas was used. In the centre of the target area is a spherical vacuum chamber. On one side is a conical extension attached to the side of the vacuum chamber. The twelve beams, having been piped around the target area, arrive at an array of twelve mirrors at one end of the conical extension. A single mirror redirects each beam to pass through first a crystal and then a lens which focuses the beam down onto the target. The crystals are used for frequency-doubling or frequency-tripling the beams from their 1ω wavelength of 1054 nm; three of the beams are set to be frequency-doubled to 527 nm, while nine are set to be frequency-tripled to 351 nm. In any shot, one or more of the beams may be used.

In the ILE experiment, four of the nine 3ω (351 nm) beams were focused onto the target in each shot. The energy per beam was typically $\sim 100-120$ J, and the pulselength of the beams was 500 ps. The beams were overlapped to create a focal spot of diameter 600 μm at the front surface of the target. The laser intensity on the surface of the conical and grooved targets is estimated to have been $\sim 2.3-2.7$ x 10^{14} W cm^{-2}, where account has been taken of the fact that the laser beams were incident on sloping surfaces. The large focal spot size was necessary due to the presence of defects in the manufactured targets: in sub-section 4.1, measurements of a conical target show the presence of an $\sim$ 300 μm diameter wide spike in its centre, and measurements of a

grooved target show that it had a flat bottom of width ∼ 200 µm instead of a pointed apex.

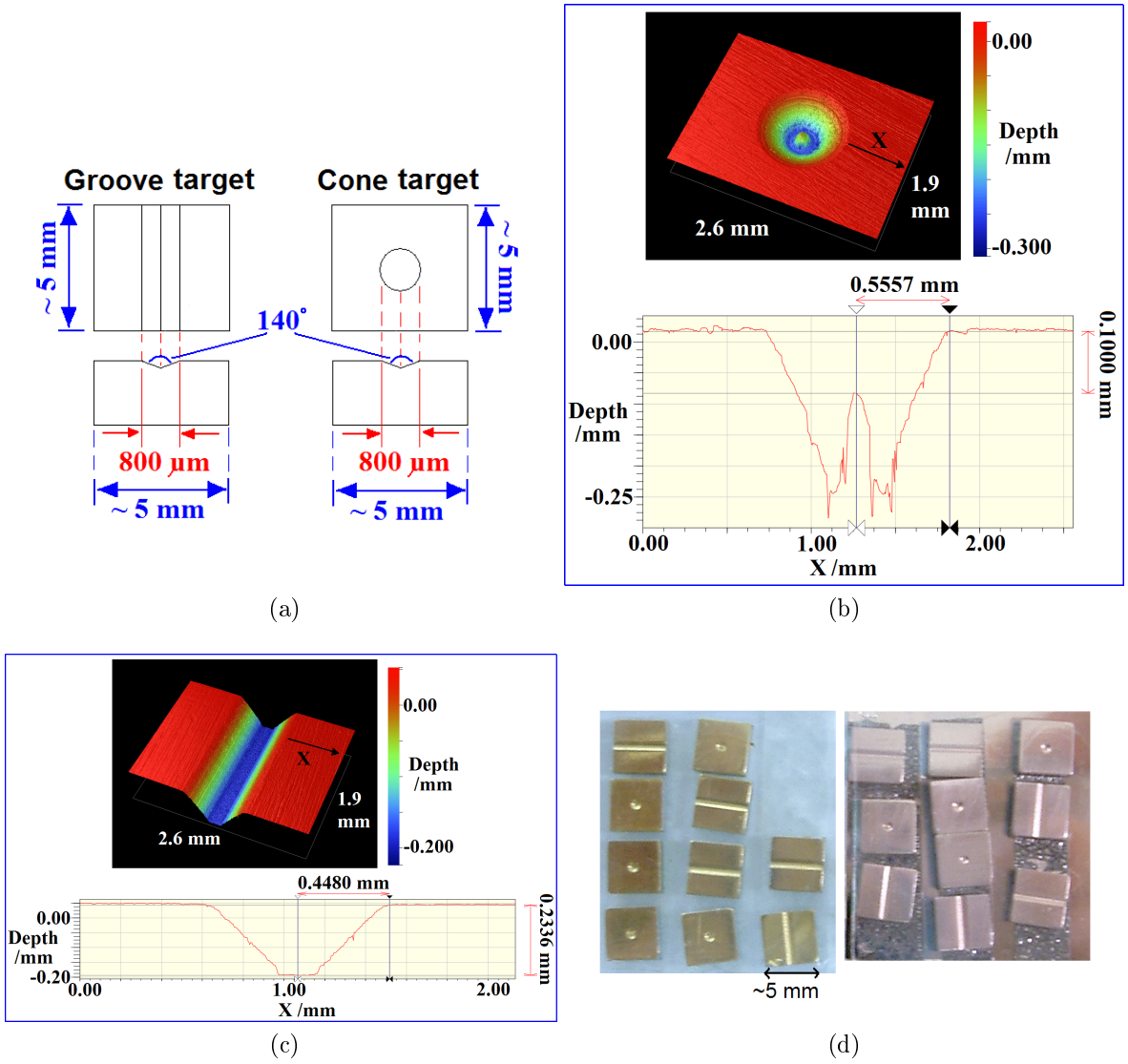

Figure 70: Targets used in the ILE experiment. (a) shows shows a sketch of the original conical and groove target designs while (b) and (c) show measurements taken from cone and groove targets manufactured for the experiment. The different target types can be seen in (d), which has Au targets on the left and Cu on the right.

6.1.2 The targets

The targets used in the ILE experiment were designed to be similar to those used in the Astra experiment. The two target types, cone and groove, are shown in the sketch in figure 70. In both cases a single impression was machined into a solid block of Cu alloy, which was then either simply polished, yielding a copper target, or polished and then coated with a thin layer of Au to give a gold target. The specifications for the target manufacture requested cones and grooves with widths of 800 µm and full opening angles of 140°.

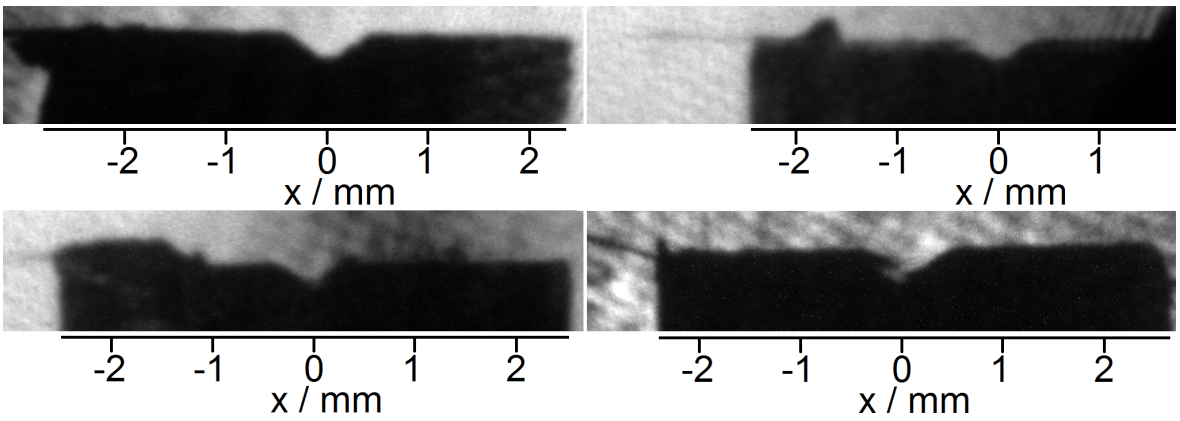

Figure 71: Shadow-images of the groove targets used in the experiment coming from the reference images for the shadowgraphy diagnostic.

After manufacture, one cone and one groove target were sent to the target fabrication facility at the CLF [104] for characterization by C. Spindloe: he used white light interferometry, the instrument being a Veeco-made Wyko NT9300 White Light Interferometer. The results of this are shown in figure 70. It can be seen that the conical target had an undesired peak on axis and had an opening angle not of 140° but nearer to 114°, while the groove target had a flat bottom and an overall opening angle of about 110° rather than 140°. The diameter of the conical target was 1.09 mm, while the width of the groove target was 0.89 mm. As only one target of each type was measured, it is not possible to accurately assess the variation in shape of supposedly identical targets. In the case of the groove targets, one can make some comment on the shape of the grooves from looking at the reference shots for the shadowgraphy diagnostic, shown in figure 71, which show the shadows produced by the targets when illuminated from behind with the probe beam. The grooves are visible end-on in the centres of the targets. Measuring from the images, groove width varies between 0.6 mm and 1.0 mm, and the opening angles vary from about 100° to about 125°. Although this suggests that there could have been a considerable variation in the parameters of the targets, it is an inaccurate way of measuring groove parameters, relying on the grooves being homogeneous right up to the edges of the target and also the rotation of the targets being set perfectly.

Whereas target strips were used in the Astra experiment, single-shot targets were used in the ILE experiment. In the Astra experiment strips were necessary to maximise the rate at which data could be gathered: the readout times of the diagnostic cameras and the time taken to align targets were both substantially greater than the minimum possible time between laser pulses, which is only 0.5 s for the Astra laser system. The situation with the GEKKO XII laser system used at ILE is very different. There,

the much higher pulse energies make it necessary for each of the main beams to cool for two hours between main shots being fired. In each shot, only four of the nine main beams which provide 3ω light were used, reducing the time between shots to one hour. This is a sufficient period of time to allow the use of single-shot targets: between shots the remains of the old single-shot target was removed from the vacuum chamber and a new target introduced and aligned. One reason for single-shot targets being advantageous is that the higher pulse energies of the GEKKO XII system mean that the survival of adjacent targets on a target strip is more of an issue. In the Astra experiment, debris and surface damage from a shot sometimes rendered the next target on a strip unusable; at ILE, the higher energies lead to a much greater volume of debris and severity of target damage. In addition, the target mount used to position targets within the vacuum chamber at ILE is not designed to handle strips of targets.

6.1.3 Ambient gas

It was not possible to use a static gas fill in the ILE experiment as the X-ray framing camera diagnostics required a vacuum in order to be used. An attempt was made to provide an ambient background for the jets to propagate into by setting up a gas jet nozzle below the target which could be triggered to release a puff of Ar gas from a gas bottle a few milliseconds before the main laser arrival at the target. However, a problem was encountered in setting the timing of the gas release, and consequently all of the data obtained from the ILE experiment were obtained in the absence of gas.

6.1.4 Diagnostics

A large array of diagnostics was fielded in the experiment, a schematic of which is shown in figure 72 on the following page. A Neodymium:Yttrium-Aluminium-Garnet (Nd:YAG) laser of wavelength 532 nm and pulselength 20 ns was used to generate a probe beam. Nd:YAG pulses were triggered using an electrical triggering signal sent from the main GEKKO XII laser system shortly before a shot in order to produce probe pulses synchronised with the main beams; the shot-to-shot uncertainty in the synchronisation, referred to as jitter, is estimated to have been ±2 ns. The probe pulses were sent past the target front surface perpendicular to target normal. The label "A" in figure 72 indicates the position of a collecting lens placed in the probe line after the target to collect the probe light and also self-emission from the plasma that happened to be travelling in the same direction. The collected light was filtered

to remove light coming from the target at the 1ω, 2ω and 3ω frequencies of the main GEKKO XII beams as at these frequencies the amount of light scattered or reflected from the target, or generated in the laser-target interaction, is large.

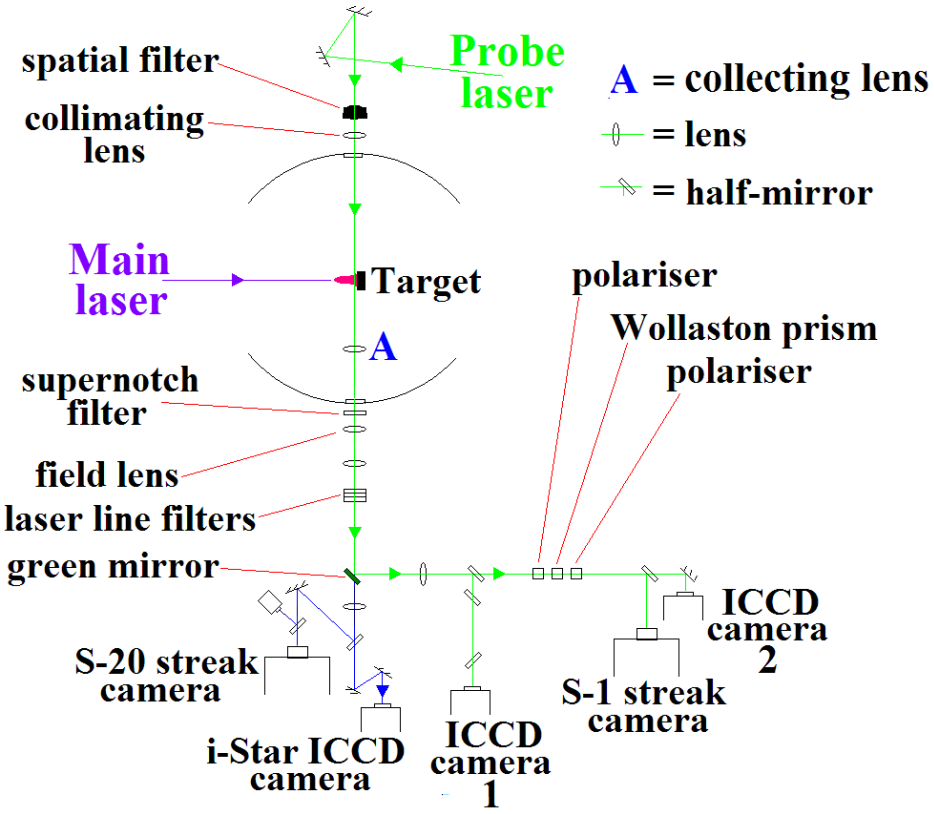

Figure 72: Diagram of the set-up for the ILE experiment as viewed from above. Not all filters are shown on the diagram.

Next, a "green" mirror was used to reflect the green probe light towards interferometry and shadowgraphy systems. These are discussed in the next paragraph. The light transmitted by the green mirror, predominantly self-emission from the plasma, was subsequently split, one part going to an Andor i-Star camera, the other part going to an S-20 streak camera. The i-Star was filtered with a 450 nm interference filter[16] and was used to take 2-D snapshots of the 450 nm self-emission from the plasma with an image exposure time below 2 ns. The streak camera was used to generate a 2-D image showing how the self-emission from a narrow slice of the plasma varied in time. It was created by sweeping the self-emission signal from a narrow slice through the plasma over a detector so that different parts of the detector recorded the self-emission signal from the slice at different times. The Andor ICCD camera diagnostic will be hereafter referred to as the GOI (Gated Optical Imager), and the streak camera diagnostic as the SOP (Streaked self-emission Optical Pyrometer).

[16]The wavelength of an interference filter is used to describe the wavelength it transmits rather than a wavelength it blocks.

The light reflected by the green mirror was also subsequently split. One part of the beam was sent to a gated CCD camera which was used to take 200 ps exposure time shadowgrams by imaging the target position onto the camera. In the absence of a plasma, these shadowgraphy image show the intensity pattern of the probe beam as it passes the target, with a shadow wherever there is an obstacle such as the target which physically obstructs its passage. With a plasma present, additional dark patches show up in the image indicating where the probe beam has encountered regions where the second derivative of the refractive index (its curvature) perpendicular to the probe beam was strong (see [92], chapter 4, pp. 112-115, for further information).

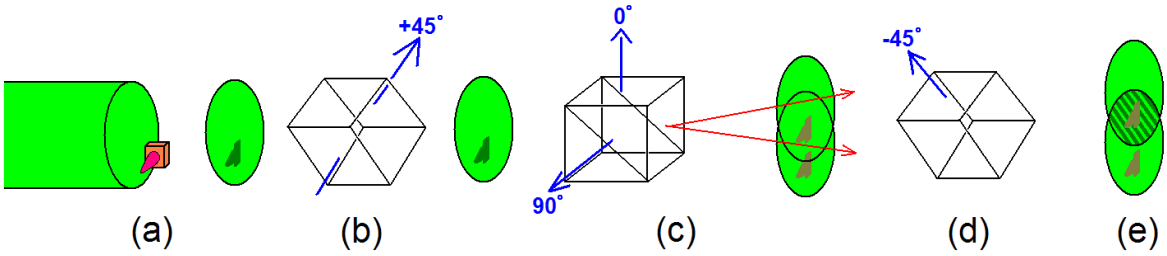

Figure 73: Cartoon showing how the Nomarski interferometer works. (a) The collimated probe beam passes the target. (b) The beam is linearly polarised at +45° by a polariser. (c) A Wollaston prism splits the beam into two diverging beams of polarisation angle 0° and -90°. (d) Both beams pass through a second polariser and are polarised at -45°. (e) The beams interfere where they overlap after the second polariser.

The second part of the beam reflected by the green mirror was sent through a Nomarski interferometer, the design of which is indicated schematically in figure 73. It works as follows. A probe beam, with a diameter larger than the size of the plasma near the target, was sent past the target perpendicular to target normal. This beam then passed through a polariser which selected one particular linear polarisation of the probe beam. The beam then travelled through a Wollaston prism. A Wollaston prism has a preferred direction such that light with its polarisation aligned with this direction exits the prism at one angle, while light polarised perpendicular to the preferred direction exits the prism at a different angle. The Wollaston prism was aligned such that its preferred axis lay at 45° to the polarisation direction of the first polariser. This means that the probe beam entering the Wollaston prism was split into two beams which subsequently diverged from one another. The diverging beams then passed through a second polariser with its polarisation direction either aligned with, or perpendicular to (it doesn't matter which), the polarisation direction of the first polariser. As a result, after the second polariser the diverging beams had the same linear polarisation and so they could interfere with one another where they overlapped.

After the interferometer, the signal was split between two detectors. The first detector was a gated CCD camera, which recorded a 2-D interferogram with an exposure time (gate width) of 200 ps. The second detector was an S-1 streak camera, which recorded a streaked (in time) image of a narrow strip of the interferometry image. The spacing of the optical components, including the focusing optics used to image the target onto the detector, were chosen to satisfy two requirements. First, the image of the plasma created by the focusing optics had to have a sufficiently small magnification to fit the limited size of the chip of the CCD camera, while being large enough to spatially resolve details of the plasma. Second, the beams diverging from the Wollaston prism had to have diverged such that the interference at the detector was between a part of the probe beam that had passed through the plasma, and a part of the beam that had not; this latter part then acted as a reference, taking the place of the reference arm in the Mach-Zehnder interferometer used in the Astra experiment. The Nomarski interferometer, in using a single, wide probe beam rather than two optical paths of equal length, can be much easier to set up than a Mach-Zehnder interferometer.

	Chip size / pixels	Field of view	Spatial Resolution	Magnification
GOI	1024 x 1024	7.7 mm x 7.7 mm	15 μm	1.7
SOP	1024 x 1024	10.4 mm x 28.7 ns		1
Shadowgraphy	1024 x 1024	5.7 mm x 5.7 mm	12 μm	1.8
Interferometry	1024 x 1024	4.9 mm x 4.9 mm	39 μm	2.0
Streaked Interferometry	1344 x 1024	9.1 mm x 17.1 ns	20 μm	2.6

Table 7: Details of the images obtained from the five main diagnostics used in the ILE experiment.

Table 7 contains a summary of the fields of view, spatial resolutions and magnifications for the five diagnostics mentioned above, specifically the GOI, the SOP, the shadow -graphy CCD camera, the interferometry CCD camera and the interferometry streak camera. Two additional diagnostics were used in the experiment, specifically X-ray framing cameras and an X-ray pinhole camera, both of which were used to record 2-D images of the X-ray emission from the interaction between the lasers and the target and from the resulting plasmas. For the cone and groove targets there is very little data from these instruments and they will not be mentioned hereafter.

6.2 Results

In the ILE experiment only 10 shots were taken onto the targets described in section 6.1. This results section includes data from all of these shots. The section is split into

two parts. First, in sub-section 6.2.1, the results gathered using all five of the main diagnostics for a shot onto a Cu cone target are presented and discussed. Then, in sub-section 6.2.2, the results from different shots are compared with one another.

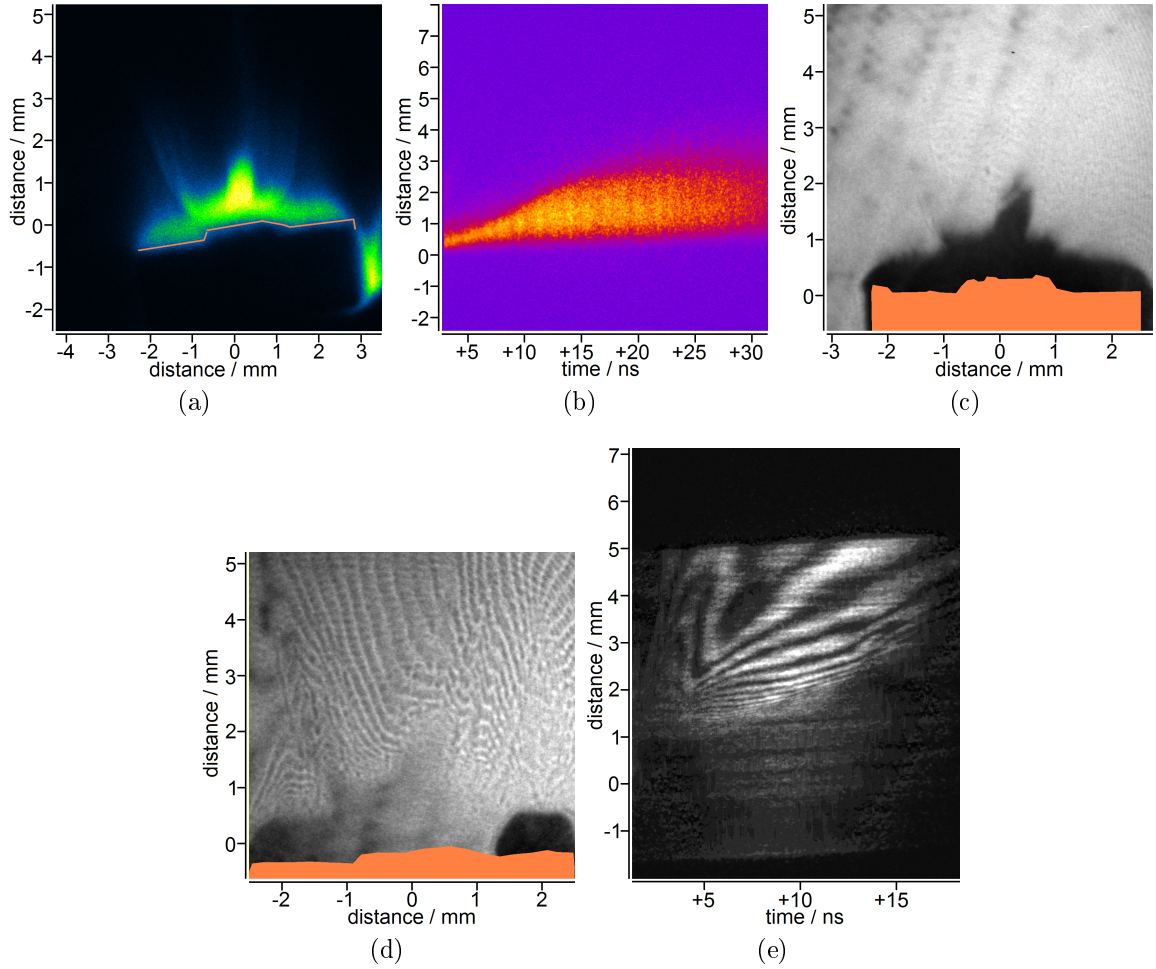

Figure 74: Data obtained from the five main diagnostics for a shot onto a Cu cone target. (a) Optical self-emission at +5 ns, obtained using the GOI. (b) Streaked optical self-emission for times between +2.75 and +31.45 ns, obtained using the SOP camera. (c) Shadowgram taken at +10 ns. (d) Interferogram taken at +10 ns. (e) Streaked interferogram for times between +1.26 and +18.36 ns. Target position is indicated in orange.

6.2.1 Presentation of the data gathered from a single shot

Figure 74 shows a set of data for a shot onto a Cu cone target. One image is shown for each of the five main diagnostics described in section 6.1. In the Astra experiment described in chapter 4, interferometry was the main diagnostic and the analysis and interpretation of interferometry data is described in detail in section 4.3 of that chapter. The analysis of the interferometry data obtained in the ILE experiment works in exactly the same way. However, the quality of the data obtained in the ILE experiment was not as high. The best data was produced by the GOI, and hence the discussion of the experimental results starts with this diagnostic.

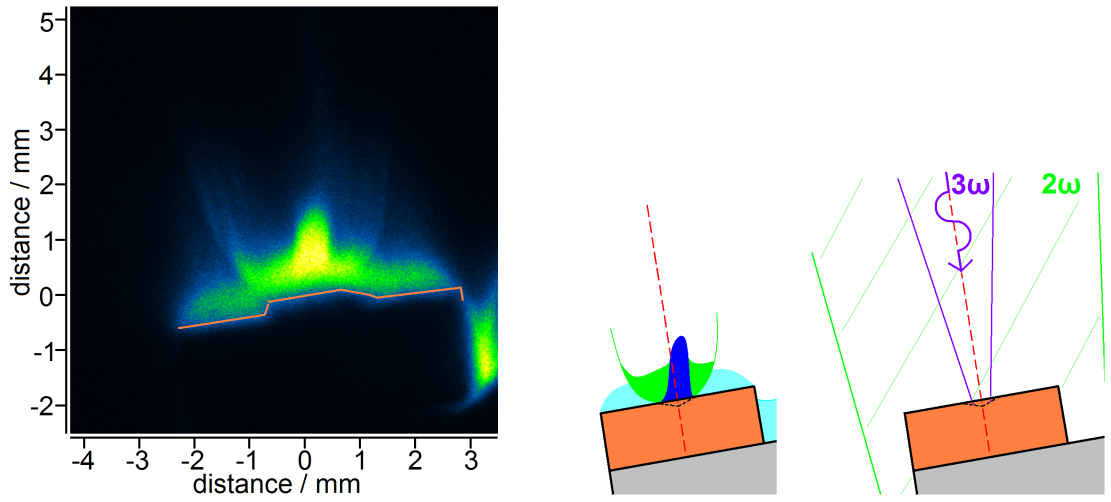

(a) (b) (c)

Figure 75: Interpretation of GOI data for a plasma from a Cu cone target at +10 ns. (a) The GOI data. (b) A cartoon dividing the plasma into three parts: a central jet, in dark blue; a plasma bar, in light blue; a pedestal between the central jet and the bar in green. (c) A cartoon showing the difference in focusing of the 2ω and 3ω main laser radiation, used to explain the features seen in (b); see text for details.

Figure 75 shows a duplicate of the GOI image in figure 74. It contains several features. In the centre of the image is a bright jet travelling slightly to the right of target normal. A very faint signal from the jet can be traced extending all the way to the top of the GOI image, indicating it extends over 5 mm from the target at this time, and hence that the plasma in the jet moves at an average speed of over (5 mm / 10 ns =) 500 km s^{-1} during its first 10 ns. Moving sideways from the central jet, on either side of this there appear to be several plasma filaments and then a very sharply defined, curved edge. Moving yet further out, plasma is seen near to the target surface reaching right to its outer edges. On the right hand side there is in addition a bright region down to the side of the target.

In interpreting the features seen in the image it is helpful to split the plasma into three parts as shown in figure 75b. In the centre, indicated in dark blue, is the jet leaving the cone. Near the target surface there is a "bar" of plasma extending to the edges of the target. This is indicated in light blue. Finally, there is the region of the plasma between the central jet and the bar, which will hereafter be referred to as the pedestal as it appears to extend further from the target than the bar, and the jet appears to emerge out of it. This is indicated in green.

The presence of the central jet does not need explanation. However, the presence of the bar does, as it is not obvious why, if the diameter of the focal spot was 600 μm, a fairly uniform bar of plasma should be seen extending all the way across the front

surface of the target, which has a width of about 5 mm. In section 6.1 it was described how four of the twelve beams of the GEKKO XII laser were used in each shot. Each of the beams arrived in the room where the vacuum chamber containing the target was located as a collimated beam at a wavelength of 1054 nm. They were directed around the room by a series of mirrors. In each case the final mirror directed the beam along a path passing through first a frequency-tripling crystal and then second a lens which focused the beam onto the target.

The frequency-tripling process at the crystals has a conversion efficiency of only 25-30%. Of the remainder of the light falling on the crystals, some passes straight through at the base frequency of 1ω while some becomes frequency doubled to 2ω. As a consequence, radiation at frequencies of 1ω, 2ω and 3ω would have reached the focusing lenses and been focused down towards the target. For these lenses, the focal length is not the same for all three frequencies. As a result, while the 3ω light was focused to produce a spot of diameter 600 μm, illuminating only the inside of a cone in the centre of a target, the widths of the beams of 1ω and 2ω radiation at the target were much wider, illuminating the whole of the front face of the target. This is sketched in figure 75c. Rough calculations suggest that the combined intensity of the defocused 1ω and 2ω beams would have been above 10^{12} W cm^{-2}. This is sufficient to ionise the surface of a target, and it is thought that this is the cause of the plasma bar seen in the data. This conclusion is supported by the observation of plasma in the bottom right of figure 75a, located to the side of the target and behind the front face: this region is inaccessible to plasma or radiation from the laser-target interaction in the cone, and can be simply explained if it is the result of direct illumination by a beam coming from the same direction as the main laser beams.

The green pedestal region in figure 75b has sharp outer edges. In explaining the cause of this it is helpful to summarise part of the discussion in sub-section 4.4. There, results from the Astra experiment for targets shot in a vacuum were presented. In the data shown it was seen that on either side of the central plasmas coming from the targets there were a pair of edges and the explanation for these features was discussed at length (see the discussion of figure 18). It was suggested that the edges could be where the plasma from the inside of a cone/groove was interacting with the plasma ablated from the flat target on either side of this. The series of jet experiments described in the papers Purvis *et al.* [68], Grava *et al.* [69] and Filevich *et al.* [70] were mentioned as they all show evidence of the production of features to either side of the main jet as a result of an interaction between two plasmas. Of the three papers, Filevich *et al.* was

potentially the most significant as the features at the sides in that experiment were unmistakably identified as resulting from the interaction between plasma formed in a groove target and plasma ablated from the flat surface on either side of the groove. However, the observation of edges in the plasmas from flat targets challenged this explanation. In this case, the geometry of the target does not naturally divide the plasma generated by the laser into two parts that later interact. In the ILE experiment, the different width of the 3ω beam at the target from the 1ω and 2ω beams resulted in the formation of two plasmas irrespective of the geometry of the target struck by the 3ω beam. It is a plausible conclusion that the edges of the pedestal mark the location of the interaction between these two plasmas.

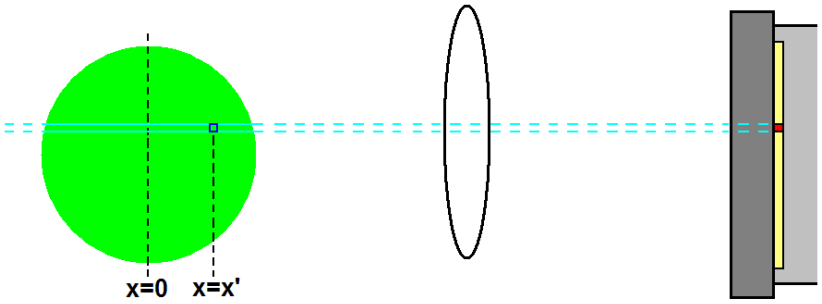

Figure 76: Cartoon to illustrate the formation of an image using the GOI. The green circle on the left of the image represents a plasma. Light emitted by plasma lying along the path indicated in blue is imaged by an optical system, represented by the lens, onto the red pixel of the yellow CCD chip in the camera on the right of the image.

A parallel can be drawn between the images from the GOI and the phasemaps extracted from interferometry data, the interpretation and analysis of which has already been treated in detail in section 4.3.2. There it was discussed how, when refraction of a probe beam is negligible, the phaseshift value of a pixel in a phasemap is related to the line-integral of the electron density along the straight line path taken by the probe in reaching the corresponding pixel of the detector. The value of a pixel in a GOI image is similar. This can be illustrated using figure 76. The optics lying between the plasma and the camera collect light emitted by the plasma and focus it to produce a two-dimensional image on the CCD chip within the camera. In the figure, radiation emitted by plasma lying on the path between the blue lines is imaged onto the pixel of the detector highlighted in red. The signal detected by this pixel is the line-integral along the blue path of a function which includes the radiative emission per unit volume. Features show up in GOI images where plasma is hot, and hence emits strongly, or dense, in which case there are a lot of particles emitting light, or thirdly where the plasma is deep, in which case the line-integral of the emission along the path can be large even when individual volumes of plasma only emit weakly.

In general, the signal detected is not simply proportional to the line-integral of the emission per unit volume along the path, as radiation emitted from deep within the plasma may be re-absorbed by plasma nearer to the detector and so fail to contribute to the signal. Two cases in which a relatively simple dependence of the signal on the emissivity can be obtained are when the plasma is either optically thin, meaning that absorption of radiation can be neglected, or optically thick, in which case absorption is very strong, with only radiation emitted near the outer edge of the plasma making it to the detector without being re-absorbed. In both cases, GOI data can theoretically be used to make temperature estimates provided the GOI has been absolutely calibrated: this is the process whereby a source of known intensity is placed at the target position and imaged onto the GOI camera to allow estimation of the losses in the optical system between the plasma and the camera. In the ILE experiment an in-situ absolute calibration was not done. However, losses were estimated by replicating the optical system in a different location.

In GOI images of the plasmas produced using cone targets, the sharp edges on the extreme left and right edges of the pedestal are seen to extend further from the target surface than the parts of the pedestal nearer to the centre of the target. As the plasma formed from a cone target is cylindrically symmetric, this is put down to an optical limb-brightening effect: in a GOI image, those paths through the plasma which are imaged to form the extreme left and right edges of the pedestal pass through a large physical depth of plasma at the edge of the pedestal. Hence, assuming that absorption is small, if the density and/or temperature in the pedestal is higher at the outer edges than nearer the centre, the signal at the extreme edges of the pedestal in the GOI image will be larger than that from nearer the centre, and consequently the extreme edges will be visible out to a much greater distance from the target surface. That the outer edges of the pedestal should be at a higher density and/or temperature than the inner part of the pedestal is consistent with the explanation of the edges of the pedestal as resulting from an interaction between two plasmas, as one would expect densities and temperatures to rise where a collision occurs.

While it is straightforward to infer that the plasma of the pedestal is optically thin, it is much harder to tell if the plasma in the central jet is optically thin or optically thick. An intensity pattern such as that observed, in which the centre of the jet appears brighter than the edges, can be obtained in either case.

Figure 77 on the following page shows a duplicate of the Streaked self-emission Optical

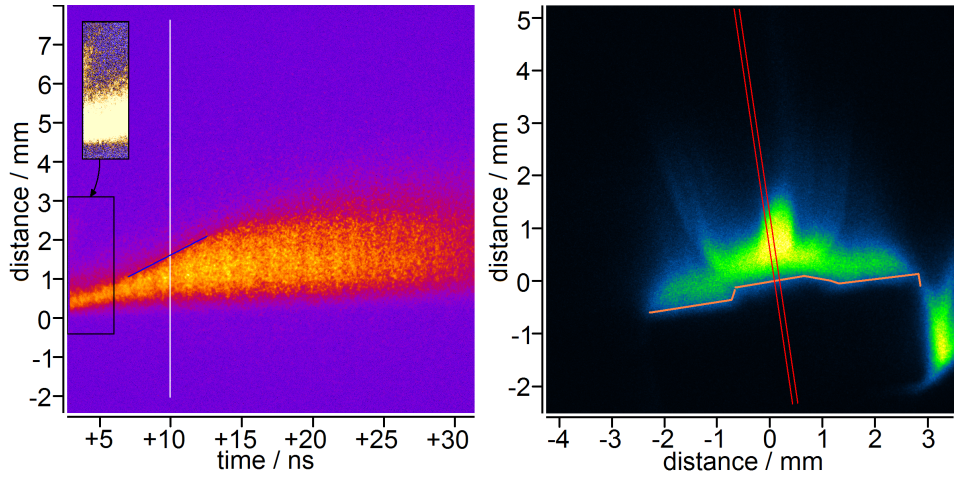

(a) (b)

Figure 77: Interpretation of SOP data. (a) shows raw SOP data, previously shown in figure 74b, with a white line added to indicate the time of +10 ns. The inset in the figure shows the plasma at early times with the contrast enhanced and the colour scheme adjusted. (b) shows the GOI image taken at +10 ns on the same shot, with a pair of red lines to indicate the approximate position of the channel that was swept in time to produce the SOP image.

Pyrometer (SOP) image of figure 74. A white line has been added to indicate the time at which the GOI image was taken on this shot, +10 ns. The SOP image was formed by streaking the image of a strip of the plasma seen by the GOI in time. The approximation position of the swept strip is indicated on the GOI image in figure 77b. GOI and SOP images are complementary. In both cases, the signal recorded is related to the radiation emitted by the plasma as it cools, which is known as self-emission. A GOI records an image with two spatial dimensions at a single instant of time and is useful for determining spatial temperature distribution. An SOP records an image with a single spatial dimension over a period of time and can provide information about how the temperature of a slice of a plasma changes in time.

A blue line has been added to the SOP data in figure 77a to indicate the movement of the front of the bright part of the signal. At +10 ns, the bright region has a depth of only about 1.2 mm. A much weaker signal is seen beyond the blue line, the slope of which corresponds to a speed of 190 km s^{-1}; this speed is far below the speed of the tip of the jet, which as already discussed averaged over 500 km s^{-1} during the first 10 ns. The GOI image shows that the jet propagates to the right of target normal, while the SOP was aligned to sweep the emission from a strip of plasma along target normal. As a result, the SOP does not record the emission from the tip of the jet as it propagates. The bright region which it does record corresponds to plasma near the target surface which is slower moving and at a higher density than the plasma in the jet further out.

The inset in figure 77 shows the region of the SOP image which lies within the black box after the contrast has been enhanced and the colour scheme altered. Along the extreme left hand side of the inset, which corresponds to a time of +2.75 ns, there is a faint yellow region. This region, which extends most of the way to the top of the inset, emits weakly and quickly fades from view. Unfortunately, the evolution of this feature at earlier times is outside the field of view of the camera, and hence it is not possible to estimate its speed.

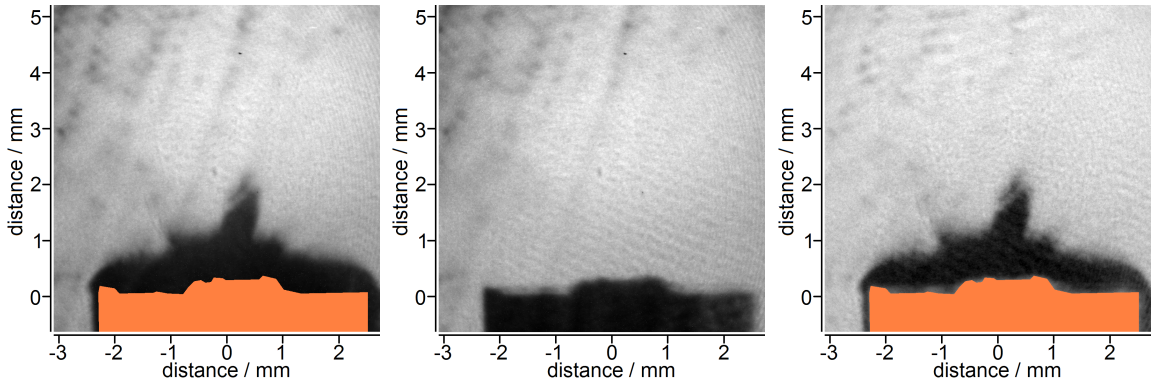

Figure 78: Interpretation of shadowgraphy data. (a) shows the raw data, previously shown as figure 74c, (b) shows the reference image taken before the shot, and (c) the result of subtracting the reference from the data image.

Figure 78a is a duplicate of the shadowgram shown in figure 74. Before the shot, a reference image was taken, shown in figure 78b which clearly shows the position of the target. In both the data and the reference images, a pattern of dark, diagonal lines is seen on the left hand side. By subtracting the reference image from the data image, figure 78c was produced. For this shot, this subtraction procedure works well, mostly removing the diagonal lines without removing or adding features to the data. For other shots, subtraction of a reference image was not so successful.

The features seen in the shadowgram are similar to those seen with the GOI. The central jet, the bar and the outer edge of the pedestal can all be made out. A light stripe appears to cut the central jet in two near its top: this stripe is an artefact produced by stray reflection of the light entering the camera. The edge of the pedestal has the appearance of thin filaments. Such features are indicative of the presence of steep electron density gradients in the plasma, such as those seen at shocks, causing a sharp deflection of the probe beam. This observation is consistent with the explanation for the edges of the pedestal as being the result of an interaction between two plasmas; this interaction could involve a shock, just as in the interaction discussed by Filevich *et al.* [70]. The jet and the bar both show up as dark regions. These have two possible causes:

either the probe beam has encountered plasma above the critical density, through which it cannot propagate, or the probe beam has encountered plasma in which the curvature of the refractive index perpendicular to its direction of travel is strong.

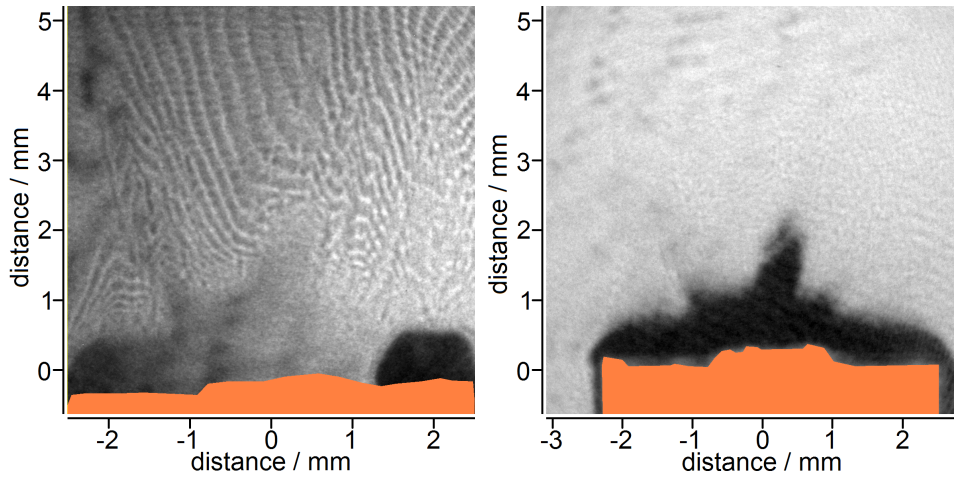

(a) (b)

Figure 79: Interpretation of interferometry data. (a) shows the raw data, previously shown as figure 74d. (b) shows the shadowgram for comparison. Both images were taken at +10 ns.

Figure 79a is a duplicate of the interferogram shown in figure 74. It can be seen that the features of the shadowgram, shown as figure 79b for comparison, are embedded in the interferogram.

At the start of this section it was mentioned how the interferometry data obtained in the experiment was of lower quality than that obtained in the Astra experiment. One cause of this was the limited field of view of the interferometry camera. In figure 79a, it can be seen that the distortions of the fringes from the pattern of parallel, evenly-spaced fringes seen in a reference image extend all the way to the edges of the image. As a result, there is no unshifted region to act as the zero point for determining absolute values of the phaseshift of pixels. In consequence of this, then even if the symmetry of the image was very good, Abel inversion to find values of electron density is not possible.

In the image, the left hand edge of the pedestal is straightforward to make out, extending the length of the left hand side. In the centre, the shadow of the central jet can be determined. The fringe pattern on the right hand side of the image is very complicated. There are several reasons for this. First, the jet is not aligned with target normal but points slightly to the right, leading to confusion between fringe distortions due to the central jet and the distortions due to the right hand edge of the pedestal; it is possible that there is even evidence of an additional plasma filament between the

central jet and the right hand edge of the pedestal. Second, the interferogram suffers from image overlap. This is illustrated in figure 80 below.

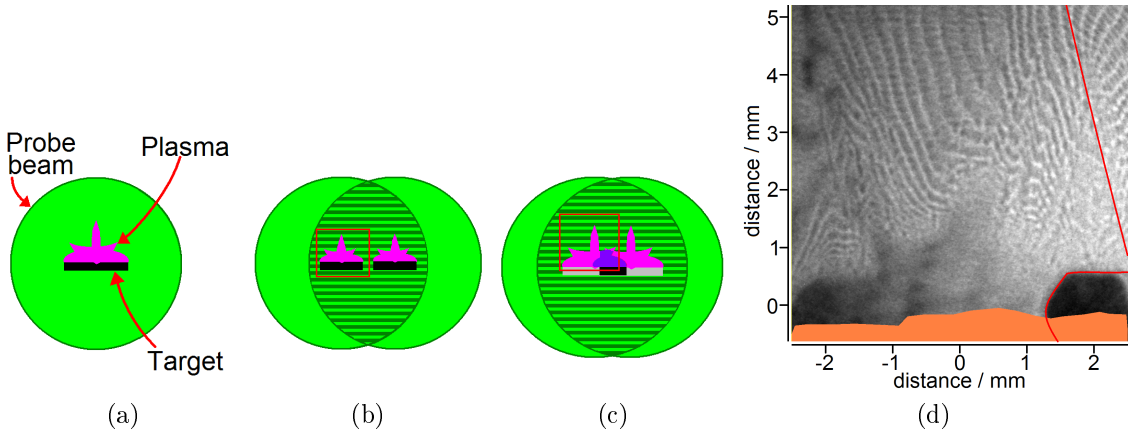

Figure 80: Cartoons to illustrate image overlap when using the Nomarski interferometer. (a) shows a cartoon of the probe beam after passing the target. (b) shows a cartoon of the ideal Nomarski set-up where no overlap occurs. (c) shows a cartoon of the situation in the ILE experiment where overlap did occur. (d) shows an interferogram from the ILE experiment with the positions of the edges of the bar and the pedestal of the overlapping image indicated in red.

The method by which an interferogram is generated by the Nomarski interferometer has previously been outlined in section 6.1. In summary: a wide probe beam is sent past the target where, as the beam is wide, part of the probe beam is affected by the plasma and part is left unaffected. This is illustrated in figure 80a. After passing the target, the probe beam is split into two; the pair of beams are then overlapped on the detector. In the ideal case this is done as in figure 80b, where the part of one of the beams that was affected by the plasma is overlapped with a part of the second beam that was unaffected by the plasma; in this way, the second beam acts as the reference arm of the interferometer. In figure 80b, the red box indicates a suitable field of view for the interferometry camera.

The situation encountered in the ILE experiment is shown in figure 80c, with the red box indicating the field of view of the camera used in the experiment. Instead of the overlap being between a part of the probe affected by the plasma and a part that was unaffected, on the right hand side of the image the overlap was between parts of the probe beam both of which had been affected by the plasma. The region of image overlap in the interferogram was quite substantial. This can be seen in figure 80d, where the left hand edges of the bar and the pedestal from the overlapping image are indicated in red.

Another factor limiting interferogram quality was the long pulselength of the probe beam. At 20 ns, this was far longer than the timescale on which the plasma evolved hydrodynamically, which was of the order of nanoseconds or below. By using a camera with a gate time (image exposure time) of 200 ps, it was still possible to take time-resolved interferometry measurements, though the motion of the plasma during the exposure time of the camera would have lead to significant blurring of the fringe pattern and would possibly also have contributed to the number of fringe splitting events. In 200 ps, the plasma of the jet, moving at a speed above 500 km s^{-1}, would have travelled over 100 μm; this corresponds to a distance of more than 20 pixels on the detector. Use of a shorter duration probe beam would have lead to a significant improvement in the results. The time taken for the probe beam to cross the plasmas, which had diameters of about 6 mm, was about 20 ps, corresponding to 2 pixels on the detector; reducing the pulselength below this would not have yielded an additional advantage in reducing motion effects.

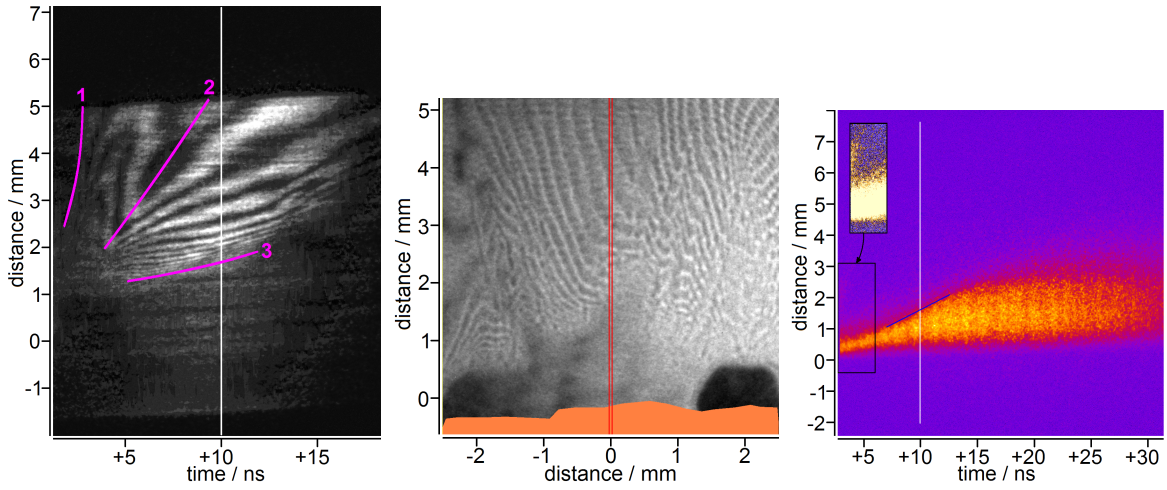

Figure 81: Interpretation of streaked interferometry data. (a) shows the raw data, previously shown as figure 74e, with a white line added to indicate the time of +10 ns. (b) shows the interferogram obtained at +10 ns with the approximate position of the channel swept to produce (a) indicated in red. (c) shows the streaked self-emission (SOP) data for purposes of comparison with (a).

Figure 81 shows a duplicate figure 74e. This image is the raw data obtained using streaked interferometry, the last of the five main diagnostics. The relationship between the streaked interferometry and the interferometric imaging discussed in the preceding paragraphs is essentially the same as the relationship between GOI and SOP data discussed previously. The streaked interferometry image is produced by sweeping the interferometry data from a thin slice of the plasma in time. The approximate position of the swept channel is indicated in the interferometry image shown as figure 81b.

In figure 81a three pink lines have been added. The interferometer was aligned such that the fringes lay parallel to the swept slice. This meant that the phase value was constant along the slice and so, unless a plasma was present to disturb the fringe pattern, the streaked image only contained this phase value and hence contained no interference fringes. Line 1 in the image marks the motion of the first plasma coming from the target that could be resolved by the interferometer. To the left of the line there are no fringes, while a pattern of fringes is seen to the right of the line. The initial gradient of the line corresponds to a speed of about 1400 km s^{-1}, and the line is seen to steepen with time.

Moving between lines 1 and 2, the fringes are seen to first become horizontal and then to turn back on themselves, before turning again at the line marked 2. At +6.5 ns, the same fringe can be seen at two spatial locations, one above line 2 and one below. As each fringe corresponds to a particular value of phaseshift, and at low values phaseshift is proportional to line-integrated electron density (see section 4.3), this implies that the line-integrated electron density encountered by the probe falls after the passage of the first plasma from the target, only to rise again at line 2, the gradient of which corresponds to a speed of 580 km s^{-1}.

Line 3 traces the advance of the dark region seen near the target surface in the interferometry image. In the Astra experiment it was found that the dark region at the base of a jet was caused by refraction of the probe beam rather than the probe encountering plasma above the critical density and being unable to propagate through it. One might suppose that the same explanation would be true in the ILE experiment, which is similar. In either case, the speed of 71 km s^{-1} to which the gradient at the left hand end of line 3 corresponds is not the speed of a bulk flow within the plasma.

The SOP image is included in figure 81c for purposes of comparison. Both the streaked interferometry and the SOP show the existence of a fast plasma at early times. Later on, both diagnostics show the presence of slower motions and it is tempting to try to connect the region of enhanced line-integrated electron density in the streaked interferometry with the bright region in the SOP data even though the measured speeds of these regions, at 580 km s^{-1} and 190 km s^{-1}, are markedly different. A possible explanation for the difference in speeds is that it is simply the result of the streaked interferometry and the SOP looking at different parameters of the plasma, the interferometry looking at electron density while the SOP signal is affected by both mass density and temperature.

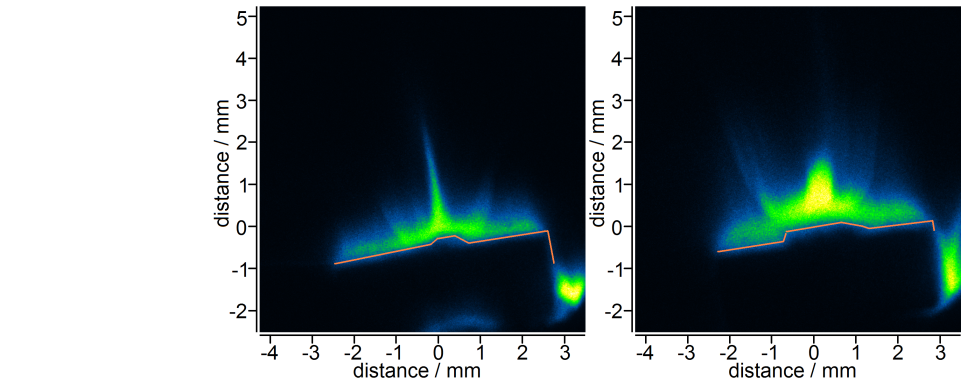

(a)

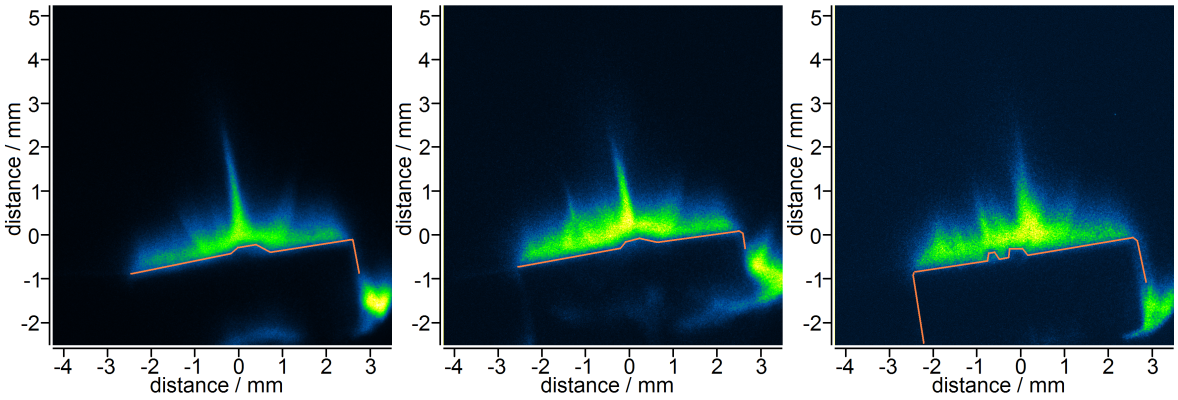

(b)

Figure 82: Jets from Cu cone targets. (a) Time series showing jets at +5 and +10 ns. (b) Image to show shot-to-shot variability of jets at +5 ns.

6.2.2 Comparison between the results of different shots

Figure 82a shows a time series for jets from Cu cone targets. At +5 ns there is a very narrow jet propagating away from the target along target normal. Later, at +10 ns, the flow along the axis has changed from being very narrow to being wider and more rounded. As with the time series obtained in the Astra experiment, the images in the series were obtained from different shots taken under nominally identical conditions. The colour scheme used for all the GOI images presented in this thesis is the same. However, the intensity scales used are different in each case.

In the experiment, three Cu cone targets were shot at +5 ns. Figure 82b shows the GOI images from all three shots. All three images show a jet emerging from the target along target normal. However, there is some variation between shots, with the symmetry of the jet in the left-hand image better than that of the other two.

Figure 83 on the following page shows the effects of changing the geometry of a Cu target. Figure 83a is the time series for cone targets shown previously as figure 82a. Next, 83b is a time series for jets from groove targets. Images are shown for times of +2.5, +5 and +10 ns. Finally, 83c shows a comparison between the jets from cone and

groove targets and the jet from a flat target at +5 ns.

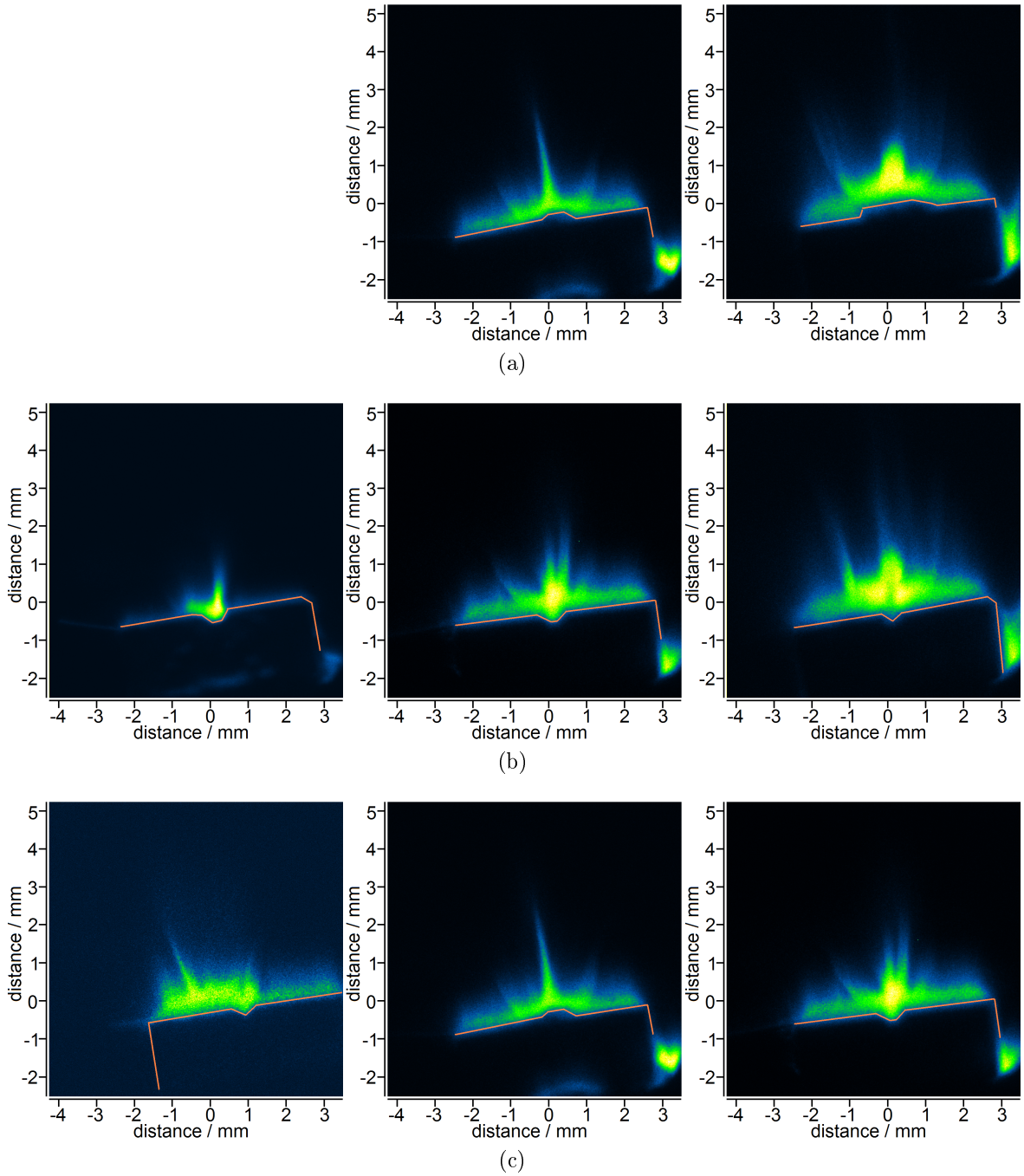

Figure 83: Jets from conical, flat and grooved Cu targets. (a) Jets from cones at +5 and +10 ns. (b) Jets from grooves at +2.5, +5 and +10 ns. (c) Jets from flat, conical and grooved targets, all at +5 ns.

The first image in the grooved target series, figure 83b, was taken at +2.5 ns, the earliest time at which a shot was taken in the experiment. The location of the bright region of the plasma to the left of the groove suggests that some of the 3ω laser energy has struck the target off-centre, explaining why the jet is sent to the right of target normal. In the +2.5 ns image only a single jet is seen emerging from the groove. However, for the shot imaged at +5 ns a pair of jets can be distinguished. In the image of the +10 ns shot, the bright green region has become more rounded, just as was seen

with the conical Cu targets. Ahead of this a pair of blue filaments can be made out, the one nearer the centre being brighter than the one further to the right. Near the original position of the groove, the self-emission has a minimum on the axis. This is the only shot on which this was seen, so it is not possible to say if this is a repeatable feature. It was, however, also the only groove shot for which the GOI image was taken as late as +10 ns. If the self-emission minimum on the axis is a genuine feature, it could perhaps be connected to variations in the density of the plasma lying within the groove between the centre of the target and the GOI camera: if the denser plasma on the axis has cooled more rapidly than the plasma to either side, one could see an on-axis minimum in the self-emission. The minimum could also be produced as the result of the denser axial plasma absorbing a much greater fraction of the light emitted by the plasma created by the 3ω beam at the centre of the target.

On the following page figure 84 shows a comparison of the results from Cu and Au targets at +5 ns. In all of the groove shots except figure 84d, the V-shaped end of the groove can be made out in the centre of the target both in the GOI image and, more clearly, in the shadowgraphy reference shot. Such a feature is not visible in figure 84d, suggesting that the groove target was mounted rotated through 90°; in this case, one does not see the plane in which plasma from the sides of the groove converges, but rather the transverse, convergence-free plane.

When shooting Au, the same features are seen as when shooting Cu, although the edges of the pedestal are harder to make out. With Cu, only a single jet is seen from a cone target. However, for Au the jet appears to split part way up. Alternatively, it is possible that there are two jets which only appear to be close together, the components of their motion perpendicular to the page being very different. For both Cu and Au grooves, a pair of jets is seen, lending weight to the suggestion that there is in fact a pair of jets coming from the Au cone target.

However, there is a third possibility. In [58], Farley *et al.* show an X-ray self-emission image (their figure 2 (a)) taken at +1.1 ns for a jet coming from an 800 μm diameter Au cone shot using 1125 J of 351 nm radiation. Their image is very similar to that shown in figure 84b, with a narrow jet appearing to split starting from about 700 μm from the front of the target. They then present a simulation result (their figure 2 (b)) obtained using the code LASNEX [105] which replicates the observed on-axis minimum in the self-emission. They explain this as resulting from radiative emission within the jet: as the rate of a plasma's radiative emission has a strong density dependence, it is possible

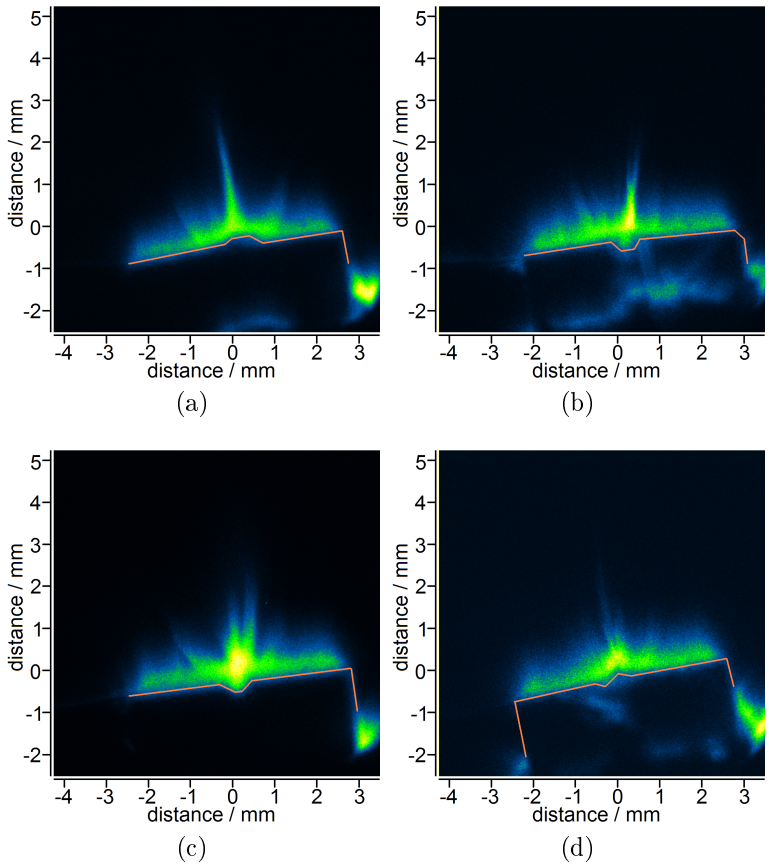

Figure 84: Comparison between jets from Cu and Au targets. (a) Cu cone (b) Au cone (c) Cu groove (d) Au groove.

that in the dense core of the jet the temperature drops faster than at the edges. In this case, it is possible that the self-emission from the edges of the jet appears stronger than the self-emission from the centre. This is an optical limb-brightening effect, just like that whereby the extreme left and right edges of the pedestal are visible to a greater distance from the target surface than the parts of the pedestal nearer the centre.

The similarity between the ILE experiment and that of Farley *et al.*, and the visual similarity between the self-emission images, make this an intriguing possibility, though there are some differences in the self-emission images, that of Farley *et al.* being taken at X-ray rather than optical wavelengths and much earlier in time, at +1.1 ns instead of +5 ns. In their paper, Farley *et al.* show an image (their figure 3 (a)) of the transmission of X-rays through the jet. These were generated by laser-illumination of a uranium foil. The transmission is related to the optical depth of the plasma, which is a line-integrated function of the mass density. Their image shows the presence of a single axial jet. In the ILE experiment no diagnostic was used to measure mass density, and it does not seem possible to unambiguously identify the behaviour of the Au jet.

6.3 Summary and discussion

The ILE experiment discussed in this chapter was designed to be similar to the Astra experiment discussed in chapter 4, with the idea of applying the scaling relations to scaling between the Astra and ILE experiments. From table 8 below it can be seen that the cone targets used in the ILE experiment were very similar to those used by Farley *et al.* and Shigemori *et al.*. It is worth highlighting here some significant differences in the results obtained from these experiments, particularly given that Shigemori *et al.* used the same laser system as that used in the ILE experiment, specifically the GEKKO XII laser system at ILE.

	Farley *et al.*	Shigemori *et al.*	ILE experiment
Diameter	800 μm	1.6 mm	1 mm
Full opening angle	120°	120°	114°
Construction	solid cones	solid cones	coated cones
Targets per strip / block	1	1	1
Materials used	Au	CH, Al, Fe, Au	Cu, Au

Table 8: A comparison of the conical targets used in the ILE experiment with those used by Farley *et al.* [58] and Shigemori *et al.* [1].

First, whereas Farley *et al.* and Shigemori *et al.* only report the use of cone targets, a wider range of target geometries were shot in the ILE experiment, with both flat and groove targets also being used. Second, the diagnostics used in the experiments were different. Both Farley *et al.* and Shigemori *et al.* primarily used X-ray diagnostics. Using X-ray radiography, in which measurements of the transmissions of pulses of X-rays through the jets were made, the optical depths of the jets at X-ray wavelengths were measured; these optical depths are related to the mass densities within the jets. Framing cameras were used to take time-resolved and time-integrated images of the X-ray self-emission from the jets, and while Farley *et al.* fielded a pinhole camera to take time-integrated images, Shigemori *et al.* used an X-ray streak camera to obtain information on the time-evolution of the self-emission from thin strips of the plasmas. In addition to these X-ray imaging diagnostics, Farley *et al.* used Thomson scattering to make electron temperature measurements. The diagnostics used in the ILE experiment, on the other hand, were used to make measurements at optical wavelengths. An optical probe was used for interferometry, with both time-resolved images and streaked data being obtained, and also for shadowgraphy; all three of these yield information related to the electron densities within the plasmas. Additionally, optical self-emission

measurements were made by using a GOI to take time-resolved images and an optical streak camera to record the time-evolution of the self-emission from a slice of each plasma.

Not only were some of the plasma properties measured in the ILE experiment different, but the measurements were also made on different space and time scales. The X-ray radiography and time-resolved X-ray self-emission measurements were used to study the axial convergence of the plasma from the cones and the behaviour of jets at early times; data is shown in [58] and [1] for axial distances from the target of less than 2 mm, and at times no later than +1.6 ns. The optical measurements in the ILE experiment were used to record data about the jets later in time, and over much larger scales; data were taken for times no earlier than 1.26 ns, and over axial distances of about 5 mm or above.

Of the five main diagnostics used in the ILE experiment, the GOI proved to be the main diagnostic, taking very clear images on each shot. In terms of making a comparison between the Astra and ILE experiments, it would have been most straightforward if the interferometry images had produced the best results, as the main diagnostic in the Astra experiment was interferometric imaging. However, the interferometry data from the ILE experiment was of lower quality than that from the Astra experiment. There were several causes contributing to this. The long pulselength of the probe beam meant that the motion of the plasma during the exposure time of the camera would have led to a significant reduction in image quality, and the quality of the optics used in the interferometry system was not as high. Also, the images suffered from image overlap, and the field of view of the camera was too small to capture the whole of the plasmas.

From the data it was found that each plasma had three components. In the centre was an axial feature coming from the cone or groove. This was produced by the main beams, which were frequency-tripled before the final focusing lenses. This process is only 25-30% efficient, and as a result first and second harmonic radiation also reached the focusing lenses and was directed towards the target. As the focal lengths of the lenses are frequency-dependent, the widths of the first and second harmonic beams were large when they reached the target, leading to the ablation of material across the entirety of the flat surface surrounding the central cone or groove. This lead to the appearance of a bar of plasma extending across the whole of the target surface. The third feature in the data was the pedestal, a region of plasma surrounding the central jet and extending further from the target surface than the bar. This feature

was bounded by a pair of sharply-defined edges which, it was hypothesised, mark the site of the interaction between the plasma generated by the main beam and the axially-moving plasma of the bar. The edges were seen to be visible further out from the target surface than the majority of the plasma within the pedestal, and this was attributed to a limb-brightening effect.

The optical self-emission data for Cu cones showed a narrow jet at +5 ns. By +10 ns, the plasma flow near to the target surface appeared more rounded, while a trail of self-emission was seen extending continuously from the target to the edge of the image, approximately 5 mm away, giving the jet an average speed in excess of 500 km s^{-1} over the first 10 ns. The results for Cu groove targets were somewhat different. While for a shot imaged at +2.5 ns a single plasma was seen emerging from the groove, for the shots imaged at +5 and +10 ns two jets were seen, both propagating to the same side of target normal. In the +10 ns image the flow near the target was more rounded than at +5 ns, as with the cone target, and trails of self-emission extending continuously to the edge of the image were also apparent. The brighter of the trails was the nearest to target normal.

The appearances of the plasmas from Au targets were similar to those from Cu, with central jets, bars and pedestals all visible. As with the Cu, a pair of jets was produced by the groove target. The result from the Au cone target was interesting: the jet appeared to split into two part way up. Comparing this result with simulated and experimental X-ray self-emission images published by Farley *et al.* [58], it was suggested that this might be an optical illusion. As the radiative emission within a jet varies non-linearly with the density, the temperature in the core of a jet can fall below that at the less dense edges. Where limb-brightening is operative, this can result in the edges of the jet appearing brighter than the centre in self-emission images. If the centre is faint enough, it would appear that the jet splits into two. Given that the results of Farley *et al.* were also obtained for an Au cone target of similar shape, and at a similar energy, this explanation seems plausible, even though the ILE data was obtained at optical rather than X-ray wavelengths. However, without the use of a diagnostic that measures mass density it cannot be confirmed whether a single axial jet was present beyond the splitting point.

The lack of quantitative measurements of properties such as temperature and mass density in the ILE experiments means that it is not possible from the experimental results alone to evaluate whether the scaling relations discussed in chapter 3 can be

applied to these experiment, either to scale to the jets created in the Astra experiment or to YSO jets. The similarity of the ILE experiment to the earlier experiments of Shigemori *et al.* and Farley *et al.* suggests that the scaling parameters calculated for their plasmas should be similar to those of the plasmas in the ILE experiment. For an Au target, this implies that, within the first nanosecond, the dense plasma on the axis within the convergence region should have had a Mach number of order 15 and a ratio of radiative cooling and hydrodynamic timescales of order one. Over the length and time scales for which observations were made using the optical diagnostics in the ILE experiment, the values of the scaling parameters can be expected to be different. Carrying out simulations of this experiment, and combining the results with those obtained experimentally in order to estimate the scaling parameters, in a similar manner to that done for the Astra experiment in chapter 5, is a potential avenue for further work.

7 Final Summary

In the preceding chapters of this thesis, work has been presented relating to the creation of scaled models of jets from Young Stellar Objects (YSOs) in the laboratory. Chapters 2 and 3, taking the form of surveys of astrophysical research into YSOs and previous attempts at jet modelling, were used to set the context for experimental and simulation work discussed in chapters 4, 5 and 6. In this final chapter the work presented in the thesis is summarised. It is split into two sections. In the first of these, section 7.1, the context of the thesis is reviewed and after this, in section 7.2, the experimental and simulation work.

7.1 Summary of chapters 2 and 3, the context for the thesis

In chapter 2, YSOs and their associated jets were discussed. It is thought that YSOs form from the gravitational collapse of dense regions of molecular clouds. As these regions collapse, the densities and temperatures in their centres rise, and eventually protostars develop. The protostars are surrounded by accretion discs and, outside the planes of the discs, lower density envelopes of material. As a protostar continues to accrete material from the disc and the envelope, gaining mass on its way to becoming a main sequence star, jets of plasma are ejected perpendicular to the disc at speeds of the order 100 km s^{-1}. This occurs via a magnetohydrodynamical process associated with the accretion of mass by the protostar, though the exact mechanism is still under discussion. The jets, seen in some cases to propagate over distances above 5 parsecs, produce spectacular shock structures where they are in collision with the interstellar medium. These structures, known as working surfaces, have a bow shock at the front, where the interstellar medium is ionised, heated and accelerated. At their rear, there is a jet shock where the beam of material from the protostar is decelerated. Between the two shocks lies a contact discontinuity, where the shocked jet and shocked interstellar medium materials are in contact and interact.

Simulations show that the morphology of the working surface produced when a jet enters an ambient medium, and its development in time, are strongly affected by the rate at which shocked material within the working surface emits radiation. When the length scale over which shocked material cools to a low temperature is large compared to the radius of the jet, which can be taken as a measure of the hydrodynamic lengthscale, the pressure within the shocked material forces it out sideways, and it forms a high

pressure cocoon (if the material comes from the jet) or shroud (if the material comes from the ambient medium) surrounding the jet beam. If, on the other hand, the shocked material cools quickly, over a lengthscale short compared to the radius of the jet, the pressure driving the material out sideways into the cocoon or shroud is significantly reduced, and instead the material contributes heavily to a thin shell which forms at the contact discontinuity. This shell is then disrupted by instabilities such as the Rayleigh-Taylor instability. If the shocked ambient medium material cools quickly, the ram pressure of the shell dominates the thermal pressure and, instead of the bow shock being a smooth arc, the bow shock takes on the shape of the shell.

In YSO jets, the mass density within the jet beam is typically larger than that of the interstellar medium ahead of the jet. In such a case, the bow shock moves quickly through the interstellar medium, with a similar speed to that of the material in the jet beam, and the material through which this shock passes is rapidly heated to a high temperature. The deceleration of the material in the beam at the jet shock is relatively weak, with the fall in speed being of the order of the difference between the speed of the material in the beam and the speed of the bowshock. As a result, the beam material is not as strongly heated. The length scales over which the shocked beam and shocked interstellar medium materials cool can be very different. The beam material, being only weakly shocked, can cool to a low temperature in a distance short compared to the radius of the jet. The interstellar medium material, being shocked to a much higher temperature, takes longer to cool to an equivalent temperature. In such a case, the shocked beam material is the main contributor to the shell at the contact discontinuity, and the long cooling length of the shocked interstellar medium maintains the bow shock as a smooth arc.

While magnetic fields are important in the launching of the jet, their importance for the continued collimation of the jet beam as it propagates, and for the structure of the working surface, is thought to be fairly minor. One way in which they can be significant is in limiting the compression of post-shock material: where radiation cooling is significant, the mass density of the material rises as the material cools in order to maintain the hydrodynamic pressure. If the magnetic field in the material being shocked has a component parallel to the shock front then, even if the magnetic field in the pre-shock material is weak, the magnetic pressure, which is proportional to the square of the flux density, can become large enough to prevent a further rise in density.

The structure of the working surface of a YSO jet can be described by a small set

of parameters. First, there is the ratio of the density in the jet beam to the density of the surrounding ambient medium. Second, there are the cooling lengths of the shocked beam and interstellar medium materials and, if the radiative cooling functions of these materials cannot be expressed as a power law, the absolute temperatures of the materials. The dependence of the structure on the internal Mach number, as long as it is above a few, is relatively weak.

In the first part of chapter 3, the possibility of performing mathematically rigorous scaling between qualitatively similar hydrodynamic plasma flows with different spatial scales was discussed in detail. In the case of a pair of purely hydrodynamic systems, if they start off geometrically similar, i.e. the spatial distributions of mass, velocity and density in the two systems differ only in spatial scale and not in functional form, the systems subsequently evolve as scale models of one another, though on different timescales, provided a single relationship between the magnitudes of the densities, velocities and pressures in the two systems is satisfied. When magnetic fields are dynamically significant, scaling is again possible, though an additional relationship between the magnetic fields and the pressures in the two systems has to be satisfied.

In both the purely hydrodynamic and magnetohydrodynamic cases, it is necessary that the fluids be dissipationless, i.e. that energy and momentum transport due to viscosity and thermal conduction are negligible. The significance of viscosity and thermal conductivity within a flow is measured using a pair of dimensionless parameters known as the Reynolds and Peclet numbers. These numbers are defined as ratios of terms in conservation equations: the Reynolds number is defined as the ratio of the viscous and advective force terms in the momentum conservation equation, while the Peclet number is defined as the ratio of the thermal conduction and advective terms in the energy conservation equation. When their values are much greater than one viscosity and thermal conduction can be neglected. Additionally, where magnetic fields are important it is necessary that the diffusion of the magnetic field is negligible. In this case, the magnetic field is effectively "frozen in" to the plasma, and magnetic field lines move with the flow. The significance of magnetic diffusion is measured using a third dimensionless number known as the magnetic Reynolds number. While the Reynolds, Peclet and magnetic Reynolds numbers can be calculated at each point within a flow, it is usual to calculate single values of these parameters using characteristic values of properties such as density, pressure and magnetic field strength in order to assess the significance of viscosity, thermal conductivity and magnetic diffusion for a flow as a whole.

In addition to the requirement that the plasmas be dissipationless, it is assumed in deriving the hydrodynamic and magnetohydrodynamic scaling relationships that the electron and ion populations within a flow are approximately in thermal equilibrium, and hence that the fluid can be described with a single temperature. Further, it is assumed that the fluids can be described with polytropic equations of state. These equations contain a parameter known as the polytropic index. Scaling assumes that the functional forms of the distributions of this parameter are the same in the two systems.

When radiative processes are dynamically significant, scaling requires that additional relationships relating the properties of the systems involved in the scaling are satisfied. Although this makes the design of scaled experiments more difficult, it is this case that is of interest when attempting to make scale models of the working surfaces of YSO jets, within which radiative cooling is important. Both dimensional analysis and Lie group analysis, of which the Lie group analysis is the more general technique, have been used to find scaling transformations for hydrodynamic systems in which radiative emission is important (e.g. [39, 41]). In the derivations it is assumed that either a plasma is optically thin, in which case radiation emitted within the plasma leaves it without being re-absorbed, or optically thick, in which case the radiation mean free path is short, and radiation transport is diffusive. As far as the author is aware, no solutions have been provided in the case that radiation transport is non-local, i.e. that radiation emitted in one region can travel some distance through a plasma before being re-absorbed. The transformations that have been found assume that the radiative flux in the energy equation may be represented by at most two terms with power law dependencies on pressure and mass density.

In order to formally establish that two systems are scaled models of one another, it is necessary first of all to show that the continuity, momentum conservation and energy conservation equations have the same form for the two systems; in the case of magnetohydrodynamic systems, there is also an additional equation derived from Maxwell's equations. Next, it has to be shown mathematically that a scaling transformation exists such that the form of the equations is left unchanged when one of the systems is spatially re-scaled. Finally, it remains to be shown that at some point the two systems are geometrically similar, and that the values of mass density, velocity etc. satisfy any constraints required by the scaling transformations when this is so. The systems evolve identically, to within constant scaling factors, after this point.

Having outlined the mathematical basis for performing scaled hydrodynamics experiments in the first half of the chapter, in the second half of chapter 3 previous work relating to the creation of scale models of astrophysical jets in the laboratory was reviewed. Three kinds of apparatus have been used for this: high-intensity lasers, Z-pinches and co-axial plasma guns. The relevance of the various experiments to YSO jets varies. In some of them, the relation is purely qualitative. Others are more quantitative, with it being shown that some of the parameters of the laboratory jets, for example their Mach numbers, match those of YSO jets.

In high-intensity laser experiments, the front side of a target is illuminated by a pulse of laser energy, leading to the creation of a jet which is subsequently observed using a range of diagnostic instruments. The experiments can be split into two categories depending on whether the jets are produced on the front sides or the rear sides of the targets. In the case of rear-side jets, the laser pulse drives a shock through the target leading to the generation of a flow of plasma when the shock breaks out of the rear surface. By shaping the target, or channeling the flow of plasma after it emerges from the rear surface, a collimated jet is produced. If there is a medium such as a low-density foam or a region of gas behind the target, the interaction of the jet with this medium can be studied. In the case of front-side targets, the laser pulse ablates material from the front surface of the target. By using a shaped target, a collimated jet can be produced from this ablation plasma and, if there is a medium in front of the target, the subsequent interaction of the jet with this medium can be studied.

A large number of different experiments have been done using both rear-side and front-side targets. Many of the jets produced from them have had some parameters matching those of their astrophysical counterparts. For example, in [5] Loupias *et al.* report an experiment in which a shock was driven through a low-density foam contained within a metal cone, resulting in a jet emerging from the narrow end of the cone into a gas. The ratio of the mass densities in the jet and the gas was similar to the density ratio between the beam of a YSO jet and the interstellar medium, and the Mach number of the jet was similar to that of an astrophysical jet. However, whereas radiative cooling is significant in YSO jets, at least in their interaction with the interstellar medium, the jets produced in these experiments were non-radiative. In another experiment reported by Gregory *et al.* [57] shocks were driven through a pair of foils arranged in a "V" shape. The plasmas produced at the rear surfaces of the foils collided on the plane of symmetry of the V, with the result that their motion transverse to this plane was at least partially arrested, the collimation of the flow in the plane perpendicular to the

plane of symmetry being seen to be better than that in the plane of symmetry. Bow shock structures were observed when shots were taken in a gas. In the experiment, the Mach number of the jet was similar to that in a YSO, and radiation was of some dynamical significance. However, the ratio of the densities in the jet and the gas was much higher than the density ratio for a YSO jet and, due to the target geometry, the jet was not cylindrically symmetric.

Astrophysical modelling has not been the only motivation for rear-side jet experiments. In [51], images of Al jets propagating through a polystyrene block are used to compare the modelling capabilities of three different simulation codes. As with the jets of Loupias *et al.* the jets produced in this experiment were non-radiative.

Of the experiments involving front-side targets, three configurations are of particular relevance to the experimental work presented in this thesis. In the first, laser radiation is used to ablate the inner surface of a cone, producing a flow of plasma which converges on its axis. There, the radial motion of the plasma is brought to zero as the plasma collides, leaving a collimated jet. As the jet leaves the convergence region, it subsequently expands as a result of its internal pressure. Using this approach, Farley *et al.* [58] produced a collimated, radiative jet from an Au cone target with an internal Mach number similar to that in a YSO jet. Shigemori *et al.* [1] expanded upon this work, showing that jets made from materials with a higher atomic number produce narrower jets as a result of the stronger radiative cooling in the core: the stronger cooling promotes energy loss, and hence pressure loss, in the core, which results in the density rising further under the ram pressure of the material converging from the sides of the cone. In this experiment, internal Mach numbers similar to those in YSO jets were again produced. However, the experiments of Farley *et al.* and Shigemori *et al.* were performed in a vacuum and so the the shock structures present in YSO jets were not observed.

In later experiments using the second and third experimental configurations, a dependence of jet collimation on atomic number was also seen. However, it is other facets of these experiments that are of primary interest. In the second experimental configuration, jets were again created in a vacuum, this time by illuminating hemispherical groove and triangular groove targets with a line-focused laser beam, producing truly two-dimensional jets on the axes of the grooves. Experimental results using this configuration are reported by Purvis *et al.* [68], Grava *et al.* [69] and Filevich *et al.* [70] in papers published in 2007, 2008 and 2009, respectively. At less than 1 J, the energies

of the laser pulses they used were significantly lower than those used in the other laser experiments reported in this summary, which had energies ranging from 13 J to over 1 kJ.

In the third experimental configuration a jet was created by illuminating a flat target with a laser pulse. In [2] and [66], which describe the same experiment, a gas jet was used to provide an ambient medium, either He or Ar, for jets created in this manner to propagate into. In shadowgraphy images, all three of the discontinuities within the resulting working surfaces can clearly be made out at certain gas pressures. Using simulation results, a Mach number of 6 was estimated for the flows, slightly below that of a YSO jet. However, radiation was dynamically significant in the experiment and the ratio of the jet and gas mass densities is similar to the mass density ratio for a YSO jet propagating into the interstellar medium.

While there is some cross-over between the results of jet experiments using high-intensity lasers and experiments using a Z-pinch, currently there are also results that have only been produced using one or other of these techniques. Whereas laser experiments have succeeded in creating working surfaces in which all three discontinuities are visible, using a Z-pinch the effect of a plasma cross-wind on a jet and the collision of a jet with a second plasma lying in its path have both been studied. Additionally, it has proven possible to create jets with angular momentum using a Z-pinch.

In terms of modelling the launching of a jet, the Z-pinch and gas gun techniques have both been used to create axial jets from an plasma flow that was initially purely radial and confined within a plane perpendicular to the axis. These experiments simulate in a qualitative way the "magnetic tower" jet launch scenario.

7.2 Summary of experimental and simulation work

In chapter 4, the first of two experiments using high-intensity lasers to create jets by illuminating the front sides of cone and groove targets was discussed. The subsequent chapter, chapter 5, describes the simulation of aspects of this experiment using the radiation hydrodynamics codes HYADES and h2d. After this, in chapter 6, the second of the experiments is described.

The motivation for performing the two experiments was slightly different. The first, the Astra experiment, was motivated by a desire to explore three factors that could affect the collimation of YSO jets by varying the parameters of scale models created in

the laboratory. The three factors were radiative emission, the presence of an ambient medium and the presence of a magnetic field, and in the experiment the first two of these were investigated. While the Astra experiment was designed with the intention of using the scaling relations to relate the laboratory jets to YSO jets, the second experiment, the ILE experiment, was motivated by a different application of the scaling relations, specifically that of scaling between two different laboratory experiments. In consequence, the targets shot in the second experiment were chosen to be similar in design to those used in the first. In both of these the basic jet creation method was the same. A high-intensity laser was used to ablate the surface of a conical or grooved target. This produced a flow of plasma which converged onto the axis, where its motion transverse to the axis was brought to zero, with the result being the production of an axial flow. This flow could later radially expand as a result of its internal thermal pressure. This jet-creation method is not in itself new, having been used previously by, for example, Farley *et al.* [58], Shigemori *et al.* [1] and Purvis *et al.* [68].

	Farley *et al.*	Shigemori *et al.*	Astra experiment	ILE experiment
Diameter	800 μm	1.6 mm	200 μm	1 mm
Full opening angle	120°	120°	140°	114°
Construction	solid cones	solid cones	coated cones	coated cones
Targets per strip / block	1	1	48	1
Materials used	Au	CH, Al, Fe, Au	CH, Al, Cu, Au	Cu, Au

Table 9: A comparison of the conical targets used in the Astra and ILE experiments with those used by Farley *et al.* [58] and Shigemori *et al.* [1].

Table 9 shows a comparison of the cone targets used by Farley *et al.* with those used by Shigemori *et al.* and those used in the two experiments. It can be seen that they differ only in minor details with two exceptions. First, the diameters of the cones in the Astra experiment were much smaller than those in the other experiment. In the Astra experiment, the energy of the laser pulses used to ablate the cones was three orders of magnitude below that used in the other experiments. Consequently, it was appropriate to use cones of a smaller diameter as smaller volumes of plasma were created. Second, the high-repetition rate of the Astra laser system meant that the time taken to align targets between shots was one of the factors limiting the rate at which data could be gathered. As a result, strips containing multiple targets were used. In the other three experiments, the minimum time between shots was limited by the time taken for the laser beamlines to cool and hence single targets could be used; their use was advantageous, as at higher laser energies the damage caused to the target and the

amount of debris generated are both greater, making the survival of targets on a strip more of an issue.

In the first experiment, several results of interest in terms of astrophysical modelling or basic laser-plasma experiments were obtained. By varying the material used to coat a conical target, jets with a range of atomic numbers were created and the collimation of these jets was studied. Jets from higher atomic number targets were seen to produce narrower flows that took longer to decollimate, consistent with results obtained previously in experiments using both lasers and Z-pinches.

Jets in 50 mb of He gas were seen experimentally to have a similar dependence on atomic number to jets in a vacuum. In the case of Cu and Au, while at an early times (+5 ns) the collimation of flows in vacuo and in the gas was similar, at +10 ns the flows in the gas were narrower. The width of the jet for the more radiative material, the Au, was much smaller than that for the Cu; in the phasemap, the sharpness of the jet tip is particularly striking. For this material only shot was taken at this time in 50 mb He, and two in vacuum. Considering this, and also that the symmetry of the jet in the gas was better than that of the shots into a vacuum, it is not possible to draw a firm conclusion as to the relative extents to which the presence of the ambient medium and shot-to-shot variation contributed to the improvement in the collimation. It is expected ([101]) that an ambient medium and radiative cooling can act together in a non-linear way to affect the collimation of a jet: the confining effect of the ambient medium keeps the density within the jet higher for longer, enhancing the effect of the radiation cooling, which depends non-linearly on the electron density. Experimentally demonstrating this non-linear combined effect is an area in which further work could be done. As far as the author is aware, the experimental study in this thesis of the variation of jet collimation with atomic number, for supersonic jets propagating into an ambient medium, is the most comprehensive, if not the only, experimental study of its kind that has been presented.

The shock structures set up in the interactions between jets and ambient gases were also of interest. When creating jets from Cu cone targets in a sufficiently high pressure of Xe, both the bow shock and the contact discontinuity between the shocked jet and shocked gas material could be resolved. When using He, at a pressure of 100 mb faint arcs that could correspond to the jet shock were seen. The bow shock, on the other hand, was very distinct even at a much lower gas pressure. These result are consistent with previous results for Cu jets reported by Nicolaï *et al.* in [2], and the results obtained

in the Astra experiment bear a strong resemblance to simulation results published in that paper. While the observation of working surfaces in a laboratory experiment is not new in itself, the 0.5 J pulse energies used in the Astra experiment are much smaller than the energies used in previous laboratory jet experiments. Exceptions to this are the experiments reported by Purvis *et al.* [68], Grava *et al.* [69] and Filevich *et al.* [70], all of which used pulses of less than 1 J. However, the jets created in their experiments were created within a vacuum and were only two-dimensional. The results of the Astra experiment show that the same physical principles govern the behaviour of a plasma at a lower energy scale. In addition, they show that laboratory experiments which model the interaction of jets with ambient media can potentially be done using university-scale as well as national-scale laser facilities.

While simulation of the jets in a vacuum was possible using h2d, even if only close to the target for materials with a high atomic number, the large differences between the densities of the solid targets and the gas atmospheres in the Astra experiment prevented modelling of the interactions between the jets and the ambient media. Just as with the experimental work, previous simulations modelling the interaction of a laser-created jet with an ambient medium have only been done for jets with larger spatial and energy scales than the jets created in the Astra experiment. A code such as that used by Nicolaï *et al.* [2] could be used to extend the range of modelled experiments to lower energies. This would be useful for designing improved experiments for the future.

The results of the Astra experiment which are of interest from the perspective of basic laser-plasma experiments rather than astrophysical modelling concern the ionised channel created by the laser on its way to the target and the behaviour of the bow shocks. The intensity of the Astra pulse was sufficiently high to directly ionise gas atoms via tunnel ionisation. For sufficiently high pressures of all the gases used in the experiment (He, N_2 and Xe) the channel ionised by the laser on its approach to the target could be clearly made out in the interferometry results. For a shot in 52 mb N_2, the ionisation within the channel at +4.6 ns was estimated from the experimental data and was found to be at over 30% of its maximum value.

At early times, the bow shocks created by jets from conical, flat and grooved targets in high pressures of He were observed to have a two-component structure. At large angles to the axes of the jets, the bow shocks had a (hemi-)spherical appearance. In line with the axes of the jets, the bow shocks were observed to extend further from the target than the parts of the shock front on either side. As this is true irrespective

of whether the axes of the jets were aligned with target normal, it is concluded that this is due to the material in the jets exerting a driving influence on the shocks. Later in time, the bow shocks were seen to have additional components aligned with target normal. A possible explanation is that these features result from the bowshocks being able to propagate more quickly through the plasmas in the laser channels, for which the projected direction in the interferometry images is aligned with target normal.

A final aspect of bow shocks that was studied was their shape, at a time of +10 ns, when using various different types and densities of gas. Although the shape of the bow shock in Xe was somewhat different from those in He and N_2, at least at low pressures, for all three of these gases the axial extent of the shocks was seen to reduce as the gas density was increased. This is consistent with the shock speed being lower in the denser medium. The behaviour in the radial direction was found to be counter-intuitive. At higher pressures, the diameters of the shocks were found to be larger. The correct interpretation of this result is not currently known to the author.

In terms of experimental technique, the Astra experiment had both good and bad features. The repetition rate of the Astra laser, at up to 2 Hz, was much greater than that of the laser systems used in most other laboratory jet experiments. In addition, the Astra laser is "on demand", meaning that users can take shots as and when they desire; on larger systems, taking a single shot is a lengthy procedure and shots can only be taken while a team of trained laser-operation personnel is available. These factors, combined with the long experimental period of six weeks, enabled data to be gathered from a large number of different configurations of target geometry, target material and gas conditions during the experiment.

The main diagnostic, optical interferometry, was used very successfully, producing images with a high enough spatial resolution to resolve the insides of jets while having a large enough field of view to show the entirety of the bow shocks formed in gases at times as late as +20 ns. The pulselength of the probe beam, at 2 ps, was short enough that the images were not greatly affected by motion blurring. In future experiments, it would ideally be possible to use a probe beam with a shorter wavelength, as such a beam is less affected by refraction and would be able to provide data on the region closest to the target surface from which data could not be obtained in the Astra experiment. In addition to optical interferometry, the only other diagnostics used in the experiment were a time-integrated X-ray pinhole camera and a time-resolved end-on optical imager. While these both produced images of the radiation emitted by the plasma (not shown in

this thesis), in neither case has it been possible to extract numerical values of plasma properties. In a future experiment it would be advantageous to use a wider range of diagnostics in order to measure properties such as mass density, temperature and ionisation. To measure mass density, X-ray radiography could be used. Temperature measurements are more difficult to make; a measurement using Thomson scattering has previously been made in a jet experiment by Farley *et al.* [58]. Spectrometry could also be useful, for example for learning about the ionisation states present in a plasma [69].

In the second of the two experiments, the ILE experiment, fewer shots were taken than in the Astra experiment. In total, six cone targets, three groove targets and one flat target were shot, all in vacuum. The plasmas created from cone and groove targets were found to have a three-component structure. In the centre was an axial jet produced by the main 3ω beam, which deposited its energy within the cone or groove in the centre of the target. Far from the axis, a bar of plasma was seen extending right out to the edges of the target. This was created by wide beams of defocused 1ω and 2ω light accompanying the main beam. In between the central jet and the bar was a pedestal region, seen to extend further from the target surface than the bar, but not as far as the jet. The edges of the pedestal were very clearly defined and were explained as being the site of an interaction between plasma from the centre of the target which had been ablated by the main beam and plasma ablated further out where only the 1ω and 2ω beams were active.

The self-emission signal from jets produced from Cu cones was seen to be narrow at +5 ns. By +10 ns, the region of self-emission near to the target had become more rounded. A weak self-emission signal extended right to the edge of the field of view of the self-emission imaging diagnostic, a distance of about 5 mm. Similar behaviour was seen with Cu groove targets, though in this case pairs of jets were seen coming from the central groove rather than the single jets seen with the cone targets. The jet from an Au cone target was interesting, appearing to split into two part way up. Comparison of the optical self-emission result with an X-ray self-emission result obtained in a similar experiment by Farley *et al.* [58] suggests that it is possible that this is an optical illusion. In a radiative jet, the dense core cools faster than the less-dense outer regions at early times as the rate of radiative emission is a non-linear function of the electron density. At later times, the emission from the hotter outer regions can be stronger than that from the centre. In this case, if the outer regions of the jet are optically thin, in a self-emission image the edges of the jet can appear brighter than the centre as a

result of limb-brightening, giving the appearance of a jet splitting into two. However, the limited data available for the Au jet means it is not possible to choose between this and other possible explanations of the observed behaviour. As with a Cu groove target, an Au groove was seen to have produced a pair of jets at +5 ns.

The number of diagnostics used on each shot in the ILE experiment was greater than that in the Astra experiment. There were five main diagnostics: time-resolved self-emission, streaked self-emission, interferometric imaging, shadowgraphy and streaked interferometry. Previous experiments by Shigemori *et al.* and Farley *et al.* [58, 1] using conical targets similar to those employed in the ILE experiment fielded mainly X-ray diagnostics and focused on investigating the dense interior of the convergence region at times below +1.6 ns. In contrast, the main five diagnostics in the ILE experiment all used optical wavelengths and show plasma behaviour outside the convergence region at times of up to +10 ns. In this regard, the results of the ILE experiment complement previous investigations.

While the number of diagnostics used in the ILE experiment was large, it is not possible to extract values for many of the plasma properties, for example mass density, needed to assess whether the scaling relations can be applied. The similarity of both the laser and target conditions used in the experiment to those used by Shigemori *et al.* and Farley *et al.* suggests that the scaling parameters for the inner regions of the flows at early times should be comparable to those reported for their experiments. For an Au cone target, this implies that within the first nanosecond the axial flow within the convergence region would have had an internal Mach number of order 15 and a ratio of radiative cooling and hydrodynamic timescales of order 1.

For the Astra experiment, values for the electron density, jet velocity and Mach number obtained experimentally were combined with HYADES simulation results to estimate the values of the scaling parameters for Cu and Au jets from cone targets in 50 mb He at +5 ns. For both of these materials, the collision lengthscales for both ions and electrons were much smaller than the jet radius, and from this it was concluded that the plasma in the jets could be modelled as a fluid. The estimates for the Reynolds numbers were all more than five orders of magnitude greater than one, indicating that the effects of viscosity were negligible. However, towards the tips of the jets the estimates of the Pe number were of order one, and hence, in contrast to the astrophysical case, thermal conduction may play a significant role in the plasma dynamics. The combination of negligible viscosity and non-negligible thermal conduction is a common feature of

laboratory experiments using both lasers and Z-pinches, and represents one of the limitations of their modelling capability.

The estimates of the Mach numbers were smaller than those of YSO jets, for which the range is about 10-40. However, near their tips the jets were still several times supersonic, and the structure of a working surface is only weakly dependent on the value of the Mach number as long as it is above a few. Near the heads of both the Cu and Au jets the ratio of the density in the beam to that in the ambient medium was estimated to be about 30, three times the upper limit for a YSO, for which the range is typically 1-10. This suggests that when using a higher pressure of He, above 150 mb, or when using a gas with a higher atomic number, the density ratio for a Cu or Au jet would have been similar to that of a YSO.

Finally, assessment of the value of the radiative cooling parameter yielded a value of order 10^1 for the shocked beam material for both Cu and Au jets, and the value for the shocked He gas can be expected to be much larger than this. From this it was concluded that radiation is less significant for the hydrodynamics than in a YSO, for which values of the cooling parameter of 0.1-1 can typically be found within at least part of the shocked material within a working surface. The similarity of the cooling parameter estimates for Cu and Au is surprising as Au has a much higher atomic number. However, it has a simple physical explanation. The cooling parameter depends on the ratio of the thermal energy density to the average power per unit volume radiated by the plasma. Although the radiated power was larger for Au than for Cu, the Au also had a higher ionisation, implying that there were more free electrons contributing to the thermal energy density. At the time for which the cooling parameter was estimated, the higher thermal energy density roughly compensated for the higher radiated power.

To conclude, the work in this thesis shows that by using a sub-Joule laser it is possible to create 3-D plasma jets with scaling parameters similar to many of those inferred for Young Stellar Objects. The experimental part of the thesis demonstrates the advantage of using such a laser. The high repetition rate of Astra made it possible to take many shots and explore a wide parameter space: the work presented encompasses time series in vacuum, and also in gases of various types and pressures, and the use of flat, groove and conical targets made of a number of different materials. To collect such a large volume of data is not possible using higher-energy facilities, such as the GEKKO XII laser. The computational work highlights some of the challenges of modelling jets, and

the experimental and simulation results are complementary: experiments can quickly explore many target and gas configurations which are hard to model numerically, while a modelling capability is central to assessing quantities that are either difficult or impossible to measure. The scaling parameter estimates in the thesis were obtained by combining experimental measurements and the results of 1-D modelling, and show that, as in other laboratory experiments, it is thermal conduction that limits the application of scaling.

Appendix: Extraction of Phasemaps From Interferometry Data Using IDEA

The procedure followed when using IDEA for interferometry analysis can be split into eight steps:

1. Convert the raw data and reference images recorded by the camera into bitmap images and open these images within IDEA.

2. Create masks for the data and reference images, such that all regions containing either no interference fringes or a scrambled fringe pattern are masked.

3. Perform a 2-D Fast Fourier Transform (FFT) on the masked data image to produce a 2-D image in spatial frequency space. The use of FFTs requires images to have a pixel size of 2^n x 2^m where both n and m are integers. For the large-area CCD images taken in the Astra experiment this requirement was automatically met; the images from the high-resolution camera had to be modified before processing.

4. Create a mask for the 2-D frequency space image. The more of a frequency space image that is masked, the greater the range of spatial frequencies that are filtered out in the inverse FFT in step 5; this has the effect of increasing the smoothing of the final image, and comes at the expense of reducing the level of detail.

5. Perform an inverse FFT on the masked frequency space image to create a modulus-2π image. This step creates a smoothed version of the original bitmap image, but instead of the pixels being assigned values according to a bitmap encoding, each pixel of the smoothed interferometry image is assigned a value between $-\pi$ and π depending on its shading; the lightest pixels of the light fringes receive values near $+\pi$, while the darkest pixels of the dark fringes receive values near $-\pi$.

6. Unwrap the modulo-2π images to produce a phasemap. A single pixel of the image, lying in a region of zero observable fringe shift, is chosen and assigned the value zero. Then, starting from this pixel, an algorithm is used to scan across the image and calculate the difference in phase between every other pixel and this starting pixel. For example, if a pixel is separated from the reference pixel by three "whole" fringes, one whole fringe consisting of a light fringe-dark fringe

pair, the phase of the pixel is separated from that of the reference pixel by a phase of (3 x 2π =) 6π.

7. Repeat steps 3 to 6 for the reference interferogram. In choosing a reference image where more than one is available, it is important that the fringe orientation and spacing is the same as in the unshifted part of the data interferogram, and that the position of the target in the reference does not cover parts of the image in which there are interference fringes in the data image. Further, in the analysis it is important that the same reference pixel is used as was used in step 6 for the data image.

8. Subtract the phasemap coming from the data image from the phasemap coming from the reference image to give a final, reference-subtracted phasemap. This phasemap can be masked using the masks generated in step 2 to cover up regions of the phasemap where the pixel values are meaningless.

Glossary and List of Abbreviations

Diagnostic An instrument used to record data during a laser-plasma experiment.

Gating The use of electronics to limit the exposure time of an image taken with a CCD camera.

Jitter In an experiment using laser beams from two or more sources, when a signal from the main laser system is used to trigger the firing of the secondary beams there is an uncertainty in the time at which the secondary beams will arrive at the target with respect to the pulse from the main beam. This is known as jitter.

Self-emission Radiation emitted by a plasma which is not the result of external stimulation.

Shot The firing of a laser pulse onto a target.

Target In a laser-plasma experiment, this describes the object with which the laser interacts in order to create the plasma. the object does not have to be a solid - if a plasma is created by ionising a volume of gas with a laser, the gas is in this case the target.

Target normal The direction normal to the front surface of a target. In the case of a cylindrically symmetric target, the axis of symmetry.

Timing Either (i) the procedure of synchronising the arrival of two laser beams at a particular point in space or (ii) the procedure used to find the correct electronic delay necessary for a CCD camera with a short exposure time to capture the exact moment when a laser pulse strikes the surface of a target.

AGN	**A**ctive **G**alactic **N**ucleus
CLF	**C**entral **L**aser **F**acility
GOI	**G**ated **O**ptical **I**mager
FWHM	**F**ull **W**idth at **H**alf **M**aximum
HD	**H**ydro**d**ynamics
HH	**H**erbig-**H**aro
ILE	**I**nstitute of **L**aser **E**ngineering
LULI	**L**aboratoire pour l'**U**tilisation des **L**asers **I**ntenses
LTE	**L**ocal **T**hermodynamic **E**quilibrium
MHD	**M**agneto-**H**ydro**d**ynamics
SOP	**S**treaked Self-emission **O**ptical **P**yrometer
YSO	**Y**oung **S**tellar **O**bject

References

[1] "Experiments on radiative collapse in laser-produced plasmas relevant to astrophysical jets", K. Shigemori, R. Kodama, D. R. Farley, T. Koase, K. G. Estabrook, B. A. Remington, D. D. Ryutov, Y. Ochi, H. Azechi, J. Stone, N. Turner, Physics Review E **62**, 6 (2000)

[2] "Studies of supersonic, radiative plasma jet interaction with gases at the Prague Asterix Laser System facility", Ph. Nicolaï, C. Stenz, A. Kasperczuk, T. Pisarczyk, D. Klir, L. Juha, E. Krousky, K. Masek, M. Pfeifer, K. Rohlena, J. Skala, V. Tikhonchuk, X. Ribeyre, S. Galera, G. Schurtz, J. Ullschmied, M. Kalal, J. Kravarik, P. Kubes, P. Pisarczyk, T. Schlegel, Physics of Plasmas **15**, 082701 (2008)

[3] The codes HYADES and h2d are proprietary software of Cascade Applied Sciences, Inc., Longmont, Colorado, USA.

[4] "Laboratory Experiments to Study Astrophysical Shock and Jets", Y. Sakawa, A. Oya, S. Dono, T. Kimura, N. Ozaki, B. Loupias, J. Waugh, H. Nagatomo, K. Shigemori, H. Takabe, T. Norimatsu, R. Kodama, M. Koenig, N. Woolsey, Journal of Physics: Conference Series **112**, 042020 (2008)

[5] "Propagation of laser-generated plasma jet in an ambient medium", B. Loupias, E. Falize, C. D. Gregory, T. Vinci, S. Pikuz, J. Waugh, M. Koenig, A. Ravasio, W. Nazarov, C. Michaut, S. Bouquet, Y. Kuramitsu, D. Seiichi, N. C. Woolsey, Y. Sakawa, H. Takabe, A. Schiavi, S. Atzeni, Plasma Physics and Controlled Fusion **51**, 124027 (2009)

[6] "The development of a Multi-Terrawatt Femtosecond Laser Facility - Astra", A. J. Langley, E. J. Divall, C. H. Hooker, M. H. R. Hutchinson, A. J.-M. P. Lecot, D. Marshall, M. E. Payne, P. F. Taday, Central Laser Facility Rutherford Appleton Laboratory Annual Report 1999-2000, pp. 196-200. The Astra laser system is located at the Central Laser Facility, Rutherford Appleton Laboratory, Harwell Science and Innovation Campus, Didcot, Oxfordshire, OX11 0QX. t the time of writing (16$^{\text{th}}$ March 2011), information on Astra may be found at http://www.clf.rl.ac.uk/Facilities/Astra/12254.aspx.

[7] "The GEKKO XII-HIPER (High Intensity Plasma Experimental Research) System Relevant to Ignition Targets", N. Miyanaga, M. Nakatsuka, H.

Azechi, H. Shiraga, T. Kanabe, H. Asahara, H. Daido, H. Fujita, K. Fujita, Y. Izawa, T. Jitsuno, T. Kawasaki, H. Kitamura, S. Matsuo, K. Mima, N. Morio, M. Nakai, S. Nakai, K. Nishihara, H. Nishimura, T. Sakamoto, K. Shigemori, K. Sueda, K. Suzuki, K. Tsubakimoto, H. Takabe, S. Urushihara, H. Yoshida, T. Yamanaka, T. Yamanaka, http://www.iaea.org/programmes/ripc/physics/fec2000/html/node275.htm.

[8] "Investigation of Jet Collimation using Astra", J. N. Waugh, C. D. Gregory, L. A. Wilson, B. Loupias, E. Brambrink, M. Koenig, Y. Sakawa, Y. Kuramitsu, H. Takabe, R. Kodama, N. C. Woolsey, Central Laser Facility Annual Report 2007/2008, 99-102

[9] "A jet production experiment using the high-repetition rate Astra laser", J. N. Waugh, C. D. Gregory, L. A. Wilson, B. Loupias, E. Brambrink, M. Koenig, Y. Sakawa, Y. Kuramitsu, H. Takabe, R. Kodama, N. C. Woolsey, Astrophysics and Space Science **322**, 31-35 (2009)

[10] "LyX - The Document Processor", at the time of writing (16$^{\text{th}}$ March 2011) freely available from http://www.lyx.org.

[11] Microsoft Paint, Microsoft Corporation, One Microsoft Way, Redmond, WA 98052-6399, USA (2007)

[12] ImageJ, W. S. Rasband, U. S. National Institutes of Health, Bethesda, Maryland, USA, available from http://rsb.info.nih.gov/ij/, 1997-2011

[13] "The Role of Magnetic Fields on Astrophysical Jets", E. M. de Gouveia Dal Pino, Invited Review at the conference "Magnetic Fields in the Universe: from Laboratory and Stars to the Primordial Structure", Angra dos Reis, Brazil (2004), arXiv:astro-ph/0505521v1 (2005)

[14] "Astrophysical Jets and Outflows", E. M. de Gouveia Dal Pino, Invited Review for the ASSE 2004 Meeting (2004), arXiv:astro-ph/0406319v1 (2004)

[15] "Magnetic fields in stellar jets", P. Hartigan, A. Frank, P. Varniére, E. G. Blackman, The Astrophysical Journal **661**, 910-918 (2007); also arXiv:astro-ph/0702174v1 (2007)

[16] "The First Three Million Years", T. Ray, Lecture Notes in Physics **723**, 3-19 (2007), published in "Jets from Young Stars", J. Ferreira, C. Dougados, E. Whelan (editors), Springer (2007), ISBN 978-3-540-68033-8

[17] "Jets from Young Stars: the Need for MHD Collimation and Acceleration Processes", S. Cabrit, Lect. Notes Phys. **723**, 21-53 (2007), published in "Jets from Young Stars", J. Ferreira, C. Dougados, E. Whelan (editors), Springer (2007), ISBN 978-3-540-68033-8

[18] "The structure and evolution of radiatively cooling jets", J. M. Blondin, B. A. Fryxell, A. Königl, The Astrophysical Journal **360**, 370-386 (1990)

[19] "The dynamic and gravitational instabilities of spherical shocks", E. T. Vishniac, The Astrophysical Journal **274**, 152-167 (1983)

[20] "The interaction of high-power lasers with plasmas", S. Eliezer, IoP (Institute of Physics Publishing), Series editors S. Cowley, P. Stott, H. Wilhelmsson (2002)

[21] "Collimation, proper motions, and physical conditions in the HH 30 jet from Hubble Space Telescope slitless spectroscopy", P. Hartigan, J. Morse, The Astrophysical Journal **660**, 426-440 (2007)

[22] "The structure of optical stellar jets: a phenomenological analysis", F. Bacciotti, C. Chiuderi, E. Oliva, Astronomy and Astrophysics **296**, 185-200 (1995)

[23] "High-Energy-Density Physics Fundamentals, Inertial Fusion, and Experimental Astrophysics", R. P. Drake, Springer, editors L. Davison, Y. Horie (2006), ISBN 3-540-29314-0

[24] "Observations of jet diameter, density and dynamics", F. Bacciotti, T. P. Ray, J. Eislöffel, J. Woitas, J. Solf, R. Mundt, C. J. Davis, Astrophysics and Space Science **287**, 3-13 (2003)

[25] "The Ionization State Along the Beam of Herbig-Haro Jets", F. Bacciotti, Herbig-Haro Flows and the Birth of Stars; IAU Symposium No. 182, eds B. Reipurth, C. Bertout, Kluwer Academic Publishers, 73-82 (1997)

[26] "Astrophysical jets: a phenomenological examination of acceleration and collimation", M. Livio, Physics Reports **311**, 225-245 (1999)

[27] "Theory of MHD Jets and Outflows", K. Tsinganos, Lect. Notes Phys. **723**, 117-159 (2007), published in "Jets from Young Stars", J. Ferreira, C. Dougados, E. Whelan (editors), Springer (2007), ISBN 978-3-540-68033-8

[28] "Further indications of jet rotation in new ultraviolet and optical Hubble Space Telescope STIS spectra", D. Coffey, F. Bacciotti, T. P. Ray, J. Eislöffel, J. Woitas, The Astrophysical Journal **663**, 350-364 (2007)

[29] "Simulating protostellar jets simultaneously at launching and observational scales", J. P. Ramsey, D. A. Clarke, The Astrophysical Journal **728**, 1, L11 (2011), arXiv: astro-ph.SR 1012.3723

[30] "Herbig-Haro Flows: Probes of Early Stellar Evolution", B. Reipurth, J. Bally, Annual Review of Astronomy and Astrophysics **39**, 403-55 (2001)

[31] At the time of writing (16^{th} March 2011), information on the JETSET Marie Curie Research Training Network can be found on the webpage http://www.jetsets.org/home.html.

[32] "Stellar Jets: Clues to the Process of Star and Planet Formation", S. Edwards, Lect. Notes Phys. **742**, 3-13 (2008), published in "Jets from Young Stars II", F. Bacciotti, E. Whelan, L. Testi (editors), Springer (2008), ISBN 978-3-540-68031-4

[33] "Transit Flows and Jet Asymptotics", T. Lery, Lect. Notes Phys. **723**, 161-180 (2007), published in "Jets from Young Stars", J. Ferreira, C. Dougados, E. Whelan (editors), Springer (2007), ISBN 978-3-540-68033-8

[34] "Similarity criteria for the laboratory simulation of supernova hydrodynamics", D. Ryutov, R. P. Drake, J. Kane, E. Liang, B. A. Remington, W. M. Wood-Vasey, The Astrophysical Journal **518**, 821-832 (1999)

[35] "Lie group invariance properties of radiation hydrodynamics equations and their associated similarity solutions", S. V. Coggeshall, R. A. Axford, Physics of Fluids **29**, 8, 2398-2420 (1986)

[36] "Criteria for scaled laboratory simulations of astrophysical MHD phenomena", D. D. Ryutov, R. P. Drake, B. A. Remington, The Astrophysical Journal Supplement Series **127**, 465-468 (2000)

[37] "Physics of Shock Waves and High-Temperature Hydrodynamic Phenomena", Ya. B. Zel'dovich, Yu. P. Raizer, Dover Publications Inc., Editors W. D. Hayes, R. F. Probstein (2002 - republication of the 1966 edition published by Academic Press, Inc.), ISBN 0-486-42002-7

[38] "Introduction to Magneto-Hydrodynamics", G. Pelletier, Lecture Notes in Physics **723**, 77-101 (2007), published in "Jets from Young Stars", J. Ferreira, C. Dougados, E. Whelan (editors), Springer (2007), ISBN 978-3-540-68033-8

[39] "Magnetohydrodynamic scaling: From astrophysics to the laboratory", D. D. Ryutov, B. A. Remington, H. F. Robey, Physics of Plasmas **8**, 5, 1804-1816 (2001)

[40] "Analytic solutions of hydrodynamics equations", S. V. Coggeshall, Physics of Fluids A **3**, 5, 757-769 (1991)

[41] "Radiation Hydrodynamics Scaling Laws in High Energy Density Physics and Laboratory Astrophysics", É. Falize, S. Bouquet, C. Michaut, Journal of Physics: Conference Series **112**, 042016 (2008)

[42] "Scaling laws for radiating fluids: the pillar of laboratory astrophysics", E. Falize, S. Bouquet, C. Michaut, Astrophysics and Space Science **322**, 107-111 (2009)

[43] "Astrophysical Radiation Dynamics: The Prospects for Scaling", J. I. Castor, Astrophysics and Space Science **307**, 207-211 (2007)

[44] "Astrophysical jet experiments with laser-produced plasmas", C. D. Gregory, PhD Thesis, University of York, Physics Department (May 2007)

[45] "High-energy-density laboratory astrophysics studies of jets and bow shocks", J. M. Foster, B. H. Wilde, P. A. Rosen, R. J. R. Williams, B. E. Blue, R. F. Coker, R. P. Drake, A. Frank, P. A. Keiter, A. M. Khokhlov, J. P. Knauer, T. S. Perry, The Astrophysical Journal **634**, L77-L80 (2005)

[46] "Laboratory-astrophysics jet experiments at the omega laser facility", P. A. Rosen, J. M. Foster, R. J. R. Williams, B. H. Wilde, R. F. Coker, B. Blue, T. S. Perry, P. Hartigan, R. P. Drake, K. Dannenberg, A. M. Khokhlov, A. Frank, J. P. Knauer, J. Phys. IV France **133**, 1019-1023 (2006)

[47] The Omega laser system is found at the Laboratory for Laser Energetics (LLE), University of Rochester, 250 E. River. Rd., Rochester, NY 14623-1212. At the time of writing (16$^{\text{th}}$ March 2011), information on Omega may be found on the wepage http://www.lle.rochester.edu/omega_facility.

[48] "Experimental Investigation of High-Mach-Number 3D Hydrodynamic Jets at the National Ignition Facility", B. E. Blue, S. V. Weber, S. G. Glendinning, N. E.

Lanier, D. T. Woods, M. J. Bono, S. N. Dixit, C. A. Haynam, J. P. Holder, D. H. Kalantar, B. J. MacGowan, A. J. Nikitin, V. V. Rekow, B. M. Van Wonterghem, E. I. Moses, P. E. Stry, B. H. Wilde, W. W. Hsing, H. F. Robey, Physical Review Letters **94**, 095005 (2005)

[49] The NIF laser system is found at the National Ignition Facility, Lawrence Livermore National Laboratory, 7000 East Avenue, Livermore, CA 94550. At the time of writing (16$^{\text{th}}$ March 2011), the NIF laboratory has its main web page at https://lasers.llnl.gov/.

[50] "NOVA high-speed jet experiments", L. M. Logory, P. L. Miller, P. E. Stry, The Astrophysical Journal Supplement Series **127**, 423-428 (2000)

[51] "Supersonic jet and shock interactions", J. M. Foster, B. H. Wilde, P. A. Rosen, T. S. Perry, M. Fell, M. J. Edwards, B. F. Lasinski, R. E. Turner, M. L. Gittings, Physics of Plasmas **9**, 5 (2002)

[52] Laboratoire pour l'Utilisation des Lasers Intenses, Ecole Polytechnique, 91128 Palaiseau Cedex, France. At the time of writing (16$^{\text{th}}$ March 2011), the LULI laboratory has its main web page at http://www.luli.polytechnique.fr/.

[53] "Plasma jet experiments in vacuum and in ambient medium using high energy lasers", B. Loupias, E. Falize, C. D. Gregory, O. Akira, T. Vinci, J. Howe, M. Koenig, N. C. Woolsey, N. Ozaki, A. Benuzzi-Mounaix, S. Bouquet, C. Michaut, M. Rabec le Goahec, W. Nazarov, T. Pikuz, A. YA. Faenov, Y. Aglitskiy, S. Atzeni, A. Schiavi, Y. Sakawa, H. Takabe, R. Kodama, Journal of Physics: Conference Series **112**, 042022 (2008)

[54] The LULI 2000 laser system is found at Laboratoire pour l'Utilisation des Lasers Intenses, Ecole Polytechnique, 91128 Palaiseau Cedex, France. At the time of writing (16$^{\text{th}}$ March 2011), it has the web page http://www.luli.polytechnique.fr/pages/facilities_overview.htm.

[55] Institute of Laser Engineering, Osaka University, 2-6 Yamadaoka, Suita, Osaka, 585-0871. At the time of writing (16$^{\text{th}}$ March 2011), the Institute has its main web page at http://www.ile.osaka-u.ac.jp/.

[56] The Vulcan laser system is located at the Central Laser Facility, Rutherford Appleton Laboratory, Harwell Science and Innovation Campus, Didcot, Oxfordshire,

OX11 0QX. At the time of writing (16th March 2011), information on Vulcan may be found at http://www.clf.rl.ac.uk/Facilities/Vulcan/12248.aspx.

[57] "Astrophysical jet experiments with colliding laser-produced plasmas", C. D. Gregory, J. Howe, B. Loupias, S. Myers, M. M. Notley, Y. Sakawa, A. Oya, R. Kodama, M. Koenig, N. C. Woolsey, The Astrophysical Journal **676**, 420-426 (2008)

[58] "Radiative Jet Experiments of Astrophysical Interest Using Intense Lasers", D. R. Farley, K. G. Estabrook, S. G. Glendinning, S. H. Glenzer, B. A. Remington, K. Shigemori, J. M. Stone, R. J. Wallace, G. B. Zimmerman, J. A. Harte, Physical Review Letters **83**, 10 (1999)

[59] "Recent results from the Nova program at LLNL", E. M. Campbell, Lasers and Particle Beams **9**, 209-231 (1991)

[60] "The Prague Asterix Laser System", K. Jungwirth, A. Cejnarova, L. Juha, B. Kralikova, J. Krasa, E. Krousky, P. Krupickova, L. Laska, K. Masek, T. Mocek, M. Pfeifer, A. Präg, O. Renner, K. Rohlena, B. Rus, J. Skala, P. Straka, J. Ullschmied, Physics of Plasmas **8**, 5, 2495-2501 (2001). The Prague Asterix Laser System is located at the PALS Research Centre, Institute of Physics, Academy of Sciences of the Czech Republic, Za Slovankou 3, 182 21 Prague 8, Czech Republic. At the time of writing (16th March 2011), the laboratory has its main web page at http://www.pals.cas.cz/pals/.

[61] "Stable dense plasma jets produced at laser power densities around 10^{14} W/cm^2", A. Kasperczuk, T. Pisarczyk, S. Borodziuk, J. Ullschmied, E. Krousky, K. Masek, K. Rohlena, J. Skala, H. Hora, Physics of Plasmas **13**, 062704 (2006)

[62] "Plasma jets produced in a single laser beam interaction with a planar target", Ph. Nicolaï, V. T. Tikhonchuk, A. Kasperczuk,, T. Pisarczyk, S. Borodziuk, K. Rohlena, J. Ullschmied, Physics of Plasmas **13**, 062701 (2006)

[63] "La Fusion Thermonucléaire Inertielle par Laser", Part 3, Volume 2, p. 1117, Eyrolles, Paris (1993), author G. Schurtz, editors R. Dautray and J. P. Watteau

[64] "Influence of target material on structure of the plasma outflow produced by a partly defocused laser beam", A. Kasperczuk, T. Pisarczyk, M. Kalal, J. Ullschmied, E. Krousky, K. Masek, M. Pfeifer, K. Rohlena, J. Skala, P. Pisarczyk, Applied Physics Letters **94**, 8, 081501 (2009)

[65] "Investigation of plasma ablation and crater formation processes in the Prague Asterix Laser System laser facility", S. Borodziuk, A. Kasperczuk, T. Pisarczyk, S, Gus'kov, J. Ullschmied, B. Kralikova, K. Rohlena, J. Skala, M. Kalal, P. Pisarczyk, Optica Applicata **XXXIV**, 1 (2004)

[66] "Laboratory modeling of supersonic radiative jets propagation in plasmas and their scaling to astrophysical conditions", V. T. Tikhonchuk, Ph. Nicolaï, X. Ribeyre, C. Stenz, G. Schurtz, A. Kasperczuk, T. Pisarczyk, L. Juha, E. Krousky, K. Masek, M. Pfeifer, K. Rohlena, J. Skala, J. Ullschmied, M. Kalal, D. Klir, J. Kravarik, P. Kubes, P. Pisarczyk, Plasma Physics and Controlled Fusion **50**, 124056 (2008)

[67] "The influence of target irradiation conditions on the parameters of laser-produced plasma jets", A. Kasperczuk, T. Pisarczyk, S. Borodziuk, J. Ullschmied, E. Krousky, K. Masek, M. Pfeifer, K. Rohlena, J. Skala, P. Pisarczyk, Physics of Plasmas **14**, 032701 (2007)

[68] "Dynamics of converging laser-created plasmas in semicylindrical cavities studied using soft x-ray laser interferometry", M. Purvis, J. Grava, J. Filevich, M. C. Marconi, J. Dunn, S. J. Moon, V. N. Shlyaptsev, E. Jankowska, J. J. Rocca, Physical Review E **76**, 046402 (2007)

[69] "Dynamics of a dense laboratory plasma jet investigated using soft X-ray laser interferometry", J. Grava, M. A. Purvis, J. Filevich, M. C. Marconi, J. J. Rocca, J. Dunn, S. J. Moon, V. N. Shlyaptsev, Physical Review E **78**, 016403 (2008)

[70] "Bow shocks formed by plasma collisions in laser irradiated semi-cylindrical cavities", J. Filevich, M. Purvis, J. Grava, D. P. Ryan, J. Dunn, S. J. Moon, V. N. Shlyaptsev, J. J. Rocca, High Energy Density Physics **5**, 276-282 (2009)

[71] "Study of high Mach number laser driven blast waves". A. D. Edens, T. Ditmire, J. F. Hansen, M. J. Edwards, R. G. Adams, P. Rambo, L. Ruggles, I. C. Smith, J. L. Porter, Physics of Plasmas **11**, 11 (2004)

[72] "Laboratory astrophysics and collimated stellar outflows: the production of radiatively cooled hypersonic plasma jets", S.V. Lebedev, J. P. Chittenden. F. N. Beg, S. N. Bland, A. Ciardi, D. Ampleford, S. Hughes, M. G. Haines, A. Frank, E. G. Blackman, T. Gardiner, The Astrophysical Journal **564**, 113-119 (2002)

[73] "MHD models and laboratory experiments of jets", T. A. Gardiner, A. Frank, E. G. Blackman, S. V. Lebedev, J. P. Chittenden, D. Ampleford, S. N. Bland, A. Ciardi, M. Sherlock, M. G. Haines, Astrophysics and Space Science **287**, 69-74 (2003)

[74] "Jet deflection via crosswinds: laboratory astrophysical studies", S. V. Lebedev, D. Ampleford, A. Ciardi, S. N. Bland, J. P. Chittenden, M. G. Haines, A. Frank, E. G. Blackman, A. Cunningham, The Astrophysical Journal **616**, 988-997 (2004)

[75] "Modeling magnetic tower jets in the laboratory", A. Ciardi, S. V. Lebedev, J. P. Chittenden, D. J. Ampleford, S. N. Bland, B. S. Bott, J. Rapley, Astrophysics and Space Science **298**, 277-286 (2005)

[76] "A HED laboratory astrophysics testbed comes of age: jet deflection via cross winds", A. Frank, E. G. Blackman, A. Cunningham, S. V. Lebedev, D. Ampleford, A. Ciardi, S. N. Bland, J. P. Chittenden, M. G. Haines, Astrophysics and Space Science **298**, 107-114 (2005)

[77] "Magnetic tower outflows from a radial wire array Z-pinch", S. V. Lebedev, A. Ciardi, D. J. Ampleford, S. N. Bland, S. C. Bott, J. P. Chittenden, G. N. Hall, J. Rapley, C. A. Jennings, A. Frank, E. G. Blackman, T. Lery, Monthly Notices of the Royal Astronomical Society **361**, 97-108 (2005)

[78] "Production of radiatively cooled hypersonic plasma jets and links to astrophysical jets", S. V. Lebedev, A. Ciardi, D. J. Ampleford, S. N. Bland, S. C. Bott, J. P. Chittenden, G. N. Hall, J. Rapley, C. Jennings, M. Sherlock, A. Frank, E. G. Blackman, Plasma Physics and Controlled Fusion **47**, B465-B479 (2005)

[79] "3D MHD Simulations of Laboratory Plasma Jets", A. Ciardi, S. V. Lebedev, A. Frank, E. G. Blackman, D. J. Ampleford, C. A. Jennings, J. P. Chittenden, T. Lery, S. N. Bland, S. C. Bott, G. N. Hall, J. Rapley, F. A. Suzuki Vidal, A. Marrocchino, Astrophysics and Space Science **307**, 17-22 (2007)

[80] "The evolution of magnetic tower jets in the laboratory", A. Ciardi, S. V. Lebedev, A. Frank, E. G. Blackman, J. P. Chittenden, C. J. Jennings, D. J. Ampleford, S. N. Bland, S. C. Bott, J. Rapley G. N. Hall, F. A. Suzuki-Vidal, A. Marocchino, T. Lery, C. Stehle, Physics of Plasmas **14**, 056501 (2007)

[81] "Supersonic Radiatively Cooled Rotating Flows and Jets in the Laboratory", D. J. Ampleford, S. V. Lebedev, A. Ciardi, S. N. Bland, S. C. Bott, G. N. Hall, N.

Naz, C. A. Jennings, M. Sherlock, J. P. Chittenden, J. B. A. Palmer, A. Frank, E. Blackman, Physical Review Letters **100**, 035001 (2008)

[82] "Curved Herbig-Haro Jets: Simulations and Experiments", A. Ciardi, D. J. Ampleford, S. V. Lebedev, C. Stehle, The Astrophysical Journal **678**, 968-973 (2008)

[83] "Episodic magnetic bubbles and jets: astrophysical implications from laboratory experiments", A. Ciardi, S. V. Lebedev, A. Frank, F. Suzuki-Vidal, G. N. Hall, S. N. Bland, A. Harvey-Thompson, E. G. Blackman, M. Camenzind, The Astrophysical Journal **691**, L147-L150 (2009)

[84] "Laboratory Studies of Astrophysical Jets", A. Ciardi, arXiv:0903.0268v1 (2009)

[85] The MAGPIE (Mega-Ampere Generator for Plasma Implosion Experiments) Z-pinch is at Imperial College, London. At the time of writing (16$^{\text{th}}$ March 2011), the laboratory has its main web page at http://dorland.pp.ph.ic.ac.uk/magpie/.

[86] "A laboratory plasma experiment for studying magnetic dynamics of accretion discs and jets", S. C. Hsu, P. M. Bellan, Monthly Notices of the Royal Astronomical Society **334**, 257-261 (2002)

[87] "Experimental Identification of the Kink Instability as a Poloidal Flux Amplification Mechanism for Coaxial Gun Spheromak Formation", S. C. Hsu, P. M. Bellan, Physical Review Letters **90**, 21, 215002 (2003)

[88] "On the jets, kinks, and spheromaks formed by a planar magnetized coaxial gun", S. C. Hsu, P. M. Bellan, Physics of Plasmas **12**, 032103 (2005)

[89] "Dynamic and Stagnating Plasma Flow Leading to Magnetic-Flux-Tube Collimation", S. You, G. S. Yun, P. M. Bellan, Phys. Rev. Lett. **95**, 045002 (2005), arXiv:plasma-ph/0506221v1

[90] "Intense Picosecond X-ray pulses from Laser Plasmas by Use of Nanostructured "Velvet" Targets", G. Kulcsár, D. AlMawlawi, F. W. Budnik, P. R. Herman, M. Moskovits, L. Zhao, R. S. Marjoribanks, Physical Review Letters **84**, 22, 5149-5152 (2000)

[91] "Digital evaluation of interferograms", M. Hipp, J. Woisetschläger, P. Reiterer, T. Neger, Measurement **36**, 53-66 (2004)

[92] "Principles of Plasma Diagnostics", I. H. Hutchinson, Cambridge University Press, 1994 re-print of the paperback edition, first published 1987

[93] "Uniqueness in the Inversion of Inaccurate Gross Earth Data", G. Backus, F. Gilbert, Philosophical Transactions of the Royal Society of London A **266**, 123-192 (1970)

[94] "User Manual for IDEA 1.7", M. Hipp, P. Reiterer, Institut Für Experimental Physik, Technische Universität Graz (2003)

[95] "Transformation of Observed Radiances into Radial Distribution of the Emission of a Plasma", K. Bockasten, Journal of the Optical Society of America **51**, 9 (1961)

[96] "Generalised coefficients for Abel inversion", R. Illingworth, R. K. Thareja, Journal of Physics E: Scientific Instruments **14**, 147-148 (1981)

[97] "Reconstruction of Abel-transformable images: the Gaussian basis-set expansion Abel transform method", V. Dribinski, A. Ossadtchi, V. A. Mandelshtam, H. Reisler, Review of Scientific Instruments **73**, 7 (2002)

[98] "Tables of Physical and Chemical Constants and some Mathematical Functions", 14^{th} edition, G. W. C. Kaye, T. H. Laby, Longman, first published 1973, reprinted with corrections 1975, ISBN 0-582-46326-2

[99] "Efficient coupling of high-intensity subpicosecond laser pulses into solids", M. M. Murnane, H. C. Kapteyn, S. P. Gordon, J. Bokor, E. N. Glytsis, R. W. Falcone, Applied Physics Letters **62**, 10, 1068-1070 (1993)

[100] MATLAB®, version R2007a, The MathWorks™, Boston, Massachusetts, USA

[101] "Numerical analysis of jets produced by intense laser", A. Mizuta, S. Yamada, H. Takabe, The Astrophysical Journal **567**, 635-642 (2002)

[102] "Laboratory observation of secondary shock formation ahead of a strongly radiative blast wave", J. F. Hansen, M. J. Edwards, D. H. Froula, G. Gregori, A. D. Edens, T. Ditmire, Physics of Plasmas **13**, 022105 (2006)

[103] "A Cell-Centred Lagrangian Scheme for Two-Dimensional Compressible Flow Problems", P.-H. Maire, R. Abgrall, J. Breil, J. Ovadia, SIAM Journal on Scientific Computing **29**, 4, 1781-1824 (2007)

[104] Central Laser Facility, Rutherford Appleton Laboratory, Harwell Science and Innovation Campus, Didcot, Oxfordshire, OX11 0QX. At the time of

writing (16th March 2011), the Central Laser Facility web homepage is http://www.clf.rl.ac.uk/.

[105] "LASNEX - A 2-D Physics Code for Modeling ICF", J. A. Harte, W. E. Alley, D. S. Bailey, J. L. Eddleman, G. B. Zimmerman, Inertial Confinement Fusion quarterly report July-September 1996 **6**, 4, 150-164 (1996). This is a review article rather than the first appearance of the code in the literature.

[106] HYADES User Guide, produced by Cascade Applied Sciences, Inc., Longmont, Colorado, USA

[107] "SESAME: The Los Alamos National Laboratory Equation of State Database", S. P. Lyon and J. D. Johnson, editors, Los Alamos National Laboratory Report LA-UR-92-3407 (1992). The SESAME Equation-of-State Library is developed and maintained by the Mechanics of Materials and Equation-of-State Group (T-1) of the Theoretical Division at Los Alamos National Laboratory, USA. At the time of writing (16th March 2011), information may be obtained from the webpage http://t1web.lanl.gov/newweb_dir/t1sesame.html.

[109] "Simulations of the nonlinear Helmholtz equation: arrest of beam collapse, non-paraxial solitons and counter-propagating beams", G. Baruch, G. Fibich, S. Tsynkov, Optics Express **16**, 17, 13323-13329 (2008)

[108] "Development and applications of compact high-intensity lasers", G. Mourou, D. Umstadter, Physics of Fluids B **4**, 7, 2315-2325 (1992)

[109] "Electron density measurements of a colliding plasma using soft-x-ray laser interferometry", A. S. Wan, T. W. Barbee, Jr., R. Cauble, P. Celliers, L. B. Da Silva, J. C. Moreno, P. W. Rambo, G. F. Stone, J. E. Trebes, F. Weber, Physical Review E **55**, 5 (1997)

[110] "Tunneling ionization of Noble Gases in a High-Intensity Laser Field", S. Augst, D. Strickland, D. D. Meyerhofer, S. L. Chin, J. H. Eberly, Physics Review Letters **63**, 20, 2212-2215 (1989)

[111] "Physics of Fully Ionized Gases", L. Spitzer, Jr., Interscience, New York (1967); 2nd Revised edition, Dover Publications (2006), ISBN 0-486-44982-3

[112] "NRL Plasma Formulary", J. D. Huba, Naval Research Laboratory, Washington, DC 20375, edition revised 2002.

[113] "Kinetic to thermal energy transfer and interpenetration in the collision of laser-produced plasmas", C. Chenais-Popovics, P. Renaudin, O. Rancu, F. Gilleron, J.-C. Gauthier, O. Larroche, O. Peyrusse, M. Dirksmöller, P. Sondhauss, T. Missalla, I. Uschmann, E. Förster, O. Renner, E. Krousky, Physics of Plasmas **4**, 190 (1997)

[114] "Transport Processes in a Plasma", S. I. Braginskii, Soviet Physics JETP **6**, 358 (1958); Reviews of Plasma Physics **1**, Consultants Bureau, New York (1965), p. 205

[115] "FLYCHK: Generalized population kinetics and spectral model for rapid spectroscopic analysis for all elements", H.-K. Chung, M. H. Chen, W. L. Morgan, Y. Ralchenko, R. W. Lee, High Energy Density Physics **1**, 1, 3-12 (2005)

[116] "HYADES Book Chapter E. Thermal Energy Transport", produced by Cascade Applied Sciences, Inc., Longmont, Colorado, USA and available from http://www.casinc.com/downloads.html.

[117] "HYADES Book Chapter D. Hydrodynamics", produced by Cascade Applied Sciences, Inc., Longmont, Colorado, USA and available from http://www.casinc.com/downloads.html.

[118] "ZEUS-2D: A radiation magnetohydrodynamics code for astrophysical flows in two space dimensions. I. The hydrodynamic algorithms and tests", J. M. Stone, M. L. Norman, The Astrophysical Journal Supplement Series **80**, 753-790 (1992)

[119] "ZEUS-2D Simulations of Laser-Driven Radiative Shock Experiments", D. R. Leibrandt, R. P. Drake, J. M. Stone, Astrophysics and Space Science **298**, 1-2, 273-276 (2005)